Engineering Multifunctional Nanoparticles: Applied Nanoscale Therapeutics

by

Jason V. Gregory

A dissertation submitted in partial fulfillment
of the requirements for the degree of
Doctor of Philosophy
(Chemical Engineering)
in the University of Michigan
2022

Doctoral Committee:

Professor Joerg Lahann, Chair
Professor Maria Castro
Professor Lola Eniola-Adefeso
Professor Jinsang Kim

©Jason V. Gregory
jvgregor@umich.edu
ORCID ID: 0000-0002-7964-2027
2022

For my children.

Without their unconditional love and support,
their constant reminders of my motivation,
none of this would be possible.

TABLE OF CONTENTS

LIST OF FIGURES

LIST OF TABLES

LIST OF ACRONYMS

ADCs antibody drug conjugates

BBB blood-brain barrier

BCRP breast cancer resistance protein

CNS central nervous system

CTAB hexadecyltrimethylammonium bromide

DAMPs damage-associated molecular patterns

DLS Dynamic Light Scattering

ECM extracellular matrix

EHD electrohydrodynamic

EPR Enhanced Permeability and Retention

FBS fetal bovine serum

HSA human serum albumin

LAP lapatinib

MDR multidrug resistance

MEGM mammary epithelial cell growth medium

MIL Microscopy and Image Analysis Laboratory

MPS mononucular phagocyte system

MS median survival

NTA nanoparticle tracking analyzer

PAA polyacrylic acid

PBS phosphate buffered saline

PEG poly(ethylene glycol)

PEI polyethylenimine

PLGA poly(lactic-co-glycolic acid)

PS penicillin streptomycin

PTX paclitaxel

RBCs red blood cells

RES reticuloendothelial system

SEM Scanning Electron Microscopy

SIM Structured Illumination Microscopy

SPNPs Synthetic Protein Nanoparticles

STED stimulated emission depletion

TBS tris-buffered saline

TEM Tranmission Electron Microscopy

TFE trifloroethanool

TME tumor microenviroments

ABSTRACT

Decades of research towards the development of nanomedicines have, to date, yielded minimal clinical impact. Focused particularly on the treatment of cancer, the relatively low number of pursued technologies to reach the market can in part be attributed to the complex biological barriers and clearance mechanisms nanomedicines must overcome to reach their intended target. Together with a dynamic and heterogeneous disease landscape, the development of more sophisticated and multifunctional delivery systems may be required. Here, we leverage our ability to produce multifunctional nanoparticles through EHD co-jetting to engineer novel drug delivery systems.

Collaborative work first identified synergistic combinations of lapatinib and paclitaxel in $HER2^+$ breast cancer. Findings yielded optimized synergistic drug ratios and revealed a dependence upon the temporal delivery of the two agents. Utilizing EHD co-jetting and the synthetic polymers PLGA and pH responsive acetalated dextran, a controlled and scheduled release of two compounds was achieved from a single particle architecture. Decoupled release kinetics exhibited dependence upon bulk polymer properties, rather than chemical structures of encapsulated materials. These properties were leveraged to engineer dual drug-loaded Janus particles capable of sequentially releasing lapatinib and paclitaxel. Ultimately, we demonstrate an ability to achieve controlled delivery and similar synergistic activities in $HER2^+$ breast cancer cells, comparable to free-drug studies.

Inspired by nature, significant efforts were then directed at the development of synthetic protein nanoparticles (SPNPs). In moving away from synthetic polymers, we sought to develop more biocompatible particle systems capable of targeted delivery, rapid clearance from off-target organs, and to efficiently deliver therapeutics while minimizing harmful im-

mune responses. We began by developing an extensive protein particle platform, evaluating a range of proteins and crosslinking macromers. The engineered particles were shown to be monodisperse, stable, responsive to pH, and capable of encapsulating therapeutic molecules with diverse physical properties. The result is a modular platform, designed to evolve, with the capacity to optimize particle properties to meet disease-specific challenges. Extending beyond the bulk properties of SPNPs, we demonstrate an ability to actively target particles through cell-specific interactions and alter biodistribution. Compared to untargeted SPNPs, YN1 (Anti-ICAM) SPNPs exhibit an 80-fold increase in lung targeting following systemic delivery.

Finally, we leverage the active targeting and drug delivery capacity of SPNPs towards the treatment of glioblastoma (GBM). An axis for tumor progression and immune response in GBM, STAT3 serves as an attractive therapeutic target; however, inability to effectively traverse the blood-brain barrier (BBB) has limited clinical translation. Challenged with the task of accessing the CNS, we demonstrate an ability to successfully deliver therapeutic doses of siRNA against STAT3 across the BBB. Combined with standard of care, ionized radiation, the targeted protein particles result in 87.5% of mice reaching the long-term survival point in a highly aggressive intracranial GBM model. In addition to increased median survival, we observe a robust immune response characterized by increased tumor-antigen specific CD8 T cells and decreased immune suppressive M2 macrophages within the brain. When rechallenged, all previously cured mice are found to reach a second long-term survival time point in the absence of further treatments, suggesting the development of an anti-GBM immune response.

Moving forward, we aim to apply these fundamental understandings and design parameters towards engineering more complex protein particle systems capable of delivering multiple agents directed at diverse therapeutic targets through the use of our novel bicompartmental particle architecture.

CHAPTER 1

Introduction

This chapter contains portions of text originally published as:

"Emerging Methods in Therapeutics Using Multifunctional Nanoparticles."

N Habibi*, D Quevedo*, JV Gregory*, and Joerg Lahann

Nanomedicine and Nanobiotechnology (2020)

*Shared co-first authorship.

1.1 Motivations Towards Drug Delivery Carriers

In December of 1959, Richard P. Feynman stood before a crowd at the American Physical Society at CalTech to deliver his now famous lecture titled "Plenty of Room at the Bottom" which would later be considered a door opened to the world of nanotechnology. Since that December night in California, advances in science and medicine have gained momentum and progressed at a more rapid pace than any other equivalent period of time to date. Just a few years earlier the polio vaccine had been developed. Since that time, we have seen numerous other vaccines largely eradicate diseases, the first heart and liver transplants, synthetically produced insulin, and development of molecular therapeutics aimed to treat the most devastating diseases we have known. All in total, the advances made have added years of life expectancy and vastly improved life quality for millions. Despite these grand advances, work remains to be done.

As science and medicine has progressed, so too has our understanding of human physiology and the conditions and diseases that affect every subset of our population. This knowledge has been leveraged to develop a number of therapies, many for diseases that would have otherwise be considered untreatable. Today, cancers are routinely treated with novel small

molecule drugs and biologics. A diagnosis of HIV no longer carries with it the death sentence it once did, but instead, can be managed as a chronic condition. Genetic material can be used to encode for the synthesis of proteins designed to activate our immune system to guard against future infections or novel diseases. Yet, while recently developed therapeutics have shown promise, their dosing and administration are often limited by rapid clearance and degradation, non-specific biodistribution, and off-target side effects.

The ability to deliver a drug to an organ or tissue of interest and alter the compound's natural biodistribution has become a focus in recent decades running parallel to the development of novel pharmaceutical compounds. Of particular interest for the treatment of various cancers is the technology of antibody drug conjugates (ADCs) consisting of a monoclonal antibody with highly selective binding, a cytotoxic drug, and a linker to join the two. With dozens of ADCs currently in various stages of clinical trials, these modalities offer the promise of reduced toxicity and tumor selectively based on the antibody discriminating binding activity. In spite of their potential, examples of low efficacy compared to traditional chemotherapy and toxicity in healthy cells have meant that in some cases, they have failed to live up to their promised potential. A similar targeted approach with nanoparticles, and the added benefit of encapsulated and controlled release of cargo, may have the capacity of realizing comparable selectivity while minimizing off target effects observed in ADCs.

1.2 Nanotechnology: Current Medical Applications

Notably among the medical advances resulting from the development of nanotechnology is that of nanoparticles. Specifically, nanoparticles have been developed from an imaging and drug delivery perspective. Defined as having at least one dimension in the nanoscale, therapeutic and diagnostic nanoparticles have garnered increased attention in recent decades for their seemingly limitless potential applications. Major challenges when evaluating current therapeutic approaches, particularly for systemically administered drugs via intravenous injection, include i) non-targeted biodistribution and pharmacokinetic profiles; ii) dosing limited by off-target toxicities; iii) a need for repeated doses to maintain therapeutic relevant physiological concentrations; and iv) short circulation times as a result of rapid degradation or clearance from the body. Advances made in the drug delivery field attempt to address these limitations by providing a means of protecting therapeutic cargo, taking a targeted delivery approach, and creating a controlled release of encapsulated drugs or biologics. Despite this, few have successfully been commercially developed and managed to

make a meaningful clinical impact.

Attempts to develop nanoparticle technologies and their proposed use in a variety of medical applications have grown exponentially in recent decades. The scope of their properties, modes of preparation, compositions, and architectures vary vastly (Figure 1.1). Their mechanical, [12] [13] magnetic, [14] and optical [15] properties can be highly dependent upon their size and shape and therefore often vary dramatically from the equivalent properties of the material in their bulk form. As a result of these size and shape dependent properties, together with the extensive types of materials that can be brought into this scale, their unique properties have been applied to a vast number of emerging and advancing technologies.

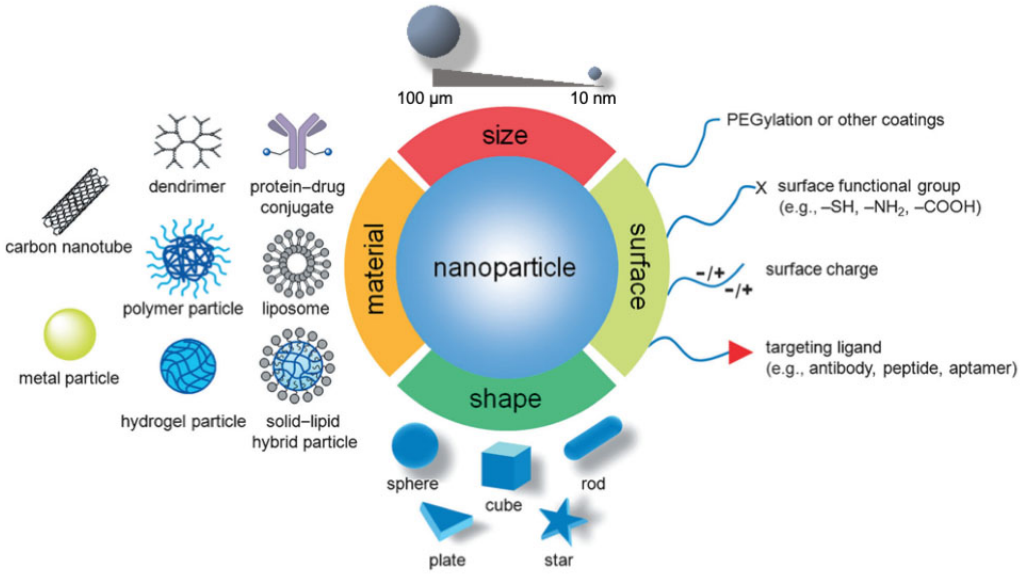

Figure 1.1: **Biophysiochemical properties of nanoparticle systems.** Nanoparticles developed for drug delivery and imaging applications include variations in particle size and shape, base material, and surface functionalities. Together, these parameters lead to an array of possible particle architectures. Reprinted with permission. Ref [1]

Researchers have leveraged nanotechnology potential to develop an array of innovations. In today's developed society, technological advances related to nanotechnology in fields such as computing, energy, imaging and medicine will undoubtedly impact a person's life on a daily basis. From a medical perspective, incredible efforts in research and development have been aimed at combating disease, improving patient health, have implications on how we detect disease conditions earlier, and the applied therapies available to treat the same. Potential impacts in a variety of biomedical applications including drug delivery, tissue engineering, and diagnostics have resulted.

As early as the 1960's, reports of synthetically produced nanoparticle systems loaded with drugs began to emerge. Beginning with the synthesis of liposomes, [16] focus evolved towards the loading and release of molecules, [17] extending circulation, [18] and creating targeted approachs (Figure 1.3). [19] In the following decades, the targeting of liposomes and increased circulation achieved through surface modification, or PEGylation, added a dimension where, combined with controlled release, offered promise in achieving truly targeted sustained drug delivery. By the turn of the century clinical studies of targeted particles were underway. [20] Despite this rapid progression and the tremendous research efforts in both industrial and academic settings, in many ways the translation of the technology towards FDA approved nano-based technologies is disappointing. To date, there are only approximately two dozen FDA approved such modalities for use in the clinic, though the number of active clinical trials continues to climb rapidly each year. [21]

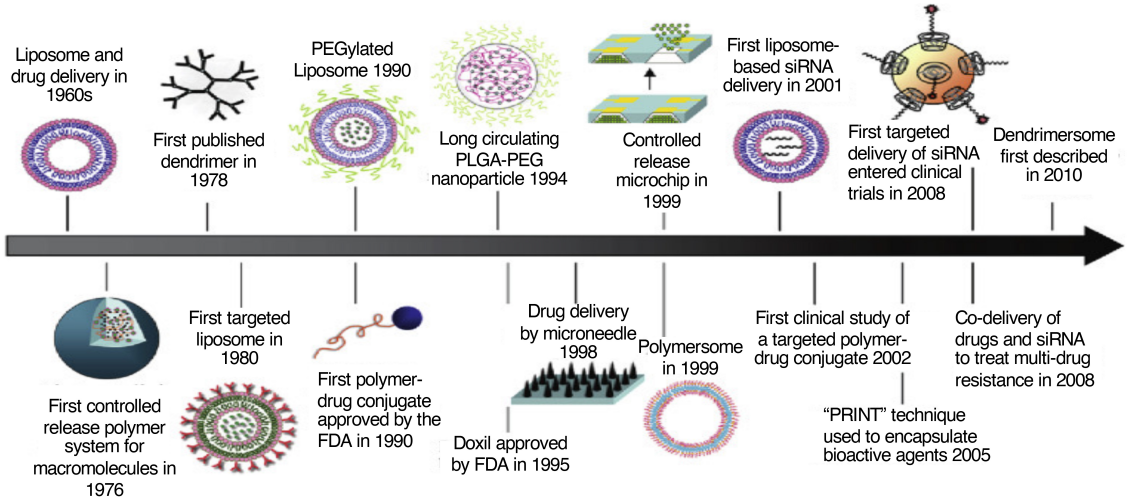

Figure 1.2: **Timeline for the development of nanoparticle drug delivery systems.** Beginning with drug delivery from liposomes nearly 60 years ago, nanoparticle systems have evolved towards more sophisticated approaches including targeted delivery. Reprinted with permission. Ref [2]

Among the limited number of therapies that have been approved and are today used in the clinic, this landscape is dominated by the delivery of small molecule drugs and the use of liposomes as a carrier system. Notable exceptions include the FDA approval of Abraxane in 2006 and recent approvals delivering biologics such as siRNA (e.g. ONPATTRO, 2018). At this time, multiple COVID vaccines delivering mRNA are currently approved for emergency use with full FDA approval expected in the near future (Figure 1.3). The breadth of FDA approved nanotechnologies used to treat or detect diseases include imaging modalities, anesthetics, fungal treatments, vaccines, treatment of chronic conditions, and cancer

therapy; the latter, makes up a significant portion of the ongoing clinical trials. It should be noted, that among these numbers include trials involving already approved nanomedicines. Abraxane for example, is being extensively evaluated for its use in additional cancers or being combined with additional chemotherapeutics for combination therapies.

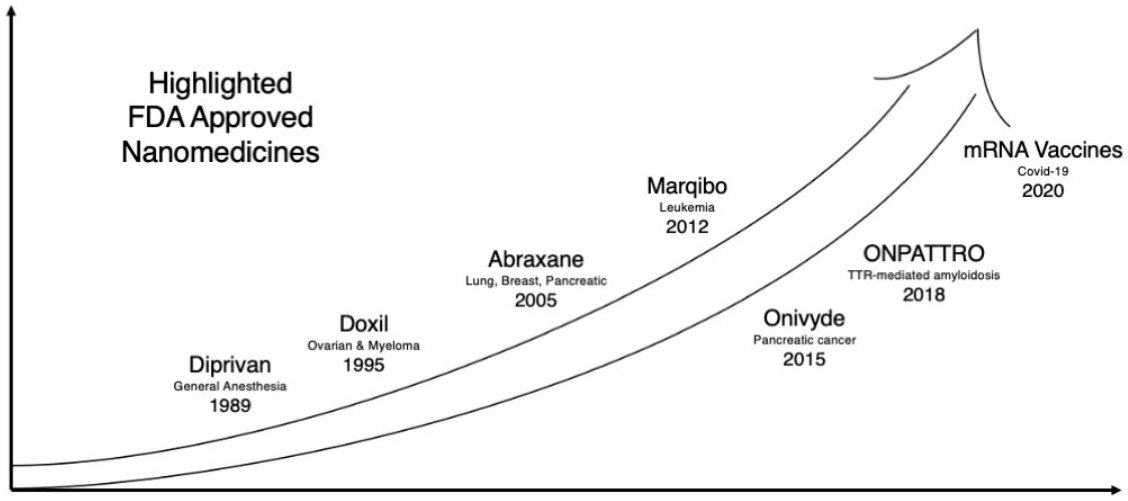

Figure 1.3: **Progression of FDA approval for nanomedicines.** Following early approvals in the late 1980's and Doxil (liposomal doxorubicin) in 1995, FDA approved nanomedicines have been limited; however, recent years have seen a steady increase. Dominated by the delivery of small molecule drugs and liposome formulations, notably outliers include Abraxane (albumin-bound paclitaxel, 2006), ONPATTRO (first FDA approved siRNA nanomedicine, 2018), and multiple mRNA vaccines receiving emergency use authorization for COVID-19 (Pfizer BioNTech, Moderna, and Johnson & Johnson, 2020).

1.3 Barriers in Targeted Drug Delivery

Nanoparticle-based drug delivery systems offer the promise of improved therapeutic outcomes through an ability to encapsulate, protect, and control the release of small molecule and biologics. Further, the potential to target these systems to organs, tissues, or specific cells of interest have motivated research into developing them in numerous therapeutic applications. Most notably among these is the development of cancer therapies in which the molecules being delivered often have severe side-effects and toxicities associated with them. Goals of encapsulation and targeted tissue accumulation therefore, drive the current science of drug delivery. While delivery systems have shown promise, the barriers which they must overcome create a multi-step process which has proved to be difficult to navigate. This is particularly true for systemic (intravenous) delivery, which require both extracellu-

lar and intracellular transport. Biological barriers responsible for the challenges in effective drug or gene delivery to the intended diseased tissue and their sequential order following systemic injection are discussed (Figure 1.4).

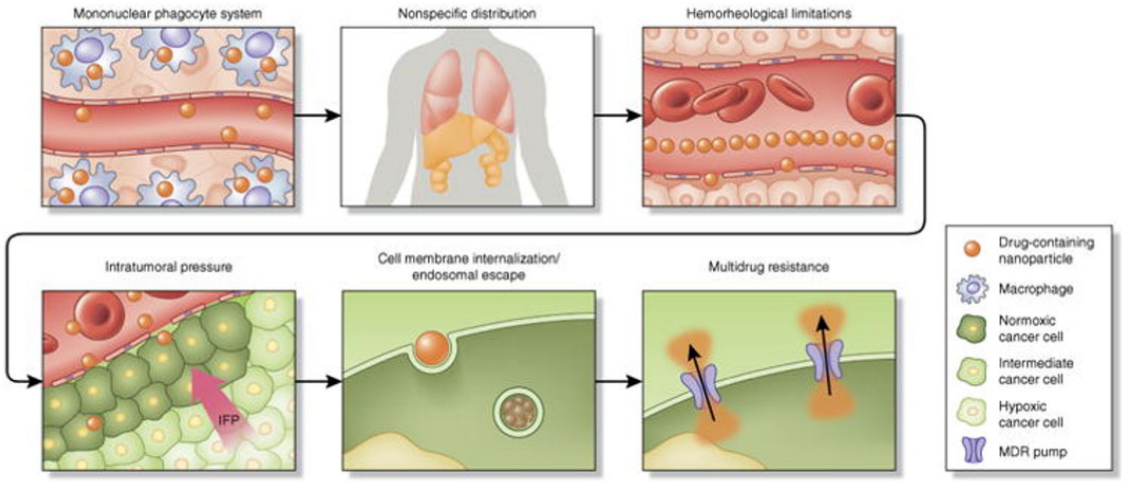

Figure 1.4: **Barriers to nanoparicle delivery.** Following systemic (intravenous) administration, injected nanoparticles encounter several sequential obstacles limiting efficacious, site-specific delivery to tumors. Reprinted with permission. Ref [3]

RES clearance

The reticuloendothelial system (RES) or mononucular phagocyte system (MPS) consists mainly of monocyte derived macrophages. Predominately found in the liver, but also in circulation, these cells are responsible for the clearance of foreign matter including circulating particles through phagocytosis. [22] Upon injection, opsonins will typically adsorb and bind to nanoparticle surfaces marking them as foreign and initiating their clearance by phagocytes. While designed to protect the body from foreign and potentially harmful materials that enter the blood stream, this acts as the initial barrier drug delivery vehicles must overcome to reach their intended target. As a result, RES clearance severely limits circulation times. To combat this, strategies to limit clearance have been implemented. a common and extensively studied approach is the coating of particle surfaces with non-fouling materials (e.g. polyethylene glycol, PEG) to inhibit the adsorption of opsonins. [23, 24] Alternatively, the addition of CD47 (Cluster of Differentiation 47) has been shown to limit this clearance. [25] Acting as a ”don’t eat me” signal, this transmembrane protein has been shown to be overexpressed on cancer cells which use a similar approach to avoid immune clearance. Another promising approach that has been explored, but to a far lesser extent, is the coating of particles with cellular membranes, wherein the particles present native cellular membrane proteins while in circulation. [26]

Nonspecific biodistribution

Clearance from circulation attributed to the RES results in a disproportionate fraction of the particles to accumulate within the liver and spleen. [27] Particles that manage to avoid clearance from the RES are thereby greatly reduced in concentration compared to the originally injected dose. Without some external force to influence their biodistribution, their probability of selective accumulation within one organ or tissue over another is minimal. Residence time of particles within specific tissues as they flow through the circulatory system are low and for the most part, essentially equal among the remaining organs. Simply increasing relative doses in order to increase those remaining in circulation have the consequence of also increasing the accumulation with the liver and spleen. Depending on the drug or gene delivered, this can have significant implications related to toxicity, particularly if the particles are not readily cleared from the body.

Vasculature extravasation

The aforementioned short residence times particles experience in any one organ while remaining in the circulatory system translates to minimal time to engage with the endothelium of blood vessels. Under normal flow conditions, hemodynamics tend towards localizing particulates in the center of the laminar flow; thus preventing particles from interacting with vessel walls. Regions where interactions with vessel endothelium are more likely include the microcapillaries, where vessel diameter is greatly reduced. Following intravenous injection, the first capillary bed particles will encounter, is that of the lung prior to being pumped through the atrial system. Mitragotri and coworkers have shown that particle shape can alter this behavior resulting in particles more readily migrating to the lower velocity flow field adjacent to the vessel walls. [28] Meanwhile, Eniola-Adefeso and coworkers were able to demonstrate that particle density alters how particles partition within the vessel cross section and may be an effective means to enhance extravasation from the vasculature. [29] Alternatively, cellular hitchhiking, the act of selective and transient binding of nanoparticles to circulating cells (e.g. red blood cells (RBCs) or lymphocytes), has been shown to increase both circulation times and increase particle-endothelium interactions. [30, 31] Recent cell-mediated delivery of nanoparticles bound to red blood cells show 40-times higher particle accumulation in the lung following intravenous administration and approximately 10-times higher accumulation in the brain compared to affinity targeted nanoparticles when injected via the intra-carotid artery. [30] In each case, the capillary beds of the target organ are the first encountered by the particles downstream of the respective injection sites.

Intratumural pressure

The rapid proliferation and growth of cancer cells requires an increased flux of supportive nutrients. As a result, new blood vessel formation via angiogenesis occurs at an abnormally high physiological level. The rapid tumor growth and exceptional vessel formation contributes to what has been termed, ”leaky” vasculature. Together, with poor lymphatic drainage, these observed physiological traits serves as the basis for the theorized Enhanced Permeability and Retention (EPR) effect (Figure 1.5). [32] Though first proposed nearly forty years ago, the EPR transport phenomenon is still highly debated among those in the field. At its core, is the postulation that endothelial dysfunction leads to the formation of vessel fenestrations, through which particles and compounds can more easily pass and accumulate within the underlying tissue. It has been shown that the extent to which this occurs is dependent upon the type of cancer, its stage, as well as the cellular and extracellular matrix (ECM). [33] These parameters will influence the tumor microenviroments (TME), importantly, increasing the intratumoral pressure. Hydrostatic and osmotic pressure gradients therefore, may be insufficient to allow for the EPR effect to impact particle transport and result in passive targeting. [34] Various attempts to circumvent this conflicting phenomenon have shown promise. One such approach evaluated the use of an antifibrotic compound, thereby inhibiting collagen production. [35] This strategy was found to be effective in reducing the intratumoral pressures associated with dense ECM and resulted in higher accumulation of drug-loaded liposomes.

Cellular uptake

If able to avoid clearance mechanisms and undergo extravasation from circulation, accessing underlying tissue, nanoparticles must then successfully enter the cells of interest. Particles measuring in the nanometer size range must do so through active uptake mechanisms. This mainly occurs through endocytosis where nanoparticle interactions with the cellular membrane is followed by migration across the membrane and into the interior of the cell. This process does not result in the direct release into the cytoplasm; instead particles are sequestered within endosomal vesicles. There are five primary mechanisms of endocytosis and the pathway through which a particle may enter the cell is both cell- and size-dependent. Additionally, surface charge has been shown to influence cellular uptake rates and pathways with increased rates of cellular uptake associated with positively charged particles. [36] The lower pH values often found in the TME could then possibly be leveraged to induce a change in particle zeta potential through the protonation of surface functional groups. Phagocytosis has been previously mentioned when discussing RES clearance as this primarily occurs in phagocytes. [27] The remaining mechanisms include macropinocy-

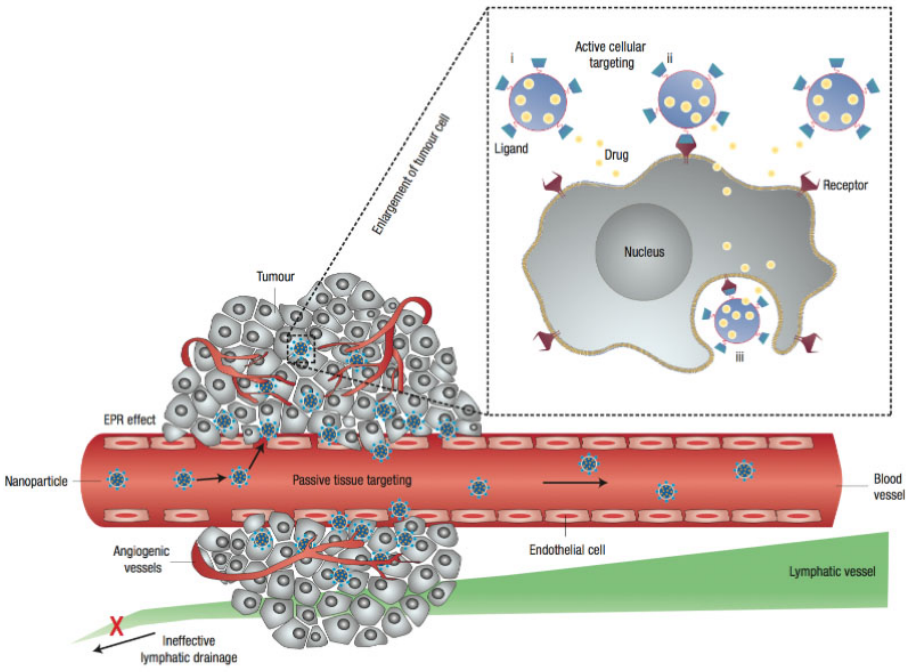

Figure 1.5: **Schematic representation nanocarriers transport drugs to tumors.** Passive tissue targeting is achieved by extravasation of nanoparticles through increased permeability of the tumour vasculature and ineffective lymphatic drainage (EPR effect). Active targeting (Inset) can be achieved by functionalizing the surface of nanoparticles with ligands that promote cell-specific recognition and binding. Reprinted with permission. Ref [4]

tosis, clathrin- and caveolin-mediated endocytosis, and clathrin/caveolae-independent endocytosis. [37] Particle fate following endocytosis can include degradation within the lysosome, recycling back to the cell surface via exocytosis or transcytosis, or under certain circumstances, endosomal rupture followed by the release of contents into the cytosol.

Endosomal escape

Once cellular entry has been achieved and particles find themselves within the endosome, it becomes imperative to escape and access the cytosol and in case of nuclear therapeutic targets, penetrate to the nuclear envelope. In instances were the particles are not recycled back to the cellular surface through exo- or transcytosis pathways, endosomes will eventually fuse with lysosomes. [38] The environment within these vesicles are harsh due to low pH and the presence of degradative enzymes. One means by which a particle can rupture and escape endosomal vesicles is through the incorporation of amine-containing polymers such as polyethylenimine (PEI). Branched PEI in particular, rich in secondary and tertiary amines, can induce swelling as an influx of water occurs referred to as the ”proton sponge effect.” [39] Alternatively, avoidance of the lysosome entrapment can be achieved through

controlling the endocytosis pathway through which the particles are taken up by the cells. A proposed pathway of cellular uptake for Abraxane (albumin-bound paclitaxel) is through caveolae-mediated uptake following the binding of albumin to the glycoprotein, gp60. [40] Caveolae-mediated uptake bypasses endosomes and instead results in particles localized within caveosomes; the conditions within which are typically less harsh and tend towards neutral pH. [41, 42] One could postulate that the coating of particles with albumin, or even the fabrication of nanoparticles entirely of this protein may lead to greater intracellular stability by altering the pathway through which they access the cytosol.

Multidrug resistance

Efflux pumps such as P-glycoprotein and breast cancer resistance protein (BCRP), are present within the cellular membrane and often overexpressed in various cancers. [43, 44] Primarily functioning to remove toxins from organs, their high levels in cancer cells is yet another example of how the disease manages to hijack evolutionary systems designed to protect the body and use it to its advantage. In instances when nanoparticles have managed to surmount the previously described physiological hurdles and effectively deliver their cargo to the cytosol of cancer cells, mechanisms to bind and transport hydrophobic compounds back across the cellular membrane exist. These mechanisms are not compound specific and as a result are effective at reducing the intracellular concentration of numerous drugs. [45] Moreover, the excretion of compounds out of the target cells, inherently increase the exposure of surrounding healthy cells to the cytotoxic compounds. Inhibition of these multidrug resistance (MDR) efflux pumps through small molecule inhibitors, [46] siRNA, [47] and pluronics, [48] co-delivered have shown promise in reducing the phenomenon.

Additional Biological Barriers

In addition to the previously described general barriers that nanomedicines must overcome to effectively achieve targeted and intracellular delivery of their therapeutic cargo, biological barriers specific to the route of administration and tissue of interest must also be considered. For example, in the context of oral delivery, in addition to the stability of the system at extremely low pH (1.0-2.5) [49] and the presence of digestive enzymes encountered in the stomach, transport across the mucosa and epithelial layers at more neutral pH values must be achieved. [50] The epithelium and mucosa layers also pose significant challenges when delivering via intranasal or pulmonary routes. [51] Considered perhaps the most challenging task of drug delivery is achieving therapeutic relevant doses to the brain and central nervous system (CNS) due to the highly selective blood-brain barrier (BBB)

(Figure 1.6). [52] Evolutionarily designed to inhibit the passage of potentially toxic solutes into the cerebrospinal fluid while selectively allowing the transport of important metabolic products, glucose, hormones, and amino acids critical to normal brain development and function, the BBB serves as a formidable barrier to the intravenous delivery of drugs to treat conditions including cancer, Alzheimer's, epilepsy, Parkinson's, and multiple sclerosis.

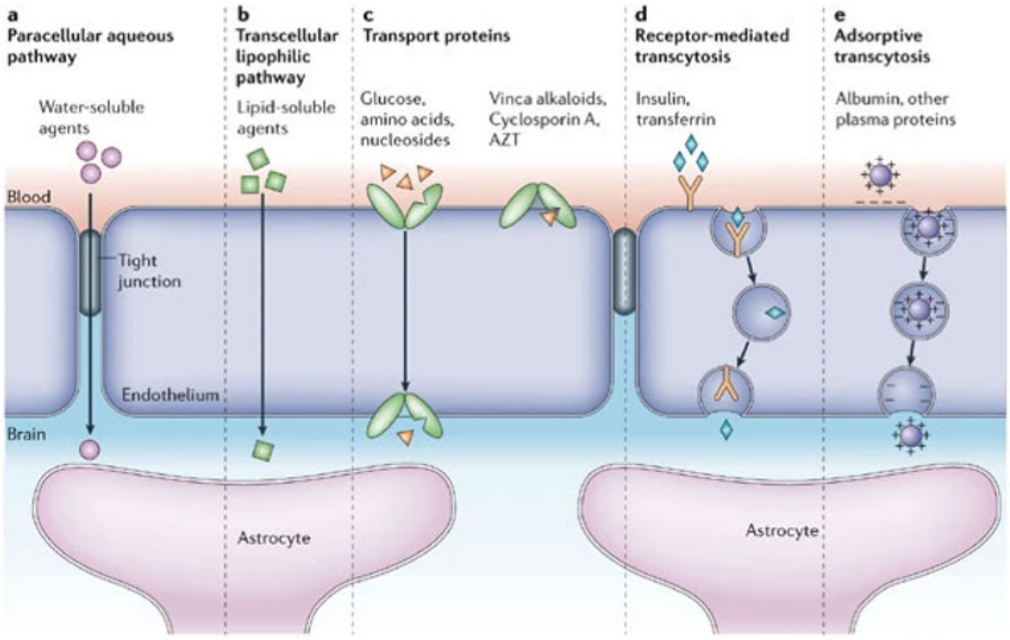

Figure 1.6: **Transport mechanisms of the Blood-brain Barrier (BBB).** The main routes for molecular traffic across the BBB (and example compounds associated with each) are shown. **a)** Paracellular (low MW, water-soluble agents), **b)** Transcellular (lipid-soluble agents) **c)** Protein-mediated transport (glucose, amino acids, nucleosides, choline) **d)** Receptor-mediated transcytosis (insulin and transferrin) **e)** Adsorptive transcytosis (select plasma proteins). Reprinted with permission. Ref [5]

The advent of nanotechnology and its application into the medical, specifically the cancer therapy field, came with a hope of revolutionizing the way we approached therapies. Beginning with the simple loading and release of molecules from liposomes, the field has advanced to create an array of particle types with unique bulk and surface properties. First proposed nearly forty years ago, the EPR effect promised a means to increase the accumulation of nanoparticle drug delivery systems in cancers; yet it has been shown that this is not a universally applicable means to do so. As a result, it has become clear that a passive targeting approach may not be sufficient in most cases. The biological barriers encountered, both from a systemic and cellular perspective, create a complex passage, often requiring

conflicting physical attributes for efficient transport. As we examine the biological landscape and the barriers imposed, it becomes clear that adaptive and multifunctional particle systems may be required to successfully navigate the complex path towards clinically impactful technologies.

1.4 Multifunctional Drug Delivery Systems

Tasked with the challenge to navigate, alter, or interact with complex biological, physiological, or pathological processes, nanoparticle designs and architectures have evolved, in an attempt to address these challenges. However, while one class of particle or material may address a single barrier, it is unlikely to address them all. For example, in the case of drug delivery for cancer therapy, the bulk and surface properties best suited for this multistep process including systemic transport, tumor localization, cellular uptake and effective drug release are conflicting. One approach to address this conundrum is the development of multifunctional particles (Figure 1.7). [6] Recent advances in the development of such particles, their potential applications with a particular focus on drug delivery, and persisting challenges follow.

Multifunctional Nanoparticles

Multifunctional particles can be defined as any particle system with two or more inherent properties. While one can classify them in numerous ways, here they are broadly categorized in one of two classes (i) those with surface anisotropy and, (ii) those with bulk anisotropy. In the case of surface anisotropic particles, the bulk composition is often uniform and controlled, post-fabrication surface modifications are used to create non-uniform surface features that diverge from their bulk properties. Conversely, bulk anisotropic particles contain multiple, distinct volumes within a single particle, often comprised of different materials, and as a result have dissimilar bulk properties. Within each class, a variety of fabrication methods have been developed, each with their own advantages. (Figure 1.8)

Surface Anisotropy

Isotropic particles synthesized through various methods can be made to have anisotropic surface properties through the application of post-modification techniques. These often include the utilization of masks, or templates to controllably restrict the regions of particles to be modified. The templates include the use of interfaces (liquid-liquid, [53] liquid-solid, [54] air-liquid, [55] and air-solid [56]) where particles are either mechanically placed

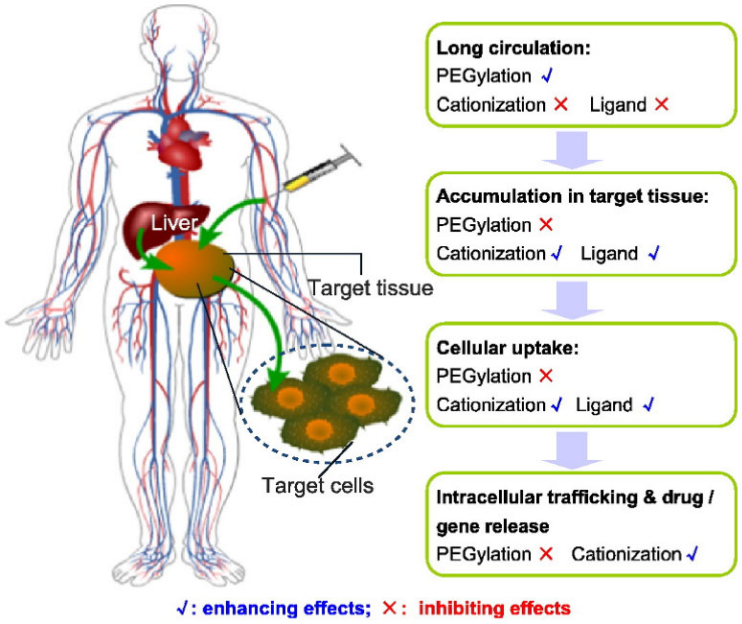

Figure 1.7: **Optimizing nanoparticle properties for systemic delivery.** Common approaches towards surface functionalization and nanoparticle properties (e.g. PEGylation, cationization, and conjugation of targeting ligands) can enhance particle transport for some processes while acting as inhibiting factors for others. This highlights the conflicting ideal properties for the multi-step process. Reprinted with permission. Ref [6]

or spontaneously accumulate to stabilize the interface. In other instances, the close packing of particles during the process, as in glancing angle deposition, self-imposes restraints on the surface areas of particles available for modification due to screening by neighboring particles. [57] Here, it is through the control of the deposition angle that dictates the surface area and pattern achieved. Processes such as physical deposition include etching, [58] chemical vapor deposition, [59, 60] or lithography [61] are used to selectively modify the exposed surfaces. In all cases, the result is a particle with regions of their surface with varied chemical, electrical, or amphiphilic properties distinct from their bulk properties.

One of the more popular approaches for biological applications is the attachment of biomolecules to inorganic particles such as gold, or mesoporous silica that would otherwise have no targeting properties and lack biocompatibility. López et al., make use of asymmetrically decorated mesoporous silica particles with controlled pore sizes to effectively target cancer cells through folate membrane receptors and then bind to mitochondria before delivering the encapsulated drug, topotecan. [62] By selectively controlling ligand placement, specific ligand density in each region is optimally maximized. Here, it is with a proper selection of ligand that aims to specifically interact with the cells of interest, namely folic acid, that facilitates increased tumor targeting.

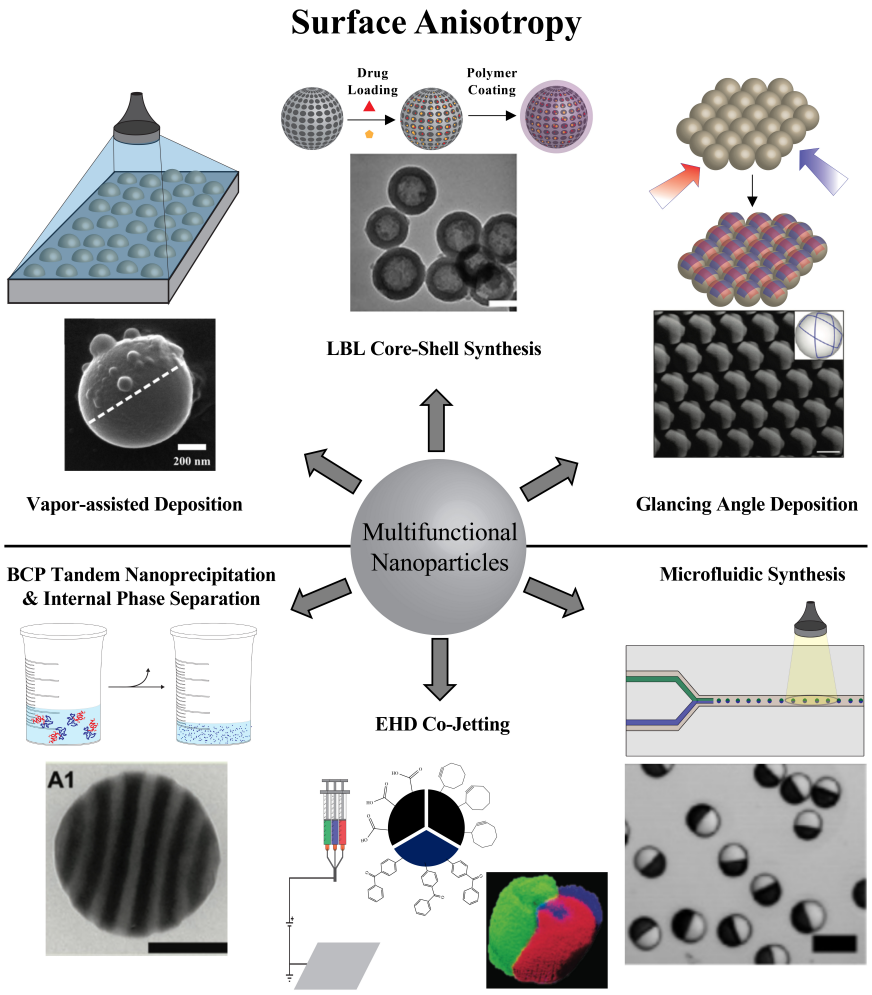

Figure 1.8: **Techniques for the synthesis of multifunctional nanoparticles. a)** Vapor-assisted deposition of macromolecules to select areas of nanoparticles through Matrix Assisted Pulsed Laser Evaporation (MAPLE). Scale bar = 200 nm. **b)** Layer-by-layer fabrication of polymer-coated, hollow silica nanoparticles for temporally controlled release of encapsulated drugs. Scale bar = 100 nm. **c)** Anisotropic, multifunctional patchy nanoparticles formed through the use of glancing angle deposition (GLAD). Scale bar = 2 μm. **d)** Tandem nanoprecipitation and internal phase separation employed to create surface-reactive, patchy nanoparticles prepared through the use of block copolymers (BCPs) and tuning of preparation conditions. Scale bar = 100 nm. **e)** Surface-reactive, multicompartmental particles fabricated using electrohydrodynamic (EHD) cojetting through the spatially controlled addition of chemically orthogonal surface functional groups. **f)** Continuous and high-throughput synthesis of multicompartmental nanoparticles through the formation of compound droplets in flow and subsequent UV initiated crosslinking. Scale bar = 100 nm. Reprinted with permission. Ref [7]

Alternatively, surface modifications can increase cellular interactions and uptake through a more general approach of controlling surface chemistry and thereby affecting surface charge density. Paula Hammond's group at MIT recently demonstrated this by controllably PEGylating cationic dendrimers for the treatment of cartilage cells to treat osteoarthritis. [63] Here, Geiger et al., take advantage of the highly controllable size and reactive surface amine groups to optimize surface charge through the subsequent attachment of polyethylene glycol. Together, with the attachment of insulin-like growth factor-1 (IGF-1), these particles show increased uptake in cartilage cells, minimized toxicity, and significantly reduced disease symptoms.

Bulk Anisotropy

In contrast to the post-modification routes that are used to create multifunctional nanoparticles with surface anisotropy, bulk anisotropic particles typically are formed with a bottom-up approach. Here, the compositions of the bulk materials and their relative orientation is controlled throughout the fabrication process. Controlled self-assembly processes can be achieved through careful selection of polymers and the solvent mixture, [64,65] on a larger scale, the selective surface functionalization of smaller building block particles. [66, 67] The formation of liposomes [68, 69] or disk shaped particles [70, 71] made of amphiphilic molecules such as lipids can also be formed through self-assembly process. In contrast, various flow processes, including microfluidics [72, 73] and electrohydrodynamic (EHD) co-jetting, [74–77] that utilize the controlled flow of polymer solutions in specific orientations to one another in combination with a method of solidifying the individual particles to form stable colloids. Lastly, by taking a layer-by-layer (LBL) approach, nanoparticles can be assembled in a stepwise fashion, resulting in radially anisotropic particles. [78–81] In each case, the bulk anisotropy of the resulting particles often directly translates to a surface anisotropy, which in some cases can be further modified for application specific properties.

Hwang et al., utilized dissimilar pH responsive polymers and the EHD co-jetting process to produce biphasic particles capable of the controlled and decoupled release of two distinct macromolecules in response to environmental conditions. [82] Building upon this work, the development of a biphasic particle system for the controlled and decoupled release of two therapeutics within the cochlear was achieved. [83] Here, the therapeutics consisted of the small molecule, piribedil and a protein, glial cell-derived neurotrophic factor (GDNF), demonstrating that the method of preparation would accommodate the loading and release of drastically different chemical moieties from individual compartments of a single particle system.

In addition to the encapsulation and release of therapeutics, the ability to track particles *in vivo* and determine intracellular particle fate can prove valuable. This could be the addition of fluorescent dye molecules, nuclear imaging agents for PET/CT (Positron Emission Tomography Computed Tomography) and SPECT (Single Photon Emission Computed Tomography), or encapsulated inorganic nanoparticles for SERS (Surface-Enhanced Raman Spectroscopy) [84] imaging. The idea of delivering multiple therapeutics can be expanded to include imaging techniques. Most notably of these is the concept of combining the delivery and release of therapeutics while also providing a method of monitoring biodistribution and intracellular fate, termed theranostics. Misra et al., demonstrated the ability to create biphasic compartments comprising of a PLGA compartment loaded with an imaging agent alongside a second pH-sensing, siRNA-loaded compartment. [85] The synthesized particles demonstrated not only the ability to serve the dual function of particle tracking and therapeutic release, but also made use of significant swelling of a single hemisphere to facilitate endosomal escape.

Creating particles that are anisotropic within the bulk lends itself to using the inherent surface anisotropy towards selectively modifying the surface without the use of templates or masks. Rahmani et al., demonstrated this through the synthesis and subsequent surface modification of three compartment particles. [9] Here, a similar poly(lactide-co-glycolide) (PLGA) base was used in combination with dopants of functional PLA polymers. It was shown that by incorporating small amounts of a functional polymer within the bulk of an otherwise isotropic particle system, controlled surface functionalization through orthogonal click chemistry reactions could be used to selectively decorate the particle surface. This approach would allow for the covalent attachment of specific targeting or stealth moieties with control over density, placement, and relative orientation of individual ligands relative to one another. Furthermore, the adaptability of the process suggests that the number of compartments and attached ligands is limited only by the number of orthogonal chemistries that can be performed on the resulting particle.

While the highlighted methods of multifunctional nanoparticles aim towards overcoming biological barriers in the field of drug delivery, a great deal of progress remains to be made. Of particular importance is the ability to translate optimal cell penetrating and drug delivery achieved within *in vitro* systems to clinical relevance. The most daunting of challenges involves maintaining favorable particle attributes for cellular uptake while minimizing *in vivo* clearance from circulation to maximize targeting capabilities. For years, the gold standard of surface modification, PEGylation promised to be a means to add a stealth-like quality to nano-sized colloids in the bloodstream. However, to date, the fractions of injected

particles remaining in circulation over extended periods of time remain disappointing using this method. [86] More concerning is the recent observation of circulating antibodies against PEG as an innate immune response. [87, 88] Together, these results motivate current research to identify alternative means to extend particle circulation, reduce their rapid clearance, increase local targeting, and effectively penetrate biological barriers such as the BBB.

1.5 Electrohydrodynamic Co-Jetting

Recent work in the Lahann Lab at the University of Michigan has focused on the development of EHD jetting as a method of producing multifunctinal particles. [8, 89–92] Based on the more common known techniques of electrospraying or electrospinning, EHD jetting uses the flow of dilute solutions coupled with an applied electrical potential acting as a driving force to produces fibers or particles with characteristic diameters in the micro- or nanoscale. Incorporating multiple and distinct inlets into the system results in what has been termed, EHD co-jetting, and an ability to create multiple compartments within a single particle or fiber architecture. [74, 75, 82, 83, 85, 93–99]

EHD co-jetting utilizes the laminar flow of two or more polymer solutions, in specific geometric arrangements, to produce bicompartmental particles with anisotropic bulk and surface properties (Figure 1.9). First described in detail by Sir G.I. Taylor, [100] the application of an electric field to the compound droplet results in the formation of a Taylor cone and electrified polymer jet. Acceleration of the viscoelastic jet in the electric field leads to the reduction in thread diameter by several orders of magnitude facilitating rapid solvent evaporation and solidification of non-volatile components. In the absence of convective mixing at the stable droplet interface as a result of the laminar flow regime, the resulting particle geometry is reflective of the original droplet orientation. [74, 75, 93, 99, 101] Capable of incorporating a wide range of materials, the EHD co-jetting process permits the synthesis of particles with several substantially dissimilar and decoupled compartments, including the encapsulation of imaging or therapeutics modalities. [83–85, 96, 99]

Variations in jetting parameters can significantly influence jet stability and ultimately the resulting shape, size, composition, and morphology (Figure 1.10). [8, 102] Solution parameters including polymer molecular weight and concentration, solvent composition, and additives (e.g. surfactants or small molecules) all affect solution viscosity, surface tension, and the dielectric constant which in turn influences jetting stability. Increased concentra-

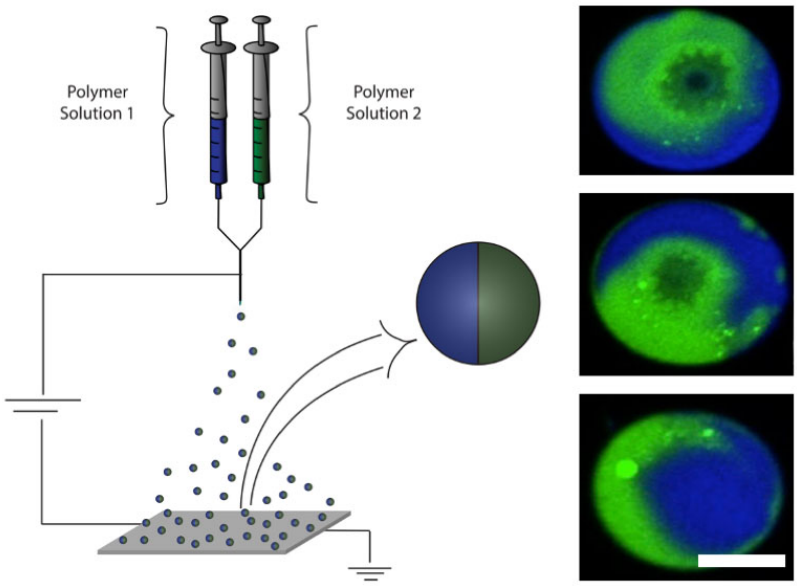

Figure 1.9: **Electrohydrodynamic (EHD) co-jetting.** The introduction of multiple inlets into the jetting system facilitates the creation of multicompartmental particles. (Left) A schematic of the EHD co-jetting system composed to two independent polymer materials. (Right) Confocal images of fluorescently labeled microparticles fabricated via EHD co-jetting. Resulting particles maintain the side-by-side orientation of the jetting capillaries, yielding bicompartmental Janus particles. Chosen images represent the first personally produced Janus particles synthesized after joining the lab. Scale bar = 2 μm.

tions and molecular weights of polymers will typically lead to more viscous solutions and stable continuous jets. When combined with low flow rates, these conditions tend towards fibers rather than particles. [92, 101, 103] Conversely, lower molecular weight bulk polymers and reduced solution concentrations will yield particles in the micro and sub-micron regime. Processing parameters including flow rate, applied electrical potential, needle geometry and needle to collector distance each can be optimized to further control the resulting particle architectures. Additionally, environmental conditions such as humidity and temperature play important roles and often must be controlled.

The EHD process has evolved to incorporate an array of bulk materials. Preliminary work to develop EHD co-jetting began with the use of water-soluble polymers poly(ethylene glycol) (PEG) or polyacrylic acid (PAA). [74, 82, 89] As a result of the material's water-soluble nature, these early particles required the use of further modifications following their fabrication to ensure stability in aqueous environments. Work quickly moved to the use of biodegradable synthetic polymers, notably poly(lactic-co-glycolic acid) (PLGA). [8,91,96] Transitioning to organic-soluble polymers eliminated the need for post-fabrication modifications to be completed as the resulting particles were instead stabilized through polymer

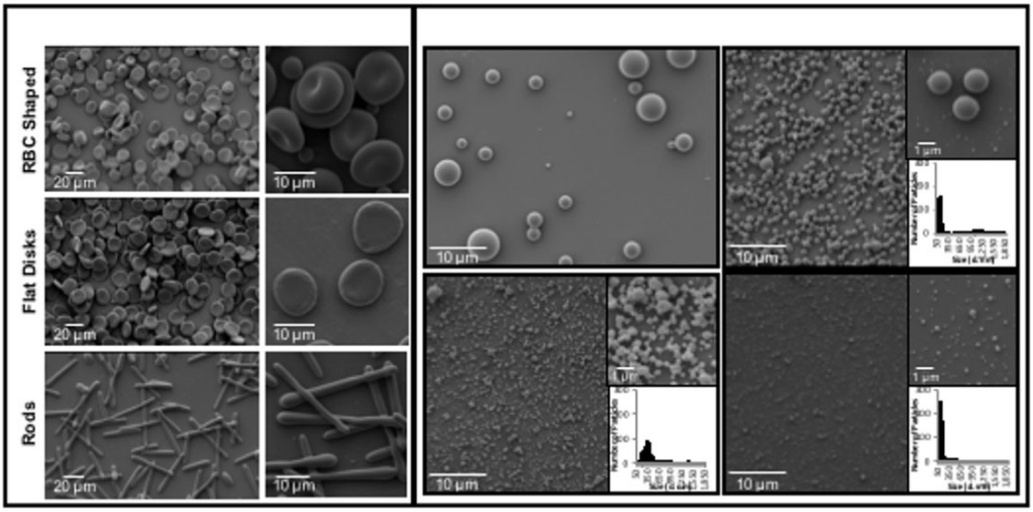

Figure 1.10: **Imparting control of particle shape and size.** Variations in process parameters including polymer concentration, carrier solvent composition, solution additives, and environmental conditions can lead to control of shape and size for the resulting particles. Particle sizes ranging from several microns to tens of nanometers are accessible. In addition to spherical particles, elongated rods, flat disks, and even more complex (e.g. red blood cell mimicking) shapes can be attained through changes in these same solution or processing parameters. Reprinted with permission. Ref [8]

chain entanglement and poor water solubility of the bulk material. Through the addition of functional PLGA molecules into distinct compartments, bulk anisotropy could be extended to the surface using orthogonal surface chemistries. [9] Chemical structures and representative confocal images following the selective conjugation of fluorescent surrogates are shown in Figure 1.11.

More recent work, presented here, is the development of a protein-based nanoparticle platform. Stabilized through chemical crosslinking, Synthetic Protein Nanoparticles (SPNPs) are predominately composed of proteins on a mass basis. [104–106] The vast choices of proteins, with varied inherent biological functions make this choice of material incredibly attractive from a particle engineering perspective. Owing to the diverse set of functional groups of the natural amino acid side chain groups, chemical modifications (both pre- and post-jetting) through well established conjugation chemistries are possible. These are typically completed under mild reaction conditions, are highly efficient, and involve straightforward purification steps to isolate modified proteins/particles from the unreacted starting materials. As a result of proteins amphiphilic nature, published and ongoing work show SPNPs are capable of effectively encapsulating a wide range of cargo including functional proteins, [105] enzymes, peptides, nucleic acids [104] and even small molecule drugs (both hydrophilic and hydrophobic).

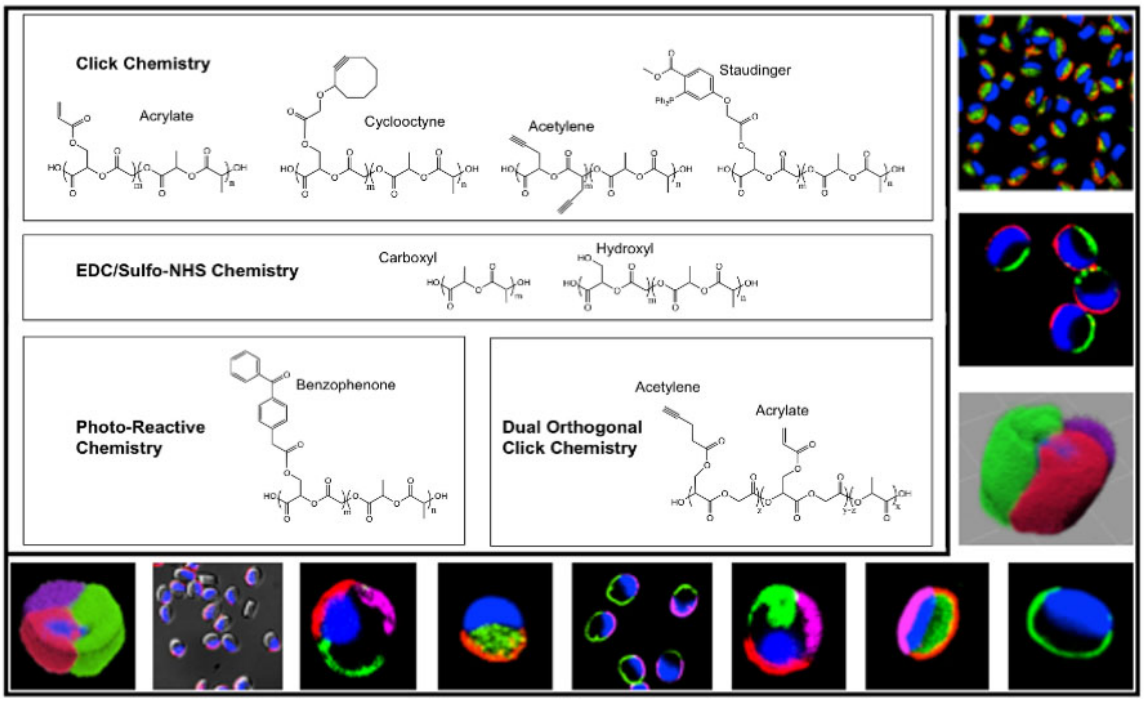

Figure 1.11: **Controlled surface functionalization.** Extending bulk anisotropy through selective surface modifications yields patchy particle surfaces. Shown here, functional PLA molecules can be doped into individual PLGA compartments. Subsequent surface chemistries are used to selectively conjugate molecules to the particle surfaces. As a proof of concept, fluorescent surrogates were used in place of active biologically relevant surface modifications. Reprinted with permission. Ref [9]

1.6 Objectives

The major objective of the work presented in this dissertation focuses on the development and validation of multifunctional drug carriers. Work includes the expansion of current materials to produce protein-based carrier systems, their effective targeting, and their application in delivering biological therapeutic cargo to the brain. Specifically, the following aims motivate the work presented.

Aim 1: Develop carriers with selective pH-responsive release of drug combinations
Here, we identify drug combinations and evaluate the role that their molar ratios and scheduled delivery play in achieving synergistic effects. Applying previous work to develop multicompartmental particles via EHD co-jetting, we produce Janus nanoparticles capable of encapsulating and releasing these same synergistic drug combinations in response to biologically relevant stimuli. The effects of controlling drug ratios and their sequential scheduled delivery from a particle system are demonstrated.

Aim 2: Extend the EHD Cojetting technology to produce protein nanoparticles

Previous work in developing EHD Cojetting technology focused on the use of biocompatible synthetic polymers, namely PLGA. Here, we expand the process capabilities and develop a robust platform to produce Synthetic Protein Nanoparticles (SPNPs). The use of various proteins, distinct crosslinking approaches, controlled chemical modifications, and their effects on particle architecture are demonstrated. Further, the ability to produce SPNPs with multiple compartments is validated.

Aim 3: To develop and validate antibody-mediated targeting of SPNPs

Given the demonstrated need for active targeting of systemically administered nanoparticle carrier systems to achieve favorable biodistribution, here we develop a robust method of conjugating molecules to SPNP surfaces. Through the addition of targeting antibodies, we demonstrate an ability to affect binding and uptake in an *in vitro* setting. Evaluating these same antibody-targeted particles following systemic administration, we demonstrate an ability to selectively alter biodistribution and accumulation of the particles in the lung.

Aim 4: To develop SPNPs capable of delivering biological cargo to glioblastoma

The effective delivery of therapeutic agents to the brain has the potential of making significant impact in patients diagnosed with glioblastoma multiforme (GBM). Despite recent advances, the inability to systemically deliver drugs, capable of crossing the blood-brain barrier (BBB), translates to minimal impacts in extending median survival. Here, we demonstrate the delivery of siRNA using SPNPs, their accumulation within the GBM tumor microenvironment (TME), and therapeutic effects when combined with standard of care.

CHAPTER 2

Programmable Synergistic Dual Drug Delivery

This chapter contains portions of text originally published as:

Programmable Delivery of Synergistic Cancer Drug Combinations Using Bicompartmental Nanoparticles
JV Gregory*, DR Vogus*, A Barajas, MA Cadena, S Mitragotri, and J Lahann
Advanced Healthcare Materials (2020)

*Shared co-first authorship.

Individual contributions to this shared publication include the synthesis of a pH-responsive modified dextran and the subsequent engineering of multicompartmental Janus nanoparticles. Additional work included the characterization the synthesized polymer and resulting nanoparticles. Finally, methods to capture and quantify the complimentary dual release was developed and applied to characterize the controlled release from the particle system.

2.1 Motivation

Cancer therapeutics are most effective when administered in combination with one another due in part to tumor heterogeneity and acquired resistance mechanisms. Combination therapy, an approach of administering two or more therapeutic agents or treatment modalities is thus increasingly applied in cancer therapy. [107] In contrast to single drugs, the administration of multiple therapeutics has the advantage that several pathways contributing to cell survival and proliferation, apoptosis, and metastatic behavior can be targeted simultaneously. The approach of targeting orthogonal pathways offers the benefit of achieving greater therapeutic effects, while also reducing the individually required doses and associated off-target side effects, blocking of pro-survival pathways, and minimizing the occurrence of drug resistance often observed in patients. [107–110] As a result,

extensive research has been conducted to identify and optimize synergistic drug combinations. [111–115] Critical challenges include the effective delivery of identified combinations, largely due to ineffective means to control the biodistribution and pharmacokinetics of the individual agents. Additionally, it has been observed in some cases that optimal synergistic effects are dependent not only on the precise control over the molar ratios delivered, but also on the sequence in which the two drugs are administered. [116]

A wide range of polymer nanoparticles have been extensively developed for the use as drug carriers. [117–119] Previous work has demonstrated electrohydrodynamic (EHD) co-jetting as a versatile and highly scalable means to synthesize multicompartmental micro- and nanoparticles. [92, 120] Bicompartmental nanoparticles have previously been engineered to carry small molecule drugs, [83, 96] siRNA, [85, 104] and imaging agents [84] for various therapeutic applications. In addition, bicompartmental particles can be synthesized at sizes less than 200 nm and selectively surface modified with functional ligands. [83, 86, 91] Downstream processing, including surface PEGylation, [86] CD-47 presentation, [25, 121] and RBC hitchhiking, [30] are each possible alone or in combination using these nanoparticles and can be leveraged to alter biodistribution of particles. Contrary to other nanoparticle fabrication methods, bicompartmental nanoparticles formed via EHD co-jetting allow for individual drugs to be loaded into distinct compartments, comprising of unique materials, capable of degrading at different rates, and thereby resulting in distinct and controlled release kinetics. [82, 90]

This research aims to develop a single nanoparticle platform, from which the controlled release of two distinct therapeutics can be achieved, independent of their chemical/biological properties. In particular, we seek to engineer programmable nanoparticles with tunable drug ratios and decoupled release kinetics (Figure 2.1).

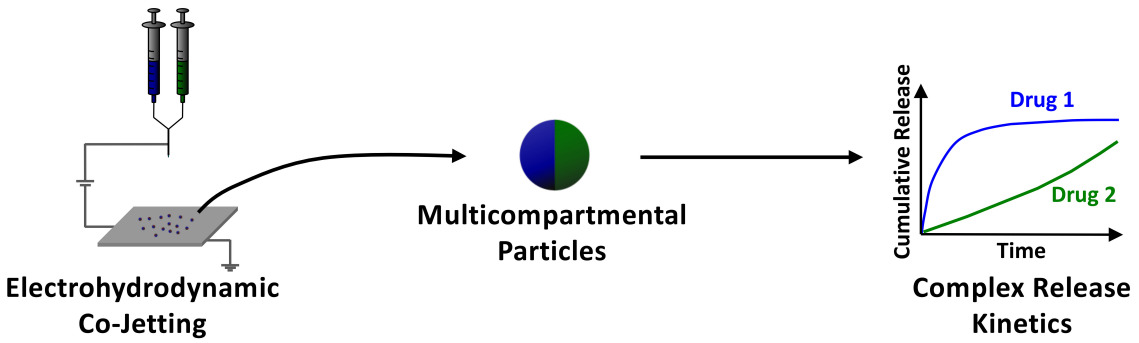

Figure 2.1: **Decoupled dual-release kinetics from Janus NPs.** Fabrication of Janus nanoparticles comprising of unique bulk materials enables the controlled release of multiple encapsulated agents with distinct release profiles.

2.2 Experimental Methods

2.2.1 Materials

Cells: MDA-MB-231 and BT-474 cells were purchased from ATCC.
Media: MEGM kit, fetal bovine serum (FBS), and penicillin streptomycin (PS) were purchased from Thermo Fisher, USA.
Drugs: Lapatinib Free Base and Paclitaxel were purchased from LC Laboratories
Reagents: Sodium chloride, dimethylsulfoxide(DMSO), ethyl acetate, poly(lactide-co-glycolide)(PLGA) 85:15, chloroform, dextran from leuconostoc mesenteroides (64-76 kDa), chloroform, dimethylformamide (DMF), 2-methoxypropene, anhydrous DMSO, pyridinium p-toluenesulfonate, methanol, acetonitrile, hexadecyltrimethylammonium bromide (CTAB), Tween 20, deuterated chloroform, phosphate buffered saline (PBS), Coumarin 314, Rhodamine B, N-(3-Dimethylaminopropyl)-N-ehtylcarbodiimide hydrochloride (EDC), triethylamine (TEA), and XTT assay were purchased from Sigma-Aldrich, USA. Sodium nitrite, dichloromethane, sodium carbonate, Optimal Cutting Temperature (OCT) compound, and N-(hydroxysulfosuccinimide) (Sulfo-NHS) were purchased from Fisher Scientific, USA. Albumin from Bovine Serum (BSA), was purchased from Life Technologies-Invitrogen, USA. PLGA 5004a was purchased from Corbion. Deuterated Water (D_2O) was purchased from TCI America. MTT assay was purchased from Abcam.

2.2.2 Methods

Cell growth

All cells were grown in a humidified incubator at 37°C and 5% CO_2. BT-474 cells were grown in Hybricare media supplemented with 10% FBS and 1% PS. MDA-MB-231 cells were grown in supplemented mammary epithelial cell growth medium (MEGM) media.

Activity assays

BT-474 and MDA-MB-231 cell suspensions (100 µL) were seeded in 96 well plates at concentrations of 1.1 x 10^4 and 1.0 x 10^4 cells per well, respectively. Cells were allowed to adhere overnight, and the media was replaced with drug or particle suspensions in media the following day. Pure drug solutions were prepared from DMSO stocks of the drugs 1 mg mL^{-1} paclitaxel (PTX) and 1 mg mL^{-1} lapatinib (LAP). Particle formulations

were prepared by suspending the lyophilized particles in phosphate buffered saline (PBS) (0.1 mg mL^{-1}) with 0.01% Tween 20 and then dispersed with ultrasonication.

After cells were incubated with drugs for 72 h, unless specified otherwise, the drug formulations were replaced with MTT reagent (0.5 mg mL^{-1} in media). Following 4 h incubation, the MTT solution was aspirated and DMSO was added to each of the wells. The plates were shaken for 30 min, and the absorbance of each well was read at 570 nm (Tecan Plate Reader). Dose response curves were calculated similarly to previous reports. Synergy between combination treatments were calculated using the combination index first published by Chou and Talalay. [122]

Synthesis of acetylated dextran

Acetylated dextran was synthesized according to a modified version of the protocol developed by Fréchet for the acetalation of low molecular weight dextrans. [123] Briefly, 1.0 g of dextran (64-76 kDa) was dissolved in 50 mL of anhydrous DMSO. Once, completely dissolved, 25 mg of pyridinium p-toluenesulfonate was introduced, followed by 5.0 mL of 2-methoxypropene, added dropwise. The reaction vessel was purged with dry N_2 and stirred for three hours under positive pressure at room temperature. Acetylated dextran was precipitated out of solution by combining the reaction mixture with 200 mL of distilled H_2O (+ 1.0 v/v% TEA). The product was washed several times with DI water via alternating centrifugation and resuspension cycles. The final product was lyophilized to remove any water, yielding a dry, white powder.

Polymer characterization

Synthesized acetylated dextran was characterized via proton NMR spectroscopy to confirm polymer structure and characterize acyclic vs. cyclic hydroxyl protection. To determine the degree of protection, protected dextran was hydrolyzed in D_2O with a small addition of DCl to acidify the solution. Proton NMR spectra was collected using a Varian 400 MHz (UM, Chemistry NMR Core) instrument. The resulting ^1H NMR spectra, with a basis of 100 glucose units per polymer chain, was used to calculate the fraction of hydroxyl groups protected through the reaction and estimate the ratio of acyclic vs. cyclic acetal protecting groups using Equations (2.1) and (2.2), respectively.

$$\text{Degree of Protection} = \frac{\left[\frac{\text{MeOH}}{3}\right] + \left[\frac{\text{Acetone}-(2)(\text{MeOH})}{3}\right]}{300} \tag{2.1}$$

$$\text{Acyclic:Cyclic Protection} \quad = \quad \text{MeOH} : \text{Acetone} - (2)(\text{MeOH}) \tag{2.2}$$

Particle degradation

Validation of the protected acetylated dextran and its degradation in acidic conditions was validated through the controlled degradation of synthesized particles. Bicompartmental nanoparticles consisting of two compartments, one PLGA only, and a second, a PLGA/AcDex blend, were synthesized via EHD co-jetting. The particles were dried under vacuum to remove any residual solvent and suspended in either neutral pH conditions (PBS + 0.1% Tween 20, pH 7.4) or acidic buffer (sodium acetate-acetic acid buffered solution + 0.1% Tween 20, pH 5.0). Particles were incubated at 37°C for predetermined periods of time. At the end of the incubation period, nanoparticles were washed three times with PBS followed by five ultrapure water washes to remove any residual salts. Final nanoparticle solutions were spin-coated onto silicon wafers and imaged via scanning electron microscopy.

Particle synthesis

All carrier formulations were fabricated using electrohydrodyamic (EHD) co-jetting as previously described. [8, 90, 96] Briefly, PLGA compartments consisted of a 7.0 w/v% PLGA in a 70:30 v/v $CHCl_3$:DMF solution. AcDex/PLGA compartments consisted of a 2.5 w/v% PLGA and 4.5 w/v% acetylated dextran in a 70:30 v/v $CHCl_3$:DMF solution. In each case, a small addition (2 w/v%) of hexadecyltrimethylammonium bromide (CTAB) was added to act as a surfactant to control for final particle size. When encapsulating chemotherapeutic drug into the particle system, drugs were first dissolved in DMSO at concentrations of 100 mg mL^{-1} and then diluted to target concentrations, relative to base polymer in $CHCl_3$. Bicompartmental particles were fabricated by flowing solutions for each of the two compartments in a side-by-side arrangement and co-jetted at a total flow rate of 0.2 mL h^{-1}, 30 cm needle to collector distance, and 9.5-11.0 kV applied electrical potential. All co-jetted particles were dried under vacuum for three weeks to ensure residual solvent was completely removed before their further use in future experiments.

Particle characterization

Particles were characterized in both their dry and hydrated states to determine size, particle morphology and structure, and drug loading efficiencies. Particles were collected on

small silicon wafers placed on the collection platform, dried under vacuum, and sputter coated with a thin (<10 nm) layer of conductive gold prior to imaging according to previously developed methods. Scanning Electron Microscopy (SEM) imaging was completed with a FEI NOVA 200 Nanolab SEM-FIB instrument (UM, $(MC)^2$ Imaging Core). Particle size distribution was determined by manually measuring particle diameter using ImageJ software ($n \geq 300$). Particles with dyes loaded into each compartment, were collected on glass cover slides, dried under vacuum and mounted in ProLong Diamond Antifade Mountant, and imaged using superresolution Structured Illumination Microscopy (SIM) with a Ziess ELYRA microscope (UM, Biointerfaces Optical Imagine and Analysis Lab). All samples were imaged following a standard Zeiss developed, channel alignment protocol to eliminate alignment artifacts when investigating bicompartmental particle architecture. Dynamic Light Scattering (DLS) was performed using a Malvern Zetasizer Nano ZSP (UM, Biointerfaces Nanotechnicum), following particle collection and purification in PBS.

Particle loading and release

To determine total loading and loading efficiency, particles were fabricated incorporating Coumarin 314 into the PLGA compartment and Rhodamine B into the AcDex/PLGA compartment. Known particle masses were collected and dissolved in chloroform. The resulting solutions were examined using a Horiba FluoroMax-3 Fluorometer with excitation/emission wavelengths of 436/485 and 543/576 nm, respectively. Results were compared to previously generated calibration curves to determine total dye loading.

A similar approach was used to determine drug loading for all drug-loaded particle variations. Particles were dried under vacuum as previously described and then dissolved in chloroform. Resulting solutions were analyzed for drug concentrations using an Agilent Q-TOF HPLC-MS instrument (UM, Chemistry Mass Spec Lab). Previously generated calibration curves were used to determine total drug loading, loading efficiency, and relative molar ratios in particles that encapsulated both compounds.

Release kinetics were determined via dialysis. In both dye and drug release experiments, known particle masses were collected and suspended in 5 mL of release media. PBS was used as neutral release media, while a sodium acetate-acetic acid buffered solution, adjusted to pH 5.0, was used for acidic release conditions. Particle solutions were placed within a Float-a-Lyzer device (100 kDa MWCO, Spectrum Labs) and submerged in an additional 40 mL of equivalent release media in 50 mL conical vials. The vials were incubated at 37°C. At pre-determined times, the dialysis device was transferred to a new conical vial

filled with pre-warmed, fresh release media.

Samples from preliminary dye release experiments were measured as described above using the Horiba FluoroMax-3 Fluorometer. Samples from drug release experiments were measured as described above using the Agilent Q-TOF HPLC-MS instrument. In each, case a previously generated calibration curve was used to quantify cumulative release.

Statistical analysis

All values are expressed as mean $\pm$ standard deviation ($n \geq 3$ biological replicates). Fractional cell inhibition and dose response curves were fit using non-linear fits and display error bars of 95% confidence intervals. Statistical analysis and non-linear median effect model fits were performed using GraphPad Prism 7. For normally distributed data sets, two-way ANOVA testing followed by Sidak post-hoc tests were used to test statistical difference between measurements; p-values less than 0.05 were considered significant.

2.3 Results and Discussion

2.3.1 Janus NP Synthesis and Characterization

Taking advantage of the biological difference in pH, typical of TME and endocytotic cellular compartments (i.e., endosomes and lysosomes), we aimed to engineer bicompartmental nanoparticles that would preferentially degrade in acidic conditions. Previous work by Fréchet et al. resulted in the synthesis of an acetal-modified dextran (AcDex) by reacting hydroxyl groups with 2-methoxypropene. [123] Acetylated dextran was explored previously as a material compatible with electrohydrodynamic jetting through the formation of fibrous scaffolds [124] and nanoparticles. [90] Following a similar synthetic route (Figure 2.2a), we modified a 70 kDa dextran to ensure that resulting polymer is no longer readily water soluble and the protecting groups impart more hydrophobic properties. Under acidic conditions, the acetal groups are readily cleaved resulting in the release of methanol and acetone moieties and a return to the water-soluble dextran structure.

Prior to the fabrication of nanoparticles, synthesized AcDex was first validated through ^{1}H NMR spectroscopy and particle degradation experiments. Together with a noticeable change in solubility, initial NMR spectra (^{1}H, $CDCl_3$, Figure 2.2b), when compared to literature first describing the synthesis of low molecular weight (10 kDa) AcDex, [123] confirmed polymer structure. Following polymer degradation via hydrolysis in D_2O/DCl, chemically cleaved protecting groups yield acetone and methanol, each detectable via ^{1}H NMR at approximately 2.2 and 3.3 ppm respectively (Figure 2.2c). In the case of acyclic protecting groups, both acetone and methanol are produced; conversely, cyclic protecting groups yield only acetone. Integration of the resulting methanol and acetone NMR peaks, together with Equation 2.1, suggested that approximately 70% of the available dextran hydroxyl groups were protected, sufficiently making the resulting polymer insoluble in neutral aqueous conditions. Further examination of the same spectra, together with Equation 2.2, indicated that the ratio of hydroxyls protected by acyclic to cyclic acetal groups was approximately 4:1. Previous studies suggest that this approaches the maximum achievable ratio of cyclic protecting groups due to the chemical structure of dextran, steric effects, and hydroxyl groups available to participate in such bonding. The ratio of acyclic to cyclic protecting groups is easily modified through reaction conditions and when incorporated into particles, this polymer property ultimately contributes to particle degradation rates. [125]

To further characterize the synthesized AcDex polymer, multicompartmental nanoparticles

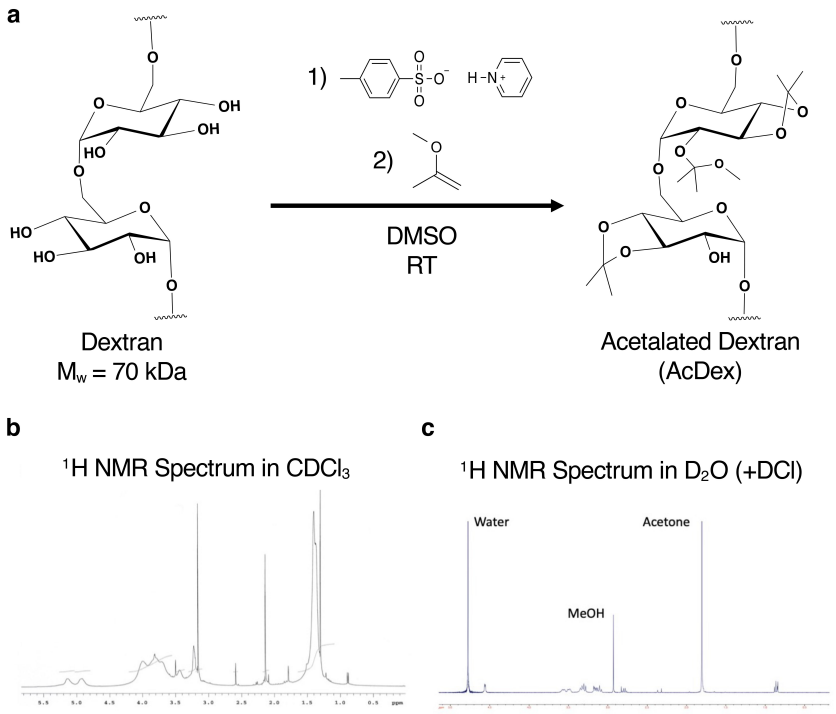

Figure 2.2: **Synthesis of pH-responsive acetalated dextran.** The addition of protective groups to dextran results in a water-insolbule derivative. Exposure to acidic aqueous conditions readily reverses this process returning the polymer to its native structure releaseing methanol (MeOH) and acetone as byproducts. **a)** Chemical synthesis scheme to generate acetalated dextran polymer. **b-c)** Proton NMR of the resulting polymer (b) before and, (c) after hydrolysis.

consisting of a PLGA and PLGA/AcDex compartments were fabricated via EHD co-jetting (Figure 2.3). Combined with PLGA within a single nanoparticle, the result is a bicompartmental particle with distinct degradation rates in response to pH. The synthesized spherical nanoparticles, when imaged using SEM (Figure 2.4a), were found to be relatively homogeneous in size with an average diameter in their dry state of 161 $\pm$ 61.2 nm (Figure 2.4a). This imaging technique allowed for both the surface morphology to be examined while simultaneously determining a statistically significant size distribution. Once collected and purified, their average hydrodynamic diameter, measured by DLS, was determined to be 240 nm (PDI = 0.316) (Figure 2.4b). The discrepancy in size can be attributed to a combination of swelling of the polymer nanoparticles in aqueous solution and inherent differences in the measurement techniques. When additional purification was performed through centrifugation methods we were able to obtain fractions of smaller particles, approximately 175 nm (PDI = 0.174) in diameter as measured by DLS (Figure 2.5).

Particles were then incubated in either neutral or acidic buffer at 37°C for 5, 10, 15 and

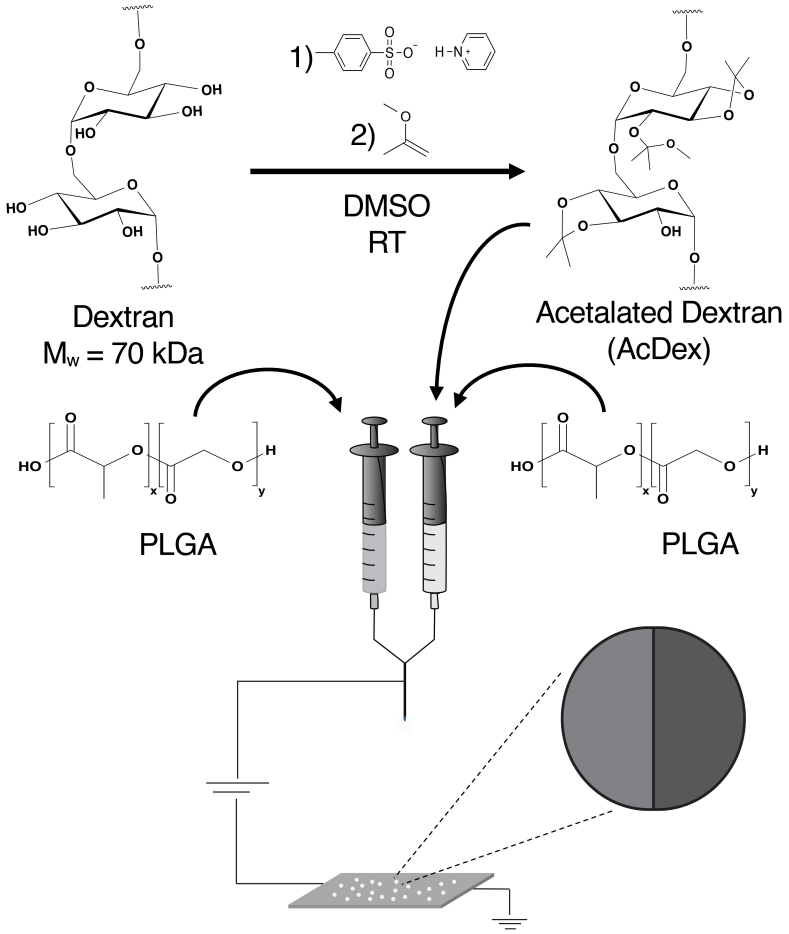

Figure 2.3: **Design and fabrication of pH-responsive Janus nanoparticles.** Bicompartmental Janus nanoparticles were fabricated via electrohydrodynamic (EHD) co-jetting. The adjacent laminar flow of two polymer solutions consiting of PLGA and a PLGA/AcDex blend entering the Taylor cone result in nanoparticles with distinct hemispheres.

20 h. These particles were then extensively washed with DI H_2O, deposited on silicon wafers, and imaged via SEM to visually investigate their degradation in response to pH. It was observed that particles in acidic buffer underwent significant swelling and rapid degradation compared to those incubated in neutral conditions (Figure 2.6). This observed difference in nanoparticle degradation would suggest that the acetal protected dextran remains water insoluble under neutral conditions; however, when exposed to acidic environments, the polymer readily undergoes acid catalyzed hydrolysis, is converted back to its water-soluble form, and results in a rapid degradation of the AcDex containing particle hemisphere. Together, these properties offer an ability to tune the release kinetics of encapsulated molecules in response to external stimuli, notably the pH of the surrounding environment.

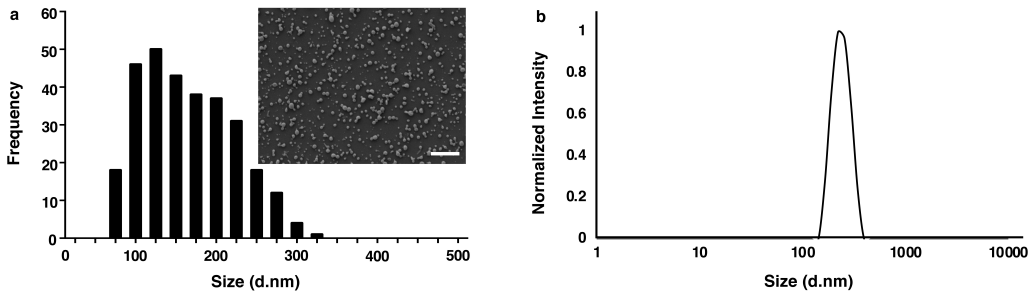

Figure 2.4: **Size distribution of PLGA/AcDex Janus nanoparticles.** Nanoparticles fabricated via EHD co-jetting have a monodisperse size distributino and spherical morphology. **a)** Represenative scanning electron microscropy (SEM) image (inset) and size distribution of cojetted bicompartmental nanoparticles. Average diameter = 161 61.2 nm. Scale bar = 1 µm. **b)** Dynamic light scattering (DLS) size characterization of bicompartmental nanoparticles. Average diameter = 240 nm.

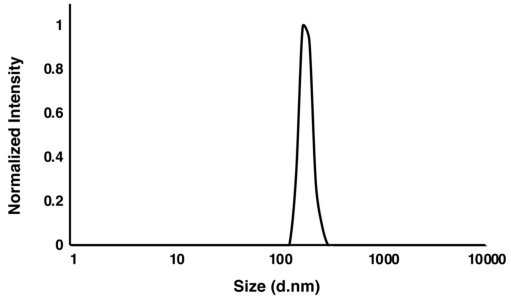

Figure 2.5: **Size distribution of PLGA/AcDex Janus nanoparticles post purification.** Dynamic light scattering (DLS) size characterization of bicompartmental PLGA and AcDex nanoparticles following size-selection via a differential centrifugation process. Average diameter = 173 nm, PDI = 0.174.

To demonstrate the difference in degradation of each of the polymer phases and its effect on the release of encapsulated small molecules, Rhodamine B was incorporated into the AcDEX/PLGA compartment while Coumarin was loaded into the PLGA compartment. The addition of dyes to the synthesized nanoparticles did not significantly change the resulting nanoparticles shape or size as confirmed by the respective SEM images (Figure 2.7). The particles were found to have diameters consistent with previous measurements taken in their dry state. Super resolution, SIM imaging of the resulting nanoparticles clearly shows the formation of two distinct compartments, each containing the loaded dye molecules (Figure 2.7).

The release kinetics of each fluorescent molecule at physiologically relevant conditions were determined (Figure 2.8). Neutral conditions (pH 7.2) were selected to inform release kinetics from particles in circulation and healthy extracellular space while pH 5.0 was eval-

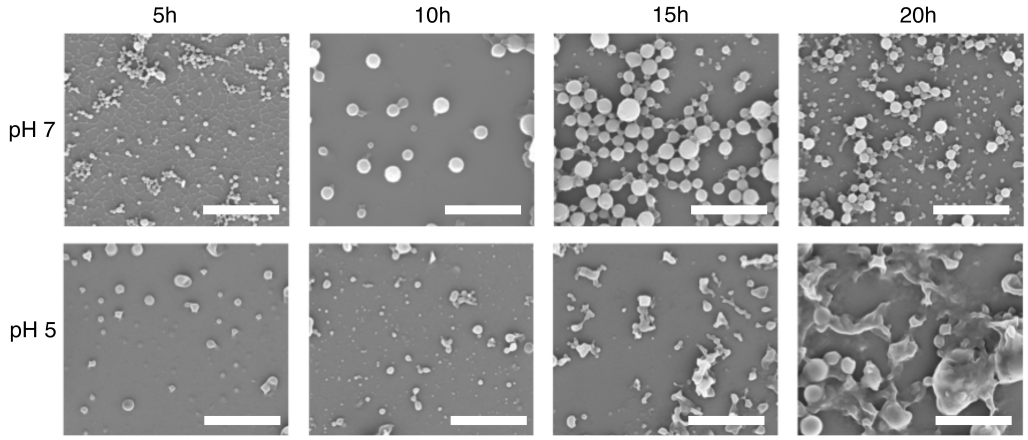

Figure 2.6: **pH dependent nanoparticle degradation** Janus nanoparticles consisting of PLGA and PLGA/AcDex compartments undergo distinctly different degradative processes in response to solution pH.

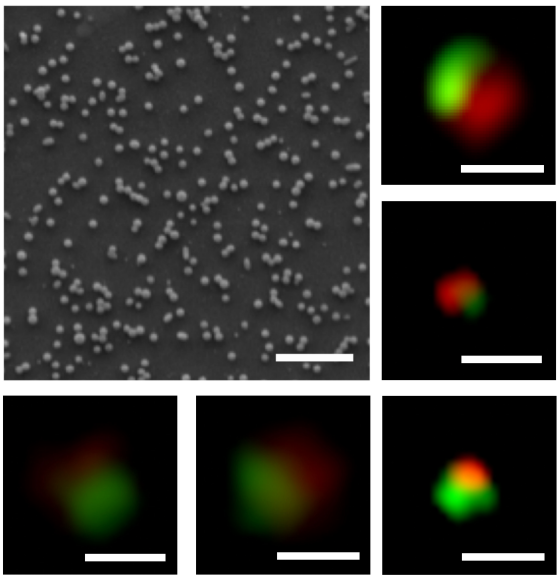

Figure 2.7: **PLGA/AcDex Janus bicompartmental structure validation** SEM image of dye-loaded bicompartmental nanoparticles. Average size = 165 $\pm$ 37 nm. Individual particles imaged with super-resolution, structured illumination microscopy (SIM) showing distinct compartments within single particles. Scale bar (SEM) = 1 μm, Scale bars (SIM) = 300 nm.

uated to characterize release in the more acidic TME and endocytotic vesicles. Together, these two conditions were chosen to provide a more complete representation of drug release following systemic delivery. The stability of both polymer phases was evident by the slow release kinetics of the fluorescent molecules at pH 7.2 (Figure 2.8a). At pH 5, the release of Rhodamine B from the AcDEX/PLGA compartment phase of the nanoparticles

is noticeably faster than that of coumarin from the PLGA compartment (Figure 2.8b). This was also evident after changing the pH of the solution from pH 7.4 to pH 5.0 at t = 24 h (Figure 2.8c). While we observed an obvious divergence of the individual release profiles following the change in pH at 24 h, it was also noted that nearly 75% of each encapsulated material had already been released; experimental designs for subsequent release experiments was adjusted to account for this. Finally, comparing the initial release of Rhodamine B from the acetylated dextran phase in acidic pH, it is clearly more rapid than when the nanoparticles are incubated at neutral conditions (Figure 2.8d).

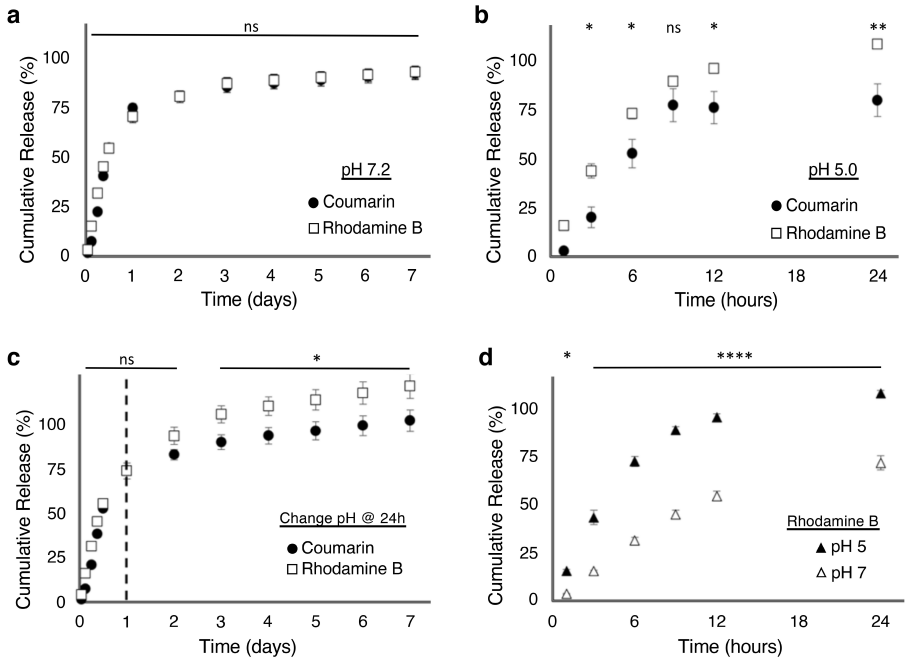

Figure 2.8: **Controlled dye release from Janus nanoparticles.** Release of encapsulated small molecule dyes Coumarin and Rhodamine B from PLGA and pH responsive PLGA/AcDex compartments respectively. Release kinetics studied at **a)** physiological pH, 7.2, **b)** acidic pH, 5.0 and **c)** a dynamic system with a change of pH from 7.2 to 5.0 at the 24 h timepoint. **d)** Release kinetics of Rhodamine B, encapsulated within the pH responsive PLGA/AcDex compartment, evaluated at both neutral and acidic conditions. Results are shown as mean $\pm$ s.d. Statistical significance defined as $p < 0.05$ ($n \geq 3$ biological replicates; two-way ANOVA and Sidaks multiple comparisons tests; **** $p < 0.0001$, ** $p < 0.005$, * $p < 0.05$).

2.3.2 Schedule-dependent synergy in breast cancer

After establishing the ability to both load and release small molecule surrogates from bi-compartmental nanoparticles, work was done to identify and optimize a potentially syner-

gistic drug combination. LAP, a dual EGFR and HER-2 kinase inhibitor was originally approved for treating late stage, $HER2^+$ breast cancer in combination with capecitabine. Since then, it has been tested in various clinical trials as a substitute for trastuzumab in combination with other chemotherapeutic agents. In particular, LAP and PTX have been evaluated for treatment of various phenotypes of metastatic breast cancer. [126–130] Overexpression of tyrosine-kinase activity is essential in many biological functions, including those contributing to chemoresistance. [131, 132] In patients that fail to respond to broadly applied chemotherapeutics such as PTX, inhibiting this pathway has been shown to regain efficacy. [133] Therefore, it has been proposed that the combination of tyrosine-kinase inhibitors with taxanes may prove to be effective treatment regimens. The addition of LAP to PTX chemotherapy regimens has extended the survival of patients with metastatic, $HER2^+$ cancer while being mostly ineffective for $HER2^-$ patients. [126, 129, 134] In addition, LAP and PTX have proven to be effective in treating $HER2^+$ breast cancer patients in the neoadjuvant setting. [130] The use of high doses of LAP has also been used to increase the delivery of albumin bound PTX to various solid tumors by reducing the hyperpermeability of the tumor vasculature. [135] While promising, other conflicting studies have found no true synergistic effect between the two drugs when delivered simultaneously. [136]

Given the early, yet conflicting, clinical success of PTX and LAP in combination, it poses the question if the combinations efficacy could be further improved if the drugs are administered in an optimal manner; however, designing the optimal combination regimen for PTX and LAP in their free forms is a challenge due to the drugs being administered through different routes: LAP as an oral pill and PTX intravenously with Cremaphor EL. To ensure the drugs reach the tumor site simultaneously, various delivery systems have been synthesized to co-deliver the two hydrophobic agents. In particular, LAP and PTX have been loaded into the core of micelles, [133, 137–139] liposomes, [140] injectable hydrogels, [141] and layer-by-layer nanoparticles. [142] In many of the studies, the combination vehicles were effective at inhibiting the growth of both $HER2^+$ cancer cells and many multi-drug resistant cancer cell lines.

While current delivery platforms are capable of delivering LAP and PTX in combination, their release rates can not be independently controlled. Further efficacy may be achieved by programmable delivery aimed at optimizing the sequence and ratio in which the drugs are administered. Previously, pretreatment with trastuzumab (which also inhibits the HER2 receptor) prior to PTX was more effective at initiating apoptosis in $HER2^+$ cancer cells than the simultaneous exposure of the two agents. [143] It was postulated that a similar mechanistic advantage might also contribute to the combined LAP and PTX therapy. How-

ever, there is no way to manipulate the relative release rates of the drugs from the current delivery platforms. Therefore, we hypothesized that our pH responsive Janus nanoparticle delivery system would allow for the drugs to release at different rates and could result in a greater degree of synergy.

2.3.3 Free Drug Synergy

Using BT-474 cells as a representative cell line for $HER2^+$ breast cancer, the activity of both LAP and PTX were individually determined for different drug exposure times (Figure 2.9a-d). In all cases, efficacy and individual drug IC_{50} values were determined at the 72 h timepoint. LAP (Figure 2.9 a-b) and PTX (Figure 2.9 c-d) were either incubated with the cells for the e ntire 72 h (blue line) or introduced for a shorter periods (red, 24 h and black, 4 h) while the remaining time the cells were incubated in drug-free media. The 72 h IC_{50} doses for LAP and PTX, when administered for the entire 72 h, were determined to be 85 $\pm$ 10 nM and 14 $\pm$ 1 nM, respectively. Decreasing the exposure time of each drug from 72 h to 24 h increased the IC_{50} dose 3x and 6x for LAP and PTX respectively. On the contrary, delaying the exposure of LAP and PTX for 24 h increased the IC_{50} dose approximately 3x for both drugs.

After identifying the relative activity of each drug on its own, cellular proliferation was measured following exposure to combinations of LAP and PTX. Exploring a range of molar ratios, it was found that a 3:1 (LAP:PTX) molar ratio provided the greatest synergistic effect. Treating cells with that same fixed molar ratio, (3:1, LAP:PTX), near the IC_{50} of each drug, the cells were exposed to different schedules of drugs (Figure 2.10a). Given the cell viability after exposure to the individual drugs compared to the combination treatments (Figure 2.10b), it was determined that giving LAP 4 h prior to PTX (Schedule 2) is significantly more effective than giving the two drugs simultaneously (Schedule 3) (Figure 2.10b). This holds true whether LAP is present after PTX exposure or whether extracellular LAP is removed prior to PTX exposure. In addition, synergistic effects were observed if PTX is given prior to LAP (Schedules 4 and 5); however, this combination is less active than the reverse schedule where LAP was delivered first.

Using the optimal schedule of LAP (4 h) $\rightarrow$ PTX/LAP (68 h), the effect of molar ratio on synergy between the two drugs was studied. With a PTX dose below the IC_{50} (0.10 μM), molar ratios of LAP:PTX greater than 1 are synergistic ($CI < 1$) (Figure 2.11). However, as the dose of PTX is increased significantly above the IC_{50} (0.30 μM), the synergy decreases compared to lower PTX doses. This is likely due to the fact that at this high concentration,

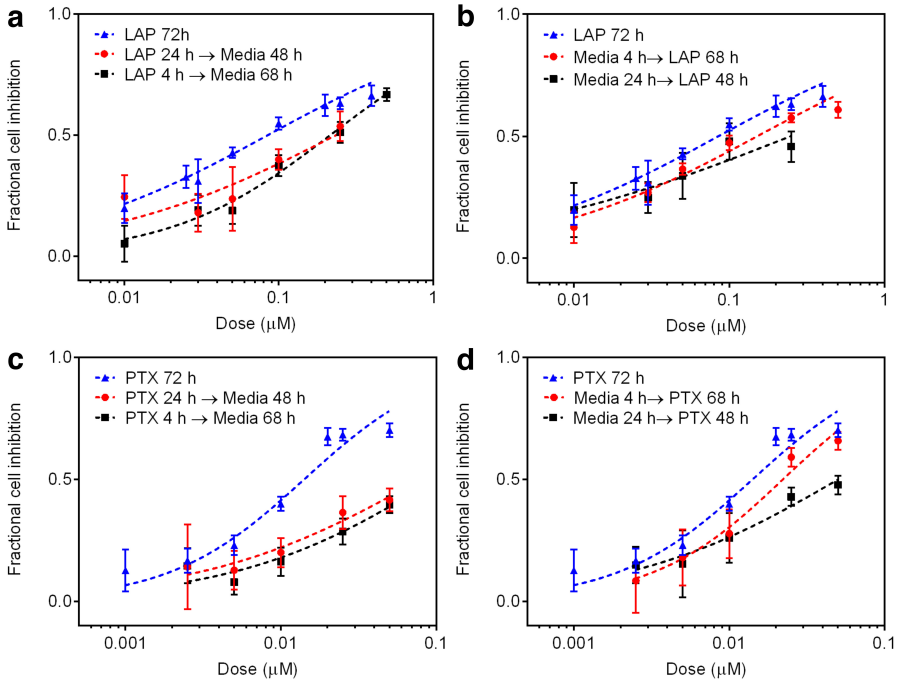

Figure 2.9: **Synergistic free-drug combination studies in HER2$^+$ breast cancer cells.** Fractional cell inhibition and relevant dose response cPTrves for BT-474 cells after prolonged exposure to (A) LAP → media, (B) media → LAP, (C) PTX → media, and (D) media → PTX. Cell viability was assessed at 72 h for each schedule. Error bars represent 95% confidence intervals (n ≥ 12 wells).

PTX is already significantly potent as a single drug. Together, these data motivated the proposed design of loading and rapidly releasing LAP from the PLGA/AcDex compartment while complimenting it with a slow and sustained release of PTX from the PLGA compartment.

2.3.4 Drug-loaded NPs Synthesis and Characterization

To characterize the release kinetics of each drug, a full release study was completed for the particles of interest. Again, LAP was encapsulated within the AcDex/PLGA compartment, designed to release quickly in response to acidic environments; meanwhile, PTX was encapsulated within the PLGA-only compartment with a goal of creating a delayed release relative to that of LAP (Figure 2.12a). Following a similar approach to the release of dyes, three different conditions were evaluated, pH 7.4, pH 5.0, and a dynamic release condition consisting of a change of pH (at t = 3 h) from physiological to acidic conditions.

In all cases, it is observed that a significant release of drugs from the particles occurs within

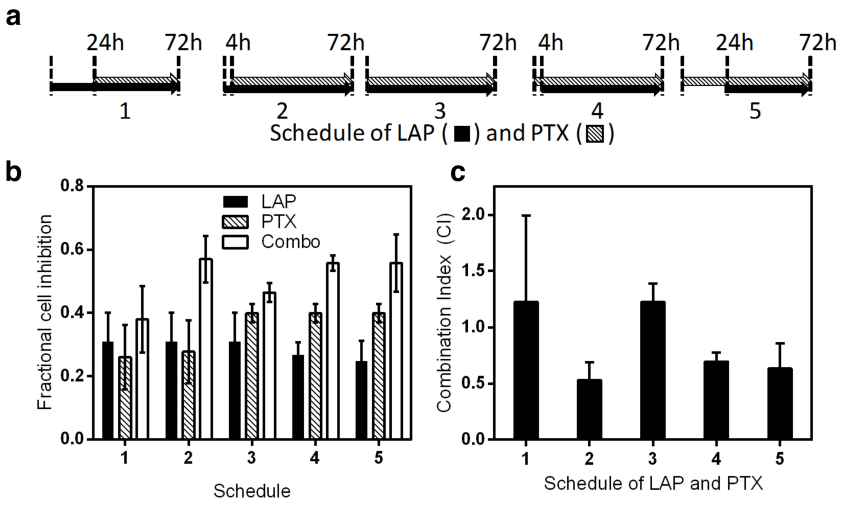

Figure 2.10: **Effect of LAP and PTX schedule on drug synergy.** Efficacy and synergistic effects of combined LAP:PTX treatment dependence on exposure schedule. **a)** 72 h incubation schedule of LAP and PTX combinations. **b)** Fractional cell inhibition as a function of different LAP and PTX schedules evaluated with MTT assay. **c)** Combination index as a function of schedule. Error bars represent 95% confidence interval (n $\geq$ 6 wells).

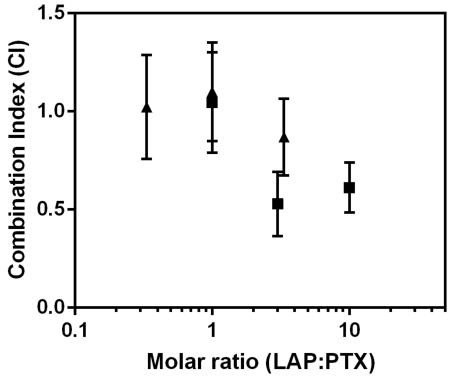

Figure 2.11: **Effect of LAP and PTX molar ratio drug synergy.** Synergy as a function of LAP:PTX molar ratio when exposing cells to LAP (4 h) $\rightarrow$ LAP/PTX (68 h). Relative to PTX concentrations of 0.03 μM (▲) and 0.01 μM (■). Error bars represent 95% confidence intervals (n $\geq$ 12 wells).

the first 72 hours. In neutral conditions, an extended release of each drug is observed with no significant difference seen between the release profiles of the individual drugs (Figure 2.12b). However, it is evident that in acidic release conditions, LAP is preferentially released due to the rapid and selective degradation of the AcDex/PLGA compartment (Figure 2.12c). Furthermore, when the release buffer is exchanged at t = 3 h, a rapid burst release of LAP is observed compared to that of the PTX (Figure 2.12d). This is most clearly seen in the first 24 h, highlighted in Figure 2.12e.

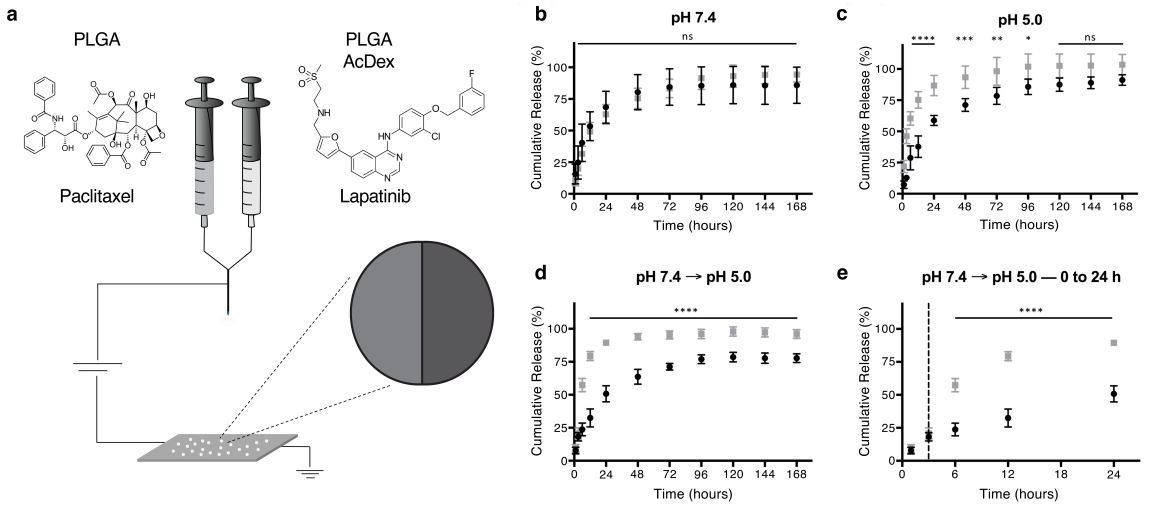

Figure 2.12: **Synthesis and combined release from pH responsive Janus nanoparticles. a)** Fabrication of pH responsive, dual drug-loaded particles. PTX and LAP were encapsulated within distinct PLGA and pH responsive PLGA/AcDex compartments respectively. **b-d)** Controlled release of PTX (black) and LAP (gray) from PLGA and AcDex/PLGA nanoparticle compartments, respectively. (b) Extended and uniform cumulative release is observed at physiological pH, 7.4. (c) Release under acidic conditions indicate a pH dependency on release kinetics with rapid degradation and release of LAP from the AcDex/PLGA compartment. A statistically significant difference in cumulative release is observed during the initial 48 h of drug release. (d) A change in pH at t = 3 h from 7.4 (physiological, circulation) to 5.0 (acidic, cellular uptake), designed to simulate in vivo systemic delivery, further demonstrates pH dependency on release kinetics. All timepoints greater than 6 h show significant differences comparing PTX and LAP cumulative release. **e)** A focused look at the first 24 hours of (d), more clearly shows the significant departure of the combined release kinetics following the pH change at t = 3 h. Results are shown as mean SD. Statistical significance defined as $p < 0.05$ (n = 6 biological replicates; two-way ANOVA and Sidak's multiple comparisons tests; **** $p < 0.0001$, *** $p < 0.0005$, ** $p < 0.005$, * $p < 0.05$).

2.3.5 Anti-cancer Activity of Programmable NPs

A variety of bicompartmental nanoparticles were co-jetted with LAP and PTX (Table)2.1). Both LAP and PTX were loaded into bicompartmental nanoparticles by dissolving the drugs in the individual polymeric solutions. The drugs were loaded into different compartments to change the relative release rate of each drug (Table 2.1). While each particle system was jetted with LAP and PTX concentrations to give final drug loadings of 2.7 and 5.5 wt.%, respectively, approximately a 4-fold lower drug loading remained after collecting, purifying, and washing each particle type, determined with HPLC-MS. Despite this, the approximate target 3:1 molar ratio of LAP:PTX was achieved in each of the final par-

ticle formulations with loading efficiencies ranging from 22-28%. Control particles were also made with just a single drug or no drug encapsulated to further investigate the advantage of dual-loaded bicompartmental particles and possible toxicities associated with the polymers themselves. Particles, regardless of their drug content, were found to have an average size of approximately 160 nm with low polydispersity in their dry state, similar to both unloaded and dye loaded particles previously synthesized.

Table 2.1: Compositions of Janus NPs synthesized via EHD co-jetting

Particle	Compartment 1 PLGA/AcDex	Compartment 2 PLGA	Drug Loading		
			LAP wt %	PTX wt %	Molar Ratio
LAP_1PTX_2	LAP	PTX	1.24	0.71	2.58
$LAP_{1,2}PTX_{1,2}$	LAP/PTX	LAP/PTX	1.29	0.65	2.94
LAP_2PTX_1	PTX	LAP	1.22	0.61	2.96
PTX_2	–	PTX	–	0.76	–
LAP_1	LAP	–	1.23	–	–
Blank	–	–	–	–	–

The activity of the different bicompartmental nanoparticle iterations (Table 2.1) was evaluated on BT-474 cells (Figure 2.13b). Drug loadings of each formulation were determined by HPLC-MS and used to standardize all experimental groups to produce comparable data points for dose response curves allowing a direct comparison to be made between all particle types and previously conducted free drug studies. Bicompartmental particles which contained LAP in the AcDEX/PLGA compartment and PTX in the PLGA compartment (LAP_1PTX_2) induced the most cellular toxicity of the particles loaded with both drugs. Both particles which contained PTX and LAP in different compartments (LAP_1PTX_2 and LAP_2PTX_1), have a lower PTX IC_{50} (4.3 ± 0.5 nM and 6.6 ± 0.7 nM, respectively) than free PTX (14 ± 1 nM). Interestingly, the particle system which contained both drugs in the AcDEX/PLGA compartment ($LAP_{1,2}PTX_{1,2}$), is not as potent as free PTX. All combination particle systems were significantly more potent than free LAP at the concentrations tested.

The cellular activity of the most potent nanoparticle (LAP_1PTX_2) was then compared to a physical mixture of single drug loaded particles with LAP and PTX in the AcDEX/PLGA and PLGA compartments, respectively. Again, HPLC-MS measured drug loadings informed the study to ensure equal dosing between the various experimental groups. The dual loaded Janus particle (LAP_1PTX_2) was considerably more potent than both the PTX and LAP control particles (Figure 2.13c) which had similar drug loadings to the dual loaded

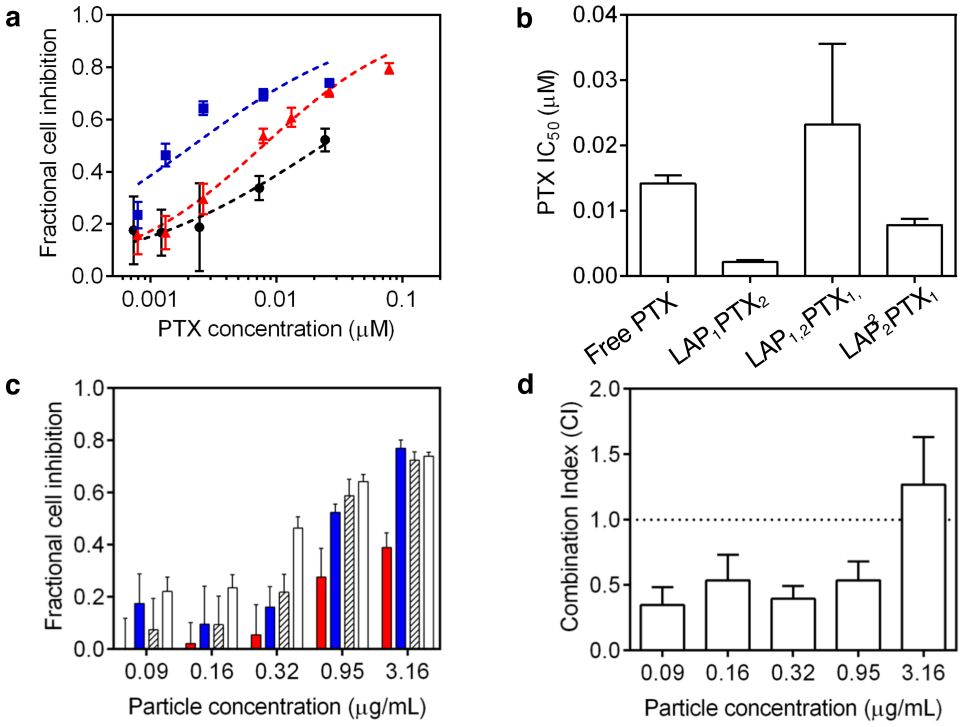

Figure 2.13: **Cancer activity and synergism in HER2$^+$ breast cancer cells. a)** Fractional cell inhibition of BT-474 cells after 72 h exposure to the following bicompartmental particles: LAP_1PTX_2 (AcDEX/PLGA: LAP, PLGA: PTX, blue), $LAP_{1,2}PTX_{1,2}$ (AcDEX/PLGA: LAP + PTX, PLGA: LAP + PTX, red), and LAP_2PTX_1 (AcDEX/PLGA: PTX, PLGA: LAP, black) Points are experimental data and lines are best fit median effect model. **b)** PTX IC_{50} concentrations for each particle type. Error bars represent 95% confidence interval ($n \geq 12$ wells). **c)** Fractional cell inhibition of BT-474 cells after 72 h exposure to the following bicompartmental particles: LAP_1 (AcDEX/PLGA: LAP, PLGA: blank, red), PTX_2 (AcDEX/PLGA:blank, PLGA:PTX, blue), LAP_1 + PTX_2 (black), and LAP_1PTX_2 (AcDEX/PLGA: LAP, PLGA: PTX, white). Points are experimental data and lines are best fit median effect model. **d)** Combination index for particle LAP_1PTX_2. Error bars represent 95% confidence intervals ($n \geq 6$ wells).

particle. In addition, the dual loaded particle (LAP_1PTX_2) is much more effective at inhibiting BT-474 cell growth than a physical mixture of LAP and PTX control particles (LAP_1 and PTX_2) at similar drug concentration. Compared to the single drug loaded particles, the dual loaded particles are synergistic at inhibiting cell growth ($CI < 0.5$) for particle concentrations less than 1 μg mL^{-1} (Figure 2.13d).

Prior to determining the efficacy of the drug loaded particles at inhibiting cancer cell growth, the toxicity of the blank particles was determined on MDA-MB-231 (HER2$^-$) and BT-474 (HER2$^+$) cells (Figure 2.14). Up to a particle concentration of 3 μg mL^{-1}, no toxicity was observed for the blank particles in either cell line. Higher particle concen-

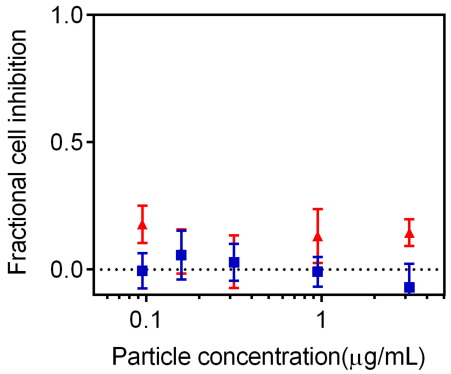

Figure 2.14: **PLGA/AcDex Janus nanoparticle cellular toxicity.** Fractional cell inhibition of MDA-MB-231 (blue, HER2$^-$) and BT-474 (red, HER2$^+$) cells after 72 h exposure to blank bicompartmental nanoparticles. Error bars represent 95% confidence intervals (n $\geq$ 6 wells).

trations were not evaluated because these particle concentrations were sufficiently high for toxicity testing in vitro with the drug loaded particles.

The activity of the bicompartmental nanoparticles was also evaluated in triple negative breast cancer cells (MDA-MB-231). Because triple negative cells are HER2$^-$, LAP is typically ineffective at inhibiting MDA-MB-231 growth. Using LAP concentrations which are relevant to the particle systems (up to 100 nM), LAP does not inhibit any MDA-MB-231 growth. However, LAP has shown to enhance the activity of other cytotoxic drugs on HER2$^-$ cancer cells by inhibiting drug efflux pumps. [136, 144]

Interestingly, both dual loaded particle systems are more active than the single loaded PTX particles against MDA-MB-231 cells, even though the single loaded LAP particles show no signs of toxicity (Figure 2.15). The IC_{50} for the dual loaded particles LAP_1PTX_2 and $LAP_{1,2}PTX_{1,2}$ is 3x and 2x lower, respectively, than the single loaded PTX particles. In addition, the most toxic dual loaded particle (LAP_1PTX_2) has a significantly lower IC_{50} than free PTX (LAP_1PTX_2: 4.3 $\pm$ 0.6 nM, free PTX: 11 $\pm$ 2 nM). When tested in non-tumorigenic mammary epithelial MCF 10a cells, lower IC_{50} values were found for all particle types compared to each of the breast cancer cells lines. The results follow a similar trend to free PTX in the various cell lines (Table 2.2).

LAP has been used in combination with many other chemotherapeutics in the clinic due to its ability to enhance tumor inhibition. In particular, the combination of LAP and PTX has proven to be an effective drug combination for treating late stage, metastatic breast cancer. Here, we show that the drug pair is synergistic at inhibiting the growth of HER2$^+$ breast cancer cells if given in the correct sequence. We then demonstrate that we can synthesize

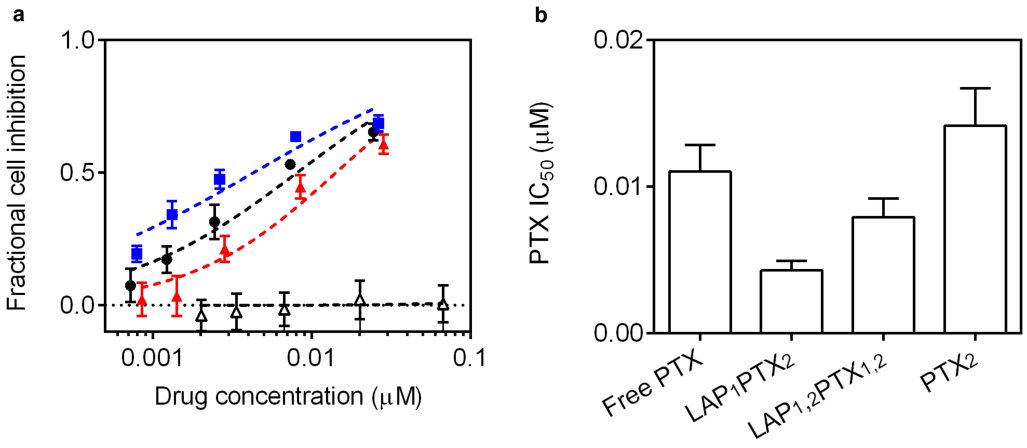

Figure 2.15: **Cancer activity of programmable nanoparticles in HER2 cells. a)** Fractional cell inhibition of MDA-MB-231 cells after 72 h exposure to the following bicompartmental particles: LAP_1PTX_2 (blue), and $LAP_{1,2}PTX_{1,2}$ (black) compared to particles containing a single therapeutic, PTX_2 (PTX only, PLGA, red) and LAP_1 (LAP only, AcDex, △). Points are experimental data and lines are best fit median effect model. **b)** PTX IC_{50} concentrations for each particle type. Error bars represent 95% confidence intervals (n ≥ 12 wells).

Table 2.2: PTX IC_{50} values (nM) in cultured breast cancer cell lines

	MCF 10a	BT-474	MDA MB 231
Free PTX	4.4 ± 0.7	14 ± 1.0	$11. \pm 2.0$
LAP_1PTX_2	1.1 ± 0.1	4.3 ± 0.4	4.3 ± 0.6
$LAP_{1,2}PTX_{1,2}$	3.4 ± 0.4	23 ± 10	8.0 ± 1.9
LAP_2PTX_1	1.9 ± 0.4	6.6 ± 0.7	–
PTX_2	3.1 ± 0.4	8.8 ± 1.7	$14. \pm 2.1$

programmable nanoparticles which are capable of controlling both the molar ratio of LAP and PTX and the relative release rate of each drug.

The $HER2^+$ cell line BT-474 is responsive to both LAP and PTX with single drug IC_{50} values in the nM range; however, the combination of LAP and PTX is not synergistic, if the cells are exposed to both drugs simultaneously. If the schedule of drug administration is controlled, such that the one drug is exposed prior to the other, the combination becomes synergistic indicating a lower drug dose can be administered to achieve the same cellular growth inhibition. In free drug studies, synergy is the highest when LAP is given 4 h prior to PTX at a molar ratio of LAP:PTX of 3:1. For the optimal schedule, the combination index (CI) is approximately 0.5, indicating that a 2x fold lower dose of PTX can be given. It is evident that synergy between LAP and PTX is highly dependent upon both the schedule

and molar ratio of LAP and PTX while treating BT-474 cells. This is consistent with a previous study which showed that trastuzumab can only enhance the activity of PTX on $HER2^+$ cancer cells if the cells are exposed to trastuzumab first. [143]

The strong dependence of drug ratio and temporal schedule on drug synergy makes it difficult to translate an effective combination dosing regimen to the clinic due to the complicated pharmacokinetics. Various nano-sized delivery vehicles have been synthesized to carry both LAP and PTX to ensure that cancer cells are exposed to the drugs simultaneously; however, drug release from these vehicles cannot be changed without changing the physical structure of the vehicle and/or drug loading process. [133, 138–142, 144] Here, we used EHD co-jetting to synthesize Janus nanoparticles which enable us to manipulate the release rate and molar ratio of drug-loaded particles without drastically changing the drug loading technique and/or overall particle structure.

Both LAP and PTX could be loaded into either particle compartment, so dual loaded particles were synthesized varying which compartment each drug was loaded in. Particles which contained LAP in the AcDEX/PLGA compartment and PTX in the PLGA compartment were considerably more potent to BT-474 ($HER2^+$) cells than the particles which contained both LAP and PTX in the AcDEX/PLGA compartment. This is consistent with the free drug data, which shows that exposing BT-474 cells to LAP prior to PTX is more synergistic than exposing the cells to both drugs concurrently. Furthermore, the dual-loaded particles were more potent than the combined delivery of single drug loaded particles at the same drug dose, demonstrating that synergy is maintained between PTX and LAP. Surprisingly, the dual drug loaded particles were also more potent to triple negative breast cancer cells (MDA-MB-231), even though the cells are unresponsive to LAP on its own. The enhanced activity is likely due to the inhibition of efflux drug pumps with LAP; [136, 144] however, further research is required to explore this effect in detail.

The primary advantage of using dual drug loaded particles is that cells are exposed to the drug pair simultaneously *in vivo*, regardless of how the individual free drugs distribute in the body. However, it is often advantageous to expose the cells to one drug prior to the other drug. Here, the therapeutic activity of dual loaded PTX/LAP particles could be manipulated *in vitro* by changing the relative release kinetics of the drug pair by changing which compartment the drugs were incorporated into and their bulk composition. The ability to manipulate individual drug release kinetics, provides another adjustable parameter while designing combination drug particles. Previous studies have synthesized core-shell particles to release one drug relatively faster than another drug; however many of these systems rely on differences in drug hydrophobicity to load into different regions of the par-

ticle. [68,79,145–147] On the contrary, by using EHD co-jetting, the relative release rate of PTX and LAP, and the resulting cellular toxicity, could easily be manipulated by changing reaction conditions and final particle architecture. This observed control of release kinetics is not limited to this particular drug pair.

While the dual loaded particles containing LAP in the AcDEX/PLGA compartment were most effective at inhibiting cancer cell growth *in vitro* on BT-474 cells and MDA-MB-231 cells, this will not be true for all cell lines. Furthermore, other pairs of chemotherapeutic agents will demonstrate schedule-dependence, motivating the development of new delivery platforms capable of controlling the release rate of multiple therapeutics. Moving forward, the effect of drug release needs to not only be evaluated with respect to cancer cell activity *in vitro*, but also with respect to healthy cell activity and *in vivo* efficacy. Regardless of the drug combination, the effect of drug schedule should be critically evaluated when designing a delivery vehicle to carry multiple agents.

2.4 Summary

Here, we aimed to develop a single nanoparticle system capable of delivering a synergistic combination of cancer therapeutics for $HER2^+$ breast cancer. After characterizing the activity of paclitaxel and lapatinib, free drug studies identified both a molar ratio and temporally dependent synergy when the drugs were combined. Leveraging prior work, a pH responsive, bicompartmental particle system was optimized.

Bicompartmental nanoparticles were synthesized with one compartment containing PLGA and one compartment containing AcDex/PLGA. The particles are less than 250 nm in diameter and can be further purified to isolate smaller fractions. The Janus morphology of the nanoparticles was verified with super resolution microscopy. Electron microscopy confirmed each compartment degrades differently in response to pH; the pH responsive AcDEX/PLGA compartment degrades significantly faster in acidic pH than the pure PLGA compartment. Two independent release studies confirm this selective degradation, wherein independent release kinetics are observed from the distinct compartments. Due to rapid bulk polymer degradation in response to acidic environments, similar to those of endosomes, we hypothesized we could achieve an intracellular controlled of the delivery of our two compounds. When delivered to $HER2^+$ breast cancer cells, we observe a synergistic effect mirroring that of the optimized free drug studies. Moving forward, prior work in our lab developing methods of surface modifications (e.g. PEGylation or receptor specific

targeting) of PLGA-based particle systems, can be applied. This approach has the potential to extend particle circulation and targeted accumulation in tumors with leaky vasculature following systemic administration.

CHAPTER 3

Synthetic Protein Nanoparticles: Emerging Parameters of SPNP Design

This chapter contains portions of text/data originally published as:

Red Blood Cell-hitchhiking Boosts Delivery of Nanocarriers to Chosen Organs by Orders of Magnitude.
JS Brenner, DC Pan, JW Myerson, OA Marcos-Contreras, CH Villa, P Patel, H Hekierski, S Chatterjee, J Tao, H Parhiz, K Bhamidipati, TG Uhler, ED Hood, RY Kiseleva, VS Shuvaev, T Shuvaeva, M Khoshnejad, I Johnston, JV Gregory, J Lahann, T Wang, ECantu, WM Armstead, S Mitragotri, V Muzykantov
Nature Communications (2018)

Contributions to this multi-institute collaborative work included the design and synthesis of albumin nanoparticles to be tested against a range of nano-constructs. Synthesized particles were fully characterized prior to their inclusion in both *in vitro* and *in vivo* studies. Work initiated here, served as a basis for further developments presented in Chapter 4.

Multifunctional Synthetic Protein Nanoparticles via Reactive Electrojetting.
D Quevedo*, N Habibi*, JV Gregory, Y Hernandez, TD Brown, R Miki, BN Plummer, S Rahmani, J Raymond, S Mitragotri, J Lahann
Macromolecular Rapid Communications (2020)

Individual contributions to this collaboration included the design, production, and characterization of protein nanoparticles. Specifically, efforts focused on the development of water-stable protein particles without the use of crosslinking macromers. Additionally, super resolution microscopy was utilized to validate the multicompartmental architecture of Janus protein nanoparticles.

Supramolecular Arrangement of Protein in Nanoparticle Structures Predicts Nanoparticle Tropism for Neutrophils in Acute Lung Inflammation
JW Myerson*, PN Patel*, KM Rubey*, ME Zamora, MH Zaleski, N Habibi, LR Walsh, Y Lee, DC Luther, LT Ferguson, OA Marcos-Contreras, PM Glassman, LL Mazaleuskaya, I Johnston, ED Hood, T Shuvaeva, J Wu, H Zhang, JV Gregory, RY Kiseleva, J Nong, T Grosser, CF Greineder, S Mitragotri, GS Worthen, VM Rotello, J Lahann, VR Muzykantov, JS Brenner
Nature Nanotechnology (2021)

Individual contributions to this multi-institute collaborative work included the design and synthesis of albumin nanoparticles to be tested as part of a library of nanoparticles. Efforts yielded the fabrication of non-spherical, rod-shaped protein particles, a distinct particle class unique from all others included in the study. Synthesized particles were fully characterized prior to their inclusion in both *in vitro* and *in vivo* studies.

3.1 Motivation

Decades of research and development aimed at creating drug delivery vehicles capable of controlled release of therapeutics and minimizing toxic off-target effects have resulted in a limited number of FDA approved nanomedicines. While early examples consist primarily of liposome-based delivery systems, a range of materials have been since explored. Notably, biocompatible and biodegradable synthetic polymers, such as PLGA, emerged as a promising means to encapsulate small molecule drugs and tune their release kinetics through variations in the copolymer's molecular weight and balance of glycolic and lactic acid monomers. As discussed in Chapter 1, our group has explored the use of PLGA in EHD co-jetting extensively, developed a library of functional PLA polymers to allow for surface functionalization, and have successfully leveraged the particles for drug delivery. Despite this, synthetic polymers degrade relatively slowly in the body and carry the potential risk of accumulation, toxicity, and immunogenicity.

An attractive alternative to use of synthetic polymers is that of biologically derived materials. Proteins in particular have been recently explored as a base material for the synthesis of nanoparticles. Composed of 20 naturally occurring amino acid side chains (Figure 3.1), proteins are chemically diverse biomolecules, are readily degraded in the body, and have the potential for reduced toxicity and immunogenicity. Abraxane (albumin-bound paclitaxel) was first approved by the FDA for the treatment of breast cancer, non-small cell lung

cancer, and pancreatic cancer. Since its approval, Abraxane has been the focus of numerous clinical studies, with goals of identifying additional applications, either as a standalone treatment or in combination with existing standard of care approaches.

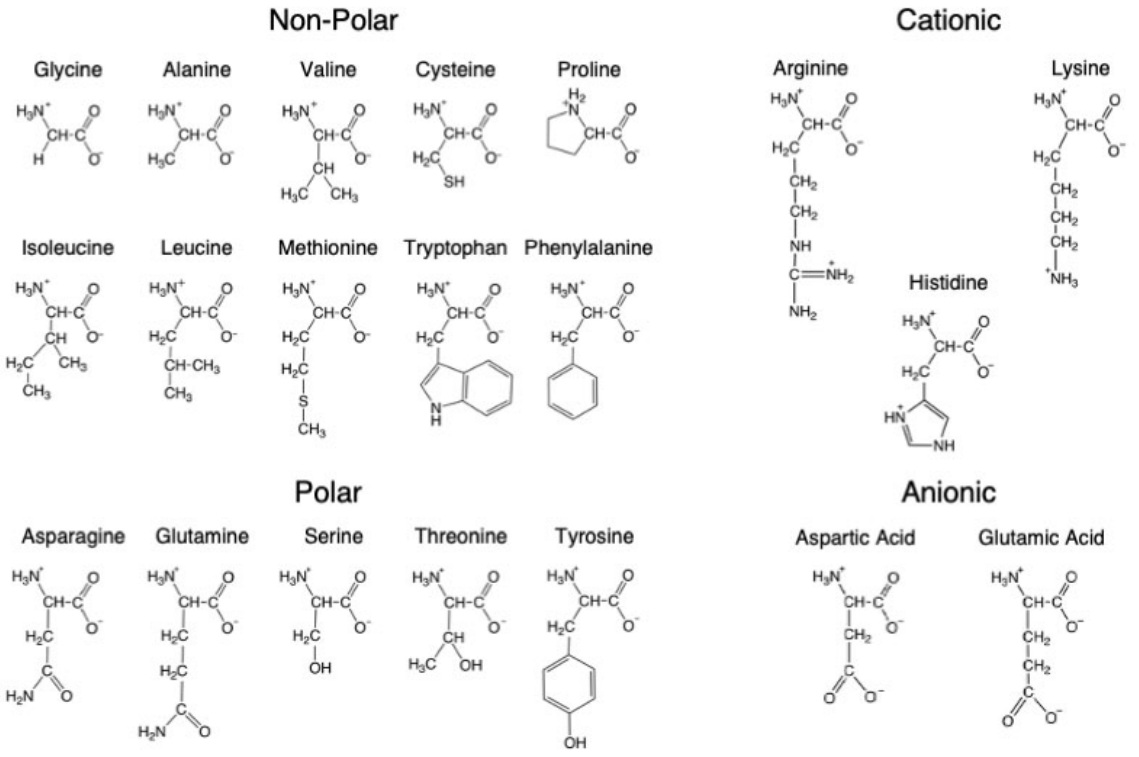

Figure 3.1: **Amino Acid Chemical Structures.** Proteins, comprised of 20 naturally occurring amino acid residues (shown above), can be categorized as non-polar, polar, cationic, and anionic. Resulting from the distinct chemical moieties of the amino acid side chains, synthetic routes towards controlled protein modifications are possible.

Currently, primary protein-based nanoparticle synthesis routes include nab-technology, [148] directed self assembly, [149] and coacervation. [150] While each as been successfully leveraged to produce protein nanoparticles, drawbacks with each exist. Serving as the basis for the synthesis of Abraxane, nab-technology, has thus far been limited to the complexation of small molecule, hydrophobic drugs and has been found to result in denaturing of the protein structure. The latter, becomes a concern when employing proteins or enzymes where protein structure plays an integral role in function. Directed self-assembly avoids issues of denaturing and be used to create complex particle architectures, yet finds severe limitations in the library of proteins where this approach can be applied. Conversely, the coacervation approach typically maintains protein structure and is widely applicable across the entirety of protein families. With high yields, diverse protein libraries, and control over particle size, coacervation is currently the most widely applied method of protein

particle synthesis; however, coacervation, like nab-technologies, lacks the ability to create more complex architectures. As discussed in Chapter 1, the synthesis of multifunctional particles may be key to overcoming the various biological barriers to successful targeted drug delivery.

Here, we aim to leverage our expertise using the EHD jetting process to develop a robust platform for the synthesis of protein nanoparticles. The primary goals include the development of reproducible and controlled methods towards stable nanoparticles and means to thoroughly characterize their biophysiochemical properties. Additionally, the work aims to expand the versatility of the platform to ultimately allow for the development of more complex, multifunctional, synthetic protein nanoparticles (SPNPs).

3.2 Experimental Methods

3.2.1 Materials

Reagents: Human serum albumin, human transferrin, human recombinant insulin, human hemoglobin, lysozyme from chicken egg white, O,O-Bis[2-(N-Succinimidyl-succinylamino) ethyl]polyethylene glycol (NHS-PEG-NHS, 2 kDa), 4,7,10,13,16,19,22,25,32,35,38,41,44, 47,50,53-Hexadecaoxa-28,29- dithiahexapentacontanedioic acid di-N-succinimidyl ester (NHS-PEG-(S-S)-PEG-NHS), ethylene glycol, trifluoroethanol (TFE), mercaptoethanol, Sephadex 4B, glutaraldehyde, gallic acid, N-Succinimidyl-S-acetylthioacetat (SATA), triethylamine, hydrochloric acid, sodium sulfate, sodium chloride, dimethylsulfoxide(DMSO), ethyl acetate, chloroform, dimethylformamide, ascorbic acid, hydrogen peroxide solution, Tween 20, N-(3-Dimethylaminopropyl)-N-ehtylcarbodiimide hydrochloride (EDC), and phosphate buffered saline were purchased from Sigma Aldrich, USA. Succinate Succinimidyl PEG (NHS-PEG-NHS, 400 Da and NHS-PEG-NHS, 20 kDa) was purchased from NanoCS. Human serum albumin and transferrin monoclonal antibodies, Tris-HCl buffer, (5,5-dithio-bis-(2-nitrobenzoic acid) (Ellman's reagent), acetonitrile, sodium nitrite, acetone, BCA assay kit, N-(hydroxysulfosuccinimide) (Sulfo-NHS), and Protein 660 assay kit were purchased from Fisher Scientific. Paclitaxel was purchased from LC Laboratories.

3.2.2 Methods

Synthesis of NHS-PEG-NHS Crosslinked Synthetic Protein Nanoparticles (SPNPs)

SPNPs were fabricated via the electrohydrodynamic (EHD) jetting process previously developed in our group for the fabrication of synthetic polymer nanoparticles. [8, 89–92] Adapted to instead use proteins as the bulk material, human serum albumin (HSA) was dissolved in a cosolvent mixture (80:20 v/v) of ultrapure water and ethylene glycol at a concentration of 7.5 w/v%. Alternatively, a cosolvent mixture (80:20 v/v or 90:10 v/v) of ultrapure water and ethanol can be used. A bifunctional PEG (NHS-PEG-NHS, 2kDa) was added at 10 w/w% relative to HSA. In experiments evaluating the effects of crosslinking and the resulting swelling, molecular weight and mass fraction of NHS-PEG-NHS were varied. Final jetting solutions were pumped through a syringe equipped with a 26-gauge blunt tip needle at a flowrate of 0.1-0.2 mL h^{-1} while a constant voltage (ranging from 5.0 to 11.5 kV) was applied to form a stable Taylor cone at the needle tip. Particles were collected in aluminum pans at a needle to collector distance of 15 cm and then incubated for seven days at 37°C to facilitate complete polymerization. SPNPs were then stored in dark RT conditions in their dry state for future experiments.

Collection and purification of SPNPs

SPNPs were collected according to a standard protocol developed in our lab. In brief, a small volume, 5-10 mL, of water:ethanol (80:20 v/v) + 0.5% Tween 20, was added to the aluminum pans containing EHD jetted SPNPs. The resulting SPNP suspension was gently sonicated to disperse any aggregates and passed through a 40 μm cell straining filter. The resulting solution was centrifuged at 4,000 rpm (3,220 xg) for 4 minutes to pellet and remove any albumin aggregates larger than 1 μm in diameter. The supernatant was then divided into 2 mL Eppendorf tubes and centrifuged at 15,000 rpm (21,500 xg) to concentrate the samples to a single 1 mL sample for use in planned experiments. Collected SPNPs were used within 1 week of their collection and were stored at 4°C in PBS during that time.

Characterization of albumin SPNPs size, shape, and concentration

Albumin SPNPs were characterized prior to their use in any experiments to ensure they met specifications. Physical characterization included the measurement of particle size in both their dry and hydrated state. To measure particle diameter and investigate their

morphology, small silicon wafers were placed on the grounded collection surface and were subjected to the same incubation period to complete the step-growth polymerization. These samples were imaged via SEM using a FEI NOVA 200 SEM/FIB instrument (UM, MC^2 Institute). Obtained SEM images were characterized using ImageJ software. SPNPs in their hydrated state were collected and purified as described above. The stock solution was diluted in PBS + 0.5% Tween 20 for subsequent measurements using DLS and nanoparticle tracking analyzer (NTA) to investigate size and solution concentration. Analysis via DLS and NTA was performed using the Malvern Nano ZSP and NanoSight NS300 instruments and software, respectively (UM, Biointerfaces Institute). Albumin SPNP solution concentration was further validated using the BCA (bicinchoninic acid) assay.

Synthesis of Disulfide NHS-PEG-NHS Crosslinked SPNPs

Following a similar approach as described above, HSA was dissolved in a cosolvent mixture at a concentration of 7.5 w/v%. A disulfide containing, bifunctional PEG (NHS-PEG-(S-S)-PEG-NHS, 2kDa) was added at 10 w/w% relative to HSA. Final jetting solutions were pumped through a syringe equipped with a 26-gauge blunt tip needle at a flowrate of 0.1-0.2 mL h^{-1} while a constant voltage (ranging from 5.0 to 11.5 kV) was applied to form a stable Taylor cone at the needle tip. Particles were collected in aluminum pans at a needle to collector distance of 15 cm and then incubated for seven days at 37°C to facilitate complete polymerization. SPNPs were then stored in dark RT conditions in their dry state for future experiments.

Synthesis of Macromer-free Disulfide Crosslinked SPNPs

In order to create water-stable SPNPs in the absence of crosslinking macromer (XLF-SPNPs), HSA was dissolved in a cosolvent mixture (90:10 v/v) of trifluoroethanol (TFE) and ultrapure water 7.5 w/v%. Following complete dissolution and unfolding of the protein (evident by a slightly cloudy solution appearance), 10 molar excess of β-mercaptoethanol (β-ME) relative to protein disulfide bonds (e.g. 34 per albumin) was added. Final jetting solutions were pumped through a syringe equipped with a 26-gauge blunt tip needle at a flowrate of 0.1-0.2 mL h^{-1} while a constant voltage (ranging from 7.0 to 10.0 kV) was applied to form a stable Taylor cone at the needle tip. Particles were collected in aluminum pans at a needle to collector distance of 15 cm. No further incubation at elevated temperatures was required or performed. Particles collected on a dry surface were instead stored in a vacuum desiccator for a period of at least 12 h to remove any residual solvents. Disul-

fide crosslinking SPNPs were then stored in dark RT conditions in their dry state for future experiments. Alternatively, immediate collection of particles were performed by filling the collection pan with an 80:20 v/v blend of ultrapure water and ethanol. In this case, particle solutions could immediately enter our purification protocol via centrifugation.

Synthesis of Glutaraldehyde Vapor Phase Crosslinked SPNPs

In order to create water-stable SPNPs using a vapor phase crosslinking approach albumin SPNPs HSA was dissolved in a cosolvent mixture (80:20 v/v) of ultrapure water and ethylene glycol at a concentration of 7.5 w/v%. Here, no crosslinking macromer was added. Final jetting solutions were pumped through a syringe equipped with a 26-gauge blunt tip needle at a flowrate of 0.1-0.2 mL h^{-1} while a constant voltage (ranging from 5.0 to 11.5 kV) was applied to form a stable Taylor cone at the needle tip. Particles were collected in aluminum pans at a needle to collector distance of 15 cm. Collection pans were then stored in a sealed container along with an open reservoir containing a 2.5 mL volume of 20% glyceraldehyde aqueous solution for thirty minutes. SPNPs were then stored in dark RT conditions in their dry state for future experiments.

Synthesis of Thiol-rich albumin

Chemical modifications of proteins prior to entering the jetting pipeline was pursued as an alternative means to crosslinking. Following established protocols for a two-step thiolation of proteins, HSA was chemically modified. In brief, 0.5 g of HSA was dissolved in 50 mM PBS (+10 mM EDTA). Separately, a 65 mM solution of N-succinimidyl S-acetylthioacetate (SATA) was prepared in DMSO. While stirring at RT under atmospheric air, 1.0 mL of the SATA solution was added the albumin solution and the combined reaction mixture was stirred for 45 minutes. Following the reaction, the solution was placed in 10 kDa MWCO dialysis tubes and dialyzed against deionized water at 4°C for a period of 48 h with regular changes of water performed every 6 h. Prior to moving to the second step, a deprotection solution was prepared consisting of 0.5 M hydroxyamine HCl in 50 mM PBS (+25 mM EDTA). Following the complete removal of unreacted and byproduct species from the modified protein via dialysis, 10 mL of the deprotection solution was added to the dialyzed protein solution and the mixture was reacted at RT for 2 h. To purify the thiol-modified protein, the final solution was passed through a Sephadex G-25 column and fractions were analyzed using a BCA assay, before protein containing fractions were combined, frozen and lyophilized. The resulting dry off-white powder (HSA-SH) was analyzed through the use of a BCA assay in tandem with Ellman's assay to determine the

number of thiol groups per albumin of the final product.

Synthesis of Thiol-rich albumin SPNPs

Following a similar approach as described above, HSA-SH was dissolved in a cosolvent mixture (80:20 v/v) of ultrapure water and ethylene glycol at a concentration at a concentration of 2.5 w/v%. Due to the extra thiol groups added to the protein during prior chemical modifications, no crosslinking macromer is added to the jetting solution. Final jetting solutions were pumped through a syringe equipped with a 26-gauge blunt tip needle at a flowrate of 0.2 mL h^{-1} while a constant voltage (ranging from 8.0 to 10.0 kV) was applied to form a stable Taylor cone at the needle tip. Particles were collected in aluminum pans at a needle to collector distance of 15 cm. In the absence of added macromer no incubation at elevated temperature was performed. TR-SPNPs were then stored in dark RT conditions in their dry state for future experiments.

Synthesis of SPNPs Consisting of Various Proteins

While early development of the SPNP platform focused on the use of HSA, this method of protein nanoparticle fabrication is not limited to albumin. When incorporating alternative proteins, the protein of choice was generally dissolved in a cosolvent mixture (80:20 v/v) of ultrapure water and ethylene glycol at a concentration of 1.0-7.5 w/v%. Protein concentration was dependent upon both solubility and target loading of cargo. For example, when attempting to load a plasmid DNA already in solution, protein concentrations would in some cases need to be reduced to maximize pDNA loading. In some instances, additives were required to achieve stable solutions (e.g. Insulin SPNPs required the addition (10 vol%) of glacial acetic acid). Previously described crosslinking approaches could each be utilized and the addition or absence of additional macromer would follow those previously described protocols. Final jetting solutions were pumped through a syringe equipped with a 26-gauge blunt tip needle at a flowrate of 0.1-0.2 mL h^{-1} while a constant voltage (ranging from 4.0 to 15.0 kV) was applied to form a stable Taylor cone at the needle tip. Particles were collected and processed according to the chosen crosslinking method used as described above. Resulting SPNPs were then stored in dark RT conditions in their dry state for future experiments.

Synthesis of Janus SPNPs

Cojetting of two or more protein solutions to yield multicompartmental Janus SPNP can be achieved following previously developed approaches for synthetic polymer particles.

[74, 75, 93] For protein-based Janus nanoparticles, distinct protein solutions are prepared by dissolving the protein of choice in a cosolvent mixture. Ideally, protein concentration and solvent composition should be made as consistent as possible to result in matching solution properties (i.e. viscosity, dielectric constant). In some cases, particularly when additives such as small molecule hydrophobic molecules that require the compound to first be dissolved in an organic solvent (e.g. DMSO), it is beneficial to add the same small volume of pure solvent to other solutions in order to achieve similar solvent properties. Previously described crosslinking approaches could each be utilized and the addition or absence of additional macromer would follow those protocols. Final jetting solutions for bicompartmental nanoparticle synthesis were loaded into distinct syringes, each equipped with a 26-gauge blunt tip needle at a flowrate of 0.1 mL h^{-1} (total flowrate of 0.2 mL h^{-1}) while a constant voltage (ranging from 5.0 to 11.5 kV) was applied to form a stable Taylor cone at the needle tip. Particles were collected and processed according to the chosen crosslinking method used as described above. Janus SPNPs were then stored in dark RT conditions in their dry state for future experiments.

Characterization of Janus SPNPs

Janus SPNPs fabricated via EHD jetting were imaged using the Carl Zeiss Elyra super-resolution SIM microscope (UM, Biointerfaces Institute). In instances when fluorescent imaging would be completed, distinct Alexa Fluor protein conjugated dyes were incorporated into the jetting solution at 0.5 wt% relative to the total protein content for each individual solution. Typical fluorophores used included commercially available Alexa Fluor, 488, 555, and 647 and in-lab synthesized, Alexa Fluor 405 albumin conjugates. During the jetting process, small glass cover slides were placed on the grounded collection surface. Following a period of approximately 15 mins, the glass cover slide was removed and stored according to the crosslinking method being used for the formulation being evaluated. The glass cover slide, coated with Janus SPNPs was then mounted using Prolong Gold Antifade Mountant and allowed to cure for at least 48 h prior to imaging.

Synthesis of Albumin-Gallic Acid Conjugates

Chemical modifications of proteins prior to entering the jetting pipeline was pursued in an attempt to impart chemical properties and biological function onto otherwise inert proteins. Modifications of a previously developed synthetic route to antioxidant proteins, [151, 152] gallic acid (GA) was conjugated to HSA. In brief, 0.5 g of HSA was first dissolved in 50 mL of deionized water. Following complete dissolution of the protein, 0.6 mL of

30 %(w/w) H_2O_2 and 0.25 g of ascorbic acid were sequentially added at RT. After 2 h, 59.5 mg (0.35 mmol) of gallic acid was added and allowed to stir O/N at RT under atmospheric air. Following the reaction, the solution was placed in 10 kDa MWCO dialysis tubes and dialyzed against deionized water at 4°C for a period of 72 h with regular changes of water performed every 6 h. Once unreacted material had been removed via dialysis, the solution was frozen and dried using a Labconco FreeZone 4.5L Cascade lyophilzer to obtain a dry off-white powder.

Characterization of Albumin-Gallic Acid Conjugates

Characterization of albumin-gallic acid conjugates was performed to determine the degree of substitution achieved via the performed chemical modification. Lyophilized HSA-GA conjugates were resuspended at 3 mg ml^{-1} in tris-buffered saline (TBS). Utilizing the Malvern OMNISEC instrument, equipped with a Malvern PLS3030 silica column, 100 µL samples were injected in triplicate. The flowrate and temperature were maintained at 1.0 mL min^{-1} and 20°C, respectively. A triple detection method was used and included refractive index (RI), a viscometer, and right-angle light scattering detectors to measure sample molecular weight, intrinsic viscosity, and degree of aggregation.

Synthesis of HSA-GA SPNPs

Jetting of previously synthesized albumin-gallic acid conjugates followed a similar approach to previously described jetting protocols. The dried HSA-GA protein conjugate was dissolved in a cosolvent mixture (80:20 v/v) of ultrapure water and ethylene glycol (+ 0.2 vol% TEA) at a concentration of 2.5 w/v%. A bifunctional PEG (NHS-PEG-NHS, 2kDa) was added at 10 w/w% relative to HSA-GA. Final jetting solution was pumped through a syringe equipped with a 26-gauge blunt tip needle at a flowrate of 0.2 mL h^{-1} while a constant voltage (ranging from 8.0 to 10.5 kV) was applied to form a stable Taylor cone at the needle tip. Particles were collected in aluminum pans at a needle to collector distance of 15 cm and then incubated for seven days at 37°C to facilitate complete polymerization. HSA-GA SPNPs were then stored in dark RT conditions in their dry state for future experiments.

Synthesis of Albumin-Paclitaxel Protein Conjugate

Preparation of a albumin-paclitaxel protein conjugate was produced according to Example 4 of U.S. Patent, US 2007/0087022 A1. [153] In brief, 30 mg (35.1 µmol) of PTX was dissolved in 0.55 mL of chloroform ($CHCl_3$). The PTX solution was then added to 29.4 mL

of an aqueous 1%(w/v) HSA solution that had been presaturated with chloroform. The mixture was first homogenized on ice for five minutes using a tip sonicator at 10% amplitude to form an emulsion prior to moving forward. The solution was split into three, 10 mL syringes and kept on ice throughout the remaining process. Using the Avestin EmulsiFlex-B15 high pressure homogenizer and compressed nitrogen, each aliquot of the emulsion was cycled through seven cycles at 25,000 psi. The resulting homogenized dispersion was then frozen and dried using a Labconco FreeZone 4.5L Cascade lyophilzer.

Synthesis of Paclitaxel-loaded SPNPs

Jetting of previously synthesized albumin-paclitaxel conjugates followed a similar approach to previously described jetting protocols. The dried HSA-PTX protein conjugate was dissolved in a cosolvent mixture (90:10 v/v) of ultrapure water and ethanol at a concentration of 2.5 w/v%. A bifunctional PEG (NHS-PEG-NHS, 2kDa) was added at 10 w/w% relative to HSA-PTX. Final jetting solution was pumped through a syringe equipped with a 26-gauge blunt tip needle at a flowrate of 0.2 mL h^{-1} while a constant voltage (ranging from 6.5 to 9.5 kV) was applied to form a stable Taylor cone at the needle tip. Alterations to the jetting stations were performed and incorporated a modified inverted glass vessel to engineer an additional level of safety to the system in order to prevent accidental release of aerosol chemotherapeutic into the chemistry hood and potentially the extended lab space. Particles were collected in aluminum pans at a needle to collector distance of 12 cm and then incubated for seven days at 37°C to facilitate complete polymerization. HSA-PTX SPNPs were then stored in dark RT conditions in their dry state for future experiments.

Characterizing Release of Paclitaxel from SPNPs

To determine loading, loading efficiency, and release kinetics, particles were fabricated as described above, crosslinked, and then collected per standard protocol. The resulting purified nanoparticle suspensions were frozen and dried using a Labconco Freezone 4.5L Cascade lyophilzer prior to being weighed with a TA Instruments Discovery TGA. Release kinetics were determined via dialysis. Known particle masses were collected and suspended in 5 mL of PBS (pH 7.2). Particle solutions were placed within a Float-a-Lyzer device (100 kDa MWCO, Spectrum Labs) and submerged in an additional 40 mL of equivalent release media in 50 mL conical vials. The vials were incubated at 37°C. At pre-determined times, the dialysis device was transferred to a new conical vial filled with pre-warmed, fresh release media. Resulting solutions were analyzed for drug concentrations using an Agilent Q-TOF HPLC-MS instrument (UM, Chemistry Mass Spec Lab).

Previously generated calibration curves were used to determine total drug loading, loading efficiency, and the kinetics at which the PTX was released.

3.3 Results and Discussion

Applying the same principles used in the fabrication of synthetic polymer nanoparticles, EHD jetting can be used to produce particles from endogenous proteins. However, the transition to the use of water soluble bulk materials requires modifications to the process to achieve stable particle architectures for their intended use in biological systems. In particular, these alterations to the previously developed process include, i) the use of protein as the main bulk material, ii) a method to crosslink the individual proteins, iii) the use of water or water-based cosolvent systems as a carrier solvent, and iv) modifications to the processing parameters and post-fabrication treatments. Each of the aforementioned adaptations include variables and an associated design space, that when explored, has the potential to result in a robust platform capable of producing a range of particles with varied architectures and properties.

3.3.1 Albumin SPNPs - Synthesis and Characterization

As a starting point, a means to produce water-stable albumin nanoparticles was developed. Here, we maintain much of the previously developed EHD setup; consisting of a regulated syringe pump to maintain a constant volumetric flow, a power supply, and grounded collection surface, together allowing for the previously engineered infrastructure to be applied without further modifications. Our chosen base protein to develop the platform, albumin, is readily commercially available, functions as a transport protein in the body, [154] has a circulation half-life of approximately 19 days, [155] and is the most abundant protein found in serum. [154] The protein has been successfully used to formulate nanoparticles through alternative synthetic routes. [150, 156] Furthermore, albumin is widely used in the biological sciences with applications ranging from cell culture, [157] biological assays, [158] and inorganic colloid and surface functionalization. [159–161]As a means to crosslink the protein, the use of a homobifunctional PEG crosslinker capped on each end with an N-hydroxysuccinimide (NHS) group was first evaluated. The NHS functional group readily reacts with amines, and was chosen due to the presence of reactive amine groups as part of the lysine side chain groups generally present in proteins. While various ratios of PEG crosslinking macromer to albumin were initially evaluated (and later revisited) a 10% w/w

relative to albumin was ultimately chosen. This mass ratio translates to approximately a 7:1 ratio of the NHS functional group to albumin molecule. Theoretically, at the upper limit, if all NHS groups were to successfully react with the protein, nearly 90% of all lysine residues would remain unmodified. Thus, the chosen mass ratio of crosslinker to albumin, strikes a balance between effective crosslinking and maintaining free and unreacted lysine residues. While pure water was evaluated, previous work and experience demonstrated that the use of a cosolvent system to modulate solution properties such as viscosity, dielectric constant, surface tension, and volatility proved advantageous in obtaining stable jetting conditions as different materials were incorporated into more complex systems. As a result, a water and ethylene glycol cosolvent was first developed; however, further work evaluated a range of secondary solvents and ratios.

To formulate SPNPs via EHD jetting, a dilute solution of the non-volatile components is first prepared. In brief, albumin and the NHS-PEG-NHS macromer (10 w/w% relative to albumin) are first dissolved in ultrapure water followed by the addition of ethylene glycol to form a 80:20 v/v cosolvent system with a final protein concentration of 7.5 wt%. Pumping the resulting protein solution at a constant flowrate through a conductive capillary and the application of an electric potential results in the deformation of the spherical droplet and formation of a Taylor cone from which a jet is formed in accordance with Rayleigh instability. [162] As previously described, rapid acceleration and solvent evaporation as the jet approaches the grounded collection surface, along with a whipping instability and low solution viscosity, results in the formation of nanoparticles via nearly instantaneous nanoprecipitation (Figure 3.2a).

The resulting protein nanoparticles were characterized to evaluate shape and size distribution, both in the dry (as-jetted) and hydrated (post-collection) states. To examine particles in their dry state immediately following their synthesis, small silicon wafers are placed directly on the grounded collection surface and the deposited particles are imaged via SEM. Image analysis performed with ImageJ, finds the generated particles to be fairly monodisperse and spherical with an average diameter of 141 $\pm$ 36.7 nm (Figure 3.2b). Following the completed crosslinking and purification protocols (Section 4.2.2), SPNP size in their hydrated state were found to be 220 $\pm$ 26.1 nm (PDI = 0.014) according to DLS (Figure 3.2c). When incubated in slightly acidic (pH = 5.0) conditions, SPNPs are observed to undergo further swelling with a diameter measuring 396 $\pm$ 31.2 nm (PDI = 0.006) (Figure 3.3). This property may prove to be advantageous during cellular uptake, endosomal escape, and cargo release pathways.

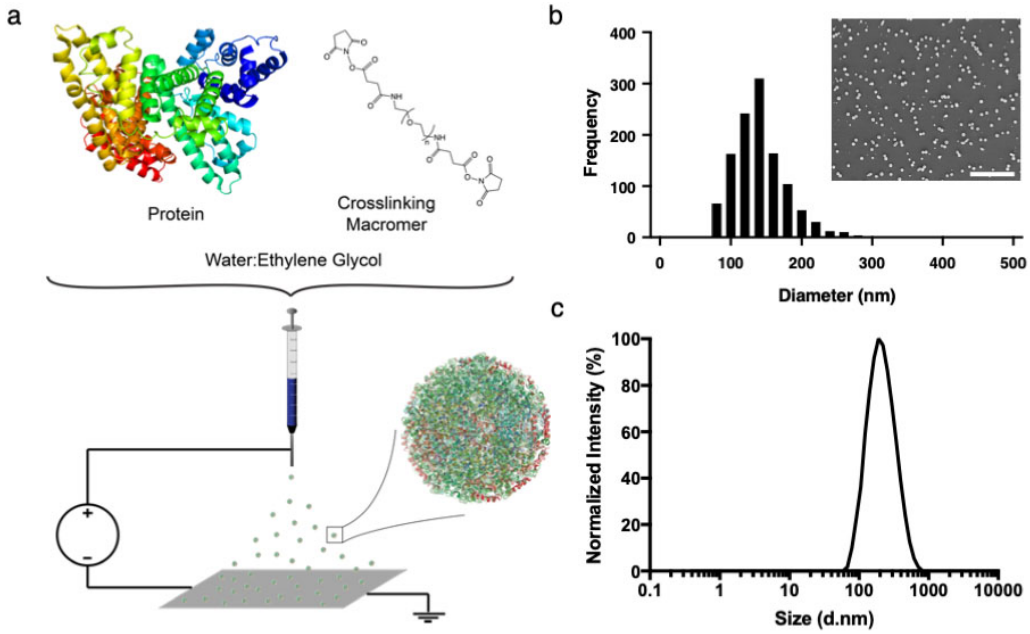

Figure 3.2: **EHD Jetting of Synthetic Protein Nanoparticles.** **a)** General schematic of the jetting process for synthetic protein nanoparticles (SPNPs). **b)** Size distribution of EHD jetted SPNPs. Distribution characterized through image analysis of greater than 500 individual SPNPs using ImageJ software. SPNPs have a average diameter of 141 $\pm$ 36.7 nm (PDI = 0.067) in their dry state. Representative SEM micrograph (inset). Scale bar = 3 µm. **c)** Normalized DLS size distribution of fully crosslinked and collected SPNPs in PBS. Hydrated SPNPs in solution were found to have an average diameter of 220 $\pm$ 26.1 nm (PDI = 0.014).

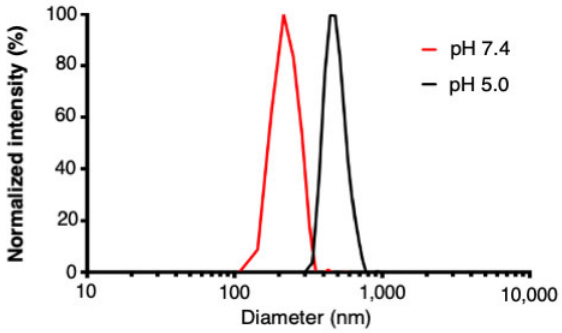

Figure 3.3: **pH Induced Swelling of SPNPs.** Normalized DLS size distribution of fully crosslinked and collected SPNPs in PBS (pH = 7.4, red) and NaOAc-AcOH (pH = 5.0, black). Particles undergo swelling in their hydrated state and further swell at reduced pH. Average diameters: pH 7.4, 220 $\pm$ 26.1 nm (PDI = 0.014) pH 5.0, 396 $\pm$ 31.2 nm (PDI = 0.006).

3.3.2 Beyond Albumin SPNPs - Expanded Protein Library

The use of albumin as base material for the initial development of the SPNP platform and the motivations for its use allowed for rapid optimization of key process parameters. However, we quickly sought to evaluate additional proteins, including those with more relevant and specific biological functions. To assess the feasibility of jetting additional proteins, we first identified several proteins of interest with varied biological functions and physiological properties. In addition to albumin, other transport proteins such as hemoglobin [163, 164] and transferrin [165–167] are of particular interest for their potential carrier or transport properties. Similarly, nanoparticles formed from hormone and enzymatic proteins such as insulin and lysozyme could have potential therapeutic applications parallel to their innate biological functions, glucose regulation [168] and antimicrobial [169, 170] properties, respectively.

Utilizing the previously established methods for general albumin SPNPs as a guide, additional proteins were used to synthesize protein nanoparticles. Incorporating transferrin, hemoglobin, and lysozyme all proved to be fairly straight forward and were readily compatible with the existing solvent system and process parameters. This compatibility was observed despite the widely varied molecular weights and isoelectric points when compared with albumin (Figure 3.4). Adjustments were required for the applied voltage to achieve a stable Taylor cone and spherical particles, but these were both minimal and within the capabilities of the EHD jetting systems. Particle yield, shape, and size distributions in both their dry and hydrated states were consistent with previously synthesized albumin SPNPs.

The general jetting parameters applied to this point produced consistent SPNPs incorporating an array of proteins with minimal adjustments required. This trend held until we evaluated insulin as a bulk material. Whether insulin was used alone, or as part of a protein blend (along with albumin), solubility issues were encountered. Insulin is noted to have poor solubility at neutral pH and standard protocols typically call for the protein to be dissolved in dilute acetic acid or hydrochloric acid solutions. [171] The addition of 10 vol% glacial acetic acid to water worked well for producing a homogeneous solution, though at reduced concentrations (2.5 wt% vs 7.5 wt%). Here, the secondary component of the typical cosolvent, ethylene glycol, was omitted. Importantly, the acidic conditions did not appear to affect crosslinker stability. The jetting process, maintaining all other parameters, yielded spherical particles with similar shape, size distribution, and overall yield when accounting for the decrease in protein concentration in the jetting solution (Figure 3.5). Following the established crosslinking and collection protocols (Section 4.2.2), particle

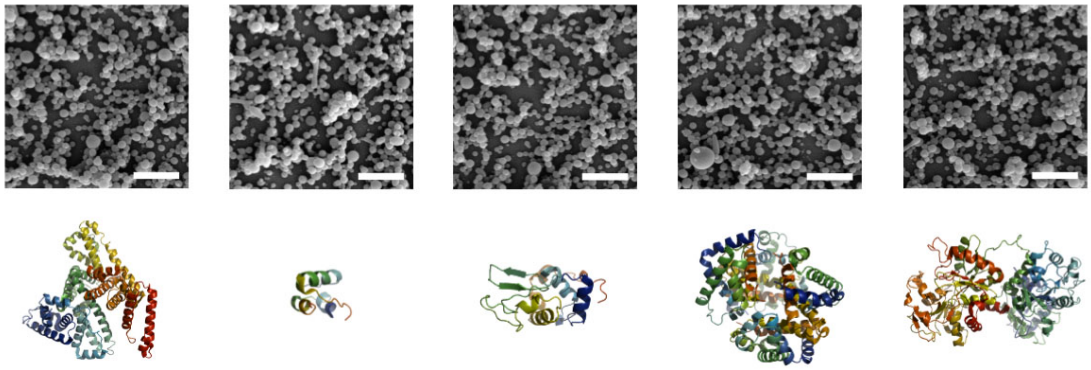

	Albumin	Insulin	Lysosyme	Hemoglobin	Transferrin
Function	Transport	Hormone	Enzyme	Transport	Transport
Mol. Wt.	66.5 kDa	5.8 kDa	14.3 kDa	64 kDa	79.5 kDa
PI	4.9	5.4	11.0	7.1	5.4

Figure 3.4: **Variations in Bulk Proteins for SPNP Synthesis** SEM micrographs of SPNPs fabricated with various bulk proteins. Scale bars = 1 µm. Included table details biological function, molecular weight, and isoelectric point of each protein as a comparison.

size and shape where characterized in their hydrated state. Table 3.1 summarizes the key intensity-based size data for nanoparticles synthesized with the various proteins.

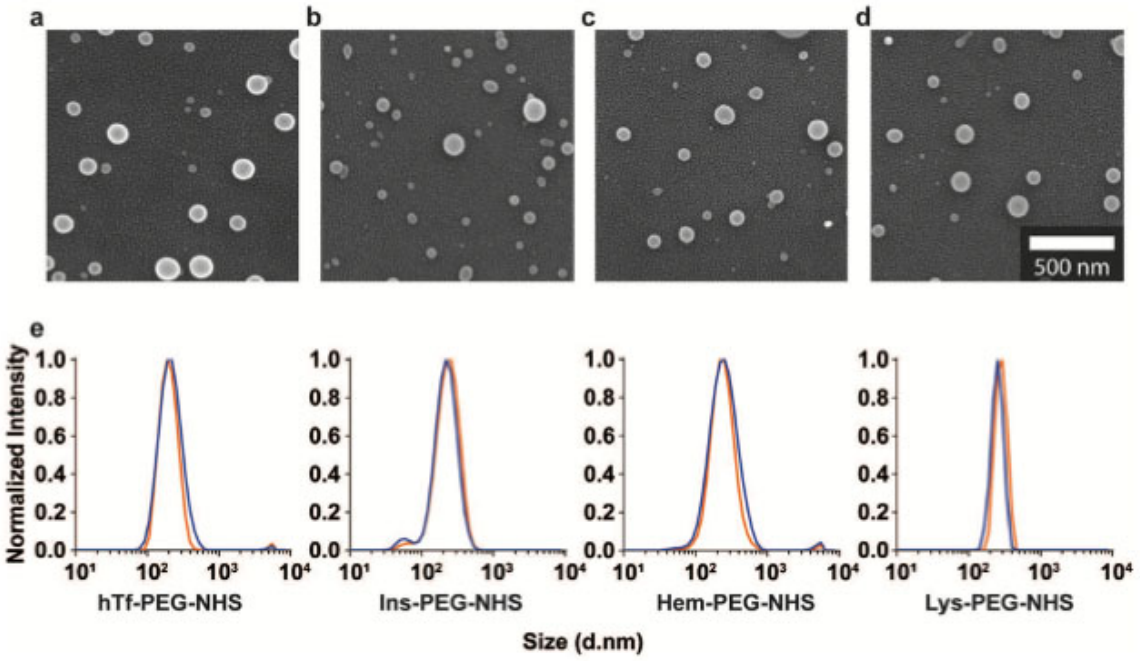

Figure 3.5: **SPNPs Derived from Various Proteins a-d)** SEM micrographs of SPNPs fabricated with, (a) transferrin, (b) insulin, (c) hemoglobin, and (d) lysozyme. Scale bar = 500 nm. **e)** Normalized DLS size distribution of each SPNP type immediately following collection (Day 0, black) and after extended storage in PBS at 4°C (Day 60, red).

Table 3.1: Alternative Protein SPNP Size and Shape Characteristics

Protein	SEM Diameter (nm)	PDI	Circularity	DLS Diameter (nm)	PDI
Albumin	116 ± 44	0.18	0.83 ± 0.09	283 ± 115	0.44
Transferrin	109 ± 36	0.19	0.85 ± 0.08	284 ± 124	0.22
Lysozyme	116 ± 44	0.18	0.83 ± 0.09	283 ± 115	0.44
Hemoglobin	64 ± 12	0.15	0.85 ± 0.08	382 ± 106	0.38
Insulin	49 ± 10	0.17	0.77 ± 0.16	220 ± 082	0.47

3.3.3 Crosslinking - Variations and Expanded Macromers

3.3.3.1 Controlled Particle Swelling

The use of the bifunctional NHS-PEG to crosslink the particles had thus far proven an effective means to produce stable SPNPs from a range of proteins. There was an obvious change in the particle size as they transitioned from their dry to hydrated state with noticeable swelling. This behavior, while varied from protein to protein, was observed to occur across all protein variations. This swelling effect, as described earlier, was even more pronounced at acidic pH. Given the particle architecture and its propensity to swell in solution, we sought to impart an additional level of control over this behavior. Maintaining the same crosslinking approach there were two readily accessible variables to explore, i) the relative mass ratios of protein to crosslinker, and ii) the molecular weight (length) of the synthetic crosslinking component.

In an attempt to modulate the extent at which SPNPs swell in solution, variations in the relative ratios of crosslinking macromer to protein was first studied. In essence, through the covalent linking of individual proteins within the resulting nanoparticle structures, a confined hydrogel is formed. When introduced to an aqueous environment (i.e. buffered solution, saline, or serum) particles are observed to significantly swell as water molecules infiltrate the particle volume. As shown previously (Section 3.3.1), this effect is augmented further as the pH of the solution is changed; an inverse correlation between pH values and particle size exists. The pore sizes within the particle volume and the observed swelling behavior can be related to the extent at which the particles are crosslinked. Therefore, it stood to reason that by varying the amount of crosslinker, and thereby the extent at which the proteins are tethered together, swelling behavior could be controlled. To validate this hypothesis, four distinct particle formulations were prepared consisting of 10, 20, 30, and 40 wt% NHS-PEG relative to the protein (Figure 3.6a-d). Particles were characterized

though SEM imaging and subsequent image analysis. [106] In their dry state, no significant difference in particle shape, size, or morphology was observed (Figure 3.6e). However, in solution, the results showed a clear relationship between the relative NHS-PEG macromer mass and observed particle size determined via DLS (Figure 3.6f). As more tether points are established, the divergence of individual proteins relative to their neighbors and the relative swelling of the particle volume decreases.

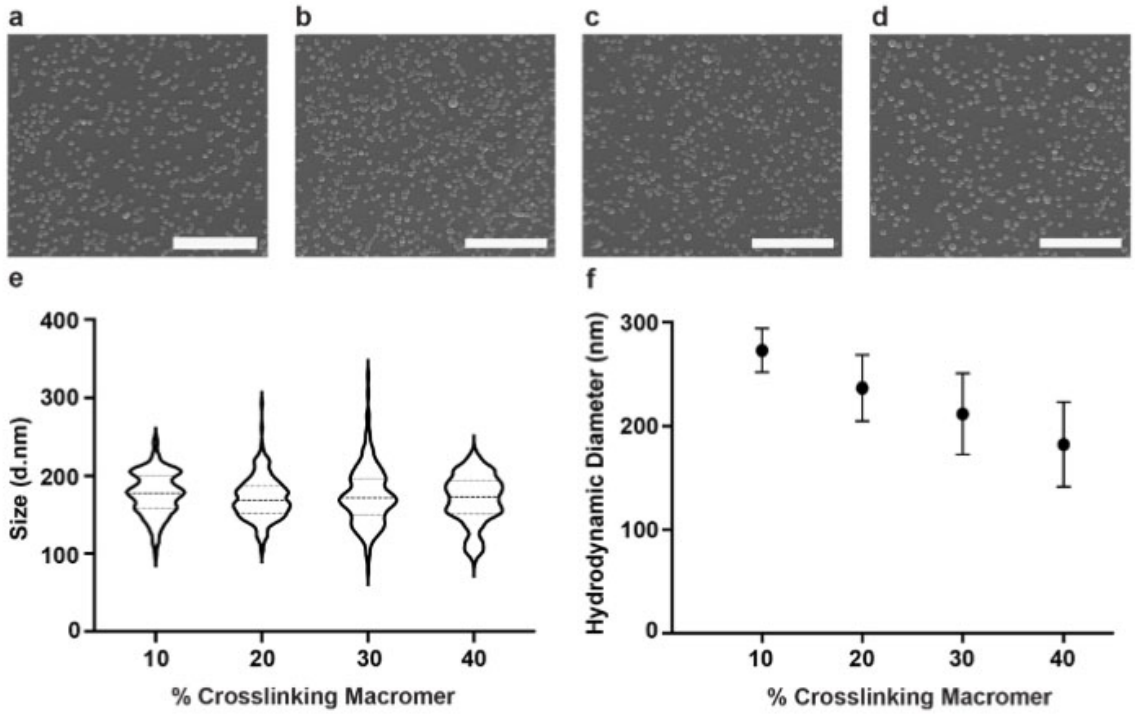

Figure 3.6: **Crosslinker Mass Ratio Effects on Swelling.** Increasing amounts of 2 kDa, NHS-PEG-NHS crosslinker relative to bulk protein was incorporated into the jetting solution. **a-d)** SEM images of SPNPs synthesized with various amounts (a) 10, (b) 20, (c) 30, and (d) 40 w/w% of crosslinking macromer relative to albumin. Scale bars = 4 μm. **e)** Diameter distributions for the SEM micrographs of SPNPs presenting as a count distribution violin graph. Individual SPNPs (n = 200) measured using ImageJ. No significant difference observed between the various formulations (ANOVA, multiple comparisons). **f)** Hydrodynamic diameters of the resulting SPNPs in PBS measured by DLS. Results displayed as median ± SD.

An alternative to increasing the extent of crosslinking includes the use of PEGs with varied molecular weights. Owing to a diverse set of commercially available PEG macromers, complete with identical terminal NHS reactive functional groups, crosslinking can be completed with macromers ranging from 0.4 to 35 kDa. Here, the premise remains the same as previously described; as water molecules access the particle volume, swelling occurs and that swelling is bounded by the how far adjacent proteins can move from one another. The

approach has the basis that while maintaining the extent of crosslinking, simply altering the length of the molecules will directly effect the degree to which the individual proteins can migrate relative to their neighbors. In addition to looking at macromer:protein ratio, work done by N. Habibi and S. Christau also evaluated the effect macromer length had on EHD ovalbumin SPNPs. [105] Their findings showed that variations in PEG crosslinker length resulted in distinct changes, not just particle and mesh size, but also additional physical properties such as the elastic modulus. The ability to control the elasticity directly correlated to how these particles interacted with cells *in vitro* and ultimately translated to increased efficacy *in vivo*. [105] From a drug delivery perspective, particularly for the delivery of small molecule drugs looking to diffuse from the particle volume, the control of particle swelling and resulting mesh size can potentially be leveraged to impart precise control over the release kinetics.

3.3.3.2 Alternative Crosslinking Macromers

Across a range of proteins with varied molecular weights, amino acid sequences, isoelectric points, and solubilities, the method of crosslinking the proteins using the bifunctional NHS-PEG proved to yield water-stable SPNPs (Figure 3.7a). However, drawbacks to its use were quickly identified and included, i) there was no additional functionality (e.g. stimuli induced responsiveness) imparted to the particles through its use, ii) the particles required an extended time at elevated temperatures to complete the crosslinking, and iii) a significant portion of the particle mass was no longer protein, but instead PEG. To address these concerns and build a more robust and diverse platform, alternative options for covalently linking the proteins were assessed.

Considering the single functionality of the NHS-PEG in crosslinking the proteins, we asked whether we could take a similar approach to stabilizing the particles but simultaneously impart a behavior responsive to physiological cues. For the application of drug delivery, particularly as it applies to the treatment of cancer, varied biological conditions will be encountered. One such physiological property is the reducing environment present within cells. In an attempt to capitalize on this phenomenon, an alternative PEG crosslinker containing a central disulfide bond was chosen. Equipped with the same NHS terminal functional groups, the crosslinking of proteins through the lysine side chains remains consistent with the original approach; however, a central and reducible bond would allow the linker to symmetrically disassociate as the disulfide bond was reduced to free thiols. Rapid and controlled degradation of the particles in response to external stimuli provides the potential

to tune the release of sequestered drugs or biologics. Substituting the NHS-PEG-(S-S)-PEG-NHS (or NHS-PEG-S) crosslinker was straightforward due to the similar chemical structure, functional reactive groups, and solubility. Added to the solution in the same 10 wt% relative to protein, identical jetting, incubation, and post-production processing steps were followed. The resulting particles were shown to have similar shape, size, and morphology to those prepared using the NHS-PEG macromer (Figure 3.7b). Furthermore, because the two macromers are very similar in structure, optimization to control the extent to which the particles respond and degrade could potentially be achieved by using a blended molar ratio of the two substituents.

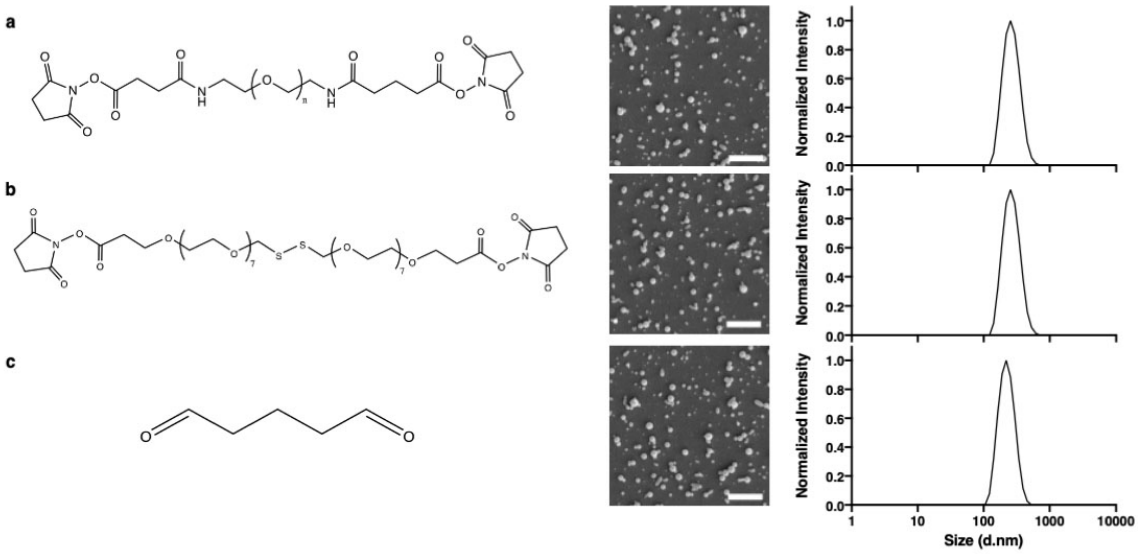

Figure 3.7: **Changes in crosslinking macromers yield similar SPNP size distributions.** Albumin SPNPs crosslinked through the use of three distinct approaches, **a)** NHS-PEG-NHS (NHS-PEG), **b)** NHS-PEG-S-S-PEG-NHS (NHS-PEG-S), **c)** glutaraldehyde chemical vapor crosslinking. In each case, the resulting particles are similar in shape and size in their dry state following image analysis of SEM images. Once collected, SPNPs stabilized through each of the crosslinking approaches are found to have no significant difference in particle size when comparing their distributions. Scale bars = 1 μm.

In order to address the extended crosslinking time and inclusion of PEG in the particles, a third approach using a vapor-based crosslinking was assessed. From a processing and scalability standpoint, eliminating the need to fabricate well in advance of the proposed final use (*in vitro*, *in vivo* animal, or clinical studies) through the development of a same-day crosslinking approach would prove extremely valuable. From a potential immune response perspective, recent studies have shown that developed antibodies against PEG exist in a portion of the population. [88, 172] This has the potential to be a cause of severe side effects and could limit the fraction of people for whom a developed therapeutic would be

a viable treatment regimen. To simultaneously address each of these concerns, the use of glutaraldehyde in its vapor phase was proposed. Glutaraldehyde has been used in the past for the crosslinking and stabilization of protein particles synthesized via coacervation. [150,173,174] Simply including the glutaraldehyde within the jetting solution would cause premature crosslinking of the protein solution inhibiting the EHD fabrication process. Here instead, the crosslinker component is omitted entirely during solution preparation; we first form the particles via EHD jetting and using a second step, incubate the particles with a 20 vol% aqueous solution of glutaraldehyde within a sealed container for thirty minutes. The resulting particles following this two-step synthetic pathway are shown to have similar size, shape, surface charge and morphology compared to previous methods (Figure 3.7c). Importantly, the obtained particles are stable in water, ready for collection and purification steps, and can potentially be moved towards future studies the same day.

3.3.4 Macromer-free SPNP Stabilization

While early efforts to develop the EHD jetting platform for the synthesis of protein nanoparticles all made use of a crosslinking agent in some form, means to eliminate the need for these additional components were also explored. Protein structure and stability are influenced by amino acid sequence. The folding, secondary and tertiary structures, and denaturing of proteins are influenced by the interactions of individual residues. One such interaction that significantly influences protein structure, stability, and function are the presence of disulfide bonds, present between between two cysteine residues [175]. As a consequence of structure, the two residues involved in a single disulfide bond can be quite distant from a primary structure (or sequence) perspective. These bonds are reversible and dependent upon the surrounding environment factors, including solution pH. Ultimately, these bonds act to stabilize and facilitate proper protein folding (and function) through entropic effects. [175] While not all proteins contain disulfide bonds, in some their presence is extensive; albumin for instance, contains 17, involving 34 of the 35 cysteine residues present within its sequence. Taking advantage of this reversible nature, and the relative abundance in albumin, we sought to leverage this in the SPNP synthesis platform.

3.3.4.1 XLF-SPNPs Synthesis

The approach of disrupting and rapid reformation of disulfide bonds in proteins, particularly associated with electro-driven material synthesis, had previously been explored. Dvir

and co-workers had used electrospinning to produce albumin fibers for for the engineering of functional cardiac tissues. [176] Here, they utilized an organic/aqueous solvent blend to disrupt native disulfide bonds. Owing to our previous work and extensive understanding on how to readily transition between the fiber and particle regimes in EHD jetting, modifications were made to yield protein nanoparticles free of macromer. In brief, albumin was first dissolved in ultrapure water followed by the addition of trifloroethanool (TFE) (90:10, TFE:water). The final protein concentration was 2.5 wt%. Following the addition of TFE, the solution was observed to be clear, though after allowing the system to rest, it become increasingly opaque suggesting that the protein had begun to denature, unfold, and slightly aggregate due to the exposure of otherwise buried hydrophobic residues. Following a period of time of no less than twenty minutes, a small addition of β-mercaptoethanol (β-ME) was added at a 10x molar excess relative to the cysteine residues present in the protein solution. This typically only amounted to 1-10 µL depending on the volume being prepared. Following solution preparation, EHD jetting proceeded as previously described.

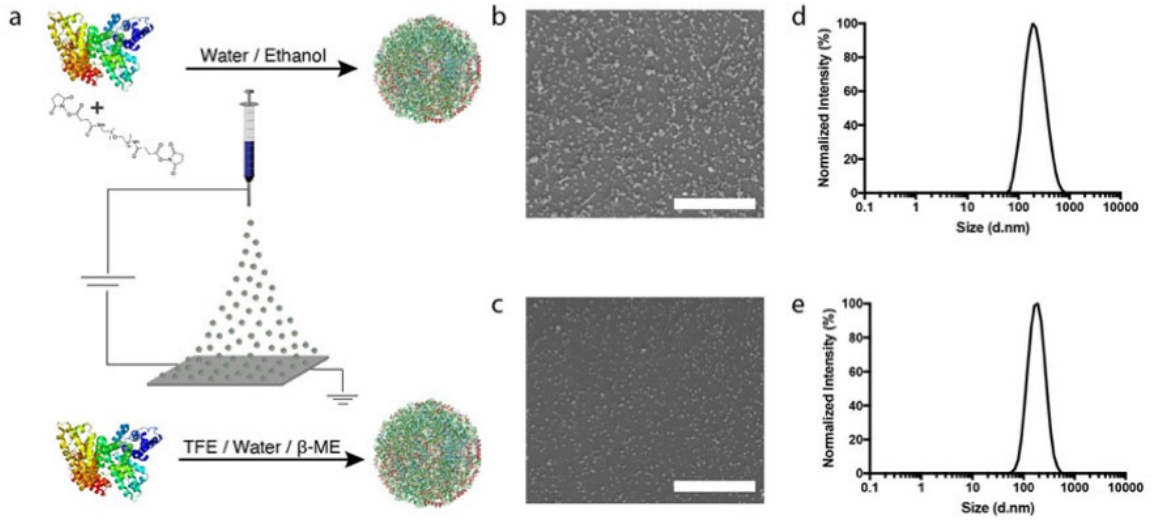

Figure 3.8: **NHS-PEG macromer versus macromer-free, disulfide crosslinked SPNPs. a)** Utilzing an identical jetting set-up, variations in solution parameters yield two distinct methods of creating water-stable SPNPs. (Top) NHS-PEG macromer crosslinked particles in a water:ethanol (80:20) co-solvent system. (Bottom) Macromer-free SPNPs stablized through intermolecular disulfide bonds in a TFE:H_2O:β-ME. **b-c)** SEM images of (b) NHS-PEG and (c) disulfide crosslinked SPNPs. **d-e)** DLS intensity size distributions of (d) NHS-PEG and (e) disulfide crosslinked SPNPs in PBS. Scale bars = 1 µm.

Following previously described SEM analysis, the resulting macromer- or crosslinker-free particles (XLF-SPNPs) were found to be monodisperse and with a similar size distribution compared to NHS-PEG crosslinked particles (Figure 3.8). As a first pass, the particles had

a mean diameter of 128 $\pm$ 39.6 nm in their dry state when SEM images were analyzed with ImageJ. Utilizing an modified approach to a previously developed protocol to evaluate our crosslinking, individual samples were incubated under vacuum to remove any residual solvent that may be present on the collection surface. Each of the following days, a droplet of water was added and then removed from the silicon surface (Figure 3.9a). SEM imaging of the regions both inside and outside of the droplet perimeter was completed. Interestingly, it was observed that in the absence of crosslinking macromer, not only were particles completely crosslinked and stable, this stability was observed as early as the first timepoint with just hours of time passing between the jetting and imaging (Figure 3.9b).

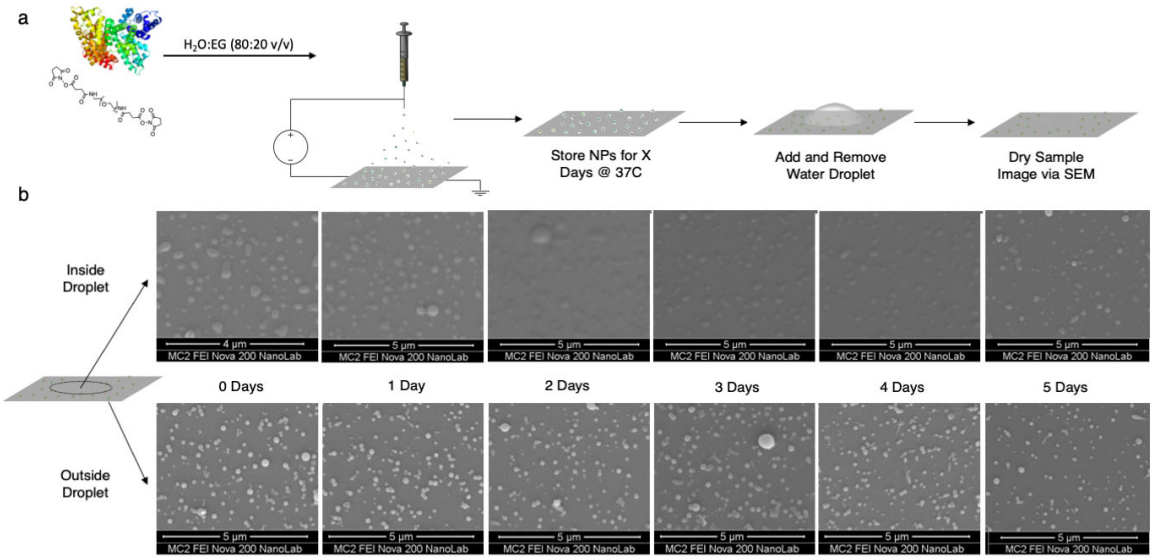

Figure 3.9: **Macromer-free SPNP stability test. a)** Experimental design to evaluate SPNP water stability and required crosslinking time. SPNPs collected on silicon wafers incubated at 37°C in accordance with previously developed methods for macromer stabilized SPNPs. At time intervals of 24 h, a single 20 µL droplet is deposited onto the center of the wafer, allowed to sit for three minutes, before the droplet is removed. **b)** SEM imaging of the resulting wafers at the various time points both inside (top) and outside (bottom) of the residual droplet perimeter. Scale bars 5 µm.

While the intention of the move to the TFE:H_2O:β-ME system had been to eliminate the use of PEG from the final particle composition, an additional method of rapidly producing water-stable SPNPs resulted. Encouraged by this rapid stabilization of the particles, with water insoluble particles observed just hours after jetting, an effort to determine at what timescale the crosslinking occurs was undertaken. It should be noted, that aside from the extended incubation time inherent in the NHS-PEG system, additional time and resources are consumed through the collection process as particles are mechanically removed with the aid of aqueous solution from the collection surface. In an attempt to answer the question

of crosslinking timescale while also addressing the laborious task of particle collection, the XLF-SPNPs were jet directly into a liquid-filled, grounded collection pan. This was first attempted with pure water; however, it was noted that a protein film formed on the surface. As a result, ethanol was added (80:20 v/v, water:ethanol) in order to reduce the surface tension allowing surface deposited particles to more easily settle. Following the experiment, the solution was sonicated and centrifuged according to our standard protocol for SPNP purification (Section 4.2.2). It was observed that despite being jet into an aqueous solution, stable particles were achieved. Measuring these particles by DLS, they were found to have an average size of 202.4 $\pm$ 93.6 nm (PDI = 0.214). This size distribution was noted to be similar to both NHS-PEG crosslinked and XLF-SPNPs jet in the traditional manner. In each of the previously described methods, SPNPs were found to have similar size distributions in their hydrated state. Furthermore, when evaluating particle stability under normal storage conditions (dark and 4°C) for a period of 60 days, no significant change was observed, suggesting the XLF-SPNPs (hTf-S) particles remain intact, stable, and are readily dispersed without the development of particle aggregates, consistent with all previously developed crosslinking approaches (Figure 3.10).

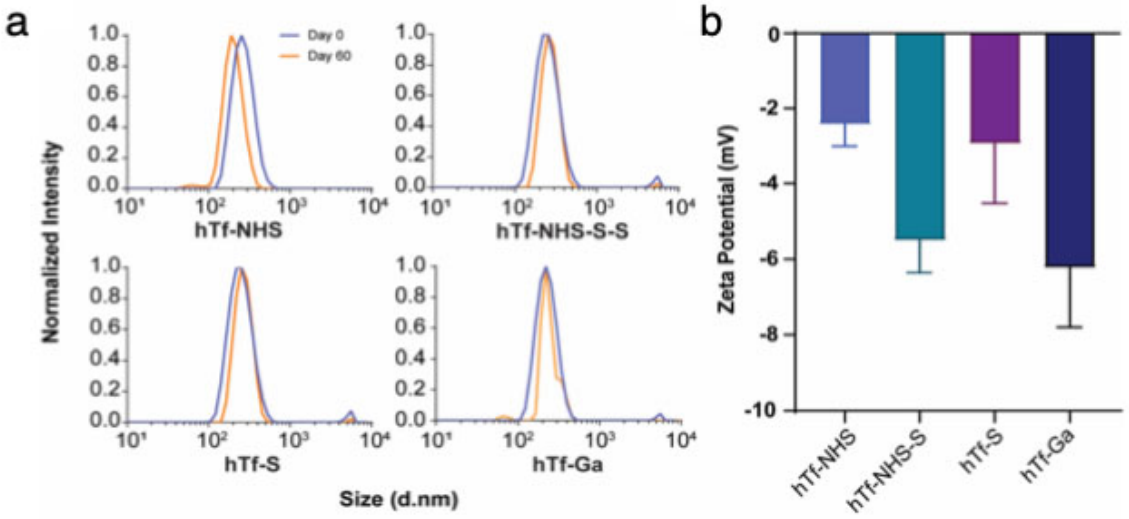

Figure 3.10: **Crosslinking variations and effects on long-term stability and ζ-potential. a)** Normalized DLS traces of transferrin SPNPs. Stabilized through the use of NHS-PEG, NHS-PEG-S, glutaraldehyde chemical vapor crosslinking, and macromer-free disulfide approaches, no significant difference is observed in particle size distribution. Particles are observed to be stable and maintain similar size distributions following 60 days (red traces) at 4°C when compared to immediately following collection (black traces). **b)** ζ-potential measurements of SPNPs stabilized through each of the crosslinking approaches show slightly negative values with no significant differences. Data is presented as mean values $\pm$ s.d. one-way ANOVA and Tukeys multiple comparison tests, ns = $p > 0.05$.

The presence of water-stable particles following their jetting into a volume of aqueous solution suggests that the crosslinking of the particles, through the reformation of disulfide bonds (both intra- and intermolecular) due to the rapid removal of solvent through the EHD jetting process was nearly instantaneous. Consequently, the move to a TFE:H_2O:β-ME system accomplished, i) the elimination of PEG (or other crosslinking agents) from the final particle architecture, ii) an alternative means to rapidly crosslink particles not requiring a secondary processing step, and iii) a means to bypass the mechanical removal of particles from a solid collection surface, further expediting the jetting to application workflow. Additionally, because we have moved to an predominately organic phase with a distinct difference in solvent polarity, this may open up the ability to incorporate more hydrophobic compounds (e.g. taxols or other non-polar chemotherapeutics) into the final particle architecture. An obvious drawback and limitation to this approach is that the protein is completely denatured during the solution preparation steps. In essence, the resulting particles are composed of a biologically-derived, bulk polymer made up of amino acid side chains with no remaining protein function. This can be especially problematic in the case of jetting functional proteins or enzymes and so limitations exist in where this approach can be applied.

3.3.4.2 Thiol-rich XLF-SPNPs

Encouraged by the recently developed streamlined approach to produce water-stable SPNPs in the absence of crosslinking macromer, yet confronted with the limitations this system imposed, further efforts focused on overcoming the inherent shortcomings of XLF-SPNPs. At its core, the production of SPNPs using the TFE:H_2O:β-ME cosolvent approach depended upon the denaturing and disruption of native, reversible bonds, followed by the rapid reformation of disulfide bridges through free sulfhydryl groups between adjacent protein molecules. Therefore, in order to maintain protein structure and function, the challenge became developing a means by which free thiol groups could be made available while not disrupting the native disulfide bonds responsible for protein structure and stability.

The development of the system consisted of two relatively straightforward tasks. The first was to generate or identify a protein with a significant amount of cysteines not participating in disulfide bonds. The second was to test whether such a protein, when processed through the EHD jetting platform would yield similar results to those observed in the XLF-SPNP system. Stemming from the developed understanding of protein synthesis and the ability to modularly design proteins in a step-wise fashion, the ultimate response to the first chal-

lenge might be to synthetically produce the proteins. Here, additional cysteine residues could be added with precision at specific locations throughout the amino acid sequence. Alternatively, as a proof of concept, an approach of chemically modifying albumin was first pursued.

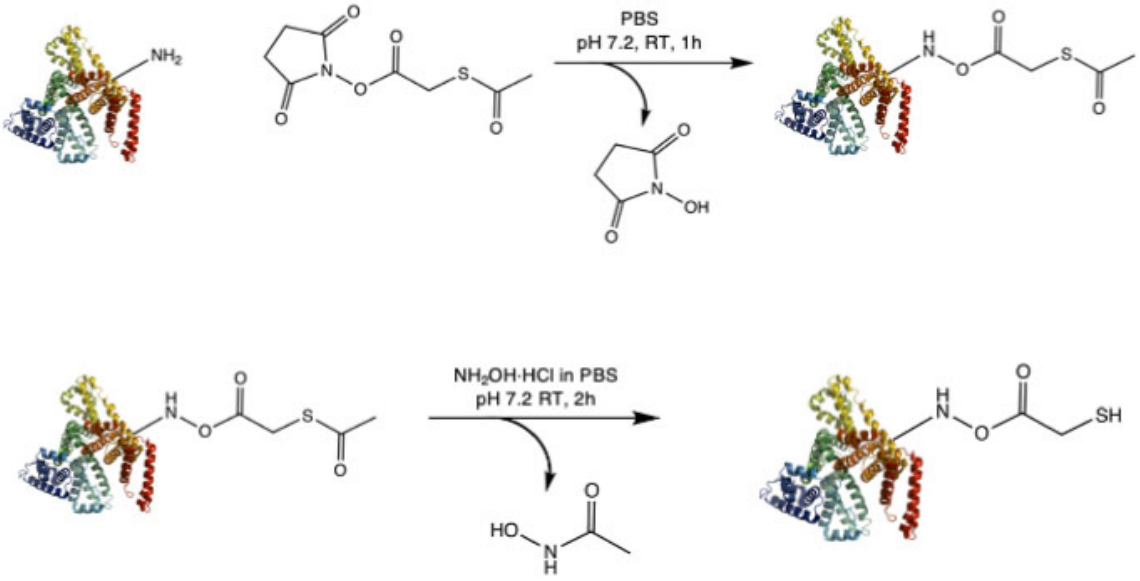

Figure 3.11: **SATA conjugation to albumin.** Reaction scheme for the conjugation of N-Succinimidyl-S-acetylthioacetate (SATA) to human serum albumin and subsequent deprotection to yield a thiol-rich version of the protein.

Protein modifications through chemical reactions with functional side groups is well established and typically is conducted under mild reaction conditions with simple purification methods. [177] Here, a simple two-step process is applied to conjugate a small molecule, N-Succinimidyl-S-acetylthioacetate (SATA) to the albumin via free amine groups present in lysine residues (Figure 3.11). Conducted in PBS at RT, consisting of a paired reaction and deprotection steps each followed by purification through either dialysis or column separation, the result is a protein decorated with free thiol groups. The extent to which the protein is modified can be controlled through stoichiometric ratios of reactants. With approximately 50 lysines available for conjugation, we aimed to react approximately 20% of those through the SATA reaction. Following the last pass through the column, fractions containing the resulting thiol-rich protein were combined, frozen, and lyophilized to yield an off-white powder. Characterization of the resulting modified protein was performed through a combination of the Ellman's assay, designed to quantify free sulfhydryl groups, and the Protein 660 assay to quantify protein concentration. It was determined that the reaction yielded the addition of ten free thiol groups per protein molecule, in agreement

with our targeted modification of 20% of available lysine residues.

Following the addition of free thiols to the native albumin, we sought to determine whether jetting of the protein would yield water stable SPNPs. A protein jetting solution was prepared in a cosolvent mixture (80:20 v/v) of ultrapure water and ethylene glycol, without the addition of a crosslinking macromer. The appearance of the solution was a transparent pale straw color and the viscosity was similar to that of other protein solutions of similar concentrations. Applying the same EHD jetting approach, a fraction of the solution was jet to a grounded collection surface. The remainder of the solution was kept at RT to observe changes in the optical appearance of the solution that might suggest crosslinking of the proteins was occurring in the syringe prior to jetting; no change in the solution color or viscosity was observed over a period of 24 h. Analysis of the particles in their dry state showed the formation of spherical nanoparticles of bimodal distribution with an average diameter of 103.6 $\pm$ 36.2 nm (PDI = 0.122) (Figure 3.12). Larger observed particles in their dry state were minimal and could certainly be separated from the smaller population through previously developed centrifugation purification steps. Collection of the particles from the surface with PBS after being stored O/N under vacuum and subsequent analysis of the particle size distribution and zeta potential showed that these particles, TR-XLF-SPNPs, were water-stable, had a average size of 162.1 $\pm$ 42.2 (PDI = 0.067), and a zeta potential of -7.2 mV. These values are in line with other SPNPs generated through the use of various crosslinking approaches. Notably, the modification of lysines to chemically conjugate the SATA molecule did not significantly alter the zeta potential of the resulting particles; typically, SPNP zeta potential values are in the slightly negative range of -3.0 to -9.0 mV. As a whole, the strategy of artificially imparting additional thiol groups capable of forming intermolecular disulfide bonds through the jetting process offers a promising means to create SPNPs without the addition of a crosslinking macromer and significantly reduces the turnaround time from jetting to application. Moreover, in contrast to the TFE:H_2O:β-ME approach used for XLF-SPNPs, the process does not require the need to denature the protein suggesting that this approach could also be applied to generate macromer-free SPNPs consisting of functional proteins or enzymes, retaining their biological activity.

3.3.5 Jetting of Chemically Modified Proteins

Owing to the diverse functional groups present in proteins as a result of the 20 amino acid building blocks and their distinct side chains, residue specific, chemically controlled modifications are possible. An example of such a modification was recently described in

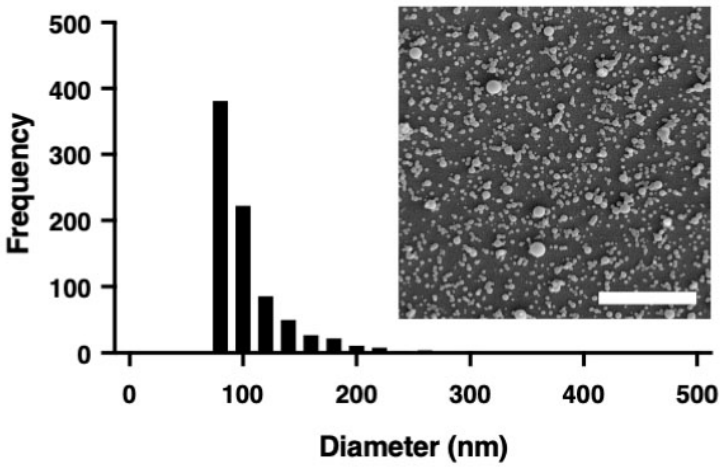

Figure 3.12: **Thiol-rich SPNP particle size distribution.** Albumin SPNPs synthesized using the thiol-rich albumin in the absence of crosslinking macromer. Size distribution following SEM image analysis. Scale bar = 2 μm.

the formation of TR-XLF-SPNPs leading to a rapid SPNP synthesis route in the absence of crosslinking macromer. This approach of pre-modifying proteins through the conjugation of small molecules can be extended for additional purposes. For example, one could theoretically conjugate small molecules with known and desireable biological effects (e.g. targeting, antioxidant activity, or pathway inhibition) similar to the approach utilized in antibody drug conjugates. In doing so, the desired biological properties and activities may be imparted to the protein and ultimately the final particle. Alternatively, chemical conjugation to the bulk protein could be used as a means prevent the rapid burst release of small molecules often observed from nanoscale particle systems.

Here, we sought to conjugate the polyphenolic acid, 3,4,5-trihydroxybenzoic acid (Gallic Acid, GA) to albumin. Derived from various plants, serving as a natural metabolite, gallic acid belongs to a family of polyphenolic acids responsible in part for the antioxidant and anti-inflammatory effects of fruits, wine, and teas. [178] Abundant in green tea, gallic acid and related compounds have been implicated as having anticarcinogenic and antimicrobial effects with possible uses in treating depression, cancer, and microbial infections. [179,180] Due to its ability to chelate metal ions, gallic acid has even found applications in the development of lapping solutions for the polishing of hard drives during their final production steps. [181] Taken together, the vast application space of polyphenols, particular for treating diseases, made it an attractive molecule to explore as a covalently linked therapeutic.

Previous work by Iemma and coworkers had developed a synthetic route to create a gallic acid-gelatin conjugate. [151, 152] Modifying the reaction, albumin protein was dissolved

and utilizing H_2O_2 and ascorbic acid to catalyze the reaction of gallic acid to cysteine, lysine, serine and threonine residues. A general reaction scheme is found in Figure 3.13. Following dialysis to remove unreacted starting materials and lyophilization of the albumin-gallic acid conjugate (HSA-GA), a white flaky powder was obtained. In order to characterize the resulting protein conjugate samples, gallic acid, unmodified protein, and HSA-GA were submitted for independent analysis. An aqueous Malvern GPC system was utilized with an array of detectors to determine molecular weights of each species. It was determined that the reaction yielded approximately 33 gallic acid residues per albumin protein with a significant shift in molecular weight compared to the native protein control (Table 3.2). Moreover, it should be noted that in addition to the shift in molecular weight indicating successful conjugation of the gallic acid, a dramatic shift in the balance of monomer and dimer population was observed. This shift would suggest an induced change in the solubility and solution stability of HSA-GA relative to HSA.

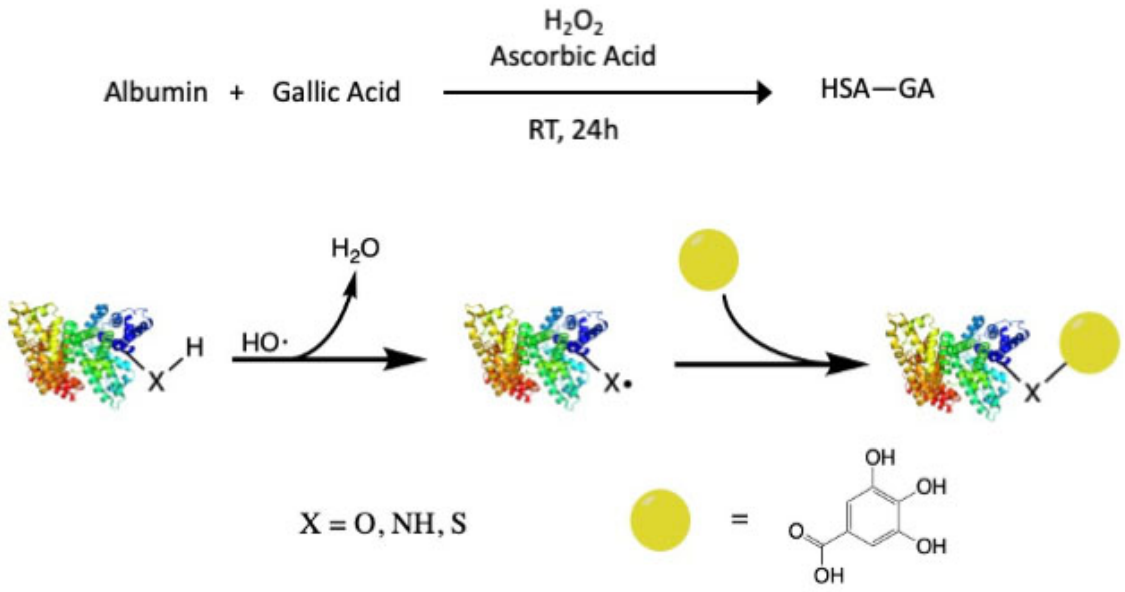

Figure 3.13: **Gallic acid (GA) modification of albumin.** General reaction scheme for the H_2O_2 and ascorbic acid catalyzed reaction of gallic acid to human serum albumin to yield the HSA-GA conjugate.

The change in solubility was readily apparent and confirmed when jetting solutions were prepared. Dissolving the HSA-GA in water was increasingly difficult even at lower concentrations of 2.5 wt%, compared to proteins that had been jet in the past. In order to more readily dissolve the protein at these concentrations, a small addition of triethylamine (TEA) was used (approximately 2 µL per mL of jetting solution). Following this addi-

Table 3.2: Alumbin-Gallic Acid Conjugate GPC Analysis

	Albumin	Gallic Acid	HSA-GA
Mw (g/mol)	65,720	170.12	71,340
Mw/Mn	1.003	—	1.005
Monomer Fraction	95.51	—	50.28
Dimer Fraction	3.897	—	22.26
# GA Conjugated	—	—	**33**

tion, the solution appeared transparent and remained stable over a period of 24 h with no further indication of aggregation or precipitation of the dissolved protein. Jetting the solution was then carried out following parameters identical to those previously employed in SPNP synthesis. Upon imaging the particles in their dry state with SEM, it was observed that the particles, while monodisperse in size, were not at all spherical (Figure 3.14b). In fact, the particles had nearly a 3:1 aspect ratio when measuring their major and minor axes (Figure 3.14c). Curious whether this was conserved once the particles had been collected and hydrated in buffer, particle solutions were dropped onto copper mesh grids and imaged with Tranmission Electron Microscopy (TEM) (Figure 3.14d). Evaluating a broad population of particles following the complete collection process (hydration, sonication, and centrifugation), indicated that the non-spherical particles retained their rod-like shape in their hydrated state.

Curious whether this effect of premodifying the proteins with small molecules would universally alter the final particle architecture, or if the reaction conditions of the HSA-GA conjugation were responsible for the observed results, two additional experiments were performed. First, the H_2O_2 and ascorbic acid catalyzed reaction was repeated wherein the gallic acid was omitted. Following dialysis and lyophilization, particles were synthesized via EHD jetting using an identical carrier solvent system and imaged. In this case, spherical particles were obtained with similar size and shape to our standard albumin SPNPs suggesting it was the presence of the gallic acid and not the reaction/jetting conditions that caused the irregular shape to form. Second, in order to test whether this phenomenon was universally observed when proteins were significantly modified prior to jetting, two additional compounds of interest were evaluated in a similar manner. Dopamine, a polyphenol with an approximately equal molecular weight compared to gallic acid, and curcumin, a hydrophobic natural plant derivative with antioxidant activity, were each conjugated to albumin. Following similar purification and lyophilization processes, each protein was jet to create HSA-dopamine and HSA-curcumin SPNPs, respectively (Figure 3.15). It should be noted that while the HSA-dopamine solubility seemed unchanged compared to native

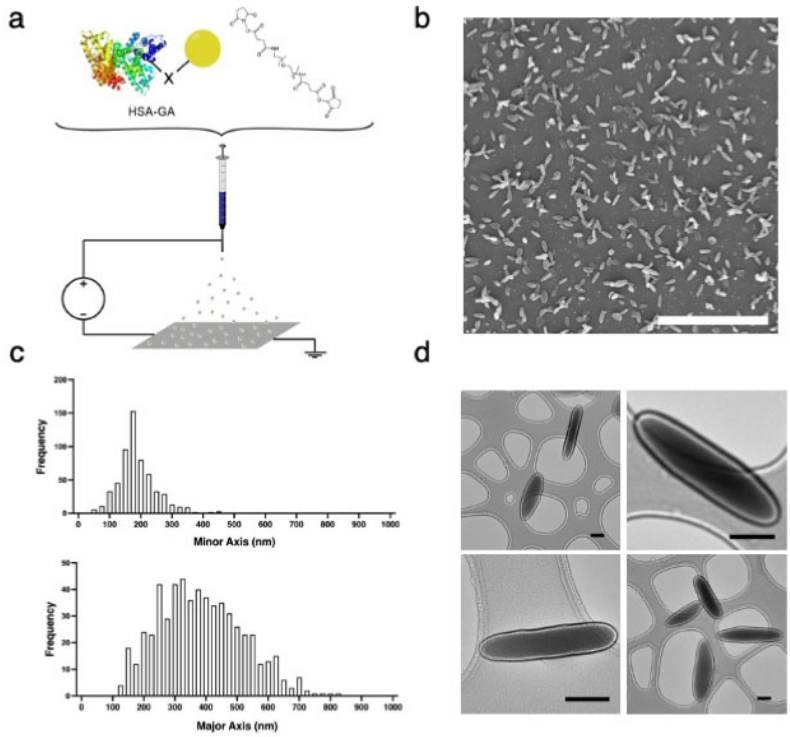

Figure 3.14: **Non-spherical SPNPs.** **a)** Jetting schematic of NHS-PEG macromer crosslinked HSA-GA. **b)** SEM image of resulting HSA-GA SPNPs in their dry state showing the spontaneously created non-spherical protein particles. Scale bar = 3 µm. **c)** SEM image analysis of the resulting particles and distributions of both the long and short axes. **d)** Following the completed collection process, HSA-GA particles were deposited onto copper mesh grids and imaged via TEM to confirm retention of non-spherical architecture. Scale bars = 100 nm.

albumin, the HSA-curcumin was significancy less soluble, similar to that of the HSA-GA. In each case, spherical particles were obtained (Figure 3.15). Together, these results suggest it is not the reaction conditions of the HSA-GA synthesis but rather the presence of the specific compound that resulted in the irregularly shaped particles.

The spontaneous formation of rod-like, protein nanoparticles had not been achieved to date. Previous work developing non-spherical polymeric (PMMA, polystyrene, and PLGA) particles had been completed both in our lab and those of groups like Michael Solomon [182] and Samir Mitragotri. [183] This process involves a simple method of embedding the particles into a water soluble polymer film, heating and stretching of the films followed by the dissolution of the sacrificial films to yield non-spherical polymer particles of similar size and shape to those achieved here. Particle shape has been shown to alter biodistribution and accumulation within organs. This is postulated, in part, as being a result of the non-spherical particles ability to partition to the peripheral regions of the hemodynamic

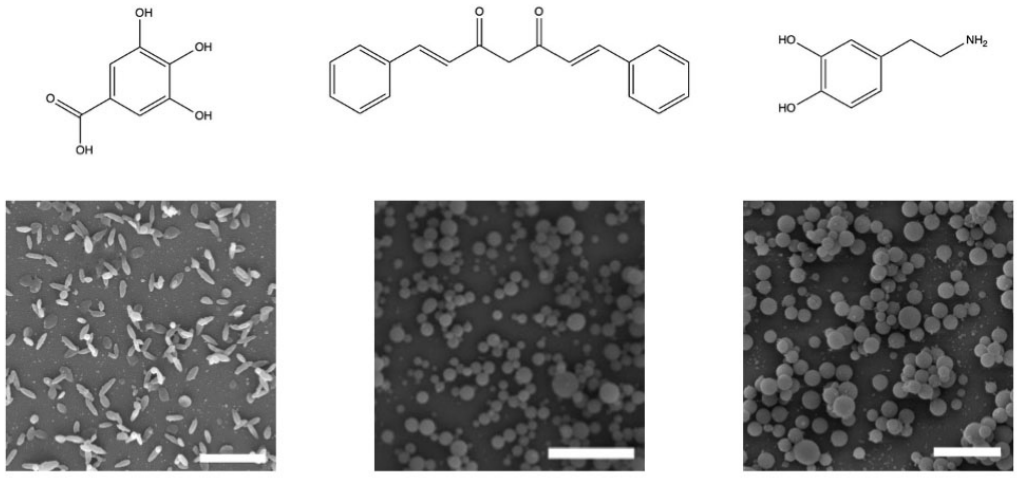

Figure 3.15: **Small molecule-albumin conjugate SPNPs.** Small molecules and SEM images of the resulting SPNPs following EHD jetting of the protein conjugates. Scale bars, HSA-GA (3 µm, left), HSA-curcumin (2 µm, middle), and HSA-dopamine (2 µm, right).

flow and interact with the endothelium more readily than their spherical counterparts. Intrigued by the observation of non-spherical protein particles and the potential role shape can play in an *in vivo* setting, HSA-GA particles were introduced into an existing study of biodistribution of particles in an LPS induced lung inflammation model. In the absence of biological targeting moieties, the HSA-GA particles showed greater than 10-fold increase in accumulation within the lung when inflammation was present compared to naïve mice (Figure 3.16).

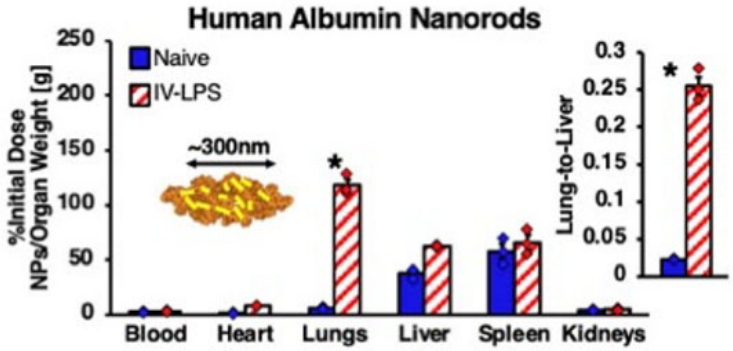

Figure 3.16: **Lung inflammation accumulation of HSA-GA SPNPs.** Biodistributions of crosslinked albumin nanoparticles indicating uptake of HSA-GA SPNPs in LPS-injured, but not naïve lungs. n = 3 biological replicates. Reprinted with permission. Ref [10]

The original intent of conjugating small molecules to proteins prior to their use in EHD jetting was to probe the technique of imparting biologically desirable properties onto the

bulk material and to retard the burst release of such compounds. Following the observation of spontaneously formed non-spherical particles, the focus of the venture quickly shifted. While I believe this is an interesting and worthwhile endeavor, this brief path seemed to generate more questions than answers. In particular, i) are small molecules conjugated to the bulk proteins able to maintain and impart their unique biological function onto the particles? and ii) what intermolecular interactions, solution properties, and forces are responsible for the observed deviation from spherical particles when gallic acid in particular is conjugated to the protein prior to jetting? Without exploring a range of interesting molecules, developing additional conjugation approaches, fully exploring the design space, and evaluating their intracellular impacts, it is difficult to provide meaningful insights. While beyond the scope of this thesis, these are challenges and questions to be addressed by those potentially looking to pursue this approach of drug delivery.

3.3.6 Loading and Controlled Release of Hydrophobic Molecules

Among the driving forces in the development of nanoparticles is the ability to load and release therapeutic cargo. Sustained and controlled release from nanoparticles offer promise in an array of chronic and acute conditions. Many cancer therapeutics have poor solubility in aqueous environments (i.e. buffer, saline, or serum) due to their hydrophobic nature; paclitaxel for instance, requires administration with Cremophor EL (polyoxyethylated castor oil) and absolute ethanol. [184] While offering a means to intravenously administer poorly soluble drugs, biological side effects have been directly related to the Cremophor EL delivery formulation itself. [185] Poor drug solubility extends beyond administration and must also be considered in particle formulation as methods to encapsulate these drugs are developed. Therefore, these same concerns must be addressed when designing drug loaded protein particles. With respect to the EHD jetting of SPNPs, in order to arrive at uniform distribution of the drug (or any molecule) across the entire particle population, stable and homogenous jetting solutions are required. Precipitation of any component (protein, drug, macromer) creates a dynamic system from which the population of particles and their overall composition changes with time. As a result, we sought to develop a method of incorporating drugs, particularly hydrophobic cancer therapeutics, into the jetting process to effectively load and release from SPNPs.

Successfully incorporating various components into the EHD jetting process to yield a final particle architecture can be achieved in multiple ways. The most direct route is the variation of solvent systems employed. In the case of water soluble small molecules or biologics,

the identification of a reasonable cosolvent system producing a stable, dilute, and homogeneous jetting solution becomes rather trivial. However, when considering hydrophobic molecules, this is often not the case. First dissolving the drug in a solvent such as DMSO, or adjusting the pH through small additions of acids or bases (e.g. glacial acetic acid or triethylamine) have proved to be promising places to start when developing these systems. In any case, these additions should be minimized to protect protein stability (ideally less than 10 vol%). While these are often successful approaches, in instances of loading increasingly hydrophobic drugs such as taxols, other means must be explored.

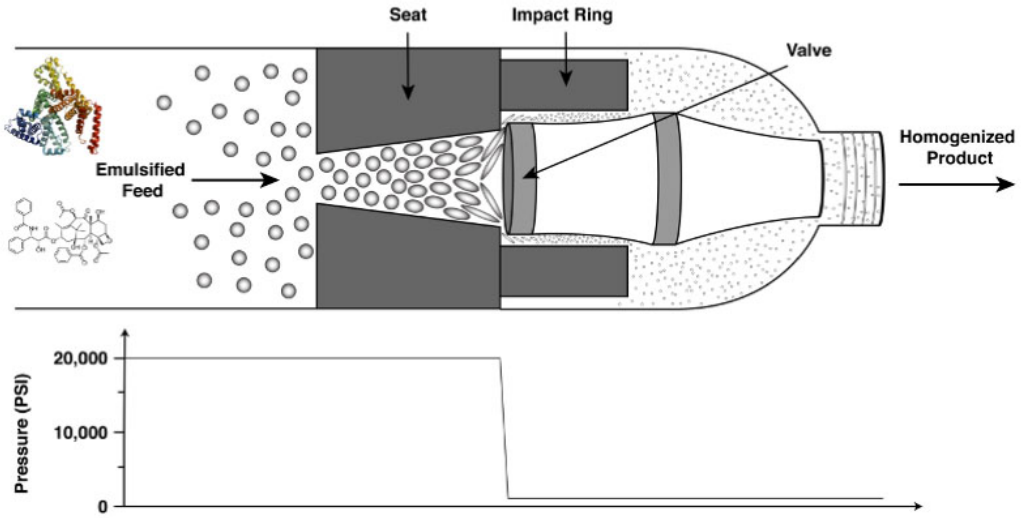

Figure 3.17: **High pressure homogenization towards an HSA-paclitaxel complex.** (Top) Experimental illustration of the high pressure homogenization process used in accordance with previously developed and patented methods related to nab technologies for the production of albumin-bound paclitaxel (Abraxane). (Bottom) Step-wise pressure drop highlighted correlating with the passage of emulsified protein-drug through the device valve.

Inspired by an approach that yielded the FDA approved therapeutic Abraxane, we sought to develop a means to solubilize these compounds prior to introducing them to the jetting solution. Utilizing the nanoparticle albumin bound (nab) approach, Abraxane offers a route of administering paclitaxel without Cremophor EL. Through high pressure homogenization, paclitaxel is sequestered within the protein hydrophobic pockets. Guided by an established protocol, we applied this same approach to produce an similar albumin-paclitaxel complex. [153] In brief, paclitaxel was first dissolved in a small volume of chloroform and then added to an aqueous protein solution. First homogenized using tip sonication, the mixture was then repeatedly passed through a small orifice at high pressures (25,000 psi) to create a stable emulsion (FIgure 3.17). In the case of Abraxane, this same process yields ”nanoparticles” approximately 130 nm in diameter that are stable in solution; however, without a

way to crosslink these particles, the individual proteins disassociate following administration. [186] Freezing and lyophilization of the complex yielded a white powder. When solubilized again at 2.5 wt% in a 90:10 v/v ultrapure water and ethanol cosolvent system, the solution appeared transparent and off-white with no observed precipitates formed. The solution was monitored for a period of 8 h at RT and by visual inspection no significant changes were noted. Incorporating the 2 kDa NHS-PEG as a crosslinker, the solution was jet and the resulting particles characterized. HSA-PTX SPNPs were found to have an average diameter of 121.4 $\pm$ 47.2 in their dry state and 191.5 $\pm$ 72.1 in their hydrated state as determined by SEM image and DLS analyses, respectively.

Release of paclitaxel from HSA-PTX SPNPs was then characterized, adhering to a previously established method thoroughly detailed in Section 2.2.2. Briefly, particles of a known mass were suspended in PBS and dialyzed against PBS at 37°C from a 100 kDa MWCO Float-a-Lyzer dialysis device. Changing the sink buffer solution at predetermined timepoints, paclitaxel concentrations in the buffer were determined through HPLC-MS analysis. Previously generated calibration curves were used to quantify release at each timepoint and the overall cumulative release. It was observed, that from SPNPs loaded with paclitaxel, the release of the drug followed controlled first order rate kinetics with approximately 90% of the drug released over a four day period (Figure 3.18). Additionally, mass spec confirmed the chemical structural integrity of the encapsulated and released drug. Subsequent studies evaluating the cellular response to PTX-STAT3*i*-SPNPs, a variation of the HSA-PTX SPNPs, is presented in Section **??**.

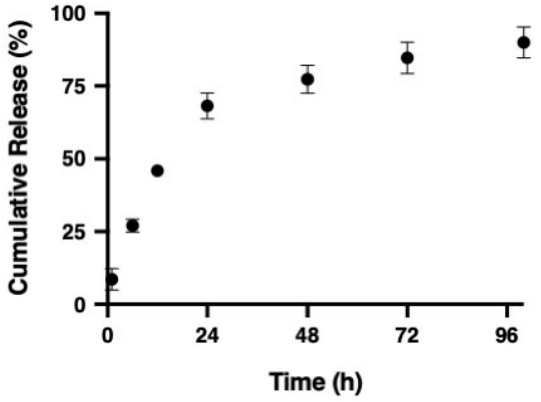

Figure 3.18: **Release of paclitaxel from albumin SPNPs.** Cumulative release of paclitaxel from albumin SPNPs formed through EHD jetting. Release conducted in PBS (pH 7.2) at 37°C. Paclitaxel release quantified via HPLC-MS. n = 3 biological replicates.

3.3.7 Janus Protein Nanoparticles

While there exists various methods to produce nanoparticles, a unique advantage to the EHD approach, as demonstrated through the fabrication of polymer Janus nanoparticles (Section 2.3), is the ease in which multiple compartments can be incorporated into a single particle architecture. EHD cojetting, has been used to create multicompartmental particles and fibers with precise control over volumetric ratios, [93] the relative spatial orientation, [187] variations in bulk and encapsulated materials, [75, 99] and even the controlled surface decoration of the individual compartments. [9] These characteristics are achieved simply through the preparation of multiple jetting solutions with similar solution properties and their subsequent coflow into the Taylor cone control volume. Here, we aimed to leverage this capability towards the development of multicompartmental protein nanoparticles.

As a proof of concept, two distinct proteins, HSA and human serum transferrin were chosen as base proteins for the individual compartments. Protein solutions were prepared in an 80:20 v/v ultrapure water and ethylene glycol cosolvent system at a protein concentration of 7.5 wt%. Fluorescently labeled, Alexa Fluor 488 and Alexa Fluor 647 conjugated versions of the albumin and transferrin were incorporated at 0.5 wt% relative to their respective proteins for imaging purposes. Particles were crosslinked through the addition of 10 wt% NHS-PEG macromer relative to the proteins. Establishing a stable Taylor cone with the two solutions flowing in a side-by-side orientation, the solutions were processed through the EHD cojetting system and incubated as previously described to yield stable SPNPs (Figure 3.19a). Characterized through SEM analysis, the particles were observed to have a size distribution consistent with previously fabricated monocompartmental SPNPs (Figure 3.19b). When imaged with super resolution SIM microscopy, we confirm the particle anisotropy through the observation of two distinct fluorescently labeled compartments (Figure 3.19c). Further experiments, incubating particles with fluorescently labeled antibodies, specific to albumin and transferrin, demonstrate that each compartment can be individually recognized by their respective antibody speaking not only to the ability to produce anisotropic protein nanoparticles, but suggesting that the crosslinked proteins retain important structural confirmations allowing the recognition and binding to occur.

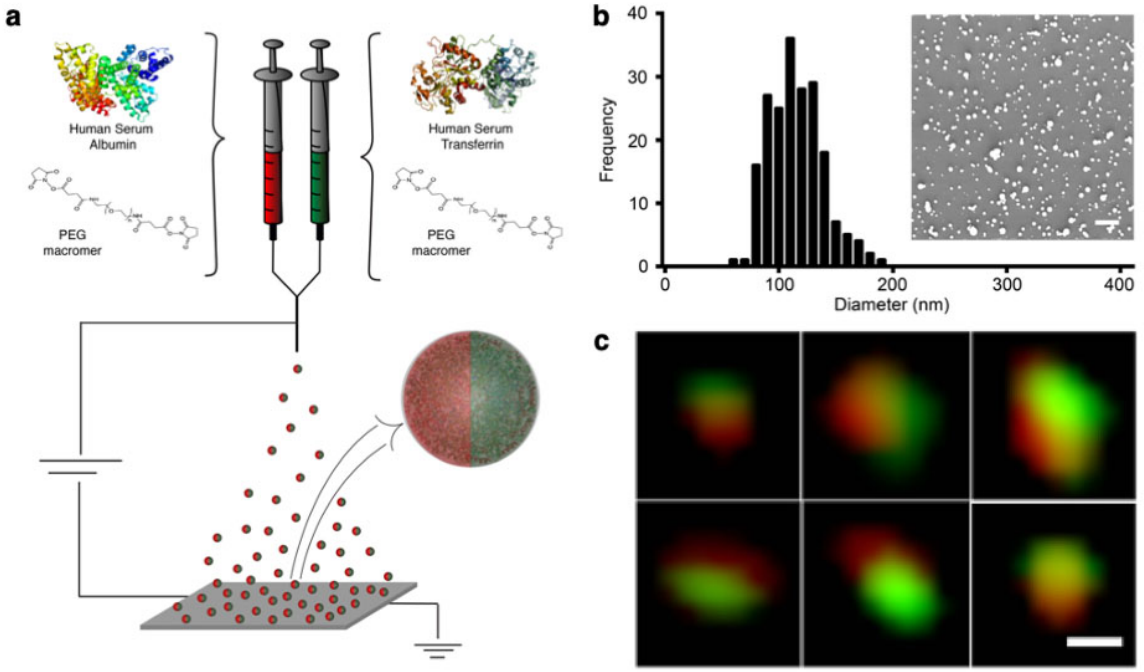

Figure 3.19: **Bicompartmental Janus SPNPs via EHD co jetting. a)** Jetting schematic for albumin/transferrin bicompartmental Janus nanoparticles. **b)** SPNP size distribution determined via SEM image analysis. (Inset) Representative SEM image, scale bar 1 μm. **c)** Super resolution SIM microscopy images of individual Janus SPNPs. Scale bar = 100 nm.

3.4 Summary

Here, we have demonstrated an ability to apply the general EHD jetting procedure to create particles using proteins as their bulk material. Important for all subsequent work, methods to reproducibly collect, fraction based on size, and characterize the resulting particles through imaging, image analysis, and light scattering based assays were optimized. In work to develop the platform and diversify the design space, the process was expanded to include a range of proteins with varied molecular weight, charge, and function. Methods were developed to vary the extent of crosslinking. Extending this work, other lab members were able to control not only physical properties such as mesh size, porosity, and elastic moduli, but demonstrated the effects these traits have on biological function. Crosslinking techniques to yield water stable SPNPs evolved from a single biologically inert PEG macromer to include physically responsive macromers, chemical vapor crosslinking approaches, and even those that avoided the use of macromers altogether through modifications to the bulk proteins inducing intermolecular disulfide bonds to form. The modification of proteins prior to jetting was extended beyond encouraging spontaneous crosslinking to occur to the proposed idea of the conjugating biologically relevant small molecules showing promise

for future development. Broadening the types of molecules that can be encapsulated beyond water soluble drugs, peptides, and nucleic acids, an approach to sequester non-polar molecules within the protein hydrophobic pockets prior to jetting was developed. This technique facilitated the loading and controlled release of paclitaxel and could be further expanded to include a host of other drugs with similar properties. Individual components of the aforementioned advances towards a robust and diverse particle platform ultimately can be combined into a single particle architecture, as demonstrated by our ability to create anisotropic Janus SPNPs. The work to expand methods of crosslinking proteins continues in our lab with the next generation of students as they work to develop multifunctional macromers capable of not only stabilizing the particles but imparting additional functions (e.g. the electrostatic binding of nucleic acids and controlled enzymatic degradation). Together, these works can be leveraged towards the development of intelligently designed multifunctional nanoparticle drug delivery systems with near limitless potential.

CHAPTER 4

Targeted Delivery of Synthetic Protein Nanoparticles

This chapter contains portions of text/data in preparation to be published as:

Antibody-mediated targeting of protein nanoparticles.
JV Gregory, A Berardi, B Zhang, A Mauser, C Greineder, J Lahann
In Preparation

Individual contributions to this work included the synthesis and characterization of albumin nanoparticles. Further work resulted in the development and full characterization of a conjugation strategy for the attachment of targeting antibodies to particle surfaces. Finally, both *in vitro* and *in vivo* work were completed to validate cell-specific uptake and altered biodistribution profiles, respectively.

4.1 Motivation

In the previous chapter, a platform for the synthesis of protein nanoparticles was developed. The results included a means to produce an array of nanoparticles with variations in composition, size, and even shape. Extending beyond the basic architecture, modifications to the proteins in the form of chemically conjugated and complexed molecules was explored. Finally, using the EHD co-jetting approach, we demonstrated an ability to create Janus protein nanoparticles using unique bulk materials. In parallel to these efforts, approaches to characterize the chemical and physical properties of the engineered particles was developed.

Focused primarily on the development and characterization of the protein nanoparticle plat-

form, select experiments looked at their *in vitro* and *in vivo* performance. Promising results were observed following the systemic delivery of non-targeted protein nanoparticles synthesized via EHD jetting in two distinct studies. The first showed a greater than ten-fold increase in the accumulation of albumin nanorods in a mouse model for lung inflammation. [10] The second realized an order of magnitude increase in uptake within the brain following injection of albumin nanoparticles via the carotid artery. [30] In each case, the observed increase in SPNP accumulation was noted to occur in the first organ capillary bed upstream of particle injection and was achieved in the absence of active targeting. While this approach may be sufficient in some therapeutic applications, a means to actively target the nanoparticles could significantly improve organ-specific uptake and minimize off-target effects.

Here, we look to extend our protein nanoparticle platform to incorporate active targeting. Previous work in the Muzykantov lab has evaluated the targeting capacity of antibodies and single chain antibody fragments. Working in collaboration here at the University of Michigan with Dr. Colin Greineder, we aim to leverage this same selectivity towards the targeted delivery of protein nanoparticles. In order to achieve a targeted delivery approach, a method of SPNP surface modification was proposed. In brief, we sought to develop a method that would be, i) compatible with each of the previously developed crosslinking methods, ii) universally compatible with an array of proteins, iii) conducted in relatively mild reaction conditions, iv) easily purified from unreacted materials and/or reaction by-products, v) simply modified to control for final ligand surface density, and vi) compatible with both mono- and multicompartmental particle architectures. As a proof of concept, we demonstrate the conjugation of targeting antibodies; however, the developed approach can be extended to instead incorporate small molecules, peptides, or antibody fragments.

4.2 Experimental Methods

4.2.1 Materials

Reagents: Human serum albumin, ethylene glycol, trifluoroethanol (TFE), O,O-Bis[2-(N-Succinimidyl-succinylamino) ethyl]polyethylene glycol (NHS-PEG-NHS, 2 kDa), beta mercaptoethanol, Sephadex G-100, triethylamine (TEA), sodium sulfate, sodium chloride, N-Succinimidyl-S-acetylthioacetate (SATA), hydrochloric acid, dimethylsulfoxide, ethyl acetate, chloroform, dimethylformamide (DMF), ascorbic acid, hydrogen peroxide solu-

tion, N-(3-Dimethylaminopropyl)-N-ehtylcarbodiimide hydrochloride (EDC), Tween 20 and phosphate buffered saline (PBS) were purchased from Sigma-Aldrich, USA. Human serum albumin and transferrin monoclonal antibodies, eGFP Silencer siRNA, Tris-HCl buffer, (5,5-dithio-bis-(2-nitrobenzoic acid) (Ellman's reagent), acetonitrile, sodium nitrite, acetone, N-(hydroxysulfosuccinimide) (Sulfo-NHS), 0.5-mL Zeba Spin Desalting Column, 1,3,4,6-tetrachloro-3,6-diphenyl-glycoluril, BCA assay kit, and Protein 660 assay kit were purchased from Fisher Scientific. Azidobutyric acid NHS ester was purchased from Lumiprobe. [125I]NaI was purchased from PerkinElmer. DBCO-NHS ester was purchased from Click Chemistry Tools.

4.2.2 Methods

Synthesis of NHS-PEG-NHS Crosslinked Synthetic Protein Nanoparticles (SPNPs)

SPNPs were fabricated via the electrohydrodynamic (EHD) jetting process previously developed in our group for the fabrication of synthetic polymer nanoparticles. [8, 89–92] Adapted to instead use proteins as the bulk material, HSA was dissolved in a cosolvent mixture (80:20 v/v) of ultrapure water and ethylene glycol at a concentration of 7.5 w/v%. Alternatively, a cosolvent mixture (80:20 v/v or 90:10 v/v) of ultrapure water and ethanol can be used. A bifunctional PEG (NHS-PEG-NHS, 2kDa) was added at 10 w/w% relative to HSA. In experiments evaluating the effects of crosslinking and the resulting swelling, molecular weight and mass fraction of NHS-PEG-NHS were varied. Final jetting solutions were pumped through a syringe equipped with a 26-gauge blunt tip needle at a flowrate of 0.1-0.2 mL h^{-1} while a constant voltage (ranging from 5.0 to 11.5 kV) was applied to form a stable Taylor cone at the needle tip. Particles were collected in aluminum pans at a needle to collector distance of 15 cm and then incubated for seven days at 37°C to facilitate complete polymerization. SPNPs were then stored in dark RT conditions in their dry state for future experiments.

Synthesis of Macromer-free Disulfide Crosslinked SPNPs

In order to create water-stable SPNPs in the absence of crosslinking macromer (XLF-SPNPs), HSA was dissolved in a cosolvent mixture (90:10 v/v) of trifluoroethanol (TFE) and ultrapure water 7.5 w/v%. Following complete dissolution and unfolding of the protein (evident by a slightly cloudy solution appearance), 10 molar excess of β-mercaptoethanol

(β-ME) relative to cysteine residues involved in disulfide bonds (e.g. 34 per albumin) was added. Final jetting solutions were pumped through a syringe equipped with a 26-gauge blunt tip needle at a flowrate of 0.1-0.2 mL h^{-1} while a constant voltage (ranging from 7.0 to 10.0 kV) was applied to form a stable Taylor cone at the needle tip. Particles were collected in aluminum pans at a needle to collector distance of 15 cm. No further incubation at elevated temperatures was required or performed. Particles collected on a dry surface were instead stored in a vacuum desiccator for a period of at least 12 h to remove any residual solvents. Disulfide crosslinking SPNPs were then stored in dark RT conditions in their dry state for future experiments.

Collection and purification of SPNPs

SPNPs were collected according to a standard protocol developed in our lab. In brief, a small volume, 5-10 mL, of water:ethanol (80:20 v/v) + 0.5% Tween 20, was added to the aluminum pans containing EHD jetted SPNPs. The resulting SPNP suspension was gently sonicated to disperse any aggregates and passed through a 40 μm cell straining filter. The resulting solution was centrifuged at 4,000 rpm (3,220 xg) for 4 minutes to pellet and remove any albumin aggregates larger than 1 μm in diameter. The supernatant was then divided into 2 mL Eppendorf tubes and centrifuged at 15,000 rpm (21,500 xg) to concentrate the samples to a single 1 mL sample for use in planned experiments. Collected SPNPs were used within 1 week of their collection and were stored at 4°C in PBS during that time.

Characterization of albumin SPNPs size, shape, and concentration

Albumin SPNPs were characterized prior to their use in any experiments to ensure they met specifications. Physical characterization included the measurement of particle size in both their dry and hydrated state. To measure particle diameter and investigate their morphology, small silicon wafers were placed on the grounded collection surface and were subjected to the same incubation period to complete the step-growth polymerization. These samples were imaged via SEM using a FEI NOVA 200 SEM/FIB instrument (UM, MC^2 Institute). Obtained SEM images were characterized using ImageJ software. SPNPs in their hydrated state were collected and purified as described above. The stock solution was diluted in PBS + 0.5% Tween 20 for subsequent measurements using DLS and NTA to investigate size and solution concentration. Analysis via DLS and NTA was performed using the Malvern Nano ZSP and NanoSight NS300 instruments and software, respectively (UM,

Biointerfaces Institute). Albumin SPNP solution concentration was further validated using the BCA (bicinchoninic acid) assay.

Azide functionalization of albumin SPNPs

Following the collection, purification and characterization of SPNPs, protein concentration of the particle suspension was estimated using the Protein 660 assay. A known mass of particles suspended in PBS buffer was transferred to a fresh 2 mL Eppendorf tube. The volume was adjusted to 1 mL with the addition of PBS. To this mixture, a small amount of an azidobutyric acid NHS ester (Azide-NHS, 35 mM) in DMSO was added at a ten molar excess relative to albumin. The reaction mixture was mixed well and placed on a rotator at 4°C O/N. The following day, the particles were centrifuged at 15,000 rpm (21,500 xg) for 1 h to pellet the suspended particles. Supernatant was carefully removed ensuring the pellet was not disturbed. The pelleted particles were resuspended in fresh PBS and the mixture was vortexed to form a homogeneous particle suspension. This process was repeated a total of three times to thoroughly remove any unreacted Azide-NHS before moving towards antibody conjugation steps.

DBCO modification of antibodies

Antibodies were incubated with DBCO-NHS ester at a 1:5 molar ratio at RT for 1 h. The unreacted DBCO-NHS ester was removed through dialysis (100 kDa MWCO), for 48 h at 4°C with multiple changes of media.

Antibody radiolabeling

Antibodies were directly radioiodinated using [125I]NaI in tubes pre-coated with 100 µg Pierce Iodination reagent, 1,3,4,6-tetrachloro- 3α,6α-diphenyl-glycoluril. Free iodine was removed using 0.5-mL Zeba Spin Desalting Column. Radiochemical purity was $\geq$ 95% by thin-layer chromatography (TLC) using a 75:25 v/v mixture of MeOH:Na-acetate pH 6.8 as the mobile phase.

Surface conjugation of antibodies to azide-SPNPs

Following the reaction to chemically conjugate the Azide-NHS to SPNP surfaces, DBCO-modified antibodies were then conjugated to the surface via a copper-free click chemistry. In brief, particles were resuspended in 0.5 mL of fresh PBS immediately following the azide modification and centrifugation steps. An antibody solution (in PBS), previously modified with DBCO functional groups and solution concentrations characterized via Nanodrop were added to achieve a desired stiochiometric ratio of antibodies to SPNPs. When validating the conjugation efficiencies and developing the methods, this ratio ranged from 500 to 5000 antibodies per particles; however, for subsequent *in vito* cellular assays and *in vivo* biodistribution experiments this ratio was fixed at 1,500 antibodies per particle. The reaction volume was increased to 1 mL through the addition of fresh PBS. Vortexing of the solution was completed to create a homogeneous solution prior to the reaction vessel being stored at 4°C O/N under constant rotation.

Column purification of antibody decorated albumin SPNPs

Once the two-step azide modification and antibody conjugation was completed, SPNPs were isolated from unreacted antibodies through column purification. Utlizing a Sephadex G-25 filled separation column, with PBS as the mobile phase, 1 mL fractions were collected for a total of 35 mL. This total volume was initially extended to 50 mL; however, it was noted that the bulk of SPNPs and free antibody eluted from the column centered about fractions 9 and 23, respectively. During process development stages, when the antibody was ^{125}I labeled, these fractions were evaluated using the PerkinElmer Wizard^2 instrument to quantify radioactive signal in tandem with plate-based fluorescent assays to identify SPNP-containing fractions. When extended to *in vitro* cellular assays and *in vivo* biodistribution studies, this process was used merely as a means to isolate antibody-SPNPs from unreacted antibodies before proceeding.

Biodistribution of albumin SPNPs in mice

Radiolabled particles were first suspended in PBS. Adjusting the final volume to yield a total volume of 100 µL per mouse, the samples were evenly aliquoted into 2 mL Eppendorf tubes. Radioactive measurements of each vial were made using the PerkinElmer Wizard^2 instrument prior to transferring the solution to 1 mL syringes equipped with 31 gauge needles. Intravenous administration of ^{125}I SPNPs was achieved via retro-orbital injection. At predetermined time points, select mice were anesthetized prior to the collection of blood,

urine, and organs (heart, lung, liver, spleen, kidney, and brain). Collected organ and fluid samples were analyzed with the same PerkinElmer Wizard^2 instrument. Additionally, each of the Eppendorf tubes and syringes were measured post particle administration to account for any loss of particles and to ensure the injected dose was accurately calculated.

4.3 Results and Discussion

4.3.1 Antibody conjugated SPNP synthesis

Proteins, and their amino acid side chains, offer a range of chemical conjugation techniques that can be performed in aqueous buffers at neutral pH. Previous work in our lab to develop the NHS-PEG crosslinked particles demonstrated an ability to reliably react NHS-terminated synthetic macromers to lysine side chains. Taken together with the availability of many commercially available hetero, bifunctional linkers equipped with bioorthogonal functional groups, a two-step process was proposed; the first designed to yield SPNPs surface decorated with functional groups (e.g. azides, alkynes, or maleimides) while the second would ultimately conjugate the molecule of interest to the particle surface utilizing an orthogonal chemistry approach. Here, we chose to utilize an azidobutyric NHS ester to add an azide functionality to the proteins. Conducted at neutral pH in PBS, this reaction allowed for a simple purification process to be performed to remove unreacted azide either through dialysis or multiple centrifugation cycles. Once functionalized, these azide SPNPs could then be reacted through a copper-free click reaction with any DBCO-modified molecule. The specificity of the azide-DBCO reaction ensures that only protein sites previously modified would be reactive and the strain promoted click reaction eliminates the need for a copper catalyst to be used. The latter point becomes important when considering copper induced cytotoxicity [188] and the ability of proteins to chelate metal ions. [189]

4.3.2 Antibody surface conjugation strategies

To address each of the desired process characteristics, two distinct strategies were evaluated (Figure 4.1). In strategy 1, both the azide modification and antibody conjugation steps are completed following particle synthesis. This approach has the advantage of ensuring that azide groups added to the protein are predominantly present on the particle surface, mini-

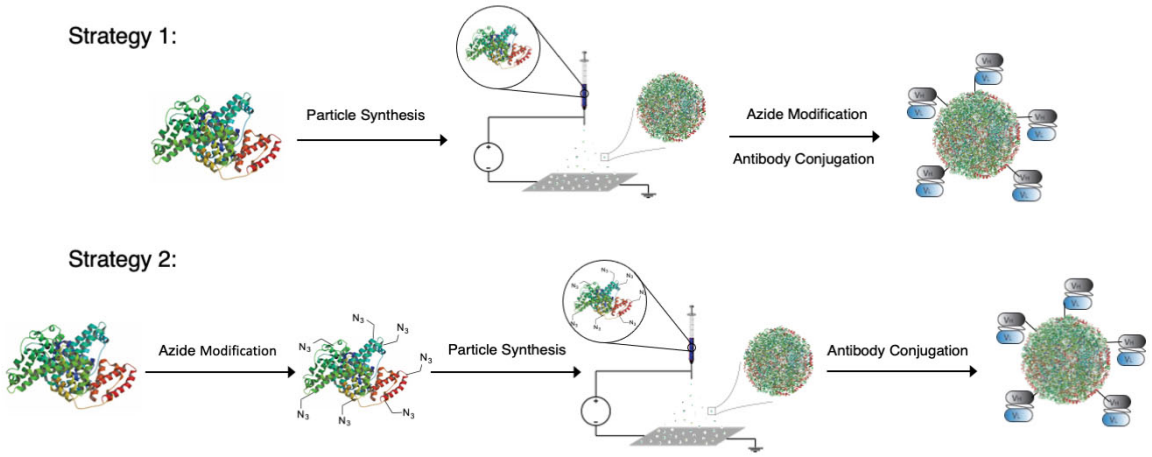

Figure 4.1: **Surface conjugation of antibodies to SPNPs.** Schematic detailing the two evaluated synthetic pathways towards the production of antibody conjugated protein nanoparticles (Ab-SPNPs) for antibody-mediated targeted delivery.

mizing the presence of functional groups that might otherwise be buried within the particle volume and unavailable for subsequent conjugation. Conversely, the second strategy involved the azide modification of free protein prior to particle synthesis via EHD jetting. While this approach will certainly result in some portion of the reactive groups inaccessible for future reactions, it addresses the desire to create multicompartmental particles with distinct surface functional groups through orthogonal chemistries.

In order to validate the paired reaction approach, we first attempted to conjugate DBCO modified dye molecules to the particle surfaces. This yielded a method that could easily be visualized through microscopy and further quantified to ultimately compare ligand surface density between the two strategies. Azide SPNPs were first synthesized, either through the conjugation of the azidobutyric acid to previously formed albumin SPNPs (Strategy 1), or through the jetting of azide modified albumin (Strategy 2). In each case, the relative stiochiometric ratios of protein to linker were maintained. Protein particles were fluorescently labeled through the addition of 0.5 wt% of Alexa Fluor 647 (AF647) albumin relative to the total protein content of the particles. SEM and DLS analysis of the two particle populations found no significant difference in their size distributions. Following each of the synthetic routes to arrive at Azide SPNPs, a sulfo-Cy3-DBCO dye was reacted O/N at 4°C in PBS. The removal of unreacted dye was achieved through a thorough centrifugation process in which particles were pelleted, supernatant and free dye was removed, and particles were resuspended in fresh PBS. This process was repeated a total of four times to ensure any unbound and surface adsorbed dye molecules were removed from the particle solution prior to further characterization.

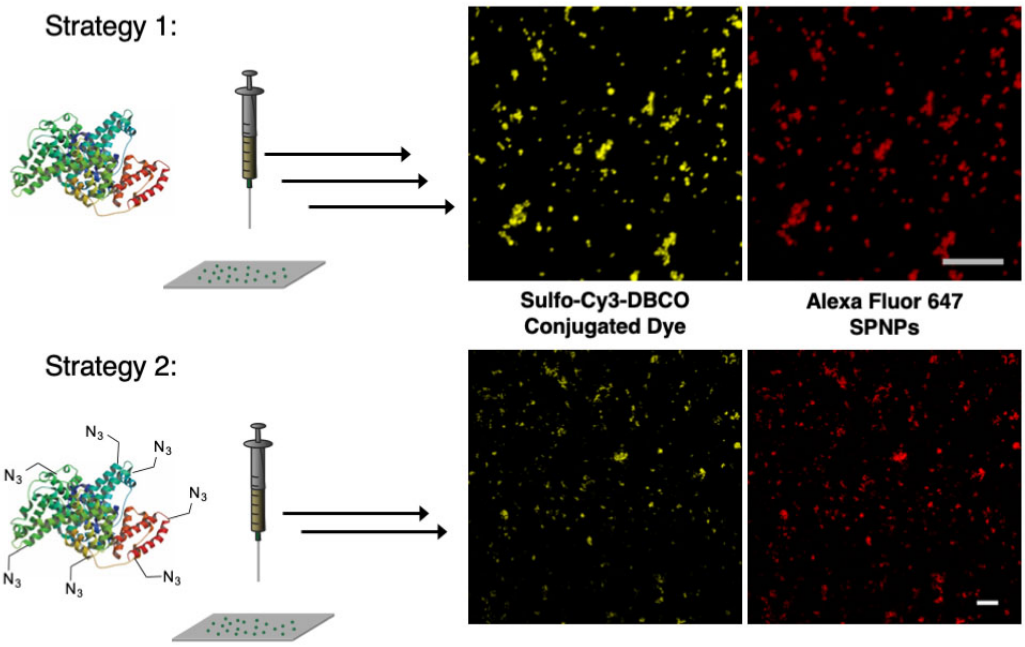

Figure 4.2: **DBCO-Cy3 conjugation to SPNP surfaces.** General schematics and qualitative characterization of surface conjugation reactions utilizing a DBCO-Cy3 dye as a surrogate molecule for imaging via confocal microscopy. Scale bars = 10 μm.

4.3.3 Surface-modified SPNP characterization

The resulting particles were characterized through a combination of imaging and plate-based assays. First, when particle populations were imaged via confocal microscopy maintaining equivalent laser settings across all samples, a clear difference in relative fluorescent signals is observed (Figure 4.2). In strategy 1, an increased Cy3 signal normalized to that of the AF647, suggests a greater extent of surface conjugation in this experimental group. Though the result was clear and consistent across all images, this only provided a qualitative comparison. Extending the characterization to quantify this difference, fluorescent signals of both the conjugated dye and particles in suspension were measured on a plate reader and compared to previously developed calibration curves for each species. Together, with NanoSight data relating particle fluorescence to particle count, along with relative size distributions, it was determined that the ligand density was approximately six-fold higher when the azide modification was directed to the particle surface through the post-fabrication approach (Strategy 1). Although significantly reduced in the strategy 2 approach, this still yielded approximately 100 ligands per SPNP at the evaluated stociometric ratio (Figure 4.3). In total, it was confirmed that completing both the azide modification and subsequent conjugation after particle synthesis and collection would more efficiently

decorate the particle surface. However, the data suggests that the alternative approach of first modifying protein could be advantageous and effective when aiming to selectively modify individual regions of multicompartmental particle surfaces.

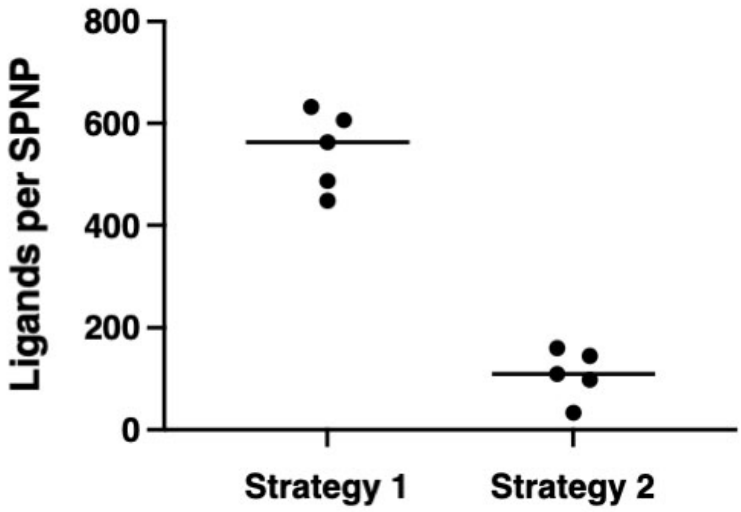

Figure 4.3: **Quantified ligand density.** Particle size distribution along with SPNP and DBCO-Cy3 fluorescence data applied to quantitatively determine the resulting ligand density, comparing the two developed SPNP surface conjugation strategies. Individual replicate data points and the calculated mean displayed (n = 5).

Based on previous data, it was decided that for the purpose of conjugating targeting antibodies to SPNP surfaces, the approach would be to first form stable SPNPs via EHD jetting followed by a two-step surface conjugation process, yielding antibody-decorated SPNPs (Figure 4.4). Moving forward, we sought to develop a reproducible method of purifying SPNPs from unreacted antibodies. To achieve this, we utilized a packed column separation approach designed to separate reaction mixtures through size exclusion (Figure 4.5a). When collecting 1 mL fractions, it was noted that for the selected column, free antibodies consistently eluted from the column broadly in fractions 20 through 35 (Figure 4.5b). SPNPs, however, due to their relatively large size, were found to elute at the solvent front and were typically only found in fractions 8 through 12 (Figure 4.5c). This distinct difference allowed for the final particle-antibody reaction mixture to be passed through the column and effectively purified from free, unbound antibody. When SPNP-containing fractions were combined through centrifugation, the result was a concentrated solution of antibody conjugated SPNPs (Ab-SPNPs). If passed through the column a second time, the purified particles showed no presence of any residual antibody (Figure 4.5d). These results were consistent whether the antibody had been fluorescently labeled or radiolabeled with ^{125}I.

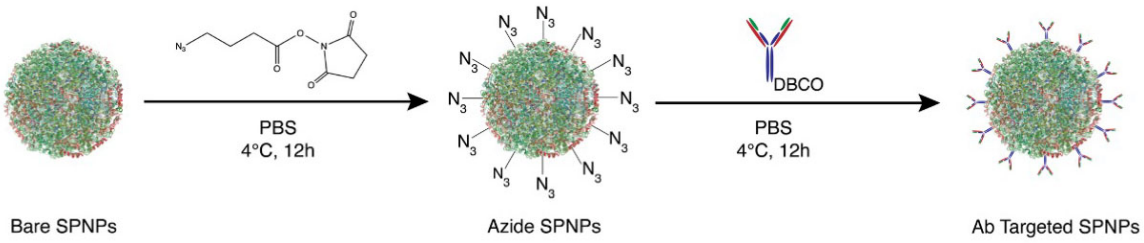

Figure 4.4: **Ab-SPNP synthetic scheme.** Optimized two-step synthetic pathway towards the synthesis of antibody targeted SPNPs consisting of a preliminary azide surface functionalization and subsequent DBCO-antibody, copper-free click conjugation.

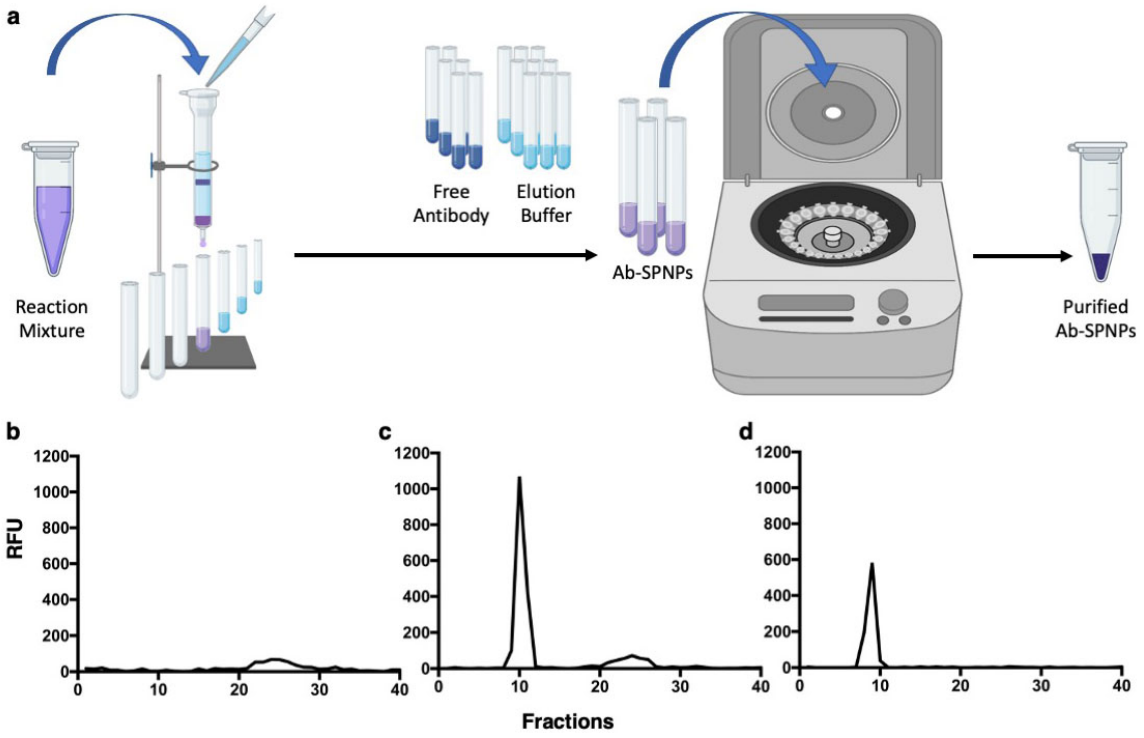

Figure 4.5: **Ab-SPNP purification.** **a)** Experimental schematic for the size exclusion column purification of Ab-SPNPs from the final antibody conjugation reaction mixture, ultimately yielding a concentration suspension of Ab-SPNPs. **b-d)** Relative fluorescent units plotted against column elution fractions. **b)** Elution of free antibody (150 kDa) in the absence of SPNPs. The bulk of the antibody mass elutes centered about fraction 23, stretching from fractions 20 through 35. **c)** Purification of the final reaction mixture with a clear separation of SPNPs (fractions 8-12) and unreacted free antibody(fractions 20-35), elution peaks centered about fractions 9 and 23 respectively. **d)** SPNP-containing fractions combined and passed through the column a second time, zero residual free antibody is observed.

Concerned by previous reports of antibody aggregation, [190, 191] particularly following chemical modifications wherein native structure might be perturbed, the effects of antibody

conjugation to the SPNP surfaces were evaluated. Albumin nanoparticles were synthesized and their size distribution characterized by SEM and subsequent image analysis. [106] Particles were observed to have an average diameter of 109.6 ± 28.3 nm (PDI = 0.067) in their dry state (Figure 4.6a). Following collection, these same particles when hydrated, were found to have an average diameter of 155.8 ± 60.1 nm (PDI = 0.148) (Figure 4.6b, black). Following the two-step surface conjugation and purification procedure, Ab-SPNPs were found to have an average diameter of 164.3 ± 42.1 nm (PDI = 0.066) (Figure 4.6b, red). As expected, the addition of antibodies to the particle surface resulted in a small increase in average particle size; however, no appreciable aggregation was observed suggesting that the surface modification of SPNPs with DBCO-antibodies does not affect their stability in suspension.

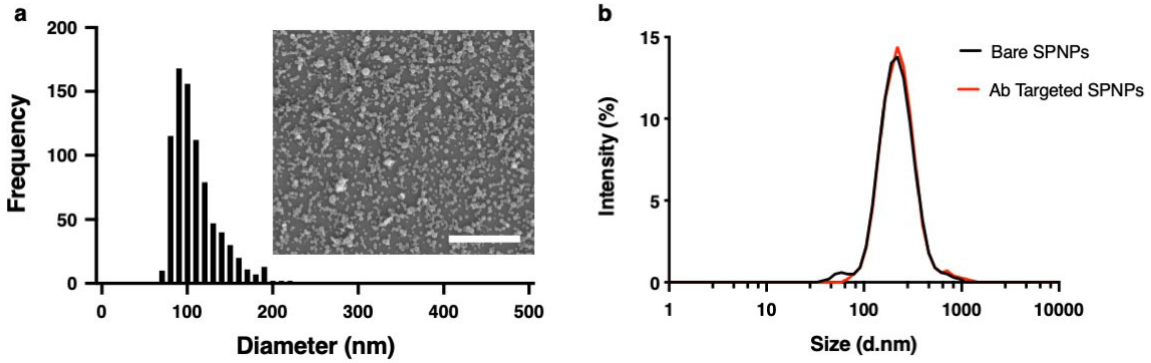

Figure 4.6: **Ab-SPNP size characterization and stability. a)** Size distribution of jetted SPNPs in their dry state and representative SEM image (inset). Size distribution quantified via image analysis of greater than 500 individual particles with ImageJ software. Particles were found to have an average diameter of 109.6 ± 28.3 (PDI = 0.067) in their dry state. Scale bar = 2 µm. **b)** DLS size distributions of fully hydrated SPNPs (black) and Ab-SPNPs (red) in PBS before and after antibody conjugation and purification steps were performed. Particles observed to have diameters of 155.8 ± 60.1 nm (PDI = 0.148) and 164.3 ± 42.1 nm (PDI = 0.066), respectively.

Having demonstrated an ability to conjugate both a small molecule dye and a 150 kDa antibody to the surface of NHS-PEG crosslinked particles, we next turned our attention towards, i) validating the system in other forms of SPNPs (disulfide crosslinked), and ii) controlling antibody surface density. To evaluate these, both NHS-PEG and disulfide crosslinked particles were fabricated, crosslinked, and collected per previously developed protocols (Section 3.2.2) developed for each particle type. Each of the resulting particle groups were reacted with a 10x molar excess of azidobutyric NHS ester relative to lysine groups present in the total albumin content prior to being split equally into five experimental groups. Azide SPNPs were then reacted with ^{125}I labeled, DBCO-modified IgG

antibodies O/N at 4°C at a ratio of 0.0, 62.5, 125, 250, and 500 antibodies per SPNP (Figure 4.7a). Adhering to the previously developed purification protocol, the final reaction mixture was separated using size exclusion column chromatography and collected in 1 mL fractions. The resulting fractions were individually measured using the PerkinElmer Wizard^2 Gamma Counter to quantify ^{125}I signal, both free and particle-bound. It was noted that a linear relationship existed between the number of antibodies reacted and those bound to the particle surfaces, suggesting a constant conjugation efficiency among each SPNP variation (Figure 4.7b). Furthermore, while both particle types exhibited this linear trend, it was the disulfide crosslinked particles that yielded the higher conjugation efficiency and therefore higher numbers of conjugated antibodies per particle across all stoichiometric ratios evaluated.

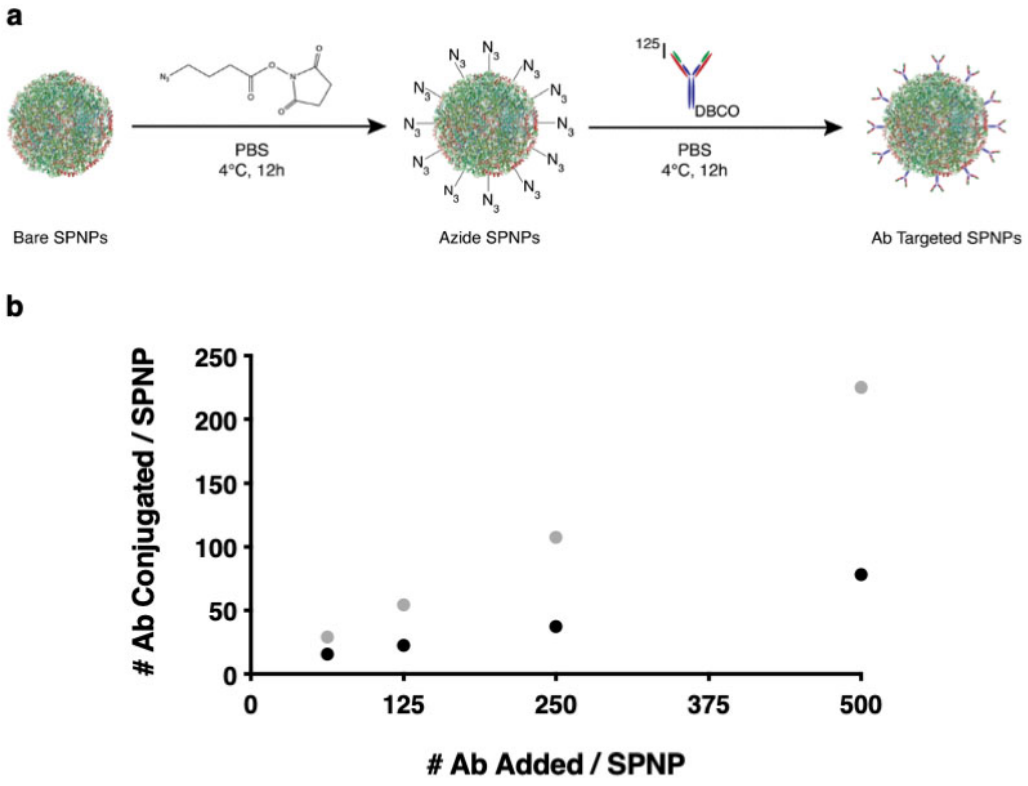

Figure 4.7: **Controlled Ab surface conjugation. a)** Schematic for the conjugation of ^{125}I labeled antibodies to SPNP surfaces to quantify antibody conjugation efficiency and overall reaction yield. **b)** Correlation of various stiochiometric antibody:SPNP reaction ratios to the resulting surface-bound antibody SPNP products comparing disulfide (grey) and NHS-PEG (black) crosslinked SPNPs.

The observed linear trend held constant in both particle types across the full range of reaction conditions. Notably, even at the highest (500 antibodies per SPNP) there did not appear to be any sign of saturation, suggesting that the limit of ligands per particle had not

yet been reached. In response, the experiment was repeated, extending the ratios by an order of magnitude, this time also evaluating 1500 and 5000 antibodies per SPNP. Following the same protocol and procedure as the previous experiment, similar trends were observed. Again, the disulfide SPNPs were found to more efficiently conjugate DBCO-antibodies and in both particle types no saturation and a linear relationship was observed (Figure 4.8). The lack of deviation from the observed linear relationship, again suggested that the saturation point of the reaction had not been reached, even when a starting ratio of 5000 antibodies per SPNP was evaluated.

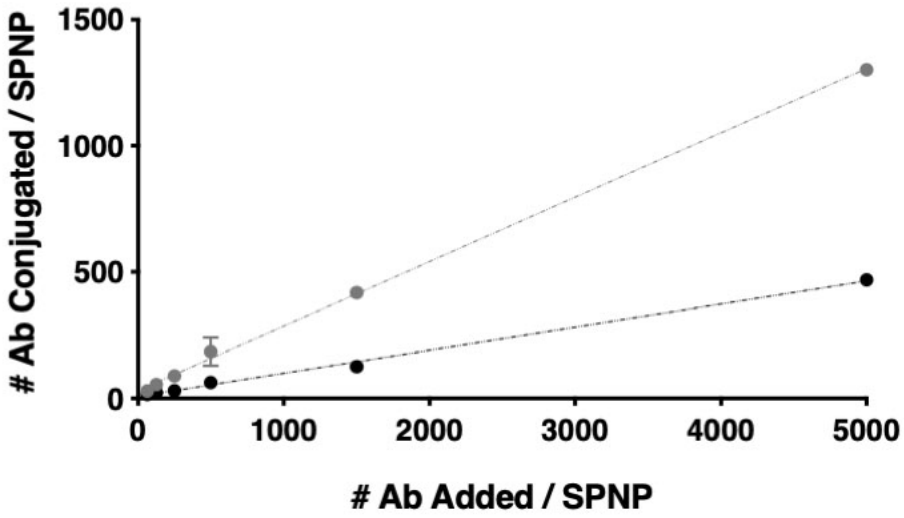

Figure 4.8: **Extended Ab surface conjugation quantification.** Extending the evaluated stiochiometric ratios of antibody:SPNPs to a maximum of 5000:1 comparing the conjugation efficiencies of disulfide (grey) and NHS-PEG crosslinked SPNPs. Dashed linear regression lines are displayed to guide the eye and highlight the linear relationships observed across all stiochiometric ratios tested.

The apparent difference between the two particle types was not anticipated but was consistently observed across the entire range of experimental groups. At their heart, the two particles differ in two key attributes. The obvious difference is the tertiary structure of the proteins as they are being jet; in the case of the disulfide SPNPs, the proteins have been denatured in solution yet retain their primary structure and therefore, their amino acid sequence and relative lysine content. More subtly, because the NHS-PEG SPNPs are crosslinked through amines it is reasonable to postulate that some of these are no longer available for two-step antibody conjugation. Though even at the theoretical maximum, assuming all of the macromer NHS groups react with a lysine residues of the protein, this still leaves approximately 90% of the lysines free for subsequent reactions. To test this, the experiment was repeated with a variation to the starting particle architecture; here, a

small addition of the polyamine, PEI, was added to the NHS-PEG SPNPs to create "amine-rich" SPNPs. A moderate ratio of 250 antibodies per SPNP was chosen and the reaction and purification steps were maintained identical to those previously described. It was observed that the amount of antibodies non-specifically bound to control SPNPs (no azide modification) was minimal compared to all other experimental groups. Among the amine-rich SPNPs, despite the presence of additional amine groups for both the crosslinking and antibody conjugation reactions, no significant difference was observed and these particles performed statistically identical to NHS-PEG SPNPs previously evaluated (Figure 4.9). From this, it would appear that the difference in protein structure during the jetting process may be responsible for the observed difference in conjugation efficiency, perhaps related to different regions of the protein being presented on the final particle surface.

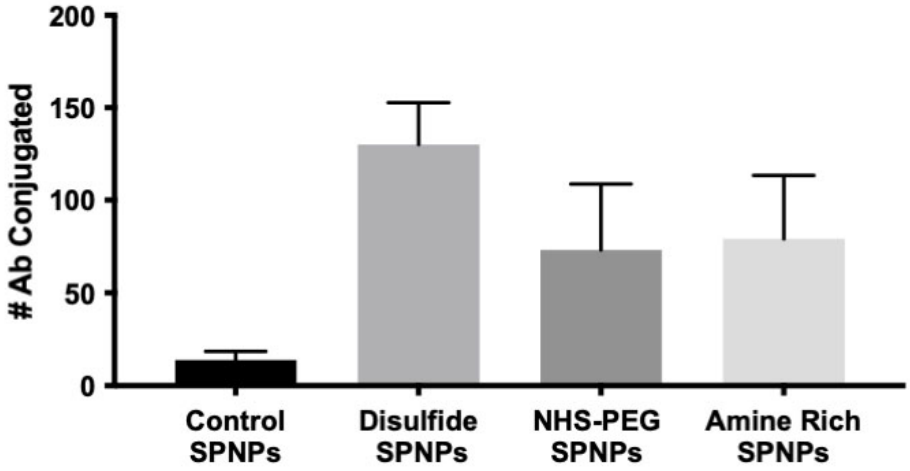

Figure 4.9: **Ab-SPNP comparison.** Comparing particle types when a 250:1 antibody to SPNP stiochiometric ratio is applied. In addition to the disulfide and NHS-PEG crosslinked particles, control (in the absence of prior azide modification) and amine-rich (with added PEI) particles were evaluated to identify non-specific adsorption and lysine depletion effects, respectively.

4.3.4 Selective binding, uptake, and knockdown

Following the successful development of a controlled and reproducible method of surface modifying SPNPs with antibodies, attention was turned to validating the selective uptake and targeting ability of these particles. Previous work by Muzykantov and coworkers had demonstrated and ability to target sub-micron polymeric particles to endothelial cells following adsorption of anti-ICAM (YN1) mAb onto the particle surface and intravenous injection of the same in mice. [192, 193] Taking a similar approach, but instead chemically

conjugating the antibodies to the SPNP surface, we sought to demonstrate an ability to selectively control particle binding, uptake, and ultimately the delivery of a biologically relevant macromolecular therapeutic.

Intercellular adhesion molecule-1 (ICAM-1 or CD54) is a member of the immunoglobulin superfamily of proteins, constitutively expressed on the surface of endothelial cells and leukocytes, and plays a key role in the transmigration of leukocytes out of blood vessels. Upon cytokine stimulation, these levels are severely elevated. [194] This response has been found to be associated with acute conditions such as general inflammation in the lung [195] and subarachnoid hemorrhage in the brain due to direct trauma. [196] Chronic conditions including atherosclerosis, [197] or the deposition of plaques along blood vessels walls, and implications in tumorigenesis [195] are also associated with increased ICAM expression. As a result, anti-ICAM, and other immunoglobulin antibodies, are attractive candidates for the targeted and selective delivery of therapeutic protein nanoparticles.

To determine whether anti-ICAM, or YN1, antibodies conjugated to SPNP surfaces could be used to influence cellular interactions and ultimately lead to their targeted delivery, we first evaluated their binding and uptake in an *in vitro* setting. Following the synthesis of AF647-labeled, NHS-PEG crosslinked SPNPs, we followed the previously developed method of conjugating DBCO-modified YN1 antibodies to the particle surface through our two-step reaction and purification processes (Figure 4.10a). As expected, the resulting YN1-SPNPs were found to have a similar size distribution to those previously prepared with IgG. Increasing concentrations of YN1-SPNPs were incubated with either REN-WT (low ICAM expressing) or REN-ICAM cells at 4°C. The choice of 4°C eliminates the ability of the cells to internalize the particles so that binding of the particles to the cellular surface can be specifically studied. Following a period of 30 mins, the cells were then thoroughly washed with PBS, fixed with paraformaldehyde, and processed via flow cytometry. Utilizing the far-red fluorescent signal of the particles, an approximately 15-fold increase in particle binding to the REN-ICAM cells compared to the WT was observed (Figure 4.10b). At the highest concentration of 100 μg mL^{-1}, we begin to see signs that the system is becoming saturated, evident by the flattening of the binding curve. This observation suggests that at high concentrations, and in the absence of cellular uptake, the available binding sites become occupied and are no longer available for additional antibody-specific interactions. Repeating the same experiment at 37°C, we observe a similar disparity between the REN-ICAM and WT cells with approximately a 30-fold increase in AF647 signal comparing the two cell types (Figure 4.10b). Notably, we do not observe a similar saturation of the receptor, even at the highest particle doses. Taken together, these data suggest that

the conjugation of YN1 antibodies to SPNP surfaces result in both preferential binding and uptake in cells expressing ICAM on their surfaces. Further, the lack of saturation observed at physiological temperature is consistent with the ability of the protein to recycle back to the cellular surface once the bound particle has been internalized.

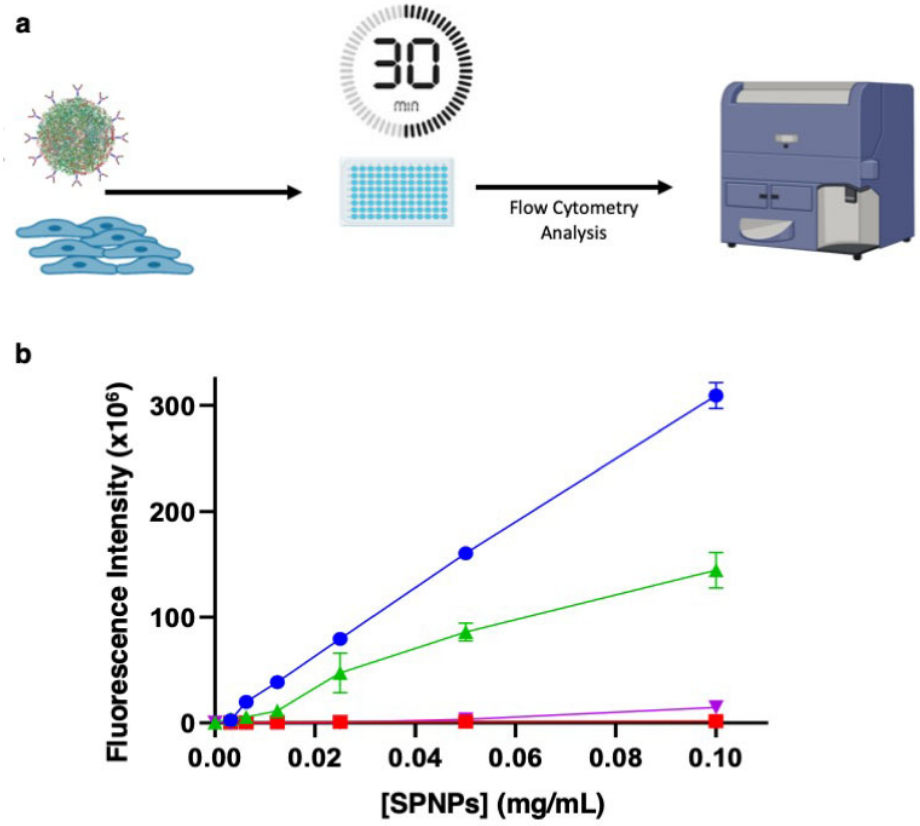

Figure 4.10: **Antibody-directed cellular binding and uptake. a)** Experimental scheme to determine selective, antibody-directed binding, cellular uptake, and dose dependence in REN-ICAM cells. **b)** Binding (REN-iCAM (green); REN-WT (purple), 4°C) and internalization (REN-ICAM (blue); REN-WT(red), 37°C) curves for YN1 (anti-ICAM) modified albumin nanoparticles. Flow cytometry analysis of treated cells performed following 30 min incubation of SPNPs with adherent cells (n = 3 biological replicates).

The technology and potential of biological therapeutics, specifically RNA, have seen remarkable growth in recent years. Protein expression within cells can vary significantly in response to disease and injury. From cancer to neurodegenerative diseases, protein expression can be correlated to the severity, progression, and response to current standard of care approaches for treatment. Modulation of protein expression through the use of mRNA and siRNA have demonstrated promise with the FDA approval of ONPATTRO in 2018 followed by the emergency use authorization of multiple mRNA-based vaccines in response to the COVID pandemic. Despite these advances, challenges remain and notably

include unfavorable immune response, off-target effects, and instability of the molecules themselves. As a result, a delivery system capable of providing a targeted and protected journey to the disease site of interest is required for the full potential to be realized.

Encouraged by results demonstrating selective uptake and binding of YN1-SPNPs to ICAM expressing cells, the role of endothelial cells in various diseases, and their accessibility from the blood stream, attention turned to the controlled delivery of therapeutics. Previous work in our lab had already developed and validated the delivery and release of biologics from protein nanoparticles fabricated via EHD jetting. [104] Here, we sought to leverage the targeted effects of YN1 antibodies conjugated to SPNPs, along with an exhibited ability to successfully deliver siRNA to the cytosol, to achieve cell-specific protein silencing.

Following a previously developed approach, albumin SPNPs encapsulating eGFP siRNA were synthesized. Briefly, siRNA was first complexed with a 60 kDa branched PEI in ultrapure water for a period of 30 mins. Once a stable complex had been formed, albumin, Alexa Fluor 647 labeled albumin (0.5 wt% relative to total protein), and a 2 kDa NHS-PEG macromer were added to the solution. The total volume was increased to yield a final protein concentration of 7.5 wt% in an 80:20 v/v cosolvent mixture of water and ethylene glycol. Jetting of the solution yielded a monodisperse population of SPNPs. Following the completed crosslinking, the particles were collected, characterized, and final solution concentration was quantified according to previously developed protocols. The SPNP suspension of siRNA SPNPs was then divided into two separate aliquots; the first remained unmodified to serve as the control bare SPNPs while the second volume was immediately introduced to the antibody conjugation and purification processes. Upon completion, the final particle suspensions were again quantified through the Protein 660 assay to determine SPNP concentration before entering the *in vitro* assay.

In order to evaluate the cell specific delivery and protein silencing of siRNA-loaded YN1-SPNPs, REN-WT and REN-ICAM cell lines engineered to express GFP were utilized. Cells were seeded in 48 well plates at 85,000 cells per well (approximately 70% confluent), allowed to adhere O/N, and were treated the following day. To treat, media was removed and cell populations received either siRNA-loaded YN1-SPNPs at various doses, siRNA via lipofectamine or unmodified siRNA SPNPs equivalent to the highest YN1-SPNP dose (18 nM eGFP siRNA). After an incubation period of 30 mins, the particle containing media was removed, cells were washed with warm PBS, and fresh particle-free media was replaced. Cells were incubated at 37°C, 5% CO_2 for a period of 48 h before they were fixed, stained for ICAM, and entered the flow cytometry protocol (Figure 4.11a). Untreated control cells received no siRNA and were cultured under identical conditions.

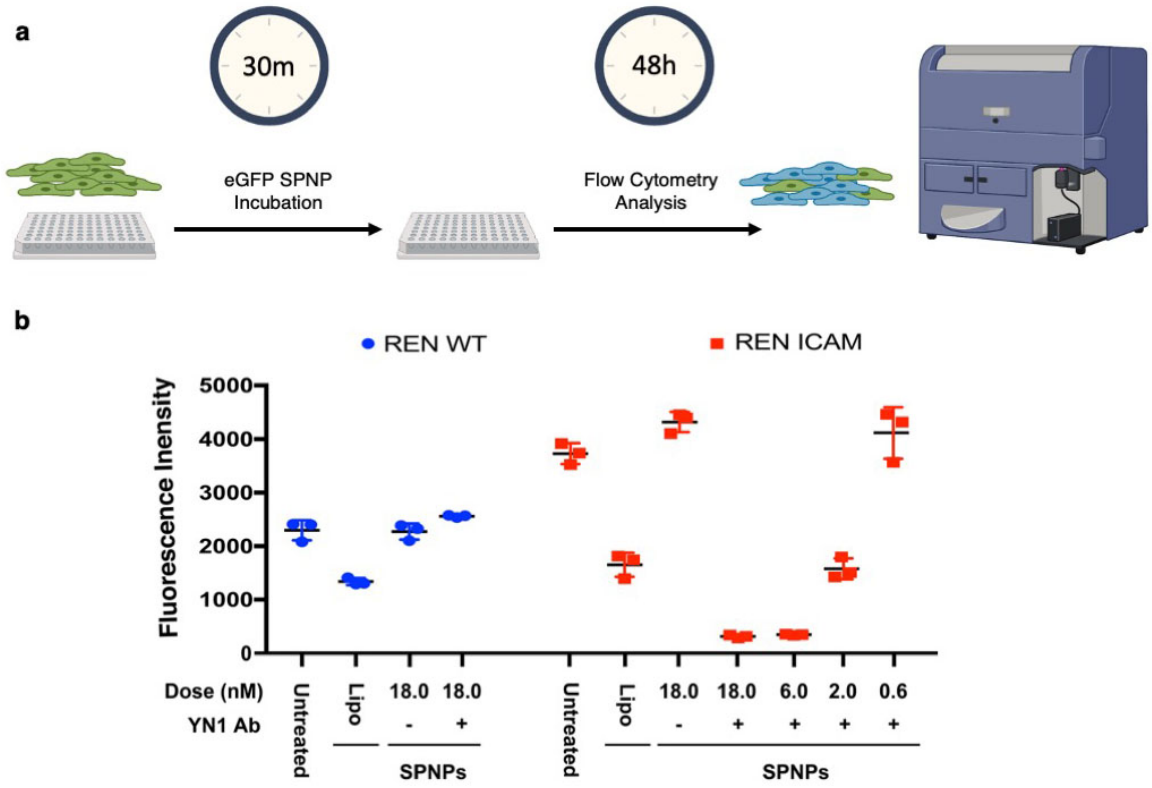

Figure 4.11: **Targeted delivery of eGFP siRNA and selective knockdown. a)** Experimental scheme to determine selective, antibody-directed protein silencing in eGFP expressing WT and ICAM expressing REN cells. **b)** Evaluated at 48 h post particle administration, eGFP expression determined across treatment groups via flow cytometry. Both REN-WT (blue) and REN-ICAM (red) groups received equivalent 18.0 nM siRNA doses delivered via lipofectamine (Lipo), untargeted SPNPs (-), or ICAM targeted YN1-SPNPs (+). A dose response among the REN-ICAM cells treated with YN1-SPNPs was investigated further with decreasing concentrations of siRNA. eGFP protein expression is compared to untreated control cells (n = 3 biological replicates).

In both the WT and ICAM expressing REN cells, ICAM and GFP expression were measured in the untreated control cells to serve as a baseline. Among the WT cells, ICAM expression was minimal as expected and approximately a 50% reduction in GFP was observed in the lipofectamine treated group (Figure 4.11b). The silencing was not observed for WT cells treated with siRNA SPNPs, with or without the addition of surface conjugated YN1 antibodies. This result was consistent with previous observations that very little uptake is observed in cells lacking surface expressed ICAM. When examining the REN ICAM cell populations, elevated levels of ICAM and GFP were noted in the untreated control cells. A moderate knockdown in GFP was noted in cells treated with lipofectamine while GFP levels were relatively unchanged when treated with unmodified siRNA SPNPs (Figure 4.11b). When looking at the cells treated with varied doses of siRNA delivered via

YN1-SPNPs, a significant and dose dependent response was observed. In both the 18.0 and 6.0 nM doses, GFP expression was reduced by nearly 90% compared to the untreated control. The effect was less pronounced at 2.0 nM and unchanged when the dose was reduced to just 0.6 nM (Figure 4.11b). Taken together, these results are consistent with previous experiments looking at binding and uptake in ICAM expressing cells. Futhermore, the effective silencing of GFP and dose dependent response observed only when the combination of ICAM expression and YN1-SPNPs exists, suggests a targeted and cell specific delivery of siRNA to the cytosol.

4.3.5 Biodistribution

From a perspective of targeted delivery following systemic administration of particles, the superfamily of immunoglobulin proteins are attractive targets. For example, expressed at low levels on the luminal surface of endothelial cells, intercellular adhesion molecule (ICAM-1) is both accessible from the blood and noted to be overly expressed in response to proinflammatory cytokines. Together, these attributes can be leveraged to alter the normal biodistribution of particles and facilitate the transmigration of particles from circulation to inflamed tissues.

To study the effects of conjugating YN1 antibodies to SPNP surfaces, a baseline of biodistribution and clearance of albumin nanoparticles was first established. Here, albumin SPNPs were synthesized, crosslinked, collected, and ^{125}I labeled through protein tyrosine residues (Figure 4.12a). Tracer doses of the resulting ^{125}I SPNPs were intravenously injected in anesthetized C57BL/6 mice. At time points of 1, 4, and 24 h, blood, urine, and organs (heart, lung, liver, spleen, kidney, and thyroid) were collected. Organs were then individually measured for radioactive signal to determine the percent injected dose per gram of organ (%ID/g) (Figure 4.12b). In the absence of any targeting, SPNPs were found to be cleared relatively quickly from the blood with less than 5% of the injected dose remaining after an hour. At this same time point, particles were found to have accumulated predominantly within the liver and spleen, known to be the primary routes of clearance for particles of this size. Interestingly, at later time points a sustained clearance from all organs is observed; across all organs measured, only the spleen showed greater than 5% ID/g after 24 h. The observed biodistribution profile is consistent with untargeted delivery of nanoparticles; however, the rapid clearance is promising suggesting that the particles are rapidly broken down and excreted from the body following systemic administration.

Previous experiments conducted *in vitro* demonstrated an selective binding and uptake by

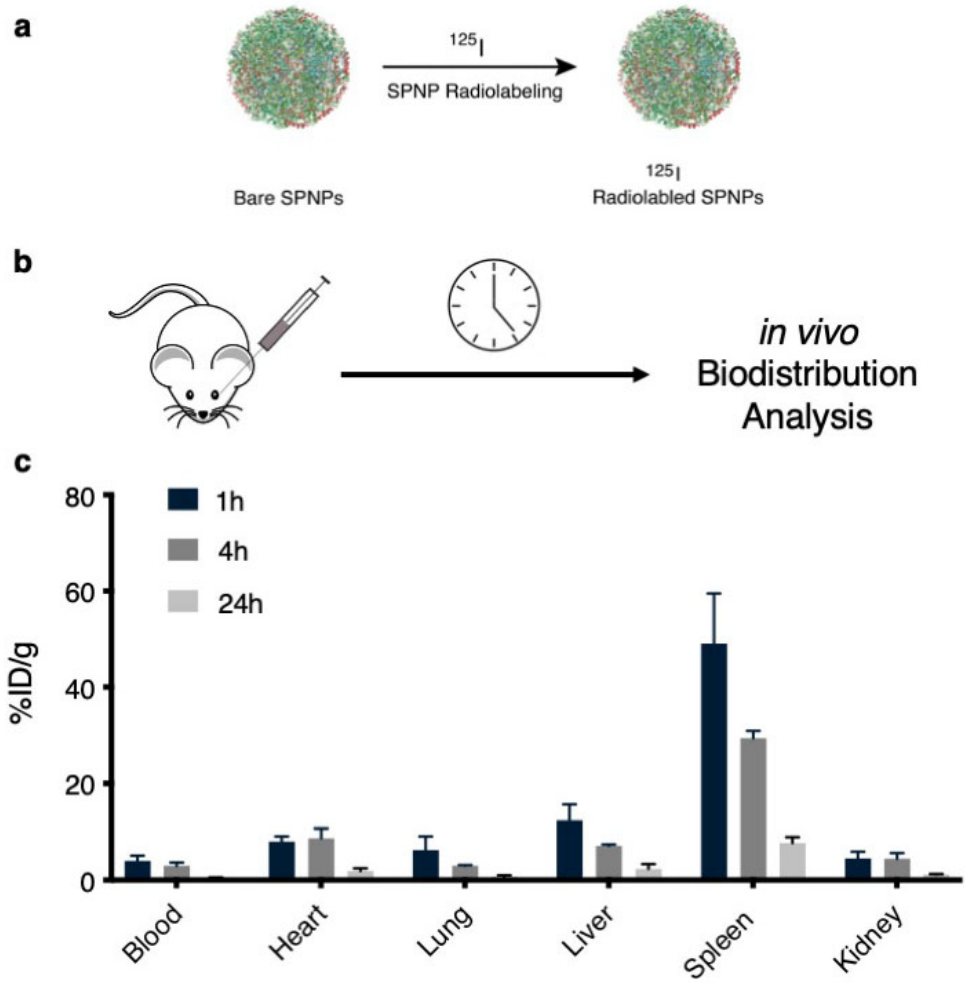

Figure 4.12: **Time course untargeted SPNP biodistribution and clearance. a)** Experimental scheme for the ^{125}I labeling of SPNPs in the absence of targeting via antibody conjugation. **b)** Mice received 100 µL retro-orbital injections of ^{125}I labeled SPNPs. Collection of blood, urine, and organs were completed 1, 4, and 24 h post particle administration to determine a baseline for SPNP biodistribution and clearance. **c)** Evaluated at pre-determined time points following systemic particle administration, ^{125}I radioactive signal was measured via the PerkinElmer Wizard^2 instruments. Biodistribution across measured organs are displayed as percent of injected dose per mass of organ (%ID/g) (n = 3 biological replicates).

ICAM expressing cells. Expressed by lung endothelial cells, and having established a baseline for the biodistribution of untargeted SPNPs, attention was turned towards validating the targeting capacity of antibody surface-decorated particles to the lung. Albumin SPNPs were prepared following an identical approach to that used in previous studies. Following their collection, the two-step method of surface modifying the particles was employed to conjugate DBCO-YN1 antibodies. Subsequent radiolabeling of the particles yielded ^{125}I YN1-SPNPs (Figure 4.13a). As experimental controls, similarly ^{125}I labeled bare and IgG

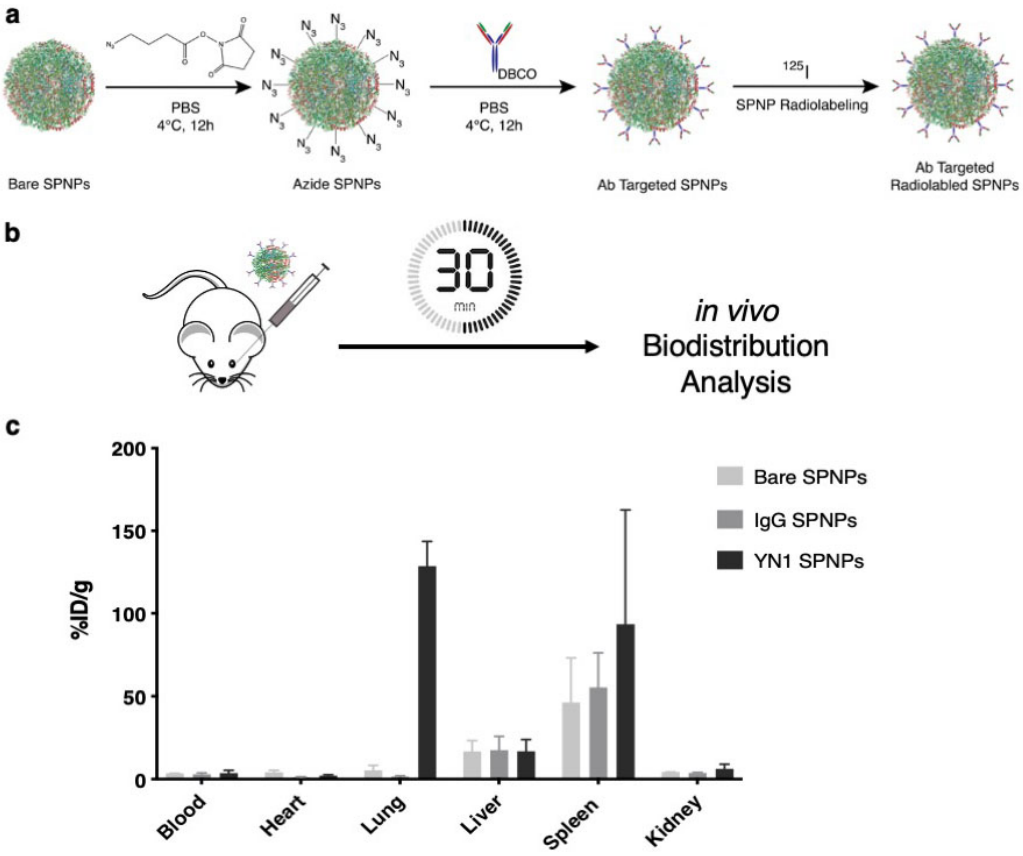

Figure 4.13: **Targeted delivery of Ab-SPNPs to the lung. a)** Experimental scheme for the two-step antibody conjugation and ^{125}I labeling of SPNPs. **b)** Mice received 100 µL retro-orbital injections of either unmodified (bare), untargeted IgG-, or ICAM-targeted YN1-^{125}I labeled SPNPs. Collection of blood, urine, and organs were completed 30 mins post particle administration. **c)** Evaluated at 30 mins following systemic particle administration, ^{125}I radioactive signal was measured via the PerkinElmer Wizard^2 instruments. Biodistribution across measured organs are displayed as percent of injected dose per mass of organ (%ID/g) (n = 3 biological replicates).

modified SPNPs were prepared. Once again, the resulting particles were intravenously injected in anesthetized C57BL/6 mice (Figure 4.13b). According to the previous study indicating that nearly all of the injected dose had been rapidly cleared from circulation, a time point of 30 mins was chosen, at which time, the blood, urine, and organs were collected. Among the untargeted particles, the biodistribution was found to consistent with early time points of the previous study; little particle accumulation was observed outside of the liver and spleen (Figure 4.13c). In contrast, while YN1-SPNPs still provided ample signal in clearance organs, a significant increase in lung accumulation was observed. This increase amounted to approximately a 25-fold increase over bare SPNPs and nearly an 80-fold increase over IgG modified SPNPs (Figure 4.13c).

4.4 Summary

Here, we sought to develop an approach to conjugate targeting moieties to our protein nanoparticle surfaces. Moreover, we aimed to create an method that would be universally applicable to the various protein particle architectures, easily varied to accommodate a range of targeting molecules, and could be adjusted to impart control over the final surface ligand density.

Results presented here demonstrate a well-defined control of resulting antibody targeted nanoparticles. Through the stiochiometric ratio of starting materials, we are able to arrive at specific surface ligand densities. The purification process to isolate the resulting particles from unreacted material or reaction by-products is straightforward, easily scalable, and allows for unreacted antibodies to be readily recovered. Importantly, the approach can be applied to each of our previously developed SPNP variations, and adapted easily to selectively modify distinct regions of multicompartmental nanoparticles.

Validation of the antibody-targeted particles included both *in vitro* and *in vivo* experiments. When incubated at short time periods with cells both expressing (REN-ICAM) and lacking (REN-WT) receptors for our chosen antibody (YN1, anti-ICAM), we observed significant differences in the relative cellular binding and uptake of the particles. Encapsulating and releasing a siRNA against GFP, we were able to achieve a selective intracellular knockdown in GFP-expressing REN-ICAM cells with a dose dependent response. When moving to *in vivo* biodistribution studies, the addition of the YN1 antibody yielded a targeted delivery of protein nanoparticles to the lung, an organ wherein endothelial cells have been shown to highly express the ICAM target. Finally, we observe a rapid clearance of the targeted particles from all organs over a 24 h period following systemic administration. Together, these results suggest a highly controllable means to actively target protein nanoparticles to an organ or tissue of interest, along with an ability to selectively delivery encapsulated therapeutics.

CHAPTER 5

Controlled Release of siRNA from Synthetic Protein Nanoparticles

This chapter contains portions of text/data originally published as:

Systemic Brain Tumor Delivery of Synthetic Protein Nanoparticles for Glioblastoma Therapy
JV Gregory*, P Kadiyala*, R Doherty, MA Cadena, S Habeel, E Ruoslahti, PR Lowenstein, MG Castro, and J Lahann
Nature Communications (2020)

Targeting gliomas with STAT3-silencing nanoparticles
P Kadiyala*, JV Gregory*, PR Lowenstein, J Lahann, and MG Castro
Molecular and Cellular Oncology (2021)

*Shared co-first authorship.

Individual contributions to this collaborative work included the design, synthesis, and characterization of an albumin-based delivery system for STAT3 siRNA. Additional work focused on validating particle stability, characterizing iRGD-mediated cellular uptake, the controlled release of siRNA, and both *in vitro* and *in vivo* protein expression in response to treatment. The design and large-scale production of STAT3*i* SPNPs facilitated numerous *in vivo* studies to evaluate survival, tumor regression, immune response, and anti-GBM immunity when tested in a highly aggressive mouse GBM model.

5.1 Motivation

Glioblastoma (GBM) is the most prevalent and aggressive form of brain cancer, currently accounting for approximately 47% of diagnosed brain cancers. [198] GBM is characterized by its high invasiveness, poor clinical prognosis, high mortality rates and frequent recurrence. [199] Current therapeutic approaches include focal radiotherapy, and adjuvant chemotherapeutics in combination with surgical resection. However, due to the delicate anatomical structure of the brain and the highly invasive nature of glioma cells, complete surgical resection is rarely achieved. [200] Residual tumor cells infiltrate the surrounding brain tissue and are protected by the blood-brain barrier (BBB), rendering them unresponsive to conventional chemotherapeutic drugs. [201] Despite recent surgical and chemotherapeutic advances, the median survival (MS) for patients diagnosed with GBM remains just 12-15 months with a 5-year survival rate of 5%. The development of alternative and targeted delivery approaches to effectively treat GBM remains one of the most pressing challenges in cancer therapy. [202]

A growing body of evidence suggests that the Signal Transducer and Activator of Transcription 3 (STAT3) pathway is involved in multiple signaling pathways related to tumor progression and evasion of the immune system. [11, 203, 204] Multiple growth factors and cytokines frequently overexpressed in cancer, such as EGF, FGF and IL-6, activate STAT3 via tyrosine phosphorylation. [205–207] Activated STAT3 (pSTAT3) translocates to the nucleus and participates in the transcription of genes that inhibit apoptosis, and promote tumor cell proliferation and metastasis (Figure 5.1). Histopathological analysis of brain tumors demonstrated STAT3 to be overexpressed in patients with grade III astrocytomas and grade IV GBMs; increased STAT3 levels are negatively associated with MS in these patients. [204] In previous studies, the STAT3 inhibitor CPA-7 induced tumor cell death in GL26 mouse GBM and HF2303 human GBM stem cells. [11] However, a positive therapeutic effect was only observed in peripheral tumors, but not in intracranial tumors, pointing towards the inability of CPA-7, like many small molecule therapeutics and biomolecules, to cross the protective BBB and enter the brain tumor compartment (Figure 5.2).

A wide range of nanoparticles (NPs) have been developed to deliver chemotherapeutic drugs, such as docetaxel, [207–209] paclitaxel, [210–212] doxorubicin, [213] or other small molecule chemotherapeutics; [214–218] or, to leverage antibodies, [219, 220] RNA, [221–224] or peptides [225] in an attempt to enhance GBM therapy. Despite these grand efforts, research conducted over the past decades has made only marginal advances with

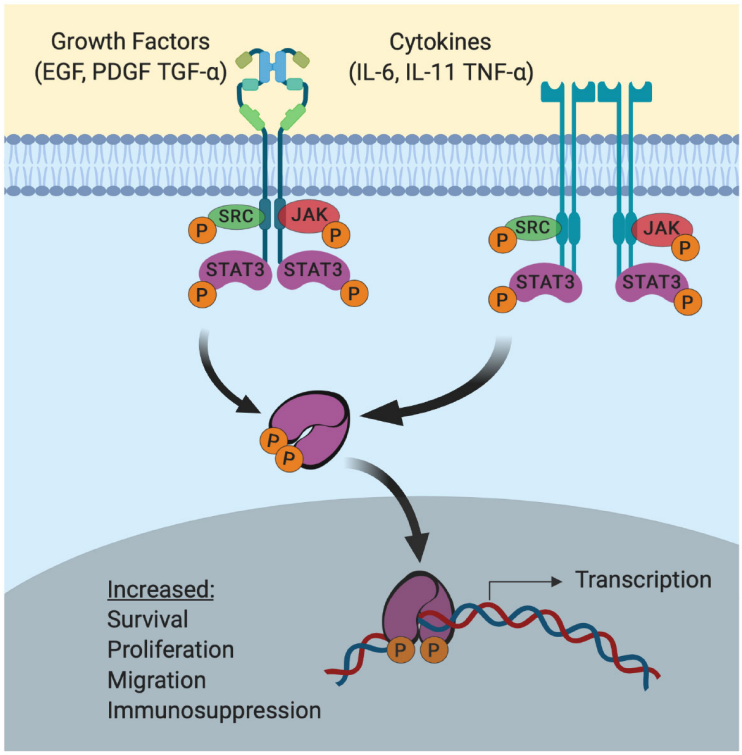

Figure 5.1: **Effects of STAT3 activation in glioblastoma.** Activation of STAT3 via tyrosine phosphorylation triggers dimerization and ultimately translocation to the nucleus. Activation of key genes follows, leading to inhibition of apoptosis, increased proliferation and migration, and enhances stem-like properties. Implications in STAT3 activation also include a developed resistance to radiation and is associated with poor patient prognosis.

no real promise of a clinical path towards a viable curative treatment. In general, these nanocarriers share a number of common characteristics, e.g., (i) they are made of synthetic materials, (ii) they tend to accumulate and persist in liver and spleen causing severe side effects, and (iii) they are incapable of passing the BBB. In contrast, natural evolution has resulted in proteins and viral particulates that can target to and transport through the BBB. [226] Inspired by the unique capabilities of biological NPs, we engineered a GBM-targeting synthetic protein nanoparticle (SPNP) comprised of polymerized human serum albumin (HSA) and oligo(ethylene glycol) (OEG), loaded with the cell-penetrating peptide iRGD [227–229] as well as STAT3 siRNA (STAT3*i*). The choice of HSA as the major matrix component was motivated by its rapid and well-understood clearance mechanisms, its demonstrated clinical relevance, and its exquisite biochemical compatibility with both, therapeutic agents and homing peptides. In addition, albumin-based nanocarriers have been shown to engage cell-surface receptors, such as SPARC [230] and gp60, [231] that are over-expressed on glioma cells and tumor vessel endothelium. [232–234]

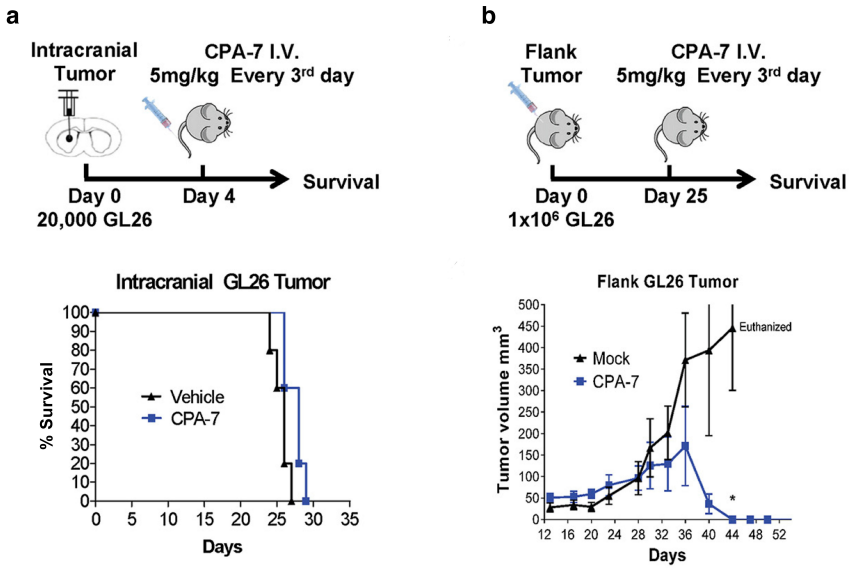

Figure 5.2: **Therapeutic efficacy of CPA-7 in peripheral subcutaneous tumors and intracranial brain tumors. a)** Twenty thousand GL26 cells were implanted in the striatum of C57BL/6J mice. Mice bearing brain tumors were treated 4 days later with CPA-7 intravenously with no discernible therapeutic effect as seen in the Kaplan-Meier curve (n = 4; 5 mg kg^{-1} every 3 days for 15 days). **b)** C57BL/6J mice were injected with 1.0 x 10^6 GL26 cells in the hind flank to generate subcutaneous tumors. Mice bearing flank tumors were treated with CPA-7 (n = 5; 5 mg kg^{-1} every three days for 15 days) when tumors reached an approximate volume of 3060 mm^3. Plotted values represent the means of tumor volumes $\pm$ S.E.M. (*p $<$ 0.05). Adapted with permission. Ref [11]

5.2 Experimental Methods

5.2.1 Materials

Cells: GL26-WT, GL26-Cit were graciously provided by our collaborators, Dr. Maria G. Castro and Dr. Pedro R. Lowenstein.

Cell culture: Dulbecco's modified eagle medium (DMEM), heat-inactivated fetal bovine serum (FBS), Penstrep (10,000 U mL^{-1}), G418, Trypsin-EDTA (0.05%), DPBS

Cell culture media: Dulbecco's modified eagle medium (DMEM), heat-inactivated fetal bovine serum (FBS), Penstrep (10,000 U mL^{-1}), G418, Trypsin-EDTA (0.05%), DPBS

Reagents: Human serum albumin, O,O-Bis[2-(N-Succinimidyl-succinylamino) ethyl] poly ethylene glycol (NHS-PEG-NHS, 2 kDa), polyethyleneimine (PEI), sodium sulfate, sodium chloride, dimethylsulfoxide(DMSO), dimethylformamide (DMF), Tween 20, and phosphate buffered saline (PBS) were purchased from Sigma-Aldrich, USA. Tris-HCl buffer, acetonitrile, sodium nitrite, acetone, BCA assay kit, and Protein 660 assay kit were pur-

chased from Fisher Scientific. iRGD was generously provided by our collaborator Professor Erkki Ruoslahti at Sanford-Burnham Medical Research Institute.

5.2.2 Methods

Synthesis of STAT3 siRNA-loaded, iRGD albumin nanoparticles

Albumin NPs were fabricated via the electrohydrodynamic (EHD) jetting process previously established in our group (Figure 5.3). [74, 99, 105] Briefly, for all particle types, human serum albumin (HSA) was dissolved in a cosolvent mixture (80:20 v/v) of ultrapure water and ethylene glycol at a concentration of 7.5 w/v%. A bifunctional OEG (NHS-OEG-NHS, 2kDa) was added at 10 w/w% relative to HSA. When iRGD was incorporated in the NPs, 355 ng per mg of albumin was added directly to the jetting solution. In contrast, when incorporating siRNA into the particles, the siRNA was first complexed with a branched polyethyleneimine (bPEI, 60 kDa) for 30 minutes in ultrapure water and the mixture was then added to the jetting solution resulting in 40 μg and 355 ng (26 pmol) of bPEI and siRNA per mg of protein nanoparticle, respectively. In instances when siRNA was not included (control NPs), an addition of bPEI in ultrapure water was still included. Final jetting solutions were pumped through a syringe equipped with a 26-gauge blunt tip needle at a flowrate of 0.1 mL h^{-1} while a constant voltage (ranging from 7.5 to 9.0 kV) was applied to form a stable Taylor cone at the needle tip. Particles were collected in aluminum pans at a needle to collector distance of 15 cm and then incubated for seven days at 37°C to facilitate complete polymerization. Albumin SPNPs were then stored in dark RT conditions in their dry state for future experiments.

Collection and purification of albumin nanoparticles

Albumin NPs were collected according to a standard protocol developed in our lab. In brief, a small volume, 5-10 mL, of water:ethanol (80:20 v/v) + 0.5% Tween 20, was added to the aluminum pans containing EHD jetted SPNPs. The resulting NP suspension was gently sonicated to disperse any aggregates and passed through a 40 μm cell straining filter. The resulting solution was centrifuged at 4,000 rpm (3,220 xg) for 4 minutes to pellet and remove any albumin aggregates larger than 1 μm in diameter. The supernatant was then divided into 2 mL Eppendorf tubes and centrifuged at 15,000 rpm (21,500 xg) to concentrate the samples to a single 1 mL sample for use in planned experiments. Collected SPNPs were used within 1 week of their collection and were stored at 4°C during that time.

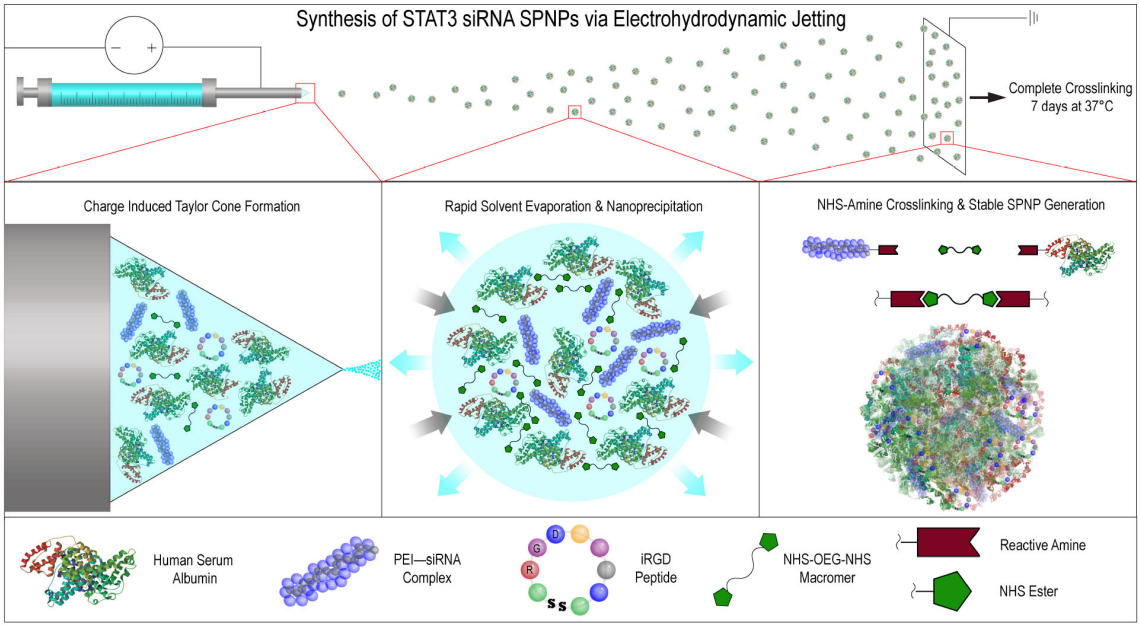

Figure 5.3: **Synthesis of STAT3*i* SPNPs.** Electrohydrodynamic (EHD) jetting uses a dilute solution of all components to be incorporated into the ultimate protein nanoparticle (here: HSA, OEG macromer, STA3i-PEI complex, and iRGD in an aqueous system). Using controlled flow through a single capillary, the application of an electric field distorts the droplet to form a stable Taylor Cone from which a jet of charged droplets emanates. Once atomized, rapid evaporation of the solvent induces nearly instantaneous nanoprecipitation of all non-volatile components to form solid protein nanoparticles. The bifunctional OEG macromer covalently links the protein and PEI units through reactive amine groups, resulting in a continuous network. The STAT3*i* is complexed to the PEI through electrostatic interactions, while the iRGD is encapsulated.

Characterization of albumin SPNPs size, shape, and concentration

Albumin SPNPs were characterized prior to their use in any experiments to ensure they met specifications. Physical characterization included the measurement of particle size in both their dry and hydrated state. To measure particle diameter and investigate their morphology, small silicon wafers were placed on the grounded collection surface and were subjected to the same incubation period to complete the step-growth polymerization. These samples were imaged via SEM using a FEI NOVA 200 SEM/FIB instrument. Obtained SEM images were characterized using ImageJ software. SPNPs in their hydrated state were collected and purified as described above. The stock solution was diluted in PBS + 0.5% Tween 20 for subsequent measurements using DLS and NTA to investigate size and solution concentration. Analysis via DLS and NTA was performed using the Malvern Nano

ZSP and NanoSight NS300 instruments and software, respectively. Albumin NP solution concentration was further validated using the BCA (bicinchoninic acid) assay.

Albumin NP stability and swelling characterization

Albumin SPNPs collected and purified as described above were studied to determine their swelling behavior in response to changes in pH and stability in their hydrated state. SPNPs from the concentrated stock solution were diluted into either a solution of PBS + 0.5% Tween 20 (pH 7.4) or sodium acetate acetic acid buffer + 0.5% Tween 20 (pH 5.0). The final NP solutions were stored at 37°C for a period of 10 days. Particle diameter was measured throughout this period to compare the particle size distribution in response to acidic vs. neutral pH conditions and their overall stability at physiological temperatures.

Loading and release of siRNA from albumin nanoparticles

To validate siRNA loading and characterize its release from the albumin SPNPs, a fluorescently labeled, Silencer^{TM} Cy3-labeled negative control siRNA was incorporated into the NP formulation following the same process as described above. SPNPs were incubated and collected as described above. To validate siRNA incorporation into the particles, a Alexa Fluor 488 BSA conjugate was added at 0.5% of the total albumin mass. Colocalization of the fluorescent albumin NP and siRNA were confirmed using super-resolution stimulated emission depletion (STED) microscopy. Imaging was performed with the University of Michigan Microscopy and Image Analysis Laboratory (MIL) Cores Leica 1x STED instrument and processed using the Leica LAS X software. Release of the same fluorescent siRNA was conducted over a period of four days in PBS + 0.5% Tween 20 at 37°C. The supernatant was analyzed using a Horiba fluorimeter and compared against a previously generated calibration curve.

Cell line and cell culture conditions

GL26, GL26-Cit, and GL26-OVA glioblastoma cells were cultured in Dulbeccos modified eagle (DMEM) media supplemented with 10% fetal bovine serum (FBS), 100 units mL^{-1} penicillin, and 0.3 mg mL^{-1} L-glutamine. For mCitrine and OVA selection, culturing medium was additionally supplemented with 6 μg mL^{-1} G418. Cells were passaged every 2-3 days and were maintained in a humidified incubator at 95% air/5% CO_2 at 37°C.

Immunofluorescence uptake/lysosome colocalization

To study the effect iRGD has on particle fate upon uptake by glioma cells, GL26 cells were cultured as described above in 4-well Nunc Lab-Tek™ chamber slides. Cells were seeded at 50,000 cells per well and allowed to adhere overnight. Twelve hours after initial seeding, media was exchanged. Fresh media contained either iRGD albumin SPNPs or albumin SPNPs (without iRGD), each labeled by incorporating an Alexa Fluor 647 BSA, at a concentration of 13.3 μg mL^{-1}. Thirty minutes after particle administration, the media was removed, cells were washed three times with warm PBS, and fresh NP-free media was then added to each well. Cells were cultured normally for an additional three hours before the cells were washed, fixed and stained. In brief, cells were washed with PBS and fixed in 2% paraformaldehyde in PBS for 15 minutes and then permealized with 0.1% Triton X-100 in PBS for an additional 15 minutes. Cells were then rinsed three times with PBS, and five times with PBS + 0.5% BSA (PBB) and blocked with a one hour incubation in 2% BSA in PBS. Following a rinse with fresh PBB, cells were incubated with primary antibody for LAMP-1, a lysosomal marker, at 5 μg mL^{-1} in a PBB solution at room temperature for one hour. After five rinses with fresh PBB, a mixture of Goat Anti-Rabbit IgG H&L Alexa Fluor 555 and Phalloidin Alexa Fluor 488, prepared in PBB was added and incubated for one hour at room temperature. Each well was rinsed five times with PBB, incubated for one minute with Hoescht at 10 μg mL^{-1} in DI water, and washed three times with fresh PBS. Finally, the chamber potion of the device was removed, the glass slide allowed to dry and samples were mounted using Prolong Diamond Antifade Mountant to preserve the samples and protect against fluorescent signal bleaching. Once stained and mounted, each sample was imaged using the University of Michigan MIL Nikon A1SI confocal microscope and processed using NIS-Elements AR software. Settings for all samples were optimized and kept consistent from sample to sample. Z-stack images were collected from multiple regions within each well and the resulting three dimensional images were analyzed using an established protocol and the CellProfiler software. Analyzed data was used to calculate the relative number of SPNPs internalized by the cells and the percent of these cells colocalized within the lysosomes.

In vitro albumin SPNP delivered siRNA GFP silencing

As a preliminary experiment, to validate the ability of siRNA delivered via the albumin SPNPs, particles loaded with siRNA against GFP were synthesized as described above. GL26-cit cells were cultured consistent with previously conducted experiments. Twelve hours after initial seeding at 50,000 cells per well in 4-well Nunc Lab-Tek chamber slides,

SPNPs were administered at a concentration of 1.0 x 10^{11} NP mL^{-1}. Cells were incubated with particles for a period of two hours before they were washed three times with PBS and fresh media was added to each well. Cells were then cultured for an additional five days. On each day, one sample from each experimental group was washed, fixed, and stained according to an established protocol. In brief, cells were washed three times with warm PBS and fixed in 3.7% paraformaldehyde solution in PBS for 15 minutes. Finally, cells were washed three times with fresh PBS, dried, and samples were mounted using Prolong Diamond with DAPI Antifade Mountant to both stain the nucleus and preserve the samples. Samples from each experimental group and time point were imaged using the University of Michigan MIL Nikon A1SI confocal microscope and processed with the NIS-Elements AR software. Multiple Z-stacks from each sample were taken, maintaining constant laser settings across all samples. GFP signal, normalized to that of the nucleus, was quantified using ImageJ software.

In vitro STAT3 silencing via albumin SPNP delivered siRNA

To validate the ability of STAT3 siRNA delivered via SPNPs, particles loaded with siRNA against STAT3 were synthesized as described above. Twelve hours after initial seeding of GL26 glioma cells at 300,000 cells per well in 6-well cell culture plates, SPNPs were administered at a concentration of 1.0 x 10^{11} NP mL^{-1}. Cells were incubated with particles for a period of two hours before they were washed three times with PBS and fresh media was added to each well. Cells were then cultured for an additional three days with a daily exchange of fresh media. Whole cell extracts were prepared by lysing the cells with RIPA buffer for five minutes on ice, then centrifuged at 10,000 xg for five minutes at 4°C to remove cellular debris. Protein concentration was quantified using the Pierce BCA Protein Assay Kit. STAT3 expression was quantified using the ProteinSimple capillary electrophoresis-based western blot assay and normalized to the expression of GAPDH. Relative protein expression was measured and analyzed using the Compass for SW software.

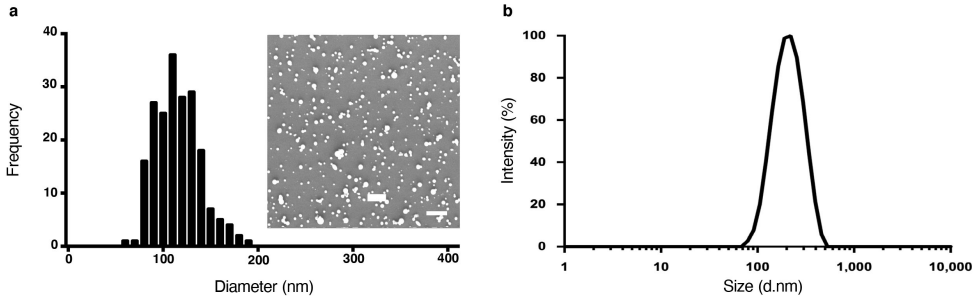

Figure 5.4: **SPNP physical characterization. a)** Particle size characterization and analysis was performed using Scanning Electron Microscopy (SEM). Average particle diameter, 115 $\pm$ 23.4 nm. Scale bar = 1 μm. **b)** Particles undergo swelling in their hydrated state. Average diameter as measured in PBS (pH = 7.4) with DLS, 220 $\pm$ 26.1 nm.

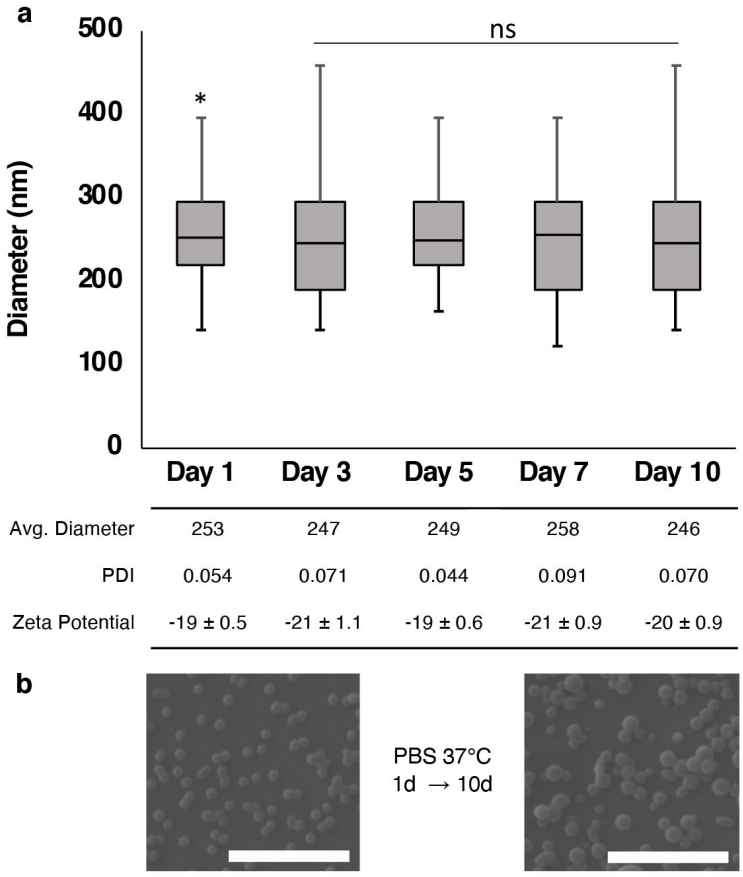

Figure 5.5: **SPNPs remain stable in solution under relevant physiological conditions. a)** After a single day in PBS at 37°C, SPNPs show no significant change in particle size as measured by dynamic light scattering. Particles appear to both remain intact and do not aggregate under these conditions. *$p < 0.05$ **b)** No change in particle shape or morphology is observed following the incubation at physiological conditions as imaged by scanning electron microscopy. Scale bars = 2 μm.

5.3 Results and Discussion

5.3.1 SPNP design, synthesis and characterization

SPNPs were prepared via electrohydrodynamic (EHD) jetting, a process that utilizes atomization of dilute solutions of polymers to produce well-defined SPNPs. [8,75] Rapid acceleration of a viscoelastic jet in an electric field leads to a size reduction by several orders of magnitude facilitating rapid solvent evaporation and solidification of the non-volatile components into SPNPs (Figure 5.3). Here, the jetting solution was comprised of human serum albumin and a bifunctional OEG macromer (NHS-OEG-NHS, 2kDa), which were mixed with various additional components, such as a therapeutic siRNA, polyethyleneimine (PEI, a siRNA complexing agent), and the tissue penetrating peptide, iRGD, prior to nanoparticle preparation. Similar to a step-growth polymerization, the OEG macromer combined with albumin molecules through reaction with its lysine residues resulting in water-stable SPNPs. After EHD jetting and collection, the resulting SPNPs had an average diameter of 115 ± 23 nm in their dry state (Figure 5.4a). Once fully hydrated, the average diameter of SPNPs increased to 220 ± 26 nm based on DLS measurements (Figure 5.4b). The degree of nanoparticle swelling was controlled by varying the HSA-to-OEG ratios between 4:1 and 20:1 and the molecular weight of the OEG macromer between 1 kDa and 20 kDa. An increase of the OEG content from 5% to 20% resulted in a reduction of particle swelling by 20 volume %. SPNPs were stable for at least 10 days at 37°C under physiological conditions; with no significant change in particle size or morphology (Figure 5.5). When exposed to mildly acidic conditions (pH 5.0), similar to those observed in endosomes of cancer cells, the diameters of SPNPs increased to 396 ± 31 nm. We note that defining particle properties, such as particle size, shape and swelling behavior, was, within the margins of error, identical for fully loaded SPNPs, empty SPNPs and SPNPs loaded with siRNA and/or iRGD.

5.3.2 SPNP targeting

Previously, co-delivery of the cell-penetrating peptide iRGD has increased tumor targeting for both, small drugs and iron oxide NPs. The iRGD peptide has been shown to act in a three-stage process, first binding to $\alpha v\beta 3$ and $\alpha v\beta 5$ integrins, followed by a proteolytic cleavage step and a secondary binding event to neurophilin-1 (NRP-1), which activates an endocytotic/exocytotic transport pathway (Figure 5.6). [235] In the past, iRGD mediated

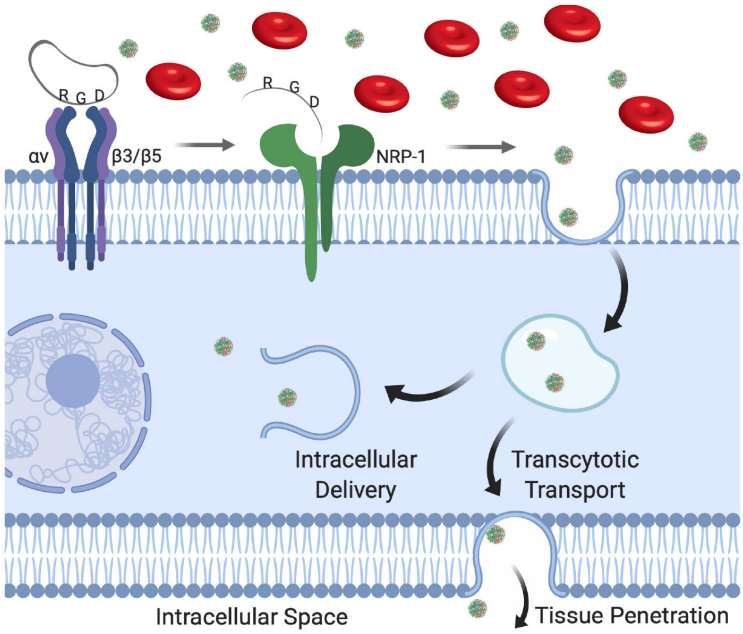

Figure 5.6: **iRGD transcytotic transport.** The cyclic tumor-targeting, tissue penetrating peptide, iRGD has been demonstrated to act in a three-step process promoting transcytosis. i) RGD peptide sequence binding to αvβ3 and αvβ5 integrins; ii) proteolytic cleavage exposing the CendR binding motif; and iii) transcytosis transport initiated following CendR binding to NRP-1.

tumor homing has been approached either in the form of systemic co-delivery of iRGD with NPs [236, 237] or by decorating the NPs with surface-bound iRGD. [238, 239] In our case, the iRGD peptide is preloaded into SPNPs during EHD jetting to promote local release at the vicinity of the BBB. To investigate the intracellular fate of SPNPs and the effect of iRGD as a targeting ligand, *in vitro* uptake experiments were performed. When iRGD-loaded SPNPs were incubated with GL26 glioma cells for a period of 30 minutes, particle uptake increased by ∼5-fold compared to SPNPs without iRGD (Figure 5.7). Image analysis of 3D confocal images (Figure 5.7a) using CellProfiler revealed that significantly less particles colocalized with lysosomes of GL26 glioma cells compared to SPNPs without iRGD (Figure 5.7c). These data suggest that loading iRGD into SPNPs results in higher uptake and higher cytosolic nanoparticle concentrations. The pH-dependent swelling of SPNPs, along with the proton sponge effect previously postulated for PEI, [39] may contribute to more effective particle escape from endocytotic vesicles, enhancing overall siRNA delivery to the cytosol and RNA-induced silencing. [240, 241] We note however, that the concentration of PEI in SPNPs is about 200-fold lower than what has previously been reported to be harmful to cells. [242]

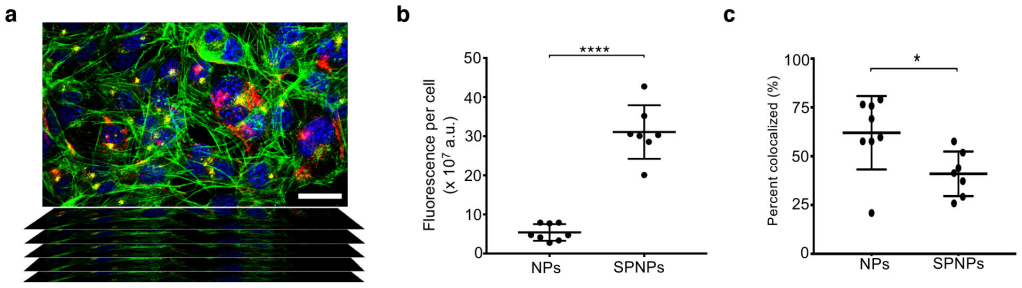

Figure 5.7: **SPNP cellular uptake and lysosome colocalization in GL26 glioma cells.** **a)** Representative confocal z-stack image of cells seeded in the presence of SPNPs **b)** Local release of iRGD from SPNPs increases particle uptake in GL26 glioma cells by greater than five-fold. **c)** Internalized SPNPs colocalize with lysosomes to a lesser extent than untargeted particles.

5.3.3 SPNP siRNA release and specific activity

We next evaluated, if siRNA loaded into SPNPs during EHD jetting remains biologically active. First, siRNA loading and release from SPNPs was evaluated using a Cy3-labeled STAT3*i* surrogate. Utilizing STED microscopy, we confirmed uniform distribution of siRNA throughout the entire NP volume (Figure 5.8a). In vitro release of fluorescently tagged siRNA confirmed that 96% of the initial amount of siRNA was encapsulated into SPNPs; corresponding to a siRNA loading of 340 ng, or 25 pmol of siRNA per mg of SPNPs. Furthermore, we observed that approximately 60% of the encapsulated siRNA was released over the first 96 hours, followed by a sustained release period progressing for 21 days (Figure 5.8b). When albumin SPNPs were loaded with siRNA against GFP, SPNPs significantly suppressed GFP expression in mouse glioma cells transfected to express mCitrine (Figure 5.9) relative to control albumin SPNPs loaded with scrambled siRNA or free GFP siRNA that was delivered using lipofectamine as the transfection agent. Moreover, protein knockdown persisted significantly longer in the SPNP group than in lipofectamine-transfected cells (Figure 5.9e). While the latter entered a recovery phase after two days and nearly returned to normal GFP levels by day five, cells treated with GFPi SPNPs showed sustained protein knockdown throughout the experiment. There were no significant differences in particle size, surface charge, or morphology between siRNA-loaded SPNPs and the control particles (Figure 5.10).

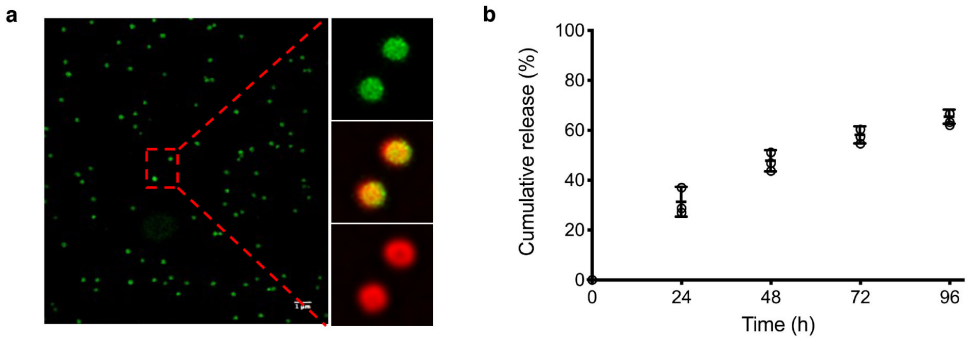

Figure 5.8: **SPNPs loaded with Cy3-siRNA exhibit controlled siRNA release.**
a) Alexa Fluor 488 (green) labeled SPNPs loaded with a fluorescently (Cy3, red) labeled, scrambled siRNA. Imaging was performed using super-resolution, Stimulation Emission Depletion (STED) microscopy, which confirmed the localization of siRNA within the particles. Scale bar = 1 µm. **b)** Loading and subsequent release of Cy3-labeled scrambled siRNA demonstrates a controlled and extended release of incorporated NP cargo. While 60% of the initially encapsulated siRNA is released in the first 96 h at pH 7.4 and 37°C, continued release is observed for up to 21 days. Complete release confirms a loading efficiency of 96%.

5.3.4 STAT3 silencing in GL26 glioma cells

For particle concentrations of 2.5 and 25 µg mL^{-1}, SPNPs co-loaded with iRGD and STAT3*i* significantly reduced total STAT3 protein expression relative to the untreated control group or empty SPNPs (Figure 5.11). Moreover, we observed a dose-dependent response in that a higher particle concentration resulted in ∼2-fold further decrease in total STAT3 expression. No detectable signs of cytotoxicity were observed for any of the tested NP groups, which we attributed to the fact that the delivered siRNA concentrations were below the cytotoxicity limit observed for free STAT3 siRNA in GL26 cells (Figure 5.12). Based on these in vitro experiments, we chose an effective dose of 5 µg kg^{-1} in subsequent animal studies.

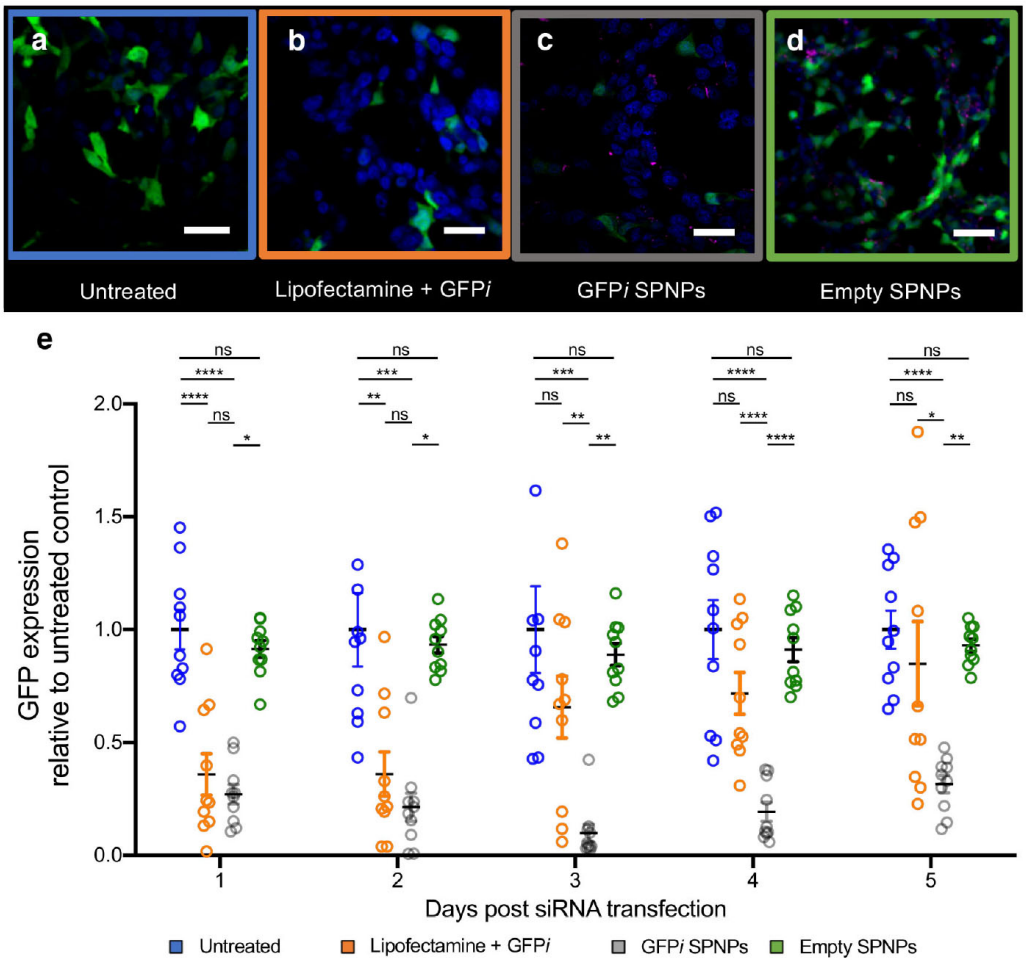

Figure 5.9: **in vitro GFP siRNA-loaded SPNPs selectively reduce protein expression. a-d)** Representative Confocal Scanning Laser Microscopy (CSLM) images of GL26-Cit cells incubated with SPNPs at 48 h time point. (a) Control group receiving no treatment. (b) Positive control group transfected with GFP siRNA (GFP*i*) using Lipofectamine 2000. (c) Cells treated with GFP*i* loaded nanoparticles at a concentration of 25 µg SPNPs mL^{-1}. (d) Cells treated with empty albumin nanoparticles. **e)** GFP expression plotted relative to untreated control group over a period of five days. A significant and prolonged suppression of target protein is observed in cells that received the siRNA-loaded nanoparticles. A similar knockdown was observed in cells transfected with free siRNA using Lipofectamine at early time points, but a rapid recovery was observed after 48 h. Bars represent the mean relative to untreated control ± standard error (n = 3). **** $p < 0.0001$, *** $p < 0.0005$, ** $p < 0.005$, * $p < 0.05$; unpaired t-test. Scale bars = 50 µm.

5.4 Summary

In collaboration with Dr. Maria Castro, we sought to leverage our combined expertise to develop a delivery system for the treatment of glioblastoma. Previous work had identified

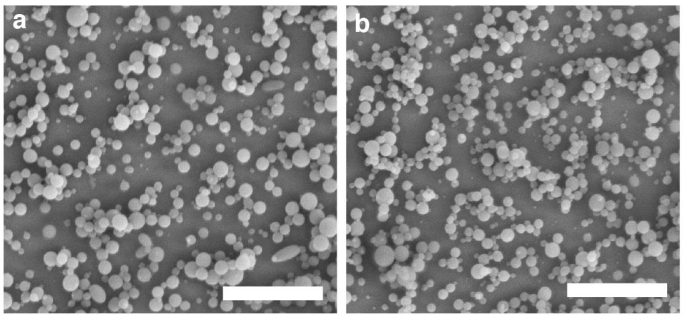

Figure 5.10: **siRNA-loaded SPNPs exhibit similar size to control albumin SPNPs.** The addition of the siRNA/PEI complex to the jetting solution to create **a)** siRNA-loaded SPNPs results in no significant change in particle size, shape or surface morphology when compared to **b)** control (empty) SPNPs. Scale bars = 2 μm.

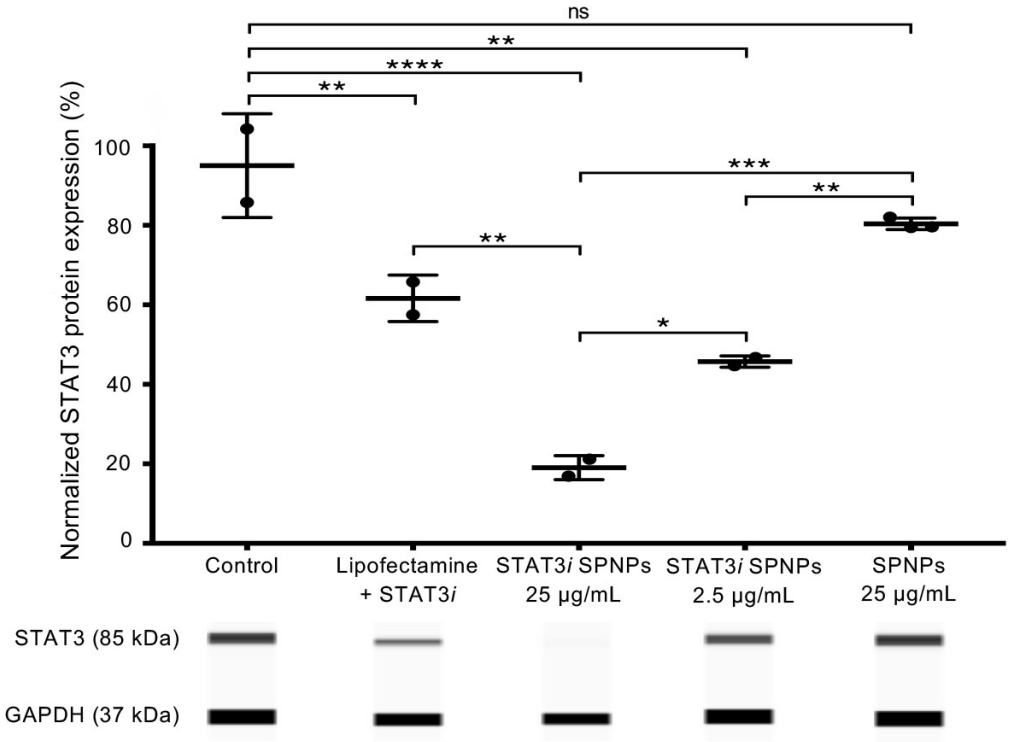

Figure 5.11: ***in vitro* STAT3 knockdown.** STAT3 siRNA-loaded SPNPs significantly reduce in vitro expression of target protein in GL26 glioma cells compared to untreated and empty particle control groups. Bars represent mean ± standard error, (**** $p < 0.0001$, *** $p < 0.0005$, ** $p < 0.005$, * $p < 0.05$, two-way ANOVA test) ($n \geq 3$ wells/treatment group).

STAT3 as a central hub for GBM tumor progression and evasion of the immune system. Additional work in the Ruoslahti lab had characterized iRGD integrin-mediated transport related to $\alpha v\beta 3$ and $\alpha v\beta 5$, each highly expressed in gliomas. Together, with disappointing

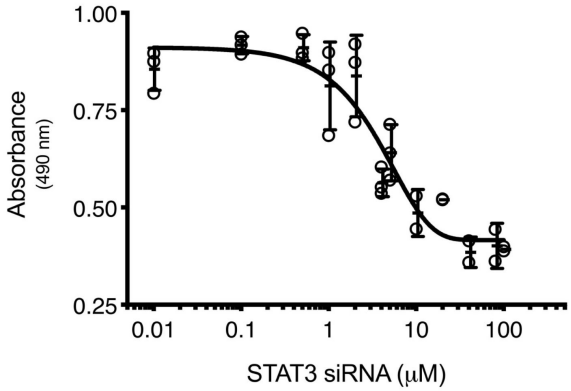

Figure 5.12: **STAT3 siRNA activity is non-toxic towards glioma cells.** Evaluating toxicity associated with free STAT3*i*, no toxicity was observed at relevant therapeutic concentrations. Concentrations delivered via SPNPs showed a significant silencing ability (6.5 x 10^{-4} μM), 6,000x less than the IC_{50} (3.85 μM) for soluble siRNA delivered via traditional transfection methods.

results treating intracranial tumor-bearing mice with small molecule inhibitors of STAT3, we asked whether a nanoparticle delivery system capable of penetrating the BBB could be applied.

Inspired by nature and the capacity of proteins to transport across the BBB, we engineered a protein-based nanoparticle delivery system. Composed of human serum albumin as a bulk material and the cyclic tissue penetrating and tumor targeting peptide, iRGD, we found the particles to be preferentially taken up by GL26 glioma cells. As a proof of concept, we validated the loading and controlled release of surrogate siRNA molecules. Release of siRNA from SPNPs was characterized and *in vitro* assays showed significant and sustained protein silencing in GFP expressing GL26 cells. When loaded with siRNA against STAT3, we again observed significant knockdown of our target protein with a dose dependent response. Encouraged by these results, we proceeded to validate the particle system in a highly aggressive mouse model for GBM. This *in vivo* work is presented in Chapter 6.

CHAPTER 6

Targeted Delivery of STAT3 siRNA to Glioblastoma

This chapter contains portions of text/data originally published as:

Systemic Brain Tumor Delivery of Synthetic Protein Nanoparticles for Glioblastoma Therapy
JV Gregory*, P Kadiyala*, R Doherty, MA Cadena, S Habeel, E Ruoslahti, PR Lowenstein, MG Castro, and J Lahann
Nature Communications (2020)

Targeting gliomas with STAT3-silencing nanoparticles
P Kadiyala*, JV Gregory*, PR Lowenstein, J Lahann, and MG Castro
Molecular and Cellular Oncology (2021)

*Shared co-first authorship.

Individual contributions to this collaborative work included the design, synthesis, and characterization of an albumin-based delivery system for STAT3 siRNA. Additional work focused on validating particle stability, characterizing iRGD-mediated cellular uptake, the controlled release of siRNA, and both *in vitro* and *in vivo* protein expression in response to treatment. The design and large-scale production of STAT3*i* SPNPs facilitated numerous *in vivo* studies to evaluate survival, tumor regression, immune response, and anti-GBM immunity when tested in a highly aggressive mouse GBM model.

6.1 Motivation

Despite research efforts made over the past several decades, GBM remains one of the most aggressive forms of cancer with characteristically high levels of recurrence and low MS rates. [199] While the identification of key biological pathways has yielded promising approaches towards effective therapeutic targets, for the most part, these have ultimately resulted in marginal advances. In the case of STAT3, which is involved in multiple signaling pathways related to GBM tumor progression and immune response, [204] previous studies have demonstrated positive therapeutic effects *in vitro* and in peripheral tumors, but small molecule inhibitors of STAT3 proved to be ineffective in intracranial models of the disease. [11] This can be directly attributed to the inability of therapeutics to penetrate the BBB and reach the tumor in clinically relevant concentrations.

A wide range of experimental approaches have been proposed in recent years to address challenges associated with drug delivery to the brain and are based on either systemic or intracranial delivery strategies. To date, experimental studies that report even modest levels of efficacy in GBM are scarce and almost exclusively require invasive convection-enhanced intracranial delivery. [214, 221] As for systemic delivery, the situation is even more troublesome with only a couple of studies reporting long-term survivors. [208, 225]

Contrary to previous approaches utilizing carriers made from synthetic materials, we took our inspiration from nature and the ability of native proteins and viral particulates to target and get transported across the BBB. HSA, when polymerized, forms water-stable nanoparticles. Previous studies have shown albumin-based nanocarriers to engage cell-surface receptors overexpressed in glioma cells and tumor vessel endothelium, SPARC, [230] and gp60. [231] We observe that the resulting particles undergo pH responsive swelling, suggesting a flexible and dynamic architecture contrary to more rigid synthetic polymer-based nanoparticles. In addition, the amphiphilic protein structure makes it biochemically compatible with small molecule drugs, biological therapeutics (siRNA), and targeting peptides. Together, with promising *in vitro* data demonstrating an ability for STAT3*i* SPNPs to elicit protein-specific silencing in GL26 glioma cells, we sought to evaluate their efficacy in an aggressive intracranial GBM model.

6.2 Experimental Methods

6.2.1 Materials

Cells: GL26-WT, GL26-Cit were graciously provided by our collaborators, Dr. Maria G. Castro and Dr. Pedro R. Lowenstein.
Cell culture: Dulbecco's modified eagle medium (DMEM), heat-inactivated fetal bovine serum (FBS), Penstrep (10,000 U mL^{-1}), G418, Trypsin-EDTA (0.05%), DPBS
Cell culture media: Dulbecco's modified eagle medium (DMEM), heat-inactivated fetal bovine serum (FBS), Penstrep (10,000 U mL^{-1}), G418, Trypsin-EDTA (0.05%), DPBS
Reagents: Human serum albumin, O,O-Bis[2-(N-Succinimidyl-succinylamino) ethyl] poly ethylene glycol (NHS-PEG-NHS, 2 kDa), polyethyleneimine (PEI), sodium sulfate, sodium chloride, dimethylsulfoxide(DMSO), dimethylformamide (DMF), Tween 20, and phosphate buffered saline (PBS) were purchased from Sigma-Aldrich, USA. Tris-HCl buffer, acetonitrile, sodium nitrite, acetone, BCA assay kit, and Protein 660 assay kit were purchased from Fisher Scientific. iRGD was generously provided by our collaborator Professor Erkki Ruoslahti at Sanford-Burnham Medical Research Institute.

6.2.2 Methods

Synthesis of STAT3 siRNA-loaded, iRGD albumin nanoparticles

Albumin SPNPs were fabricated via the electrohydrodynamic (EHD) jetting process previously established in our group (Figure 5.3). [74, 99, 105] Briefly, for all particle types, human serum albumin (HSA) was dissolved in a cosolvent mixture (80:20 v/v) of ultrapure water and ethylene glycol at a concentration of 7.5 w/v%. A bifunctional OEG (NHS-OEG-NHS, 2kDa) was added at 10 w/w% relative to HSA. When iRGD was incorporated in the SPNPs, 355 ng of iRGD per mg of albumin was added directly to the jetting solution. In contrast, when incorporating siRNA into the particles, the siRNA was first complexed with a branched polyethyleneimine (bPEI, 60 kDa) for 30 minutes in ultrapure water and the mixture was then added to the jetting solution resulting in 40 µg and 355 ng (26 pmol) of bPEI and siRNA per mg of protein nanoparticle, respectively. In instances when siRNA was not included (control SPNPs) an addition of bPEI in ultrapure water was still included. Final jetting solutions were pumped through a syringe equipped with a 26-gauge blunt tip needle at a flowrate of 0.1 mL h^{-1} while a constant voltage (ranging from 7.5 to 9.0 kV)

was applied to form a stable Taylor cone at the needle tip. Particles were collected in aluminum pans at a needle to collector distance of 15 cm and then incubated for seven days at 37°C to facilitate complete polymerization. Albumin SPNPs were then stored in dark RT conditions in their dry state for future experiments.

Intracranial GBM models

Six to eight-week-old female C57BL/6 were purchased from Jackson Laboratory (Bar Harbor, ME) and were housed in pathogen free conditions at the University of Michigan. Animals were treated according to the University of Michigan Committee on Use and Care of Animals (IACUC) protocol PRO00007666. Immune-competent mice were housed in a pathogen-free, humidity (40%-60%) and temperature (65-75°F) controlled vivarium on a 12:12 hour light:dark cycle (lights on 0700) with free access to food and water. Intracranial surgeries were performed in 6-8 week old C57BL/6 mice weighing 17-24g in the University of Michigan Unit for Laboratory and Animal Medicine (ULAM). All experimental studies were performed in compliance with Institutional Animal Care & Use Committee (IACUC). Orthotopic tumors were established in C57BL/6 mice by stereotactically injecting 20,000 GL26, GL26-Cit or 60,000 GL26-OVA cells into the right striatum of the brain using a 22-gauge Hamilton syringe (1 μL over 1 minute) with the following coordinates: +1.00 mm anterior, 2.5 mm lateral, and 3.00 mm deep.

Intratumoral diffusion of iRGD-functionalized albumin SPNPs

To assess Albumin SPNPs accumulation within the GBM tumor microenvironment, Alexa Fluor 647 dye was loaded into albumin SPNPs, which were administered intratumorally into GBM bearing mice. Fourteen days post GL26-mTomato tumor implantation, mice (n = 2 per group) were intratumorally injected with 3.6 x 10^8 or 3.6 x 10^9 Alexa Fluor 647 labeled Albumin SPNPs in 3 μL volume. From each group, mice were transcardially perfused 4 h or 24 h after SPNP administration, and brains were processed for imaging. Alexa Fluor 647 labeled albumin SPNP accumulation within the TME was imaged with confocal microscopy (Carl Zeiss: MIC System) at 5x and 20x magnification.

Intravenous iRGD Nanoparticle Delivery

To assess the accumulation of systemically administered iRGD-Albumin SPNPs within the GBM tumor microenvironment, Alexa Fluor 647 dye was loaded into the SPNPs, which were injected i.v. into GBM bearing mice via the tail vein. Seven days post GL26-cit tumor implantation, mice were i.v. injected with 2.0 x 10^{11} SPNPs in 100 μL volume. From each

group, mice were transcardially perfused at 4 h (n = 3 mice) and 24 h (n = 3 mice), and brains were processed for imaging. Accumulation of SPNPs within the tumor microenvironment was imaged with confocal microscopy (Carl Zeiss: MIC System) at 63x with an oil-immersion lens.

Biodistribution of iRGD Nanoparticles Post Systemic Delivery

To evaluate the biodistribution of iRGD-albumin SPNP *in vivo*, SPNPs were loaded with Alexa Fluor 647 dye. C57BL/6 mice bearing GL26 tumors (n = 4) were injected intravenously with 2.0 x 10^{11} Alexa Fluor 647 iRGD-albumin or albumin alone SPNPs in 100 μL volume, 7, 10, and 13 days post tumor implantation. For the control group, tumor naïve mice were injected i.v. with 2.0 x 10^{11} Alexa Fluor 647 iRGD-albumin or albumin alone SPNPs in 100 μL volume. From each group, mice were transcardially perfused 24 h post the last injection of SPNPs (day 14), and vital organs (i.e., lungs, spleen, liver, brain, and kidneys) were harvested. Fluorescent signal within each organ was measured with IVIS spectrum analysis.

To assess the iRGD-Albumin SPNPs accumulation within the GBM tumor microenvironment, SPNPs loaded with Alexa Fluor 647 dye were administered intravenously into GBM bearing mice. Seven days post GL26-cit tumor implantation, 2.0 x 10^{11} SPNPs in 100 μL volume were administered intravenously to mice (n = 4). Mice were then transcardially perfused at either at 4 h (n = 2) or 24 h (n = 2) post the SPNP injection. Brains were collected and processed for imaging. Accumulation of SPNPs within the tumor microenvironment was imaged with confocal microscopy (Carl Zeiss: MIC System) at 63x with an oil-immersion lens.

STAT3 expression following systemic administration of STAT3

To evaluate the ability of STAT3 siRNA loaded SPNPs to reach the tumor *in vivo*, particles loaded with siRNA against STAT3 were synthesized as described above. C57BL/6 mice bearing GL26 tumors (n = 5) were injected intravenously with 2.0 x 10^{11} Alexa Fluor SPNPs, STAT3*i* SPNPs, or free STAT3*i* in 100 μL volume on 5, 7, 11, 15, 18 and 22 days post tumor implantation. For the control group, tumor-bearing mice were injected with an equal volume of saline. Mice from each group were transcardially perfused with Tyrodes solution 24 h post the last injection of SPNPs or saline and brains were extracted. Tumors were dissected from the brain, and single cell suspension was obtained. Whole cell lysates were prepared by incubating the dissociated cells pellet with protease inhibitors and 1.4 mL RIPA lysis buffer on ice for 5 minutes. Resulting cell lysates were centrifuged at 13,000

rpm (25,000 xg) at 4°C for 10 mins and supernatants were collected to determine protein concertation in comparison to standard bovine serum albumin (BSA) protein concentrations through bicinchonicinc acid (BCA) assay. STAT3 and downstream targets protein expression was quantified using the ProteinSimple capillary electrophoresis-based western blot assay and normalized to total protein expression.

Therapeutic study in tumor bearing animals

To evaluate the therapeutic efficacy of iRGD-Albumin SPNPs loaded with STAT3*i*, saline, 2.0 x 10^{11} of empty SPNPs, STAT3*i* SPNPs or an equivalent dose of 330 μg of free STAT3*i* were administered intravenously in 100 μL volume into GL26 tumor bearing mice on 5, 8, 11, 15, 18, 22 and 25 days post tumor implantation. Doses of 2 Gy irradiation (IR) was administered to tumor bearing mice 5 days a week for two weeks beginning at 7 days post tumor implantation. Each treatment group consisted of at least n = 5 mice. When mice displayed signs of neurological deficits, they were transcardiacly perfused with tyrodes solution and 4% paraformaldehyde (PFA).

Blood cell counts and serum biochemistry

Blood from GL26 GBM bearing mice was taken from the submandibular vein and transferred to EDTA coated microtainer tubes (BD Biosciences) or serum separation tubes (Biotang). Samples in the serum separation tubes were left at room temperature for 20 min to allow for blood coagulation before centrifugation at 2,000 rpm (400 xg). Complete blood cell counts and serum chemistry for each sample were determined by *in vivo* animal core at the University of Michigan.

Liver histopathology

Liver tissues from treated animals were collected following the completion of the full STAT3*i* SPNP + IR therapeutic regimen described in Figure 4a. PFA-fixed tissues were embedded, sectioned at 4 μm, and stained with Hematoxylin and Eosin (H&E). Histopathological characterization for each sample was performed by the UM *in vivo* animal core.

Immunohistochemistry

Using the vibratome system, PFA-fixed brains were serially sectioned 50 μm thick and placed in PBS with 0.01% sodium azide. Immunohistochemistry for macrophages was performed by permeabilizing the brain sections with TBS-0.5% Triton-X (TBS-Tx) for 5

min, followed by antigen retrieval at 96°C with 10 mM sodium citrate (pH 6) for 20 min. Then, the sections were allowed to cool to RT and washed 5 times with TBS-Tx (5 min per wash). Next, the brain sections were blocked with 10% goat serum in TBS-Tx for 1 h at RT followed by overnight primary antibody F4/80 (BioRad, MCA497GA, 1:250) incubation at RT. The primary antibody was diluted in 1% goat serum in TBS-Tx. The next day, brain sections were washed with TBS-Tx five times and incubated in fluorescent-dye conjugated secondary antibody (Thermofisher, A21209, 1:1000) diluted in 1% goat serum TBS-Tx in the dark for 6 h. Finally, brain sections were washed in PBS 3 times and mounted onto microspore slides and coverslipped with ProLong Gold. High magnification images at 63x were obtained using confocal microscopy (Carl Zeiss: MIC-System). H&E staining on whole brain sections was performed according to standard H&E staining protocols. Similarly, H&E staining was performed on livers that were embedded in paraffin and sectioned 5 μm thick using the microtome system. Brightfield images of the stains were obtained using Olympus BX53 microscope.

ELISA

To evaluate whether human albumin within the SPNPs is immunogenic, expression of antibodies against human albumin or mouse albumin in the serum of mice treated with saline, free SPNPs, free STAT3*i*, STAT3*i* SPNPs, IR, or STAT3*i* SPNPs + IR was determined using ELISA. Briefly, 96-well plates were coated with SPNPs fabricated with either mouse albumin or human albumin overnight at 4°C. The coated plates were washed the next day with 1X PBS + 0.05% Tween 20 (PBS-Tween) 5 times, and then blocked with PBS-Tween containing 5% goat serum at RT for 2 h. This was followed by 5 more washes with PBS-Tween. Next, mouse serum diluted 1:100 from each treatment group was added to the SPNP coated wells in a 100 μL volume and incubated at 4°C for 24 h. For a positive control, primary antibody against human serum albumin (abcam, ab10241, 1:1000) or mouse serum albumin (abcam, ab34807, 1:1000) was added to the appropriate wells. The next day, the plates were washed five times with PBS-Tween and 100 μL of anti-mouse (Thermofisher, 62-6520, 1:3000) or anti-rabbit (abcam, ab6721, 1:3000) secondary antibody was added to the appropriate plate, followed by 1 h incubation at 37°C. For a negative control, secondary anti-body against human serum albumin or mouse serum albumin was added to the appropriate wells. Plates were then washed 5 times with PBS-Tween. Substrate solution (TMB) was added and the plate was incubated in the dark at RT for 30 min and the reaction was quenched by the addition of 2M Sulfuric Acid. Plates were read on a 96-well plate reader (Spectramax Plus, Molecular Devices) at O.D. 450 nm.

Flow cytometry

Antibodies for flow cytometry analysis were obtained from Biolegend unless indicated otherwise. To assess the immune cell population within the GL26-OVA tumor microenvironment, two days post STAT3*i* alone, empty SPNP, STAT3*i* SPNP or STAT3*i* SPNP + IR treatment detailed above, mice were euthanized and the tumor mass with the brain was dissected and homogenized using Tenbroeck (Corning) homogenizer in DMEM media containing 10% FBS. Tumor infiltrating immune cells were enriched with 30%-70% Percoll (GE Lifesciences) density gradient and the cells were resuspended in PBS containing 2% FBS (flow buffer). Live/dead staining was carried out using fixable viability dye (eBioscience). Non-specific antibody binding was blocked with CD16 / CD32. Dendritic cells were labeled with CD45, CD11c, and B220 antibodies. Plasmacytoid dendritic cells (pDCs) were identified as $CD45^+$ /$CD11c^+$ /$B220^+$ and conventional dendritic (cDCs) cells were identified as $CD45^+$ / $CD11c^+$ / $B220^-$. Macrophages were labeled with CD45, F4/80, and CD206 antibodies. M1 macrophages were identified as $CD45^+$ / $F4/80^+$ / $CD206^{low}$ and M2 macrophages were identified as $CD45^+$ / $F4/80^+$ / $CD206^{high}$. Tumor specific T cells were labeled with CD45, CD3, CD8 and SIINFEKL-$H2K^b$-tetramer. Granzyme B and IFNγ were stained using BD intracellular staining kit following the manufacturers instructions. For T cell functional analysis, purified immune cells from the tumor microenvironment were stimulated with 100 µg mL^{-1} of GL26-OVA lysate for 16 h in DMEM media containing 10% FBS followed by 6 h incubation with Brefeldin and monensin. For integrin $\alpha v\beta 3$ and $\alpha v\beta 5$ analysis, untreated GL26-tumor bearing mice were euthanized at 23 DPI and both tumor bearing hemisphere and the contralateral hemisphere were dissected. Cells were dissociated from both the hemispheres into single cell suspension and CD45 cells were labeled with magnetic beads (Miltenyi) using the manufactures instructions at 4°C. Purified cells were washed and passed through a preconditioned MS column placed in the magnetic field of a MACS separator. Cells that were negative for CD45 were collected, resuspended in flow buffer and labeled with $\alpha v\beta 3$ (Novus, NBP2-67557) and $\alpha v\beta 5$ (BD Bioscience, 565836) for flowcytometry analysis. All stains were carried out for 30 min at 4°C with 3x flow buffer washes between live/dead staining, blocking, surface staining, cell fixation, intracellular staining and data measurement. All flow measurements have been made utilizing with FACSAria flow cytometer (BD Bioscience).

6.3 Results and Discussion

6.3.1 GBM Murine Model

The cell-penetrating peptide iRGD has been shown to increase the accumulation of both small molecule drugs and NP drug delivery systems when co-delivered or conjugated to particle surfaces. [236] Shown to initially bind to $\alpha v\beta 3$ and $\alpha v\beta 5$ integrins, iRGD initiates an endocytotic/exocytotic transport mechanism responsible for its tissue penetrative properties. [235] To provide a rationale for the increased accumulation of SPNPs in the brains of tumor-bearing mice, we searched for integrin-expressing cells in the tumor microenvironment. Specifically, we focused on the relative expression of $\alpha v\beta 3$ and $\alpha v\beta 5$ integrins, because these ligands have been shown to play pivotal roles in the iRGD-induced accumulation of NPs and small drugs in tumors, [227] and have been shown to be overexpressed both in gliomas and their supporting blood vessels. [228] Using the GBM model and a multi-dose schedule beginning at 7 DPI, brains from GBM tumor-bearing mice were collected at 23 DPI. Normal brain and tumor tissue were dissected from the brain, processed, and stained with $\alpha v\beta 3$ and $\alpha v\beta 5$ antibodies for flow cytometry analysis. Here, we observe increased levels of each of these key integrins in GBM tumor-bearing mice (Figure 6.1). More than 60% of the GBM tumor population expressed $\alpha v\beta 3$ and $\alpha v\beta 5$ integrins at high levels, while normal brain tissue showed minimal expression of these proteins (Figure 6.1). These results, along with the observed differences in brain accumulation in the biodistribution study, appear to be consistent with the previously postulated hypothesis that iRGD promotes local brain tumor accumulation. [235]

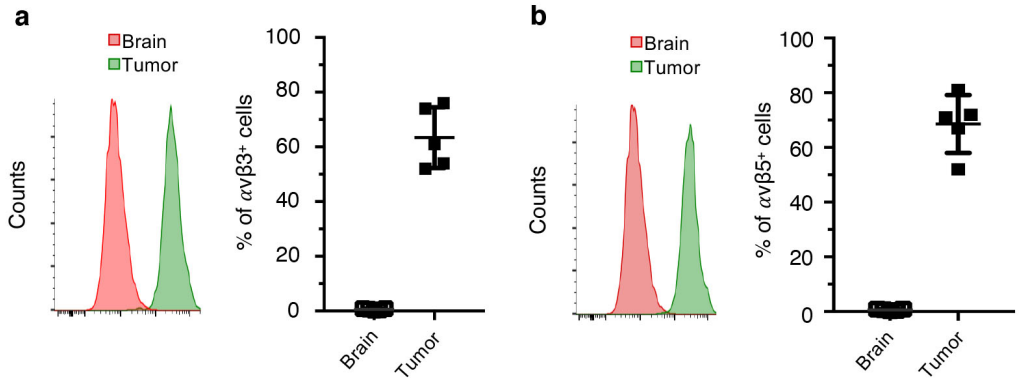

Figure 6.1: **GBM integrin expression in surgically resected GBM samples.** Quantitative flow cytometry results of **a)** $\alpha v\beta 3$ and **b)** $\alpha v\beta 5$ integrin expression in normal brain tissue and GL26 tumors. Data presented as mean values $\pm$ s.d. (n = 5 biological replicates; two-tailed unpaired t-test; **** $p < 0.0001$).

In order to simultaneously evaluate particle stability and diffusion within the TME, Alexa Fluor 647 SPNPs were administered intratumorally. Previous studies had demonstrated that iRGD enhances the penetration of co-delivered therapeutics throughout the tumor volume. This becomes increasingly relevant in GBM where recurrence occurs locally in regions adjacent to the tumor resection cavity. Following intratumoral injection, SPNPs were widely distributed throughout the tumor volume extending from the injection site (Figure 6.2). Furthermore, we observed persistent fluorescent signal associated with SPNPs within the tumor hours after intratumoral administration.

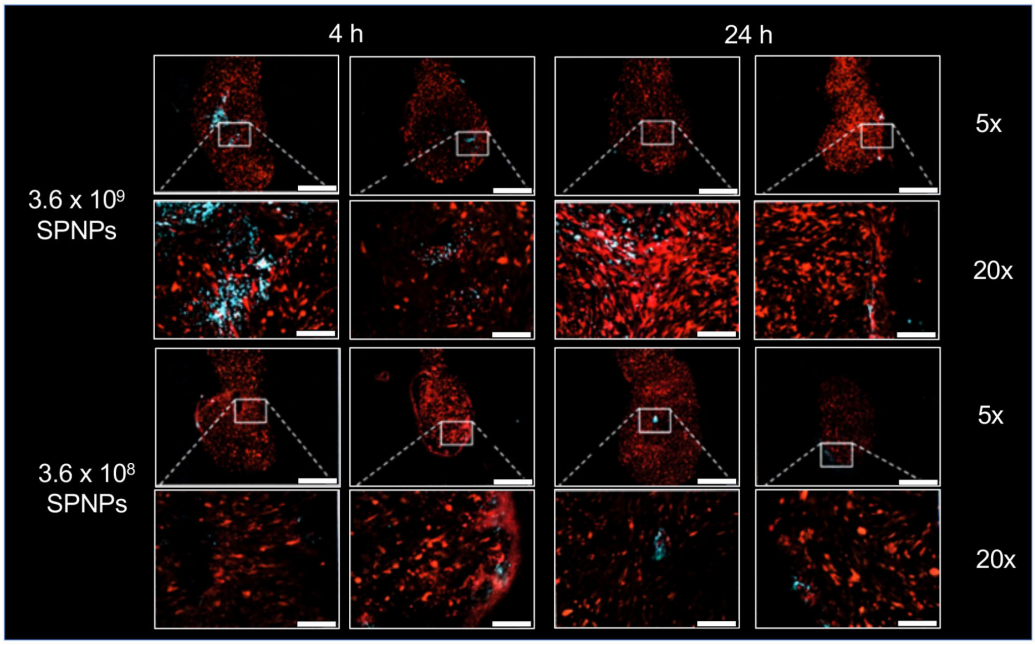

Figure 6.2: **SPNP intracranial tumor transport.** Following the implantation of m-Tomato expressing GL26 tumors (red), C57BL/6 mice received 3 µL intracranial injections of either 3.6 x 10^8 or 3.6 x 10^9 SPNPs (cyan) per mouse. Images suggest that the particles actively and rapidly distribute throughout the tumor mass. Scale bars = 150 µm (5x), 600 µm (20x).

6.3.2 Systemic Delivery of SPNPs

In the past, the BBB has been an unsurmountable delivery challenge for nanocarriers that are systemically administrated via IV injection. [209, 243] To evaluate if systemically delivered SPNPs can home to brain tumors, SPNPs loaded with Alexa Fluor 647-labeled albumin were prepared as described above. In the absence of large animal GBM models, we selected the very aggressive GL26 syngeneic mouse glioma model, which is known to exhibit histopathological characteristics encountered in human GBM, [244] to evaluate

GBM-targeting of SPNPs. In addition, this model features an uncompromised immune system, which was deemed to be essential, because of the prominent role that STAT3 plays in downregulation of the immune system. A dose of 2.0 x 10^{13} SPNPs was delivered to GBM-bearing mice via a single tail vein injection seven days after glioma cell implantation (GL26-Citrine, approximate tumor size: 10 mm^3) in the right striatum of the mice (Figure 6.3). After 4 or 24 h, animals were euthanized, and brains were collected, sectioned, and stained prior to confocal imaging (Figure 6.4a). While the majority of particles were taken up by other organs, such as liver, kidney, spleen and the lungs, a significant number of SPNPs appeared to have crossed the BBB and were identified within the brain tumor microenvironment at both time points (Figure 6.4b). Tumor targeting was markedly increased after 24 h, hinting towards the possibility that secondary transport processes, such as immune-cell-mediated pathways, are contributing to the brain-homing of SPNPs, in addition to the direct targeting of the brain endothelium by circulating SPNPs. The notion of a multivariant transport mechanism is consistent with our finding that SPNPs were localized inside of tumor cells (green) and macrophages (red), suggesting that both cell types can internalize SPNPs (Figure 6.4b).

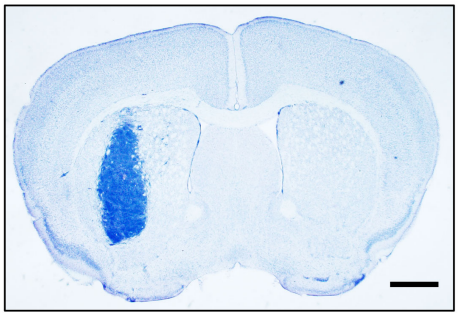

Figure 6.3: **GL26 GBM tumor volume at 7 DPI.** C57BL/6 mice were implanted with 20,000 GL26 cells orthotopically and brains were processed for Nissl staining at 7 DPI. Staining and imaging was conducted as a single independent experiment. Scale bar = 1 mm. Tumor volume = 9.61 mm^3. Tumor area = 107 pixel units.

Using the same intracranial tumor model, GBM specific biodistribution of SPNPs was assessed. Tumor-bearing mice were injected three times (7, 10, and 13 days post implantation, DPI) with Alexa Fluor 647-labeled SPNPs or SPNPs without iRGD (Figure 6.5a). In addition, naïve mice (non-tumor bearing) were subjected to the same regimen to delineate tumor-specific characteristics. After 14 d, naïve and tumor bearing mice were euthanized, their main organs were collected, and the nanoparticle distribution was analyzed via fluorescence imaging (Figure 6.5b). In both GBM-bearing and naïve mice, significantly more targeted SPNPs were observed in the brain compared to NPs without iRGD. As expected,

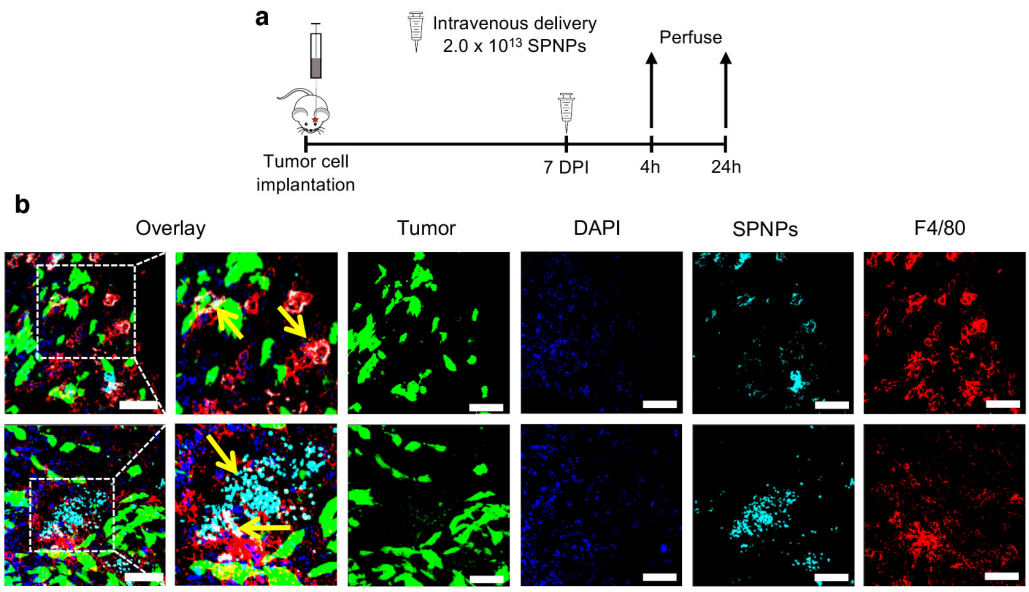

Figure 6.4: **SPNP systemic delivery to GBM. a)** Timeline for the tumor targeting study. Mice were IV administrated a single dose of 2.0 x 10^{13} SPNPs or empty SPNPs (no iRGD) via the tail vein seven days post GL26 tumor cells implantation. Confocal imaging of sectioned brains was performed 4 and 24 h post particle administration. **b)** Alexa Fluor 647 labeled SPNPs (cyan) colocalize (indicated with yellow arrows) with macrophages (red) and tumor cells (green, mCitrine). Notably less SPNPs are observed in the tumor microenvironment 4 h post systemic delivery compared to 24 h. Representative images from a single experiment consisting of three biological replicates per group are displayed. Scale bars = 50 µm

SPNPs also accumulated in the lungs and liver independent of the particular experimental group. The former can be attributed to being the first capillary bed the SPNPs would encounter following intravenous injection, while the latter represents the primary route of clearance for NPs of this size. [245] Brain accumulation of SPNPs loaded with iRGD was higher for both naïve and GBM-bearing mice compared to iRGD-free nanoparticle groups. When directly comparing SPNP localization within the brain compartment, the accumulation of iRGD-loaded SPNPs was 40% higher in tumor-bearing brains than in healthy brains (Figure 6.5c).

6.3.3 *in vivo* Survival Studies

Previous data indicate that the Signal and Transducer of Activation 3 (STAT3) transcription factor is a hub for multiple signaling pathways which mediate tumor progression and immune functions. [11, 246–248] There are currently no effective delivery strategies of

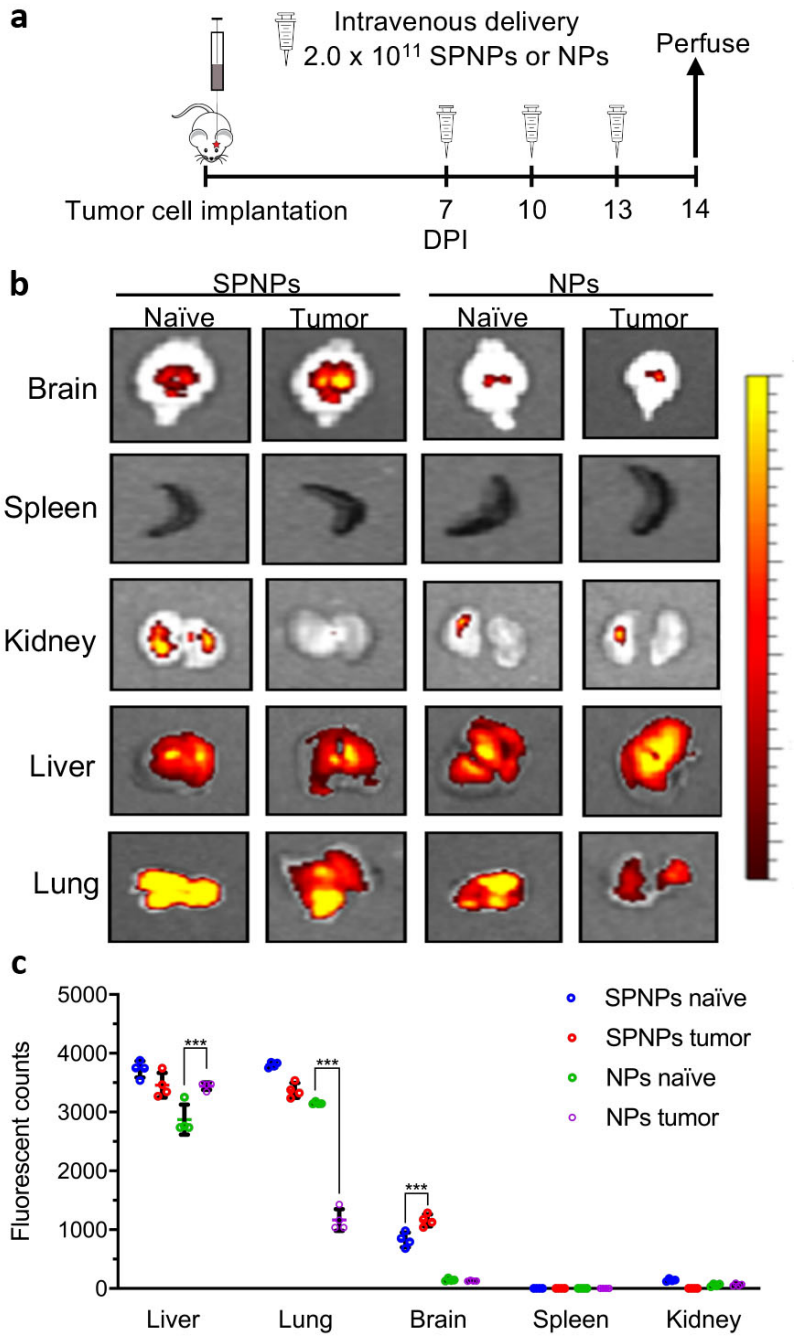

Figure 6.5: **SPNP biodistribution following systemic administration. a)** Timeline representation of the biodistribution study. Mice were IV administered 2.0 x 10^{11} SPNPs or empty SPNPs 7, 10, and 13 days post tumor cell implantation or saline injection. **b)** Fluorescence imaging of tumor-naive and tumor-bearing mice organs sacrificed at 24 h post final SPNP delivery. **c)** Quantitative analysis of SPNP biodistribution within the tumor and peripheral organs. Data are presented as mean values $\pm$ s.d. (n = 4 biological replicates, two way ANOVA; *** p $\pm$ 0.0001).

anti-STAT3 therapeutics to the brain. [11] We observed that systemic delivery of a single dose of STAT3*i* SPNPs to GMB bearing mice showed a significant increased in median survival (MS) (Figure 6.6). To further test the efficacy of SPNPs *in vivo*, GBM-bearing mice were treated intravenously with multiple doses of STAT3*i* SPNPs over the course of a three-week treatment regimen (Figure 6.7a). After tumor implantation, the MS of untreated mice was about 28 days. In mice that received multiple doses of empty SPNPs, the MS remained unaltered (28 days). In contrast, when SPNPs loaded with STAT3*i* were administered, the MS increased to 41 days, a statistically significant increase of 45% (Figure 6.7b). Delivery of the same doses of free STAT3*i* resulted in a modest extension of MS by 5 days, which is likely too low to elicit a significant therapeutic effect. The low efficacy of free STAT3*i* can be explained by the rapid degradation of genetic material following systemic administration in addition to siRNAs inability to cross the BBB. [249]

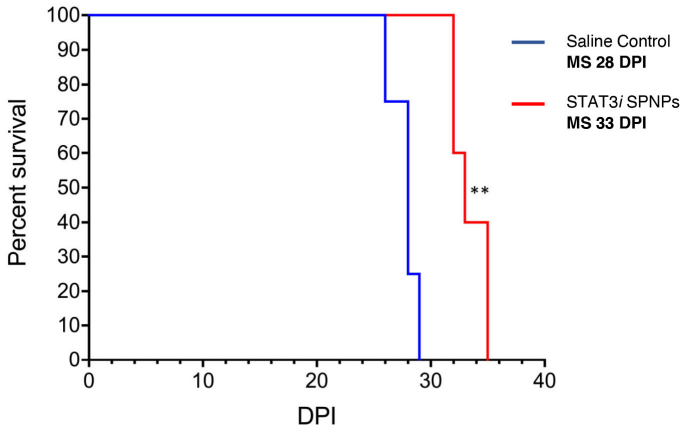

Figure 6.6: **STAT3*i* SPNP single dose.** SPNPs in combination with radiotherapy (IR) results in increased survival and primes an adaptive immune response. **a)** Timeline of treatment for the combined SPNP + IR survival study. **b)** Kaplan-Meier survival curve. Significant increase in median survival is observed in all groups receiving IR. Mice (7/8) treated with STAT3*i* SPNPs + IR reach long-term survival timepoint (100 DPI) with no signs of residual tumor.

Encouraged by the prospect of a nanoparticle formulation for STAT3*i* delivery with significant *in vivo* efficacy, we combined STAT3*i* SPNPs with the current standard of care, i.e., focused radiotherapy (IR). Previous studies have identified a direct correlation between STAT3 overexpression and radioresistance in other cancers, [250, 251] suggesting that its knockdown could contribute to enhanced efficacy. We thus established a treatment protocol that combined the previously evaluated multi-dose regimen with a repetitive, two-week focused radiotherapy regimen. [252, 253] Once GBM tumors had formed, mice received seven doses of STAT3*i* SPNPs over the course of a three-week period. During each of the

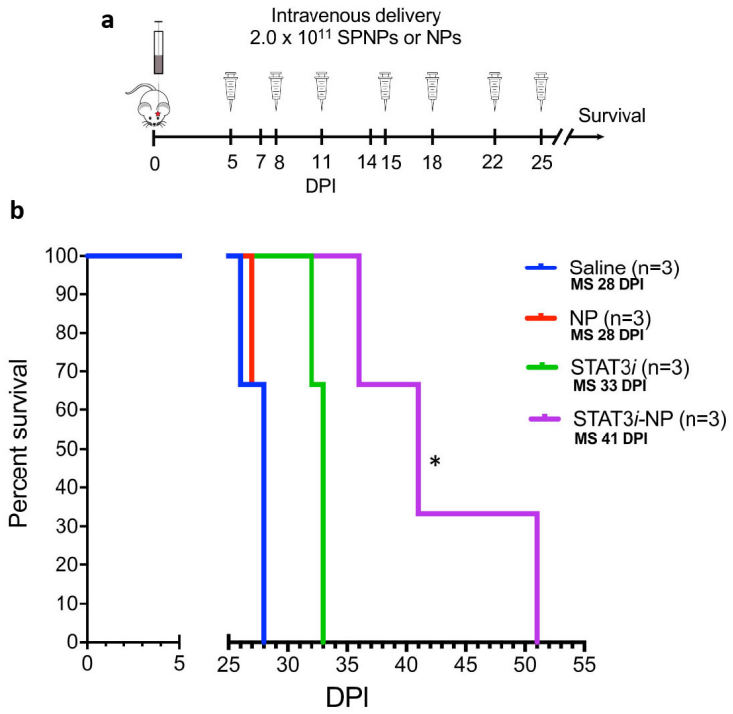

Figure 6.7: **STAT3*i* SPNP multidose survival.** SPNPs in combination with radiotherapy (IR) results in increased survival and primes an adaptive immune response. **a)** Timeline of treatment for the combined SPNP + IR survival study. **b)** Kaplan-Meier survival curve. Significant increase in median survival is observed in all groups receiving IR. Mice (7/8) treated with STAT3*i* SPNPs + IR reach long-term survival timepoint (100 DPI) with no signs of residual tumor.

first two weeks, mice also received five daily 2 Gy doses of IR for a total of ten treatments (Figure 6.8a). Experimental groups included mice that received either STAT3*i* SPNPs, empty SPNPs, free STAT3*i*, or saline with or without combined radiotherapy. In all cases, the addition of radiotherapy increased the MS, with IR alone resulting in a MS extension from 28 to 44 DPI (Figure 6.8b). Combining IR with empty SPNPs did not further alter the MS. Consistent with our previous experiment, free siRNA provided a slight, statistically significant benefit, where the MS was increased to 58 DPI when combined with IR (Figure 6.8b, brown line). However, the most significant effect was observed for the combination of STAT3*i* SPNPs with IR. Of the eight mice in this group, seven reached the standard long-term survivor time point of 90 DPI and appeared to be completely tumor-free thereafter (Figure 6.8b, blue line). The single mouse receiving this treatment that did not reach long-term survival was moribund at 67 DPI, living longer than any other non-surviving subject from all other groups.

In order to characterize the effects of the combined treatments, additional studies were per-

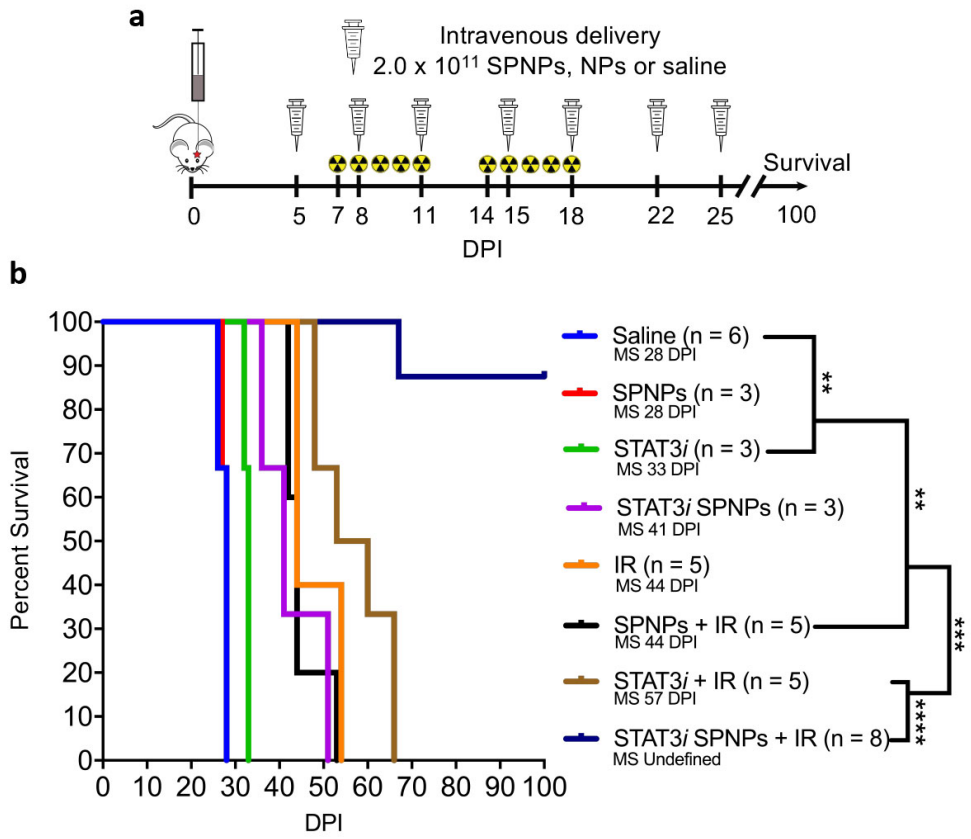

Figure 6.8: **STAT3*i* SPNP + IR survival.** **a)** Timeline of treatment for the combined SPNP + IR survival study. **b)** Kaplan-Meier survival curve. Significant increase in median survival is observed in all groups receiving IR. Mice (7/8) treated with STAT3i SPNPs + IR reach long-term survival timepoint (100 DPI) with no signs of residual tumor. (Log-rank (Mantel-Cox) test; **** $p < 0.0001$, *** $p < 0.001$, ** $p < 0.01$).

formed. Following the same treatment outlined in Figure 6.8a, we elucidated the expression of STAT3 and its active phosphorylated form, pSTAT3, in the brain tissues (Figure 6.9). As expected, the greatest reduction in both the total and phosphorylated form of the protein were found in the STAT3*i* SPNP group. Greater than 50% reduction in total STAT3 protein was observed when compared to the saline treated control. Phosphorylated STAT3 levels were even more dramatically reduced, with a greater than ten-fold reduction in pSTAT3 levels comparing the same groups. In contrast, the total STAT3 levels were relatively unchanged in both, the free STAT3*i* and empty SPNP groups, compared to untreated control. Here, pSTAT3 was increased by 110% in the cohort receiving empty SPNPs, suggesting a shift in the balance of the two protein forms, perhaps due to a localized upregulation of kinase activity.

While previous studies have demonstrated positive therapeutic effects in an *in vitro* setting

and in peripheral tumors when modulating STAT3 expression, small molecule inhibitors of STAT3 have proven to be ineffective in intracranial models of the disease. [11] As previously mentioned, this can be directly attributed to the inability of therapeutics to penetrate the BBB and reach the tumor in clinically relevant concentrations. Results from our study show a similar trend: while we previously observed effective *in vitro* knockdown of STAT3 using free siRNA, this does not translate into reduced protein expression in an intracranial GBM model. As a result, a minimal therapeutic effect is observed in mice treated with free STAT3*i*, alone or in combination with ionizing radiation. It is only when delivered in the form of SPNPs that a significant protein knockdown (Figure 6.9), coupled with a meaningful extension of MS (Figure 6.8) is observed.

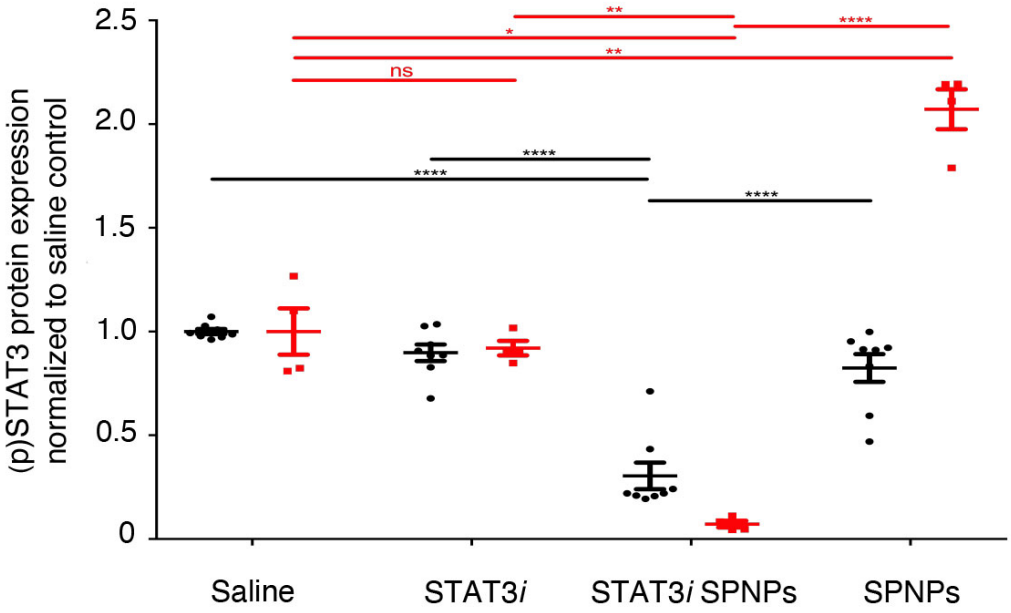

Figure 6.9: **STAT3 and pSTAT3 *in vivo* expression.** Quantified STAT3 expression for resected brains from the survival study, brains were collected when mice displayed signs of neurological deficits. A significant reduction is STAT3 (black) and pSTAT3 (red) expression was observed in the STAT3*i* SPNP cohort relative to untreated control. Both soluble STAT3i and empty SPNPs (with no siRNA) did not have high total STAT3 expression but they had increased levels of active phosphorylated STAT3 expression (pSTAT3). Data are presented as mean values $\pm$ s.d. relative to untreated control (n = 2 biological replicates for each group). Due to minimal biological samples available, three technical replicates were performed on each sample to validate the experimental protocol and rule out measurement error.

6.3.4 Immune Response

Immunohistochemistry (IHC) analysis was used to compare the brains from long-term survivors to other treatment groups. Figure 6.10 shows a direct comparison of the brain of a long-term survivor and that of a control animal that did not receive treatment. H&E staining clearly shows the presence of a fully developed tumor localized within a single hemisphere of the saline treated mice. Conversely, we observed no overt signs of tumor presence in the STAT3*i* SPNP + IR treated survivors (Figure 6.10, top). Moreover, no apparent regions of necrosis, palisades or hemorrhages were present in these animals 90 DPI after receiving a full course of therapy. Myelin basic protein (MBP) staining was performed to assess the integrity of myelin sheaths, an indicator for the disruption of surrounding brain architecture. No apparent changes in myelin sheath morphology was observed in mice that received the combined STAT3*i* SPNP + IR treatment when compared to the cancer-free right faces of mice in the saline treated control group (Figure 6.10, bottom). In addition, CD8 T cells were sparse in the TME (Figure 6.11a) and their total number was significantly reduced in STAT3*i* SPNP + IR treated mice compared to the saline treated control group (Figure 6.11b) - indicating a lack of inflammation response due to the treatment.

To further investigate the potential role of the adaptive immune system, we more closely examined the population of CD8 T cells within the TME via flow cytometry. We established tumors in mice using GBM cells that harbored a surrogate tumor antigen ovalbumin (OVA) and compared the responses elicited by the various treatment formulations (Figure 6.12a). The OVA-based GBM model was utilized to assess the frequency of tumor antigen specific T cells within the GBM microenvironment, due to the availability of OVA-specific MHC tetramers. Tumor specific T cells were characterized by staining for the SIINFEKL-H2K^{b}-OVA tetramer, an OVA cognate antigen within the CD8 T cell population. Tumor specific CD8 T cells (CD3^{+} / CD8^{+} / SIINFEKL H2K^{b} tetramer) within the STAT3*i* SPNP + IR group were increased by two-fold compared to all other groups (Figure 6.12b, top). Staining the same population of cells with interferon-γ (IFN-γ) (Figure 6.12b, middle) and granzyme B (GZB) (Figure 6.12b, bottom) revealed a two-fold increase in cytotoxic T cells in the TME in the STAT3*i* SPNP + IR group relative to all other groups. Taken together with the increased MS of GL26 GBM mice in the survival study, these results suggest a robust anti-GBM response elicited by the combined STAT3*i* SPNP + IR therapy that is likely contributing to the observed therapeutic success.

Recognizing that significant SPNPs accumulated in the liver (Figure 6.5b), complete blood cell counts, serum biochemistry and liver histopathological analysis were performed to

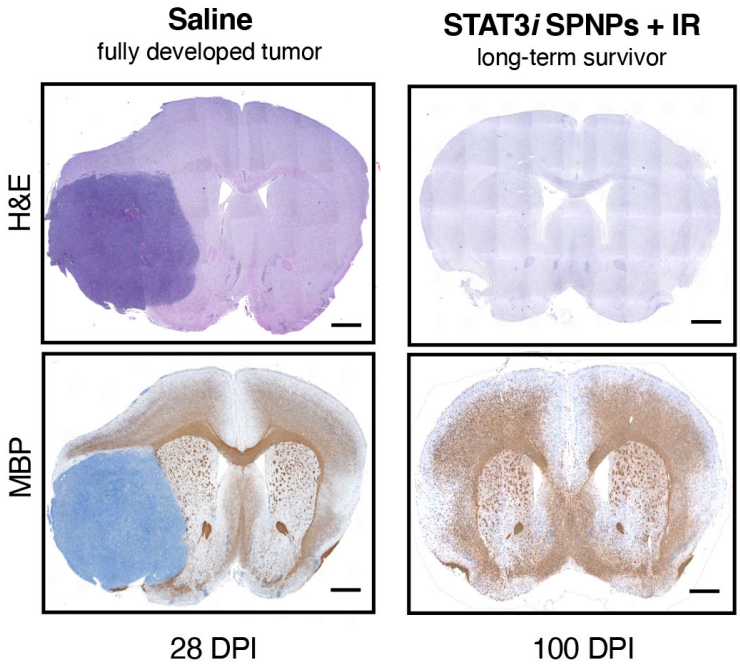

Figure 6.10: **GBM histology saline vs combined therapy.** IHC staining for untreated control and STAT3i SPNP + IR long-term survivor. **(Top)** H&E staining shows the fully formed tumor in the saline control group (28 DPI). When treated with the combination of STAT3i SPNPs + IR, no tumor or signs of necrosis were observed. **(Bottom)** MBP staining shows preserved brain structures with no apparent changes in oligodendrocyte integrity in mice that received STAT3i SPNPs + IR treatment compared to the saline control. Scale bars = 1 mm.

examine potential off-target side effects of the combined therapeutic strategy. Systemic toxicity of STAT3*i* SPNPs + IR treatment was evaluated following the treatment schedule indicated in Figure 6.13a. No significant differences in the cellular components of the blood were noted in complete blood cell counts analysis for animals receiving SPNP, STAT3*i*, STAT3*i* SPNP, or STAT3*i* SPNP + IR treatment compared with animals in saline treatment group (Figure 6.13b-i). Moreover, there was no significant difference in important enzymes involved in kidney (creatinine, blood urea nitrogen) and liver (aminotransferase, aspartate aminotransferase) physiology for animals receiving SPNP, STAT3*i*, STAT3*i* SPNP, or STAT3*i* SPNP + IR treatment compared with animals in saline treatment group (Table 6.1), indicating that no overt adverse side-effects occurred in these tissues.

Further, pathological analysis of potential side effects affecting the livers of mice treated with STAT3*i* SPNP + IR therapy reveled minimal to mild monoculear pericholangitis across all groups and it was characterized by an independent pathologist as spontaneous background rather than a direct result of the applied therapy. (Figure 6.14). In all treatment

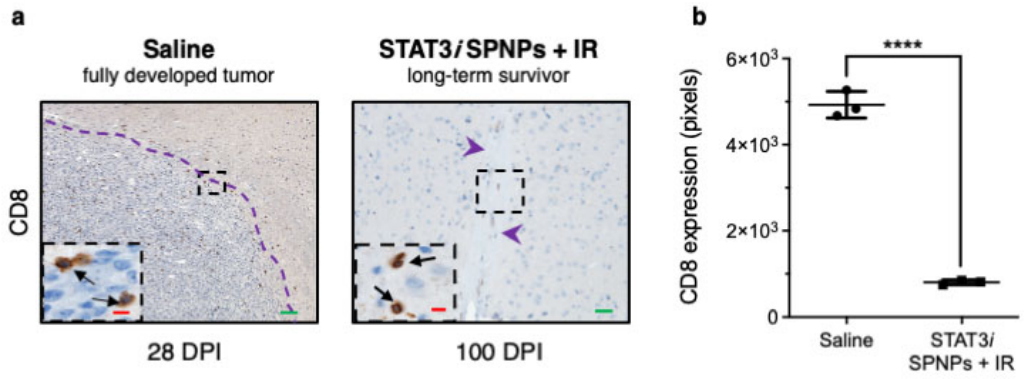

Figure 6.11: **TME CD8⁺ population.** CD8 staining shows no overt inflammation in mice that received STAT3i SPNPs + IR treatment compared to the saline control. **a)** Representative images from a single experiment consisting of three biological replicates per group are displayed. Scale bars = 100 μm (inset, 20 μm). **b)** Quantification of CD8 Expression in TME. Immunofluorescence staining of tumors in either saline or STAT3i SPNP + IR treatment groups was quantified using otsu threshold by ImageJ. Data represent total number of positive cells for CD8 in saline (28 DPI) versus. STAT3i SPNPs + IR (90 DPI) long-term survivor. Data are presented as mean ± s.d. (n = 3 biological replicates; two-tailed unpaired t-test; **** $p < 0.0001$.

Table 6.1: Mouse serum biochemical analysis following STAT3*i* SPNP + IR treatment

Group	Creatinine (μM)	BUN (mM)	ALT (U L^{-1})	AST (U L^{-1})
Saline	0.21 ± 0.10	26 ± 3.1	111 ± 45.2	328 ± 31.4
STAT3*i*	0.20 ± 0.04	23 ± 5.0	98 ± 9.2	331 ± 40.2
SPNPs	0.23 ± 0.10	27 ± 2.1	102 ± 4.0	342 ± 32.1
STAT3*i* SPNPs	0.17 ± 0.20	23 ± 3.0	97 ± 3.5	332 ± 28.2
STAT3*i* SPNPs + IR	0.20 ± 0.06	28 ± 1.2	99 ± 2.6	320 ± 45.0

groups, with the exception of the saline treated control, minimal to mild coagulative necrosis was present. In the treatment group that received free STAT3*i*, one animal displayed multiple foci of coagulative necrosis, which distinguished it from all other animals in the entire study cohort, including those from the combined STAT3*i* SPNP + IR group, where the regions of necrosis were generally small and were deemed not to induce biologically significant adverse effects on liver function.

Next, SPNP-induced immune responses were assessed using a modified enzyme-linked immunosorbent assay (ELISA) (Figure 6.15a). To avoid a species-to-species mismatch due to the use of human serum albumin in mice, otherwise identical NPs were synthesized, in which HSA was replaced with mouse serum albumin (MSA). No circulating antibodies specific to MSA SPNPs were observed in any of the treatment groups indicating negligi-

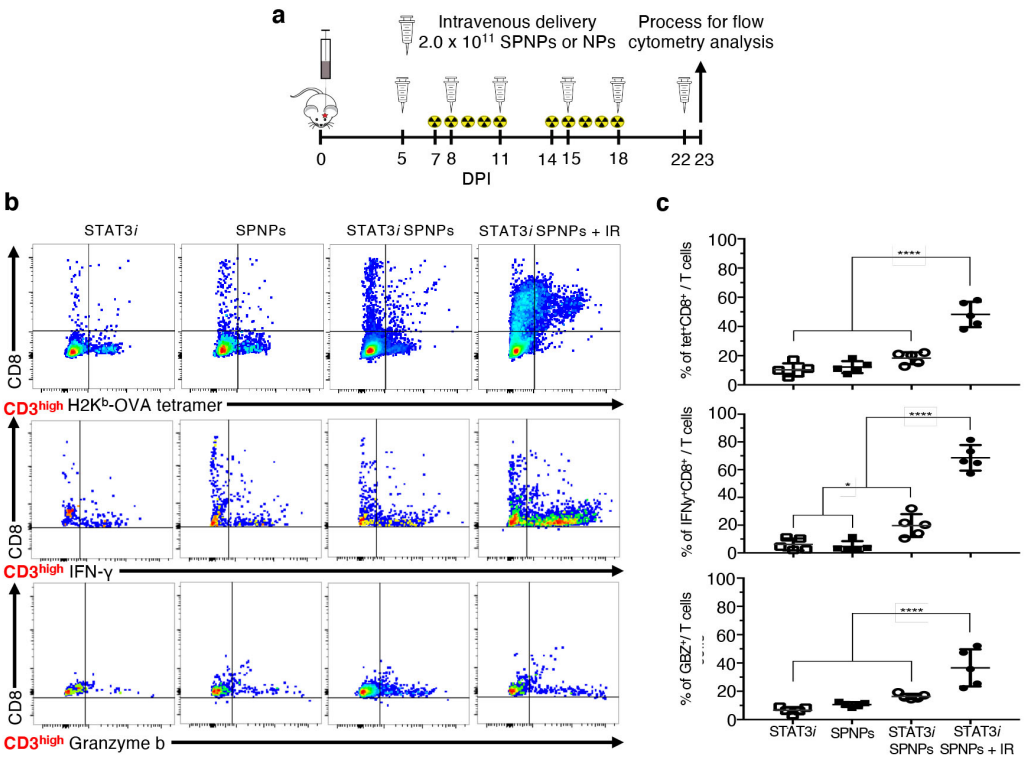

Figure 6.12: **TME immune cell population.** **a)** Timeline of TME immune population by flow cytometry. **b)** Flow cytometry analysis of CD8 cells in the TME. Representative flow plots for each group are displayed. **c)** Quantitative analysis of tumor-specific $CD8^+$ T cells within the TME. GL26-OVA tumors were analyzed by staining for the SIINFEKL-K^b tetramer. Activation status of CD8+ T cells within the TME was analyzed by staining for granzyme B (GZB) and IFN after stimulation with the tumor lysate. Data are presented as mean values $\pm$ s.d. (n = 5 biological replicates; one-way ANOVA and Tukeys multiple comparison tests; **** $p < 0.0001$).

ble immunogenicity against any of the individual components of SPNPs, such as OEG, STAT3*i*, iRGD, or PEI (Figure 6.15b). As expected, replacing MSA with HSA resulted in elevated levels of HSA antibodies for both, STAT3*i* SPNP and empty SPNP treatment groups (Figure 6.15c). Free STAT3*i* therapy did not induce this same response suggesting that antibodies were formed in response to the exposure of the SPNPs rather than the active therapeutic ingredient.

Taken together, our results indicate that sequential intravenous administration of STAT3*i* SPNP in combination with radiation does not cause systemic toxicity. It is well documented that the mononuclear phagocyte system which includes the liver and kidney tissues, uptakes intravenously injected nanoparticles. [254] Levels of biochemical parameters including creatinine, blood urea nitrogen, aminotransferase, and aspartate aminotransferase

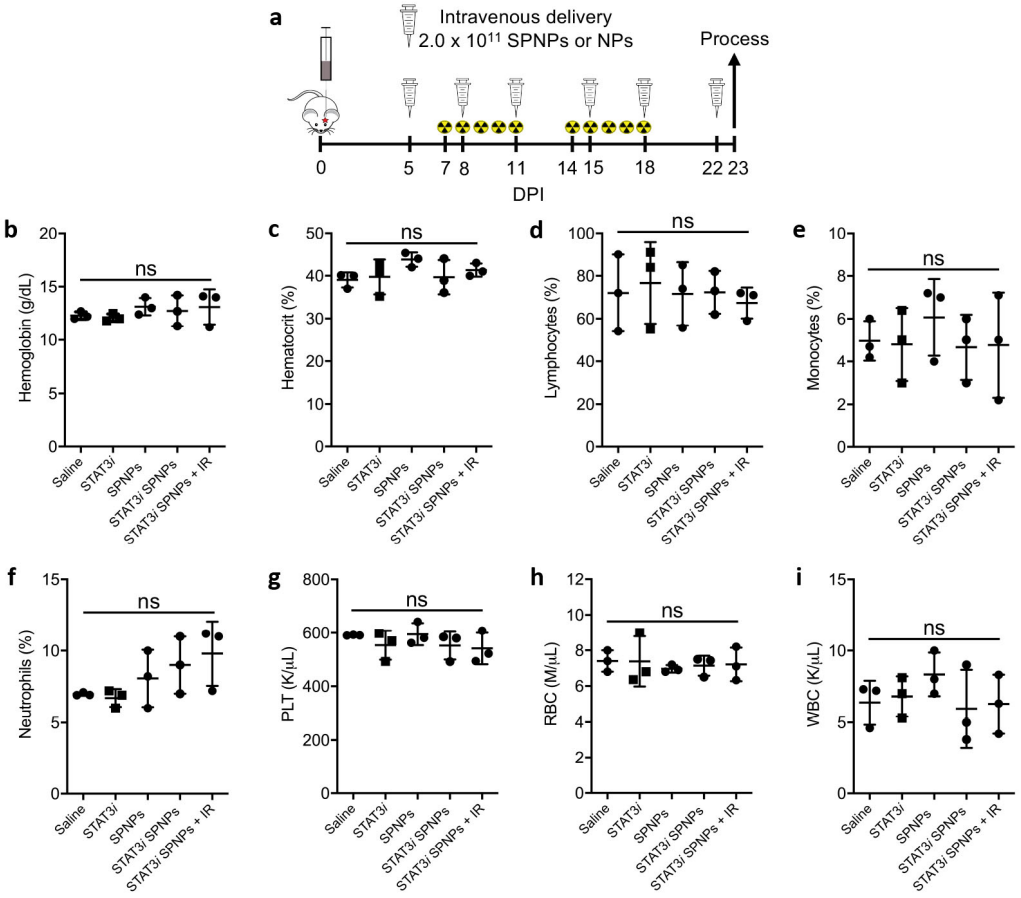

Figure 6.13: **Serum and liver effects of STAT3*i* + IR therapy. a)** Timeline of treatment to assess the effect of STAT3*i* SPNP + IR treatment. Blood and liver samples were collected from GL26 GBM bearing mice treated with saline, STAT3*i*, SPNP, STAT3*i* SPNP or STAT3*i* SPNP + IR at 23 DPI following complete therapeutic regimen. **b-i)** For each treatment group, levels of (b) hemoglobin, (c) hematocrit, (d) lymphocytes, (e) monocytes, (f) neutrophils, (g) platelet, (h) red blood cell (RBC), and (i) white blood cell (WBC) counts were quantified. Data are presented as mean values ± s.d. (n = 3 biological replicates; one-way ANOVA and Tukeys multiple comparison tests; ns = $p > 0.05$).

in the serum are good indicators of acute inflammation in these organs. In our study, there were no inflammatory reactions caused by STAT3*i* SPNP + IR therapy (Figure 6.13 and Table 6.1), indicating that our treatment strategy does not cause short-term toxicity. Further studies will need to be performed to illuminate potential long-term side effects of the STAT3*i* SPNP + IR therapy.

Flow cytometry analysis of tumor infiltrating macrophages and conventional dendritic cells (cDCs:$CD45^+$ / $CD11c^+$ / $B220^-$) was used to compare treatment groups containing free STAT3*i*, empty SPNP and STAT3*i* SPNPs in combination with IR (Figure 6.16a). Co-

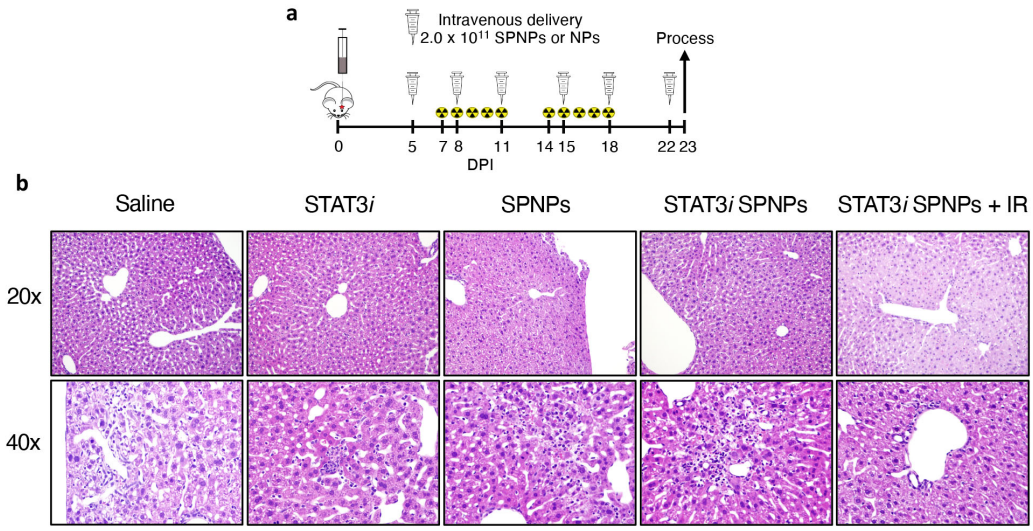

Figure 6.14: **Liver Histology following combined therapy. a)** Timeline for treatment. **b)** Histology performed on resected livers following a complete treatment of GMB tumor bearing mice find isolated regions of mild coagulative necrosis deemed to be well-contained and therefore would not induce a biological effect on liver function. In all groups, with the exception of the saline treated control, signs of hepatocellular necrosis were observed. This is attributed to water or glycogen accumulation in hepatocytes associated with a change in energy balance rather than a degenerative change. Representative images from a single experiment consisting of independent biological replicates are displayed. Scale bars = 100 µm (20x), 50 µm (40x).

staining of $CD45^+$ cells with F4/80 and CD206 antibodies was used to establish a subpopulation of tumor associated macrophages (TAMs). Within the TAM population, both, M1 ($CD45^+$ / $F4/80^+$ / $CD206^-$) and M2 ($CD45^+$ / $F4/80^+$ / $CD206^+$) macrophage phenotypes, were identified for all cohorts, but their relative abundance was significantly different in the STAT3*i* SPNP + IR group compared to all other groups. In the STAT3*i* SPNP + IR group, M1 macrophages were increased by 2.5-fold (Figure 6.16b), whereas the number of M2 macrophages was decreased by three- to four-fold (Figure 6.16c). These findings are consistent with the notion that the STAT3*i* SPNP + IR treatment selectively decreases the immune suppressive M2 macrophage subpopulation. In addition, antigen presentation by cDCs was significantly higher in animals receiving STAT3*i* SPNPs compared to free siRNA and empty SPNPs (Figure 6.17). IR treatment further elevated this effect resulting in the largest cDC population for the STAT3*i* SPNP + IR group. Co-staining of CD45 and $F4/80^{high}$ cells with CD206 and Arg1 antibodies in the STAT3*i* SPNP + IR group confirmed that the vast majority of TAMs were of the M2 phenotype (Figure 6.18). Among all TME $CD45^+$ immune cells, only M2 macrophages displayed the far-red Alexa Fluor 647 signal indicative of SPNPs, suggesting that immune suppressive M2 macrophages are the primary

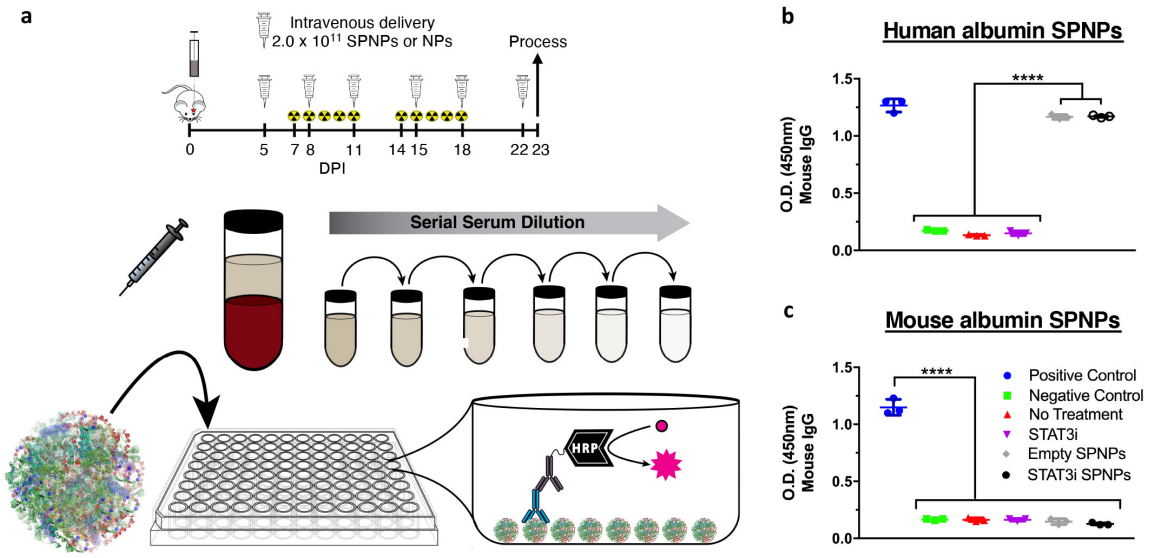

Figure 6.15: **Evaluation of circulating antibodies against STAT3*i* SPNPs. a)** A modified ELISA protocol used to detect the presence of circulating antibodies against SPNPs in serum of GL26 tumor bearing mice following complete STAT3i SPNPs + IR treatment. **b)** When formulating SPNPs with human serum albumin, measurable serum HSA-specific antibody levels are observed. **c)** Alternatively, when SPNPs are formulated with mouse serum albumin, circulating antibodies were not observed in serum of GL26 tumor bearing mice. Data is presented as mean values $\pm$ s.d. (n = 3 biological replicates; one-way ANOVA and Tukeys multiple comparison tests; **** $p < 0.0001$).

TME-based immune cells to internalize SPNPs (Figure 6.19).

Finally, we analyzed the maturation status of DCs in the draining lymph nodes (dLNs) of free STAT3*i*, SPNPs, STAT3*i* SPNPs and STAT3*i* SPNPs + IR treated GL26-OVA tumor bearing mice using flow cytometry. To examine the effect of SPNPs on DC activation in the dLNs, the expression of MHC II was assessed. We observed an increase in the frequency of DCs: $CD45^+$ / $CD11c^+$ / MHC II^+ (1.5-fold, $p < 0.0001$), in the dLN of STAT3*i* SPNPs treated mice compared to free-STAT3*i* and SPNP treated mice. This was further enhanced in the presence of IR by 1.3-fold ($p < 0.0001$) (Figure 6.20). These data suggest that STAT3*i* SPNPs in combination with radiation induces the activation of DCs by enhancing the expression of MHC II, which is involved in antigen presentation.

6.3.5 Tumor Rechallenge

Current standard of care approaches, including surgical resection combined with focused radiation and the chemotherapeutic temozolomide, have been used to treat primary GBM

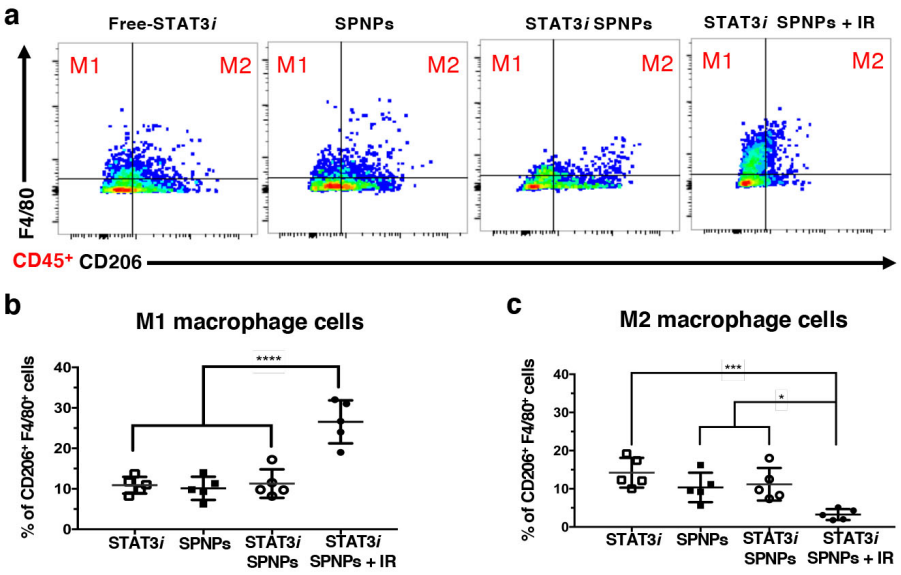

Figure 6.16: **TME infiltrating macrophage population.** Flow analysis of tumor infiltrating macrophage populations in the TME following SPNP + IR treatment regimen. **a)** Representative flow plots for each group are displayed. Quantitative analysis of the immune cellular infiltrates **b)** M1 macrophages, and **c)** M2 macrophages. Data are presented as mean values ± s.d. (n = 5 biological replicates; one-way ANOVA and Tukeys multiple comparison tests; **** $p < 0.0001$, *** $p < 0.001$, * p (M2) = 0.028, 0.013.

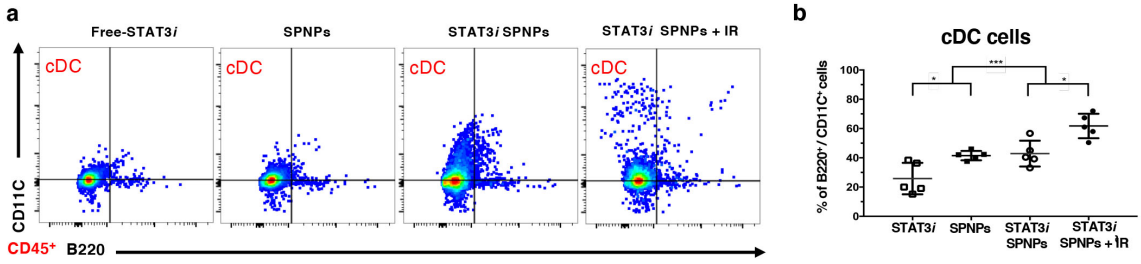

Figure 6.17: **TME infiltrating dendritic cell population.** Flow analysis of tumor infiltrating conventional dendritic cell (cDCs) populations in the TME following SPNP + IR treatment regimen. **a)** Representative flow plots for each experimental group are displayed. **b)** Quantified flow results showing the combined treatment of STAT3i SPNPs with IR displayed the highest number of cDCs in the brain TME. Data are presented as mean values ± s.d. (n = 5 biological replicates; one-way ANOVA and Tukeys multiple comparison tests; **** $p < 0.0001$, *** $p < 0.001$, * p(cDC) = 0.038, 0.011).

tumors. However, owing to the aggressive and infiltrative nature of GBM, these patients, as a rule, experience recurrence contributing to the high mortality and dismal survival rates. Based on the encouraging immune response observed in our survival study, we chose to rechallenge survivors from the STAT3*i* SPNP + IR treatment group. Tumors were implanted in the contralateral hemisphere of mice that were previously cured by the STAT3*i*

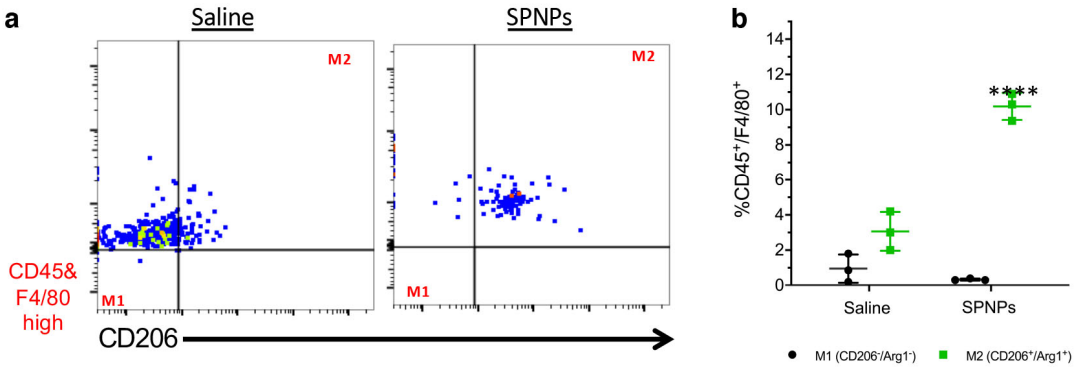

Figure 6.18: **TME macrophage populations.** **a)** Representative flow plots displayed. **b)** Quantified flow data showing the treatment of GL26 tumor-bearing mice with SPNPs produced a shift in macrophage populations within the tumor microenvironment. An increase in the M2 macrophages relative to saline treated control animals was observed. Data are presented as mean values ± s.d. (n = 3 biological replicates; two-way ANOVA; **** $p < 0.0001$)

SPNP + IR therapy. These mice did not receive any additional intervening therapy (Figure 6.21a). As a control, naïve mice were also implanted with tumors at the same timepoint and likewise received no treatment. As expected, the control group saw rapid tumor growth, increased signs of disease, and had a median survival of 27 DPI. Despite not receiving any additional treatment, all rechallenged mice survived to a second long-term survival point of 90 DPI (relative to the second tumor implantation, 180 days post initial tumor implantation) (Figure 6.21b). IHC analysis of the brains yielded comparable results to that of the original GBM challenge (Figure 6.22). H&E staining clearly showed the formation of a fully developed tumor mass in the control group, while members of the rechallenged

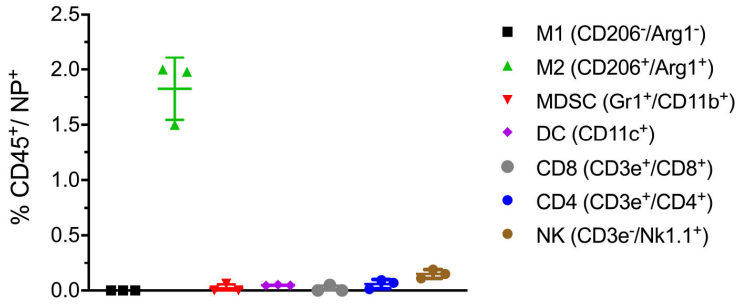

Figure 6.19: **TME immune cell SPNP uptake.** Flow cytometry analysis of immune cells collected from the tumor microenvironment of SPNPs treated mice show significant nanoparticle uptake by M2 macrophages and minimal uptake by all other immune cell types. Data are presented as mean values ± s.d. (n = 3 biological replicates; two-way ANOVA; **** $p < 0.0001$).

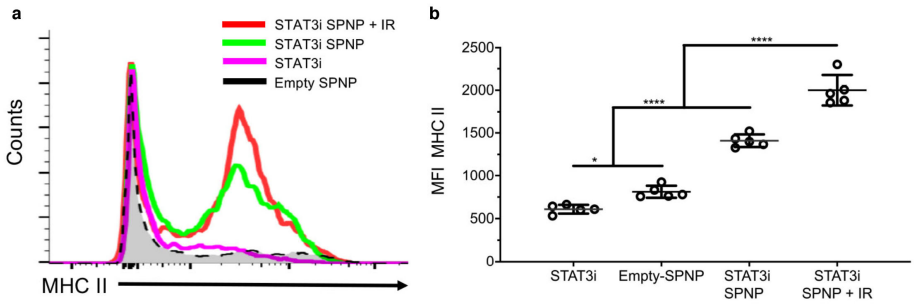

Figure 6.20: **Dendritic cell MHC II expression.** Activation status of DCs in the draining lymph node of GBM bearing mice treated with STAT3*i*, empty SPNP, STAT3*i* SPNP, and STAT3*i* SPNP + IR was assessed one day post the last day of treatment (23 DPI). Representative histograms display MHC II expression level on the DCs (purple = STAT3i, black = empty SPNP, red = STAT3*i* SPNP + IR, green = STAT3*i* SPNP). Data is presented as mean values ± s.d. (n = 5 biological replicates; one way ANOVA; **** $p < 0.0001$, * $p = 0.036$).

cohort displayed no regions of necrosis, palisades or hemorrhages in either hemisphere (Figure 6.22, top). MBP staining confirmed that there was no overt disruption of the surrounding brain architecture (Figure 6.22, bottom). Lastly, the presence of CD8 T cells was observed to be five-fold lower in the STAT3*i* SPNP rechallenge group compared to the control (Figure 6.23). Importantly, we found no adverse effects in the brains of rechallenged survivors.

Previous work has demonstrated that glioma cell death is associated with the concomitant release of antigens and damage-associated molecular patterns (DAMPs) leading to tumor

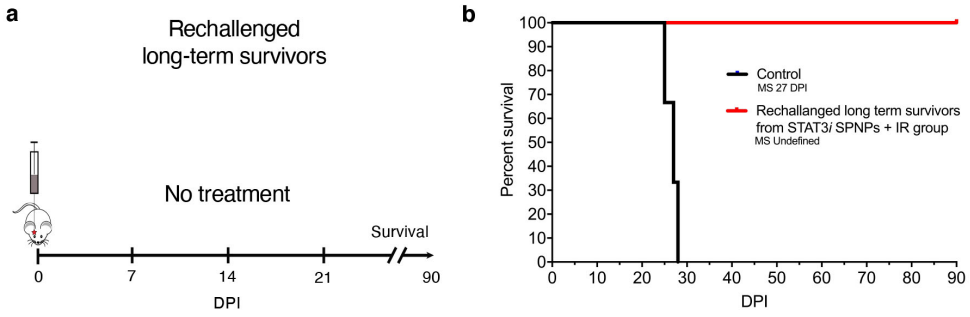

Figure 6.21: **Tumor rechallenge of long-term survivors.** Long-term survivors from original survival study were rechallenged with a second tumor. **a)** Timeline for rechallenging the long-term survivors from STAT3*i* SPNPs + IR survival study. Following tumor implantation, no further treatment was provided. **b)** Kaplan-Meier survival curve shows all rechallenged survivors reach a second long-term survival timepoint of 90 DPI in the absence of any therapeutic interventions.

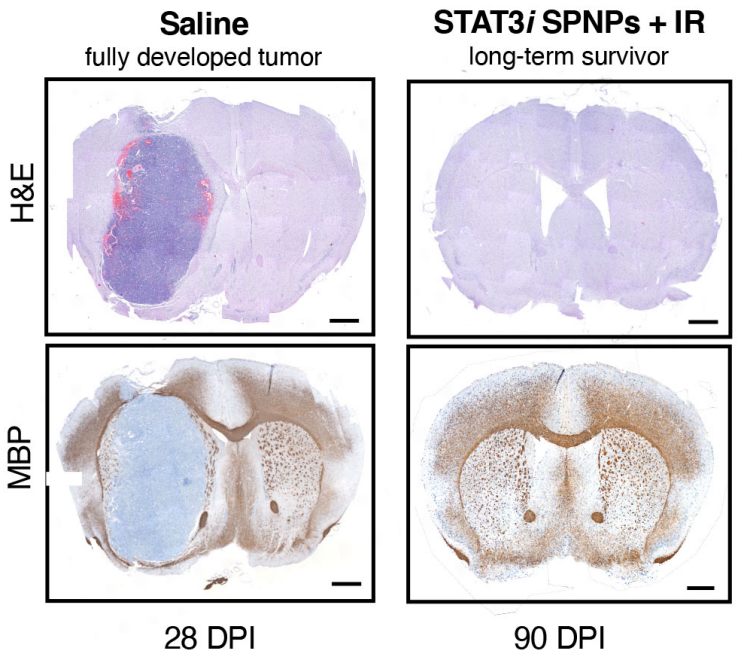

Figure 6.22: **GBM histology of rechallenged mice.** IHC staining comparing the brains of untreated and rechallenged long-term survivors. Representative images from a single experiment consisting of three biological replicates per group are displayed. No overt signs of remaining tumor, necrosis, inflammation, or disruption of normal brain architecture was observed in rechallenged long-term survivors from STAT3*i* SPNP + IR treatment group. Scale bars = 1 mm.

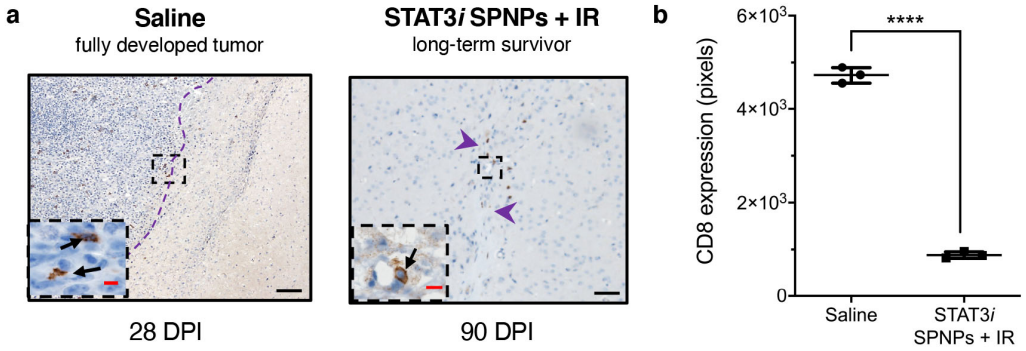

Figure 6.23: **Rechallenge TME immune cell population.** Quantification of CD8 Expression in TME following tumor rechallenge experiment. CD8 staining shows no overt inflammation in rechallenged mice compared to the saline control. **a)** Representative images from each group are displayed. **b)** Immunofluorescence staining of tumors were quantified using otsu threshold by ImageJ. Data represent total number of positive cells for CD8 in saline (28 DPI) versus rechallenged long term survivors (90 days post rechallenged; 180 days post initial tumor implantation). Data are presented as mean ± s.d. (n = 3 biological replicates; two-tailed unpaired t-test; **** $p < 0.0001$. Scale bars = 100 µm (inset, 20 µm)

antigen-specific T cell expansion and adaptive anti-glioma immunity. [255] Our findings suggest a similar involvement of an adaptive immune response that appears to guard against secondary tumors; an essential condition of any successful GBM therapy which will require long-term eradication of migrating and resistant CSCs, typically missed by traditional therapies. STAT3 signaling in conjunction with IL-6/JAK signaling has been shown to drive tumor invasiveness while suppressing anti-tumor immunity. [11,247,248] Therapeutic agents that target IL-6/JAK/STAT3 have been shown to stimulate anti-tumor immunity, thus, inhibiting STAT3 signaling in glioma will be therapeutically beneficial. [247, 248] Overall, our results demonstrate that STAT3*i* SPNPs, in combination with IR, targets distinct mechanisms to elicit immunogenic cell death of GBM cells, triggering anti-GBM immunity, and inducing immunological memory against recurring GBM as described in the proposed mechanism (Figure 6.24).

6.4 Summary

Encouraged by results showing the accumulation of SPNPs in GBM tumors we sought to evaluate the therapeutic efficacy of STAT3i SPNPs in combination with focused radiotherapy. In the highly aggressive GBM GL26 model, a significant increase in MS is observed in mice treated with the combined therapy with 87.5% of mice reaching the long-term survival timepoint. In these mice, we observed significantly reduced levels of STAT3, no apparent residual tumors, normal brain architecture, and a lack of inflammation in response to the treatment. We observed increases in both tumor-antigen specific CD8 T cells in the brain TME along with a decrease in immune suppressive M2 macrophages suggesting the activation of an anti-GBM immune response. Finally, we observed minimal signs of toxicity in the liver and no significant differences in the cellular components of blood relating to kidney and liver function suggesting no overt off-target side effects occurred as a result of the treatment.

Patients treated with conventional therapies including chemotherapeutics, radiation, and surgical resection, commonly experience recurrence in surrounding tissues contributing to GBMs high mortality rate. To further explore the observed immune response, mice reaching the long-term survival timepoint were rechallenged with a second tumor in the contralateral hemisphere. Incredibly, in the absence of therapeutic intervention, all rechallenged mice survived to a second long-term survival timepoint. Rechallenged mice showed no overt signs of residual tumor, regions of necrosis, or disruption of the surrounding brain architecture. Together, these studies further suggest the activation of an adaptive immune

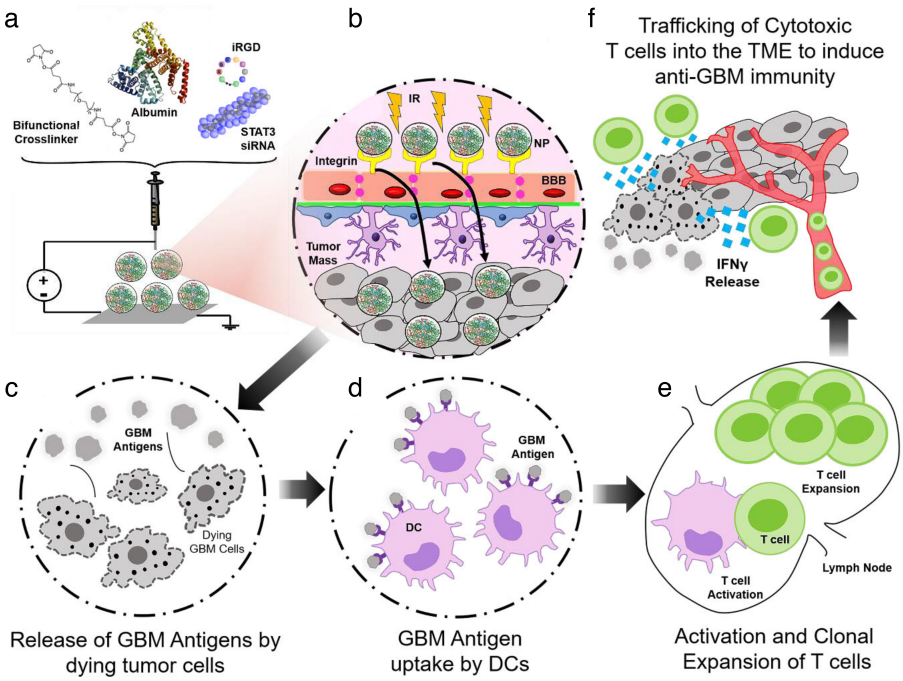

Figure 6.24: **Immunological mechanism.** Immunological mechanism targeting Glioblastoma (GBM) upon Signal and Transducer of Activation 3 (STAT3) downregulation with nanoparticles. **a)** Electrodynamic co-jetting of 200 nM STAT3 small-interfering RNA (STAT3*i*) containing SPNPs. Jetting formulation consists of bifunctional crosslinker, albumin, iRGD (tumor-targeting peptide) and STAT3*i*. **b)** Systemic delivery of STAT3 siRNA SPNPs in combination with radiation (IR). The iRGD peptide binds to the integrins on the bloodbrain barrier and GBM cells promoting the entry of STAT3*i* into the tumor cells by transcytosis. **c)** Dying GBM cells release antigens into the tumor microenvironment (TME). **d)** Dendritic cells (DCs) in the TME become activated upon encountering GBM antigens. **e)** DCs uptake and process the GBM antigens and migrate to the lymph nodes, where they present antigens to CD8 T cells and mediate the activation and clonal expansion of T cells. **f)** Cytotoxic T cells traffic to the GBM TME to kill the remaining tumor cells and promote anti-GBM immunity

response, potentially capable of eradicating secondary tumors resulting from the aggressive and infiltrative nature of GBM.

SPNPs combine the biological benefits of proteins with the precise engineering control of synthetic NPs to yield (i) high efficacy (87.5% long-term survivors in a very aggressive intracranial tumor model), (ii) effective tumor delivery using systemically administered SPNPs, and (iii) possibilities towards longterm eradication of resistant cancer cells using immunomodulatory protein NPs. While protein-based NPs have been a fairly uncharted area of research, this study demonstrates that synthetic NPs that use proteins as structural building blocks may pave a viable route towards clinical cancer therapy implementation.

We studied the NP-mediated delivery of a siRNA against STAT3, but the SPNP platform could be adopted, after further development and preclinical testing, for delivery of small-molecule drugs, other siRNA therapies, or even drug combinations to a wide variety of solid tumors.

In summary, our study demonstrates the development of a novel therapeutic systemic delivery platform for GBM, i.e., albumin-based tumor-targeting SPNPs, which could be suitable for clinical translation. The information gleaned from our study will allow for the delivery of powerful anti-tumor drugs at the target site while sparing healthy tissue. Our SPNP system can serve as a precision therapeutic platform that can cross the blood brain barrier, deliver the drug payload into the GBM and concentrate the drug within the tumor microenvironment, thus mediating tumor regression and anti-tumor immunity. The findings from our work could also be broadened to metastatic cancers to the brain, e.g., melanoma and breast as well as other solid cancers. Clinically, our therapeutic strategy will likely lead to improved patient survival, inhibit brain cancer progression, and prevent tumor relapse. Overall, the results from this study exhibit high translational potential and will have direct implications in the development of novel therapies for primary and metastatic brain tumor patients.

CHAPTER 7

Conclusions and Future Directions

This chapter contains portions of text/data originally published as:

Systemic delivery of a CXCR4-CXCL12 signaling inhibitor encapsulated in synthetic protein nanoparticles for glioma immunotherapy
MS Alghamri, K Banerjee, AA Mujeeb, A Taher, R Thalla, BL McClellan, ML Varela, SM Stamatovic, G Martinez-Revollar, A Andjelkovic-Zochowska, JV Gregory, P Kadiyala, A Calinescu, JA Jimnez, AA Apfelbaum, ER Lawlor, S Carney, A Comba, SM Faisal, M Barissi, MB Edwards, H Appelman, MR Olin, J Lahann, PR Lowenstein, MG Castro
ACS Nano - In Review (2021)

7.1 Conclusions

Thoroughly discussed in Chapter 1, the landscape of various clinically relevant diseases, particularly cancer, has been shown to be both complex and constantly evolving. As a result, single therapeutic approaches often prove to be insufficient in realizing enduring positive outcomes in patients. Nanotechnology, particularly in the form of nanoparticles, has been the focus of decades of research in attempts to leverage their unique capabilities and properties towards efficient drug delivery vehicles; however, clinically meaningful impacts have been limited to date. The biological complexities involved in effectively treating these diseases is further complicated when considering the body's natural defense and clearance mechanisms designed to guard against foreign materials. As discussed, ideal carrier properties for the various stages of effective drug delivery are often conflicting and speak towards the need of developing adaptive and complex systems. One possible approach to address these challenges is the design and synthesis of multifunctional nanoparticles.

As discussed in Chapter 2, the successful treatment of cancers is often best approached

through the use of multiple therapeutics targeting independent pathways. This strategy is a direct response to tumor heterogeneity, the various escape mechanisms cancers employ to evade innate immune responses, and developed resistance to single therapeutics. In the work presented, highlighting the development of Janus polymeric nanoparticles capable of independent encapsulation and controlled release of palitaxel and lapatinib, we demonstrated an ability to (i) load two distinct chemotherapeutics with a control over the relative molar ratios, (ii) impart control over the relative release kinetics in response to external stimuli, and (iii) produce a synergistic cellular response through the temporally controlled release of each drug from a single nanoparticle system, matching that found in free drug studies.

A natural evolution away from synthetic polymer materials, towards the development of a protein-based particle delivery system was presented in Chapter 3. As a result of the work presented, collaboratively developed by members of the Lahann lab, a broad synthetic protein nanoparticle (SPNP) platform yielded an ability to produce a wide array of particle architectures. The platform resulted in a controlled means to produce monodisperse protein nanoparticles using a vast library of proteins, crosslinking macromers, and encapsulated materials taking a modular approach to particle design. Importantly, each of the approaches were developed in a way to ensure capability across the whole of the platform. When combined with an understanding and prior experience of leveraging the EHD process towards multicompartmental particles, the result was an ability to produce multicompartmental Janus SPNPs.

Further highlighted and discussed extensively in Chapter 1 were the limitations associated with a passive targeting approach for nanomedicines. While the EPR effect has been debated for decades since it was first theorized, recent work has shown that it is not universally applicable, particularly in cancer, despite the rapid angiogenesis observed in most solid tumors. In response, work to extend the protein nanoparticle platform to a targeted approach was presented in Chapter 4. Here, we developed a straightforward, two-step approach towards the surface functionalization of protein nanoparticles. While demonstrated through the conjugation of targeting antibodies, care was taken to ensure that the approach could be more broadly applied to the surface functionalization using an array of targeting moieties. The result was (i) an effective and reproducible means to conjugate molecules to SPNP surfaces, (ii) control over surface ligand density through stiochiometric reactant ratios, (iii) an ability to selectively control binding and uptake in accordance with cell-surface expressed receptors, (iv) a demonstrated ability to deliver encapsulate cargo to influence intracellular protein expression in a cell-specific manner, and (v) an ability to influence the biodistribu-

tion of systemically injected nanoparticles influenced by their presented surface chemistry. Moreover, care was taken to ensure that the developed methods of surface conjugation could theoretically be applied to previously developed Janus SPNPs leading to an ability to independently and selectively modify particle surfaces utilizing orthogonal chemistries, similar to that which had been previously demonstrated by our group with PLGA nano- and microparticles.

Perhaps the most significant of the various biological hurdles and clearance mechanisms discussed in Chapter 1, the ability to transverse biological barriers was presented. Barriers, such as the blood-brain barrier (BBB), severely limit nanoparticle accumulation within organs of interest. When considering the BBB, this has proven to be the greatest challenge in translating promising compounds and biologics towards meaningful and impactful therapeutic outcomes in intracranial and CNS diseases. In Chapters 5 and 6, we developed and evaluated SPNP performance in an aggressive GBM mouse model. While previous work identifying the STAT3 pathway as a central hub contributing to poor patient prognosis and disease progression yielded promising results in an *in vitro* and *in vivo* flank model, the same promising therapeutic effects were absent for in situ tumors. The demonstrated ability to load and release siRNA into the cytosol from SPNPs was combined with a targeting approach leveraging the tumor targeting and tissue penetrating peptide iRGD. Distinct from previous research, iRGD was encapsulated and designed to be released from the SPNPs. In total, we demonstrated (i) an ability to selectively silence STAT3 protein expression in GBM cells, (ii) transport SPNPs across the BBB, (iii) significantly increase median survival with multiple long-term survivors, and (iv) create an immunological response, activating the immune system leading to long-term survivors of rechallenged mice in the absence of additional therapeutic intervention. Together, these results show promise for the development of clinically impactful therapies in a disease that has seen only marginal advances despite decades of intensive research and development.

Together, work presented in this thesis focused on further developing nanoparticle systems derived using the EHD jetting process. Prior work focused on the creation and optimization of the system to move to smaller sizes more relevant for systemic delivery. The comprehensive understanding of the process and resulting array of tools were leveraged towards the creation of Janus nanoparticles with properties informed by the biological understanding of the target disease. These same key concepts and process parameters were applied to move the technology to an entirely new phase of development, away from synthetic biodegradable materials, and instead towards biologically derived building blocks. Demonstrating our unique understanding of the process, the parameters at play, and effects variations in

those parameters had on the fabricated systems, control of particle architecture, bulk and surface properties, targeted interactions with biological systems, and ultimately therapeutic impacts were realized. Not thoroughly presented here, recently completed and ongoing work continues to push the frontier of nanomedicine with this work and that of recently departed lab members laying the foundation.

7.2 Applications and Future Directions

As was eluded to at the close of Chapter 6, the design of SPNPs as applied to GBM, is not limited to the presented approach of delivering siRNA against STAT3; nor is it limited to this disease in particular. Owing to the versatility of the EHD co-jetting process, the base system can be varied to deliver any number of therapeutics. Considering the development of biologics (e.g. siRNA, mRNA, DNA) and small molecule drugs seen in recent decades, secondary targets and survival mechanisms can be pursued from a single delivery system. This approach leverages an ability to simultaneously modulate multiple biological, disease-specific pathways.

Continued work in collaboration with Dr. Maria Castro's lab examined the key role that the CXCR4-CXCR12 interactions play in GBM progression (Figure 7.1a). Furthermore, promising cellular effects in response to AMD3100 (or Plerixafor), a CXCR4 receptor antagonist, in an *in vitro* setting suggests this compound could be leveraged towards improving patient outcomes, similar to that of our STAT3 approach (Figure 7.1b-c). Again, however, negligible transport of the molecule across the BBB severely limits its potential in a clinical context. Utilizing a similar approach and architecture, particles encapsulating and capable of releasing AMD3100 were formulated (Figure 7.2). When evaluated in similarly aggressive intracranial mouse models, we observed a significant extension of median survival compared to untreated or free drug cohorts. Coupled with IR, this benefit was extended even further leading to 60% of mice receiving the combined treatment reaching the long-term survival timepoint (Figure 7.3b). Rechallenged with a second tumor and in the absence of further intervention, we again observed a developed anti-GBM immune response with all surviving mice reaching a second long-term timepoint (Figure 7.3c).

The above results were achieved using the STAT3*i* SPNPs as a basis with minimal design alternations to accommodate the small molecule inhibitor. Key implications for the further development of this technology must be noted. First, while approaching the disease from an entirely different mechanism, we realized promising *in vivo* efficacy. From a disease

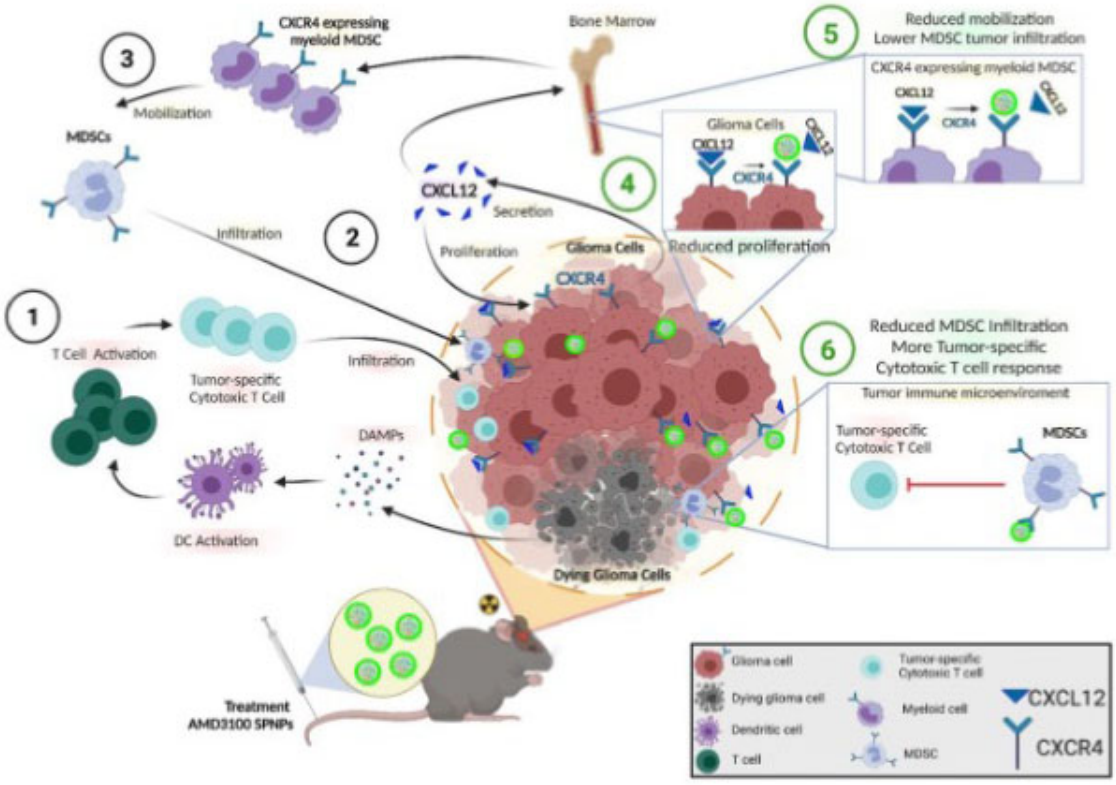

Figure 7.1: **Immunological mechanism targeting GBM upon blocking CXCR4 signaling pathway with AMD3100 SPNPs.** (1) Radiotherapy induces glioma cell death, followed by DAMPs release. Dendritic cells are activated by DAMPs and migrate to the regional lymph node where they prime cytotoxic T lymphocyte immune response. Tumor-specific cytotoxic T cells infiltrate the tumor and attack glioma cells. (2) Glioma cells express CXCR4, as well its ligand CXCL12. CXCL12 induces glioma cell proliferation and, (3) as well as mobilization in the bone marrow of CXCR4 expressing myeloid MDSC, which will infiltrate the tumor, and inhibit tumor-specific cytotoxic T cells activity. GEMM of glioma when treated systemically with SPNPs AMD3100 SPNPs plus radiation, nanoparticles block the interaction between CXCR4 and CXCL12, thus (4) inhibiting glioma cell proliferation and (5) reducing mobilization in the bone marrow of CXCR4 expressing myeloid MDSC, (6) generating a reduced MDSC tumor infiltration, as well as releasing MDSC inhibition over tumor specific cytotoxic T cell response.

perspective, this supports the notion that GBM, like many cancers, are complex and dependent upon multiple pathways to proliferate. Secondly, despite moving from a double stranded biologic to a low molecular weight, small molecule drug, the overall particle formulation, jetting parameters, and targeting approach remained relatively unchanged. This point in particular speaks to the versatility of the SPNP platform and the potential for combining the two therapies into a single particle system. Lastly, while the therapeutic cargos are quite different, the particle architecture and targeting approach proved capable to successfully transporting each across the highly impermeable BBB. This last point suggests that other potent chemotherapeutics, if able to be encapsulated and released from this sys-

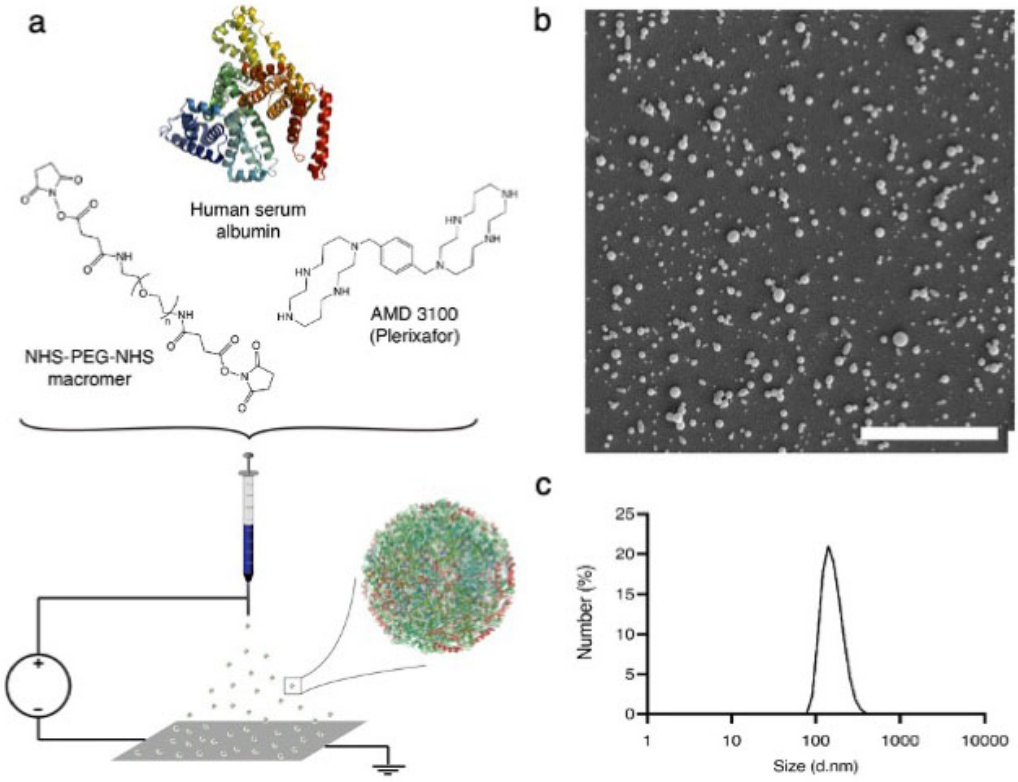

	Avg. Diameter	Std. Deviation	PDI	Circularity	Zeta Potential
SEM (Dry)	98.5	37.3	0.143	0.919	–
DLS (Hydrated)	161.2	46.5	0.083	–	- 6.50

Figure 7.2: **EHD co-jetting and characterization of AMD3100 SPNPs. a)** Schematic of the jetting process for human serum albumin SPNPs encapsulating AMD3100. **b)** Size distribution of SPNPs in their dry state. Particle size distribution and shape characterized via Scanning Electron Microscopy (SEM) and ImageJ analysis. Average diameter, 98.5 ± 37.3 nm (PDI = 0.143). Scale bar = 3 µm. **c)** Dynamic Light Scattering (DLS) size distribution of SPNPs in PBS. Average diameter 161 ± 46.5 (PDI = 0.083).

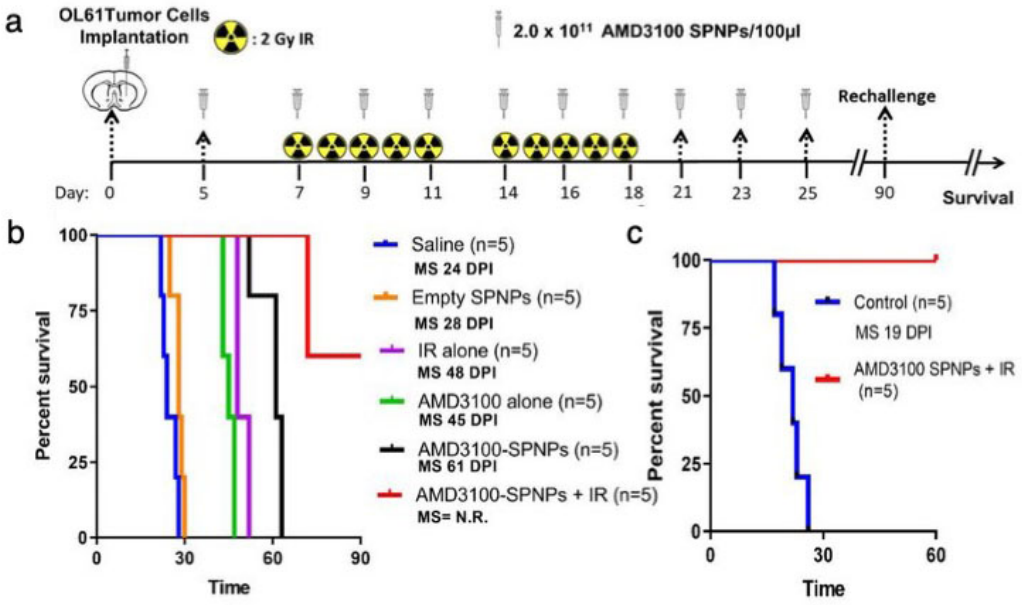

Figure 7.3: **Combining AMD3100 SPNPs with IR prolong survival of GBM tumor bearing mice.** **a)** Timeline of treatment for the combined AMD3100 SPNPs + IR survival study. **b)** KaplanMeier survival curve. Significant increase in median survival is observed in all groups receiving AMD3100 alone or IR ($p < 0.01$). Mice (3/5) treated with AMD3100 SPNPs + IR reach long-term survival timepoint (100 DPI) with no signs of residual tumor. **c)** Kaplan-Meier survival plot for re-challenged long-term survivors from AMD3100 SPNPs + IR (n = 3), or control (OL61 Untreated) (n = 5). Data were analyzed using the log-rank (Mantel-Cox) test.

tem, could also potentially find their way into the CNS. Together, these findings open up the possibility to revisit an array of molecules previously found to be ineffective at treating intracranial tumors.

Discussed in Chapter 3, we highlighted the ability to form albumin-paclitaxel complexes through high pressure homogenization. The resulting complex was then successfully introduced to the EHD jetting system to create PTX-SPNPs and the release profile of the drug from the resulting particles was characterized. Recent studies have shown that certain chemotherapeutic drugs may contribute to immune-mediated responses by inducing a special form of tumor-cell killing, known as immunogenic cell death. More recent work has explored the potential of combining paclitaxel with the already developed STAT3*i* SPNPs to form bicompartmental, STAT3*i*/PTX/biSPNPs (Figure 7.4a). Each therapeutic modality targets a distinct mechanism that elicit GBM cell death with concomitant release of DAMPs and TLR agonists, i.e., high-mobility group box 1 (HMGB1), which has been shown to elicit immunogenic cell death and triggers anti-GBM immunity, including immunological memory against GBM. Furthermore, therapeutic agents that target IL-6/JAK/STAT3 have

been shown to stimulate anti-tumor immunity.

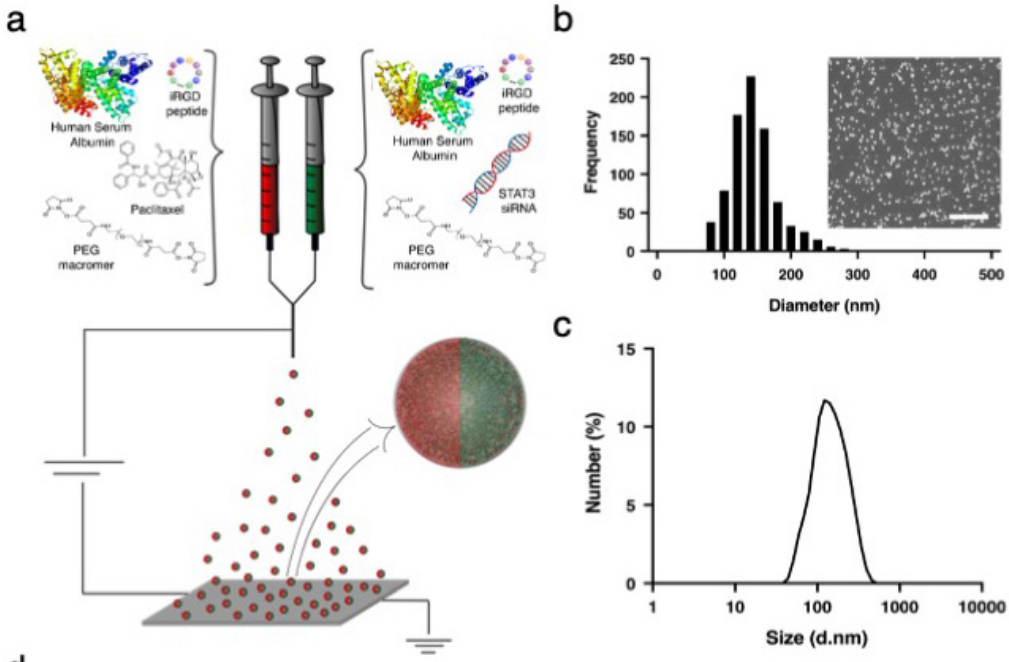

d

	Avg. Diameter (nm)	Std. Deviation (nm)	PDI	Circularity	Zeta Potential (mV)
SEM (Dry)	144.9	37.3	0.066	0.934	–
DLS (Hydrated)	206.3	91.4	0.197	–	- 7.2

Figure 7.4: **EHD co-jetting of bicompartmental protein nanoparticles (biSPNPs).** **a)** Schematic of the jetting process for STAT3*i*/PTX/biSPNPs. **b)** Size distribution of biSPNPs in their dry state. Particle size and shape characterized via Scanning Electron Microscopy (SEM). Scale bar = 2 µm. **c)** Dynamic Light Scattering (DLS) size distribution of biSPNPs in PBS. **d)** Summarized size, shape, and surface charge characteristics for biSPNPs. **e)** Structured Illumination Microscopy (SIM) super-resolution images of Janus SPNPs with distinct dyes encapsulated within the two particle hemispheres. Scale bar = 100 nm.

Merging the two therapeutic approaches into a single particle architecture through EHD co-jetting, the resulting particles are found to be monodisperse with size distributions of 145 ± 37.3 nm (PDI = 0.066) in their dry state (Figure 7.4b and d). STAT3*i*/PTX/biSPNPs, following collection, are found to be 206 ± 91.4 nm (PDI = 0.197) in PBS when measured via DLS (Figure 7.4c and d). Preliminary release and *in vitro* efficacy studies are each promising. We observe unique release profiles of the two compounds from a single particle architecture confirming an ability to encapsulate and release each agent independently (Figure 7.5). When delivered to GL26 glioma cells, we observe significantly increased cellular toxicity comparing STAT3*i*/PTX/biSPNPs to each of the individual agents, free PTX or free siRNA delivered via lipofectamine (Figure 7.6). When compared to a combined approach

wherein cells are exposed simultaneously to PTX and STAT3*i* in their free forms, it is noted that the STAT3*i*/PTX/biSPNPs perform slightly better than the free compounds, suggesting that encapsulating the two agents within a particle system does not limit the availability or efficacy of either. These findings are consistent both with and without treatment of the cells with IR.

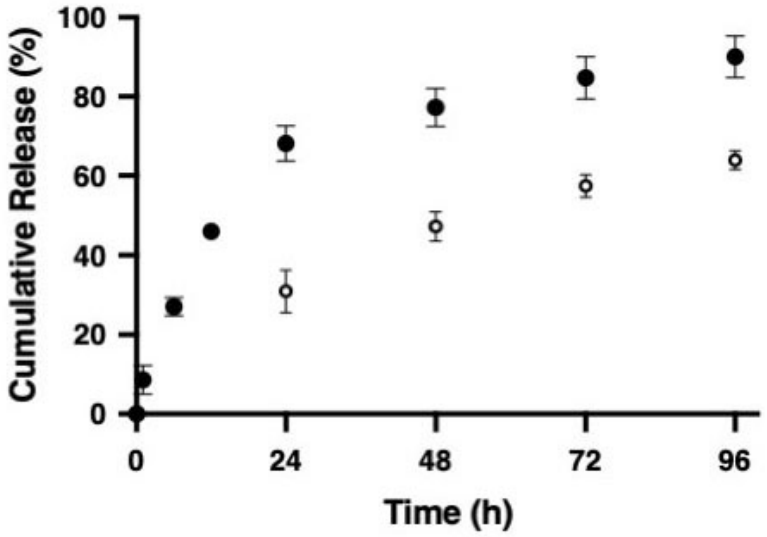

Figure 7.5: **Controlled release of paclitaxel and siRNA.** Dual release of PTX (black) and siRNA (open circles). Release observed over a period of 4+ days in PBS at 37°C. PTX release quantified via HPLC-MS; Cy3-labeled siRNA quantified via fluorescence. Data is presented as mean ± SEM (n = 3 biological replicates.)

Tumor cells undergoing immunological cell death up-regulate ”eat me” and ”danger” signals. The eat me signals, such as calreticulin (CRT) exposed on the surfaces of dying tumor cells, enable dendritic cells (DCs) to phagocytose tumor cells debris and present tumor antigen epitopes in the context of major histocompatibility complex (MHC) class I or II. In turn, the danger signals, such as HMGB1 released by dying tumor cells, promote activation of DCs and trigger antigen-specific T cell responses. Extending our *in vitro* characterization to evaluate signs of immunogenic cell death, we looked specifically at levels of HMGB1, CRT, and ATP (a marker of DAMPs). In whole, we observe increased levels of each in the STAT3*i*/PTX/biSPNPs treatment group compared to the free compounds (Figure 7.7).

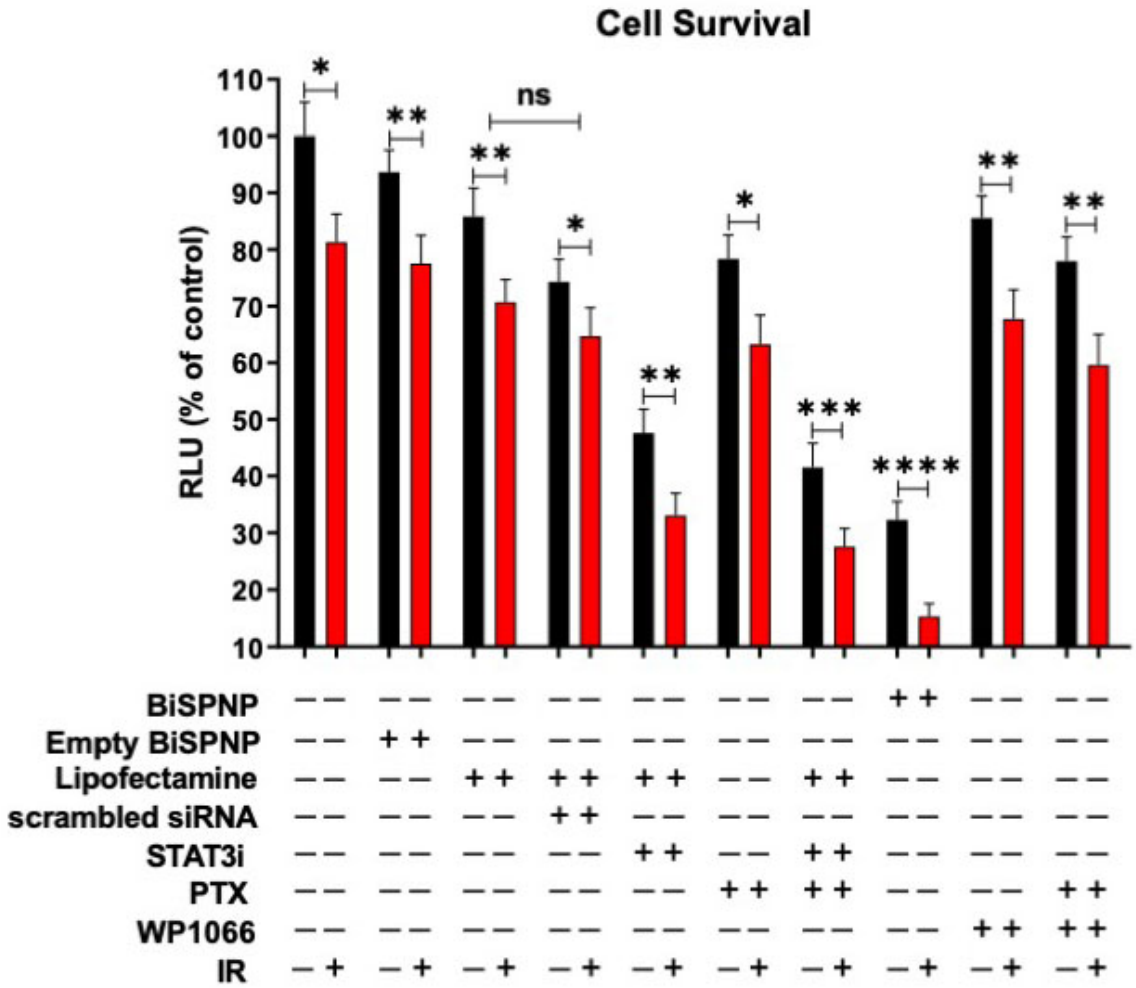

Figure 7.6: **biSPNPs enhance radio-sensitivity in mouse glioma cells.** Impact of biSPNP on radio-sensitivity on GL26 glioma cells. Cell viability assay shows the effect of the biSPNPs (at IC_{50} values) +/- IR (3Gy) on cellular proliferation in the cells. Cells were also treated with combined (STAT3*i* + PTX), free-PTX, free-STAT3*i*, scrambled-siRNA, lipofectamine-only and empty-biSPNPs at their respective IC_{50} values within the same experimental condition. To compare the efficacy of biSPNP with standard STAT3*i* inhibitor, cells were treated with either WP1066 (5 μM) or in combination with 3Gy of radiation and analyzed after 72 h. Results are expressed in relative luminescence units (RLU). ns = non-significant, *$p < 0.05$, **$p < 0.01$, ***$p < 0.0001$, ****$p < 0.0001$; two-way ANOVA (n = 3 technical replicates).

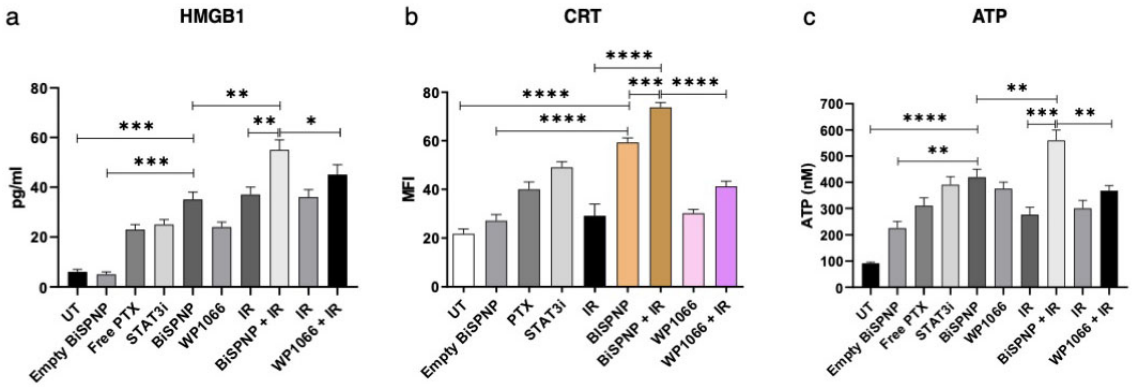

Figure 7.7: **biSPNPs enhance immunogenic cell death in mouse glioma cells. a)** Levels of immunogenic cell death (ICD) marker HMGB1 in GL26 cells were determined through ELISA following biSPNP treatment (at IC_{50} values) alone or in combination with 3Gy of IR. **b)** Levels of immunogenic cell death (ICD) marker Calreticulin (CRT) expression in GL26 cells were determined following biSPNP treatment (at IC_{50} values) alone or in combination with 3Gy of IR. **c)** Levels of ATP (marker of DAMPs) as ICD markers in the culture supernatants of GL26 cells were determined by ENLITEN ATP Assay kit according to manufacturers instructions following biSPNPs in combination with IR (3Gy) treatment. For all experiments, controls include combined (STAT3*i* + PTX), free-PTX, free-STAT3*i* and empty-biSPNPs at their respective IC_{50} values within the same experimental conditions. To compare the efficacy of biSPNPs with standard STAT3*i* inhibitor, cells were treated with either WP1066 (5 μM) or in combination with 3Gy of radiation and analyzed after 72 h. ns = non-significant, *$p < 0.05$ **$p < 0.01$, ***$p < 0.0001$, ****$p < 0.0001$; unpaired t-test. Bars represent mean ± SEM (n = 3 biological replicates).

7.3 Future Outlooks

The work presented in this dissertation serves as a framework for the further development of multifunctional nanoparticle systems. First validating the approach of dual drug delivery from a single nanoparticle system to achieve synergistic activity, we demonstrated a means to simultaneously target two distinct biological pathways. Taking advantage of responsive material properties and tumor-specific physiological traits, we engineered a nanoparticle system with responsive properties. We found that in modulating the bulk composition of the nanoparticles, controlled and decoupled release kinetics could be achieved. While the goal was to specifically deliver a synergistic combination of lapatinib and paclitaxel with temporal control, we found that release profiles were primarily dependent upon the bulk polymer properties and composition of the individual compartments, rather than the chemical structures and properties of the encapsulated materials. Additionally, this work led to the development of methods allowing for the release and cellular effects to be characterized. These findings, along with the versatility of the EHD co-jetting process, opens

the door to applying this same approach to an array of therapeutics directed at orthogonal disease pathways.

Our work quickly pivoted to the engineering of synthetic protein nanoparticles (SPNPs) with a goal of moving towards more biocompatible drug delivery systems. Throughout the development process, our work focused primarily on the evaluation of various proteins, crosslinking approaches, and encapsulated materials. In exploring this design space, we again found that the versatility of the EHD jetting process facilitated a wide range of materials to be incorporated into the final particle architecture. While a diverse library of synthetic routes were developed, this work only briefly explores the full potential of SPNP synthesis via EHD jetting. Current and future work within the group will undoubtedly continue to build on these methods. Here, we focused on the delivery of small molecule therapeutics and siRNA, briefly exploring their combined delivery. Potential exists for the incorporation of an array of both established and emerging technologies (e.g. plasmid delivery or CRISPR-Cas9) into the delivery platform. Just a handful of proteins were presented here; however, the library of proteins and enzymes to which the process can be applied is vast. One could envision multi-step, enzyme-catalyzed reactions taking place within a single particle architecture. Perhaps most exciting though, is the potential for new and functional macromers. The approach of developing responsive macromolecules capable of imparting specific and controllable properties to the overall particle system could have impacts including, but certainly not limited to, targeting cellular uptake mechanisms and controlled release kinetics.

Stepping beyond the bulk properties of SPNPs and how these contribute to particle architecture, we turned our attention to surface properties. Taking advantage of unique biological signatures of target sites, we aimed at creating a simple, yet adaptable, method of targeting SPNPs. Here, we leveraged chemical functional groups universally present in proteins alongside established bioorthogonal conjugation techniques to develop antibody-targeted protein nanoparticles. Validated in both *in vitro* and *in vivo* settings, we demonstrated selective cellular uptake and altered biodistribution, respectively. The approach of chemically conjugating antibodies to the particle surfaces translates to a targeting approach that is easily adapted through the identification and substitution of alternative antibodies specific to a disease or region of interest. Control of ligand density is easily achieved and modulated through stoichiometric ratios of staring materials. Furthermore, we developed alternative strategies compatible with multicompartmental particles; together with previous work demonstrating an ability to selectively modify regions of a single particle, we open a path towards controlled and sequential binding events. Future work will undoubtedly

extend this approach, and when combined with bulk properties, may be leveraged towards selective biodistribution, cellular targeting and transport, and intracellular trafficking.

In parallel to the work described above, we aimed to develop and validate a disease-specific application of SPNPs. Here, we were tasked with developing a particle system capable of penetrating the blood-brain barrier to target glioblastoma. Utilizing an alternative targeting approach, we drew upon previous work by our collaborators highlighting, i) a dependence on the STAT3 pathway in GBM, ii) overexpressed integrins (namely $\alpha v\beta 3$ and $\alpha v\beta 5$) within GBM, and iii) the integrin binding and tissue penetrating properties of iRGD. Together, we leveraged these properties, along with the compatibility of our SPNPs with peptides and siRNA, to develop a GBM-targeted nanoparticle system. Validated within a highly aggressive murine GBM model in combination with focused ionized radiation, we observed reproducible and sustained therapeutic effects. Speaking to the heterogeneous and dynamic disease landscape, previous work highlights the advantages, and often requirement, for the targeting of multiple pathways. Ongoing work described in this final chapter, highlights how we aim to build upon these promising results. Having established a means to penetrate the BBB in the diseased state, the development of multifunctional SPNPs targeting multiple biological pathways may prove to a significant advancement in GBM therapies not previously achieved. Future work to fully characterize the therapeutic impact and long-term effects will prove crucial to advancing the platform beyond the bench towards real clinical impacts for patients.

BIBLIOGRAPHY

[1] T. Sun, Y. S. Zhang, B. Pang, D. C. Hyun, M. Yang, and Y. Xia, "Engineered nanoparticles for drug delivery in cancer therapy," *Angew. Chemie - Int. Ed.*, vol. 53, no. 46, pp. 12320–12364, 2014.

[2] J. Shi, A. R. Votruba, O. C. Farokhzad, and R. Langer, "Nanotechnology in drug delivery and tissue engineering: From discovery to applications," *Nano Lett.*, vol. 10, no. 9, pp. 3223–3230, 2010.

[3] E. Blanco, H. Shen, and M. Ferrari, "Principles of nanoparticle design for overcoming biological barriers to drug delivery," *Nat. Biotechnol.*, vol. 33, no. 9, pp. 941–951, 2015.

[4] D. Peer, J. M. Karp, S. Hong, O. C. Farokhzad, R. Margalit, and R. Langer, "Nanocarriers as an emerging platform for cancer therapy," pp. 751–760, 2007.

[5] N. J. Abbott, L. Rönnbäck, and E. Hansson, "Astrocyte-endothelial interactions at the blood-brain barrier," *Nat. Rev. Neurosci.*, vol. 7, no. 1, pp. 41–53, 2006.

[6] H. Zou, Z. Wang, and M. Feng, "Nanocarriers with tunable surface properties to unblock bottlenecks in systemic drug and gene delivery," *J. Control. Release*, vol. 214, no. 81373332, pp. 121–133, 2015.

[7] N. Habibi, D. F. Quevedo, J. V. Gregory, and J. Lahann, "Emerging methods in therapeutics using multifunctional nanoparticles," *Wiley Interdiscip. Rev. Nanomedicine Nanobiotechnology*, vol. 12, no. 4, pp. 1–22, 2020.

[8] S. Rahmani, S. Ashraf, R. Hartmann, A. F. Dishman, M. V. Zyuzin, C. K. J. Yu, W. J. Parak, and J. Lahann, "Engineering of nanoparticle size via electrohydrodynamic jetting," *Bioeng. Transl. Med.*, vol. 1, no. 1, pp. 82–93, 2016.

[9] S. Rahmani, S. Saha, H. Durmaz, A. Donini, A. C. Misra, J. Yoon, and J. Lahann, "Chemically orthogonal three-patch microparticles," *Angew. Chemie - Int. Ed.*, vol. 53, no. 9, pp. 2332–2338, 2014.

[10] J. W. Myerson, P. N. Patel, N. Habibi, L. R. Walsh, Y. W. Lee, D. C. Luther, L. T. Ferguson, M. H. Zaleski, M. E. Zamora, O. A. Marcos-Contreras, P. M. Glassman, I. Johnston, E. D. Hood, T. Shuvaeva, J. V. Gregory, R. Y. Kiseleva, J. Nong, K. M. Rubey, C. F. Greineder, S. Mitragotri, G. S. Worthen, V. M. Rotello, J. Lahann, V. R. Muzykantov, and J. S. Brenner, "Supramolecular organization predicts pro-

tein nanoparticle delivery to neutrophils for acute lung inflammation diagnosis and treatment," *bioRxiv*, pp. 1–44, 2020.

[11] H. H. Assi, C. Paran, N. VanderVeen, J. Savakus, R. Doherty, E. Petruzzella, J. D. Hoeschele, H. Appelman, L. Raptis, T. Mikkelsen, P. R. Lowenstein, and M. G. Castro, "Preclinical characterization of signal transducer and activator of transcription 3 small molecule inhibitors for primary and metastatic brain cancer therapy.," *J. Pharmacol. Exp. Ther.*, vol. 349, no. 3, pp. 458–69, 2014.

[12] D. Guo, G. Xie, and J. Luo, "Mechanical properties of nanoparticles: Basics and applications," *J. Phys. D. Appl. Phys.*, vol. 47, no. 1, 2014.

[13] S. Lee, S. U. Choi, S. Li, and J. A. Eastman, "Measuring thermal conductivity of fluids containing oxide nanoparticles," *J. Heat Transfer*, vol. 121, no. 2, pp. 280–289, 1999.

[14] M. Qi, K. Zhang, S. Li, J. Wu, C. Pham-Huy, X. Diao, D. Xiao, and H. He, "Superparamagnetic Fe3O4 nanoparticles: Synthesis by a solvothermal process and functionalization for a magnetic targeted curcumin delivery system," *New J. Chem.*, vol. 40, no. 5, pp. 4480–4491, 2016.

[15] N. G. Khlebtsov and L. A. Dykman, "Optical properties and biomedical applications of plasmonic nanoparticles," *J. Quant. Spectrosc. Radiat. Transf.*, vol. 111, no. 1, pp. 1–35, 2010.

[16] A. D. Bangham, M. M. Standish, and J. C. Watkins, "Diffusion of univalent ions across the lamellae of swollen phospholipids," *J. Mol. Biol.*, vol. 13, no. 1, pp. 238–252, 1965.

[17] R. Langer and J. Folkman, "Polymers for the sustained release of proteins and other macromolecules," *Nature*, vol. 263, pp. 797–800, 1976.

[18] P. Arturson, T. Laakso, and P. Edman, "Acrylic microspheres in vivo IX: Blood elimination kinetics and organ distribution of microparticles with different surface characteristics," *J. Pharm. Sci.*, vol. 72, no. 12, pp. 1415–1420, 1983.

[19] L. D. Leserman, J. Barbet, F. Kourilsky, and J. N. Weinstein, "Targeting to cells of fluorescent liposomes covalently coupled with monoclonal antibody or protein A," *Nature*, vol. 288, no. 5791, pp. 602–604, 1980.

[20] J. W. Singer, "Paclitaxel poliglumex (XYOTAX, CT-2103): A macromolecular taxane," *J. Control. Release*, vol. 109, no. 1-3, pp. 120–126, 2005.

[21] A. C. Anselmo and S. Mitragotri, "Nanoparticles in the clinic: An update," *Bioeng. Transl. Med.*, vol. 4, no. 3, pp. 1–16, 2019.

[22] H. H. Gustafson, D. Holt-Casper, D. W. Grainger, and H. Ghandehari, "Nanoparticle uptake: The phagocyte problem," *Nano Today*, vol. 10, no. 4, pp. 487–510, 2015.

[23] A. Hamilton, L. Biganzoli, R. Coleman, L. Mauriac, P. Hennebert, A. Awada, M. Nooij, L. Beex, M. Piccart, I. Van Hoorebeeck, P. Bruning, and D. de Valeri-

ola, "EORTC 10968: A phase I clinical and pharamacokinetic study of polyethylene glycol liposomal doxorubicin (Caelyx®, Doxil®) at a 6-week interval in patients with metastatic breast cancer," *Ann. Oncol.*, vol. 13, no. 6, pp. 910–918, 2002.

[24] F. Alexis, E. Pridgen, L. K. Molnar, and O. C. Farokhzad, "Factors Affecting the Clearance and Biodistribution of Polymeric Nanoparticles," *Mol. Pharm.*, vol. 5, no. 4, pp. 505–15, 2008.

[25] P. L. Rodriguez, T. Harada, D. A. Christian, D. A. Pantano, R. K. Tsai, and D. E. Discher, "Minimal Self Peptides That Inhibit Phagocytic Clearance and Enhance Delivery of Nanoparticles," *Science (80-.).*, vol. 339, no. 6122, pp. 971–975, 2013.

[26] A. Parodi, N. Quattrocchi, A. L. Van De Ven, C. Chiappini, M. Evangelopoulos, J. O. Martinez, B. S. Brown, S. Z. Khaled, I. K. Yazdi, M. V. Enzo, L. Isenhart, M. Ferrari, and E. Tasciotti, "Synthetic nanoparticles functionalized with biomimetic leukocyte membranes possess cell-like functions," *Nat. Nanotechnol.*, vol. 8, no. 1, pp. 61–68, 2013.

[27] S. M. Moghimi and H. M. Patel, "Serum-mediated recognition of liposomes by phagocytic cells of the reticuloendothelial system - The concept of tissue specificity," *Adv. Drug Deliv. Rev.*, vol. 32, no. 1-2, pp. 45–60, 1998.

[28] P. Kolhar, A. C. Anselmo, V. Gupta, K. Pant, B. Prabhakarpandian, E. Ruoslahti, and S. Mitragotri, "Using shape effects to target antibody-coated nanoparticles to lung and brain endothelium.," *Proc. Natl. Acad. Sci. U. S. A.*, vol. 110, no. 26, 2013.

[29] A. J. Thompson and O. Eniola-Adefeso, "Dense nanoparticles exhibit enhanced vascular wall targeting over neutrally buoyant nanoparticles in human blood flow," *Acta Biomater.*, vol. 21, pp. 99–108, 2015.

[30] J. S. Brenner, D. C. Pan, J. W. Myerson, O. A. Marcos-contreras, C. H. Villa, P. Patel, H. Hekierski, S. Chatterjee, J.-q. Tao, H. Parhiz, K. Bhamidipati, T. G. Uhler, E. D. Hood, R. Y. Kiseleva, V. S. Shuvaev, T. Shuvaeva, M. Khoshnejad, I. Johnston, J. V. Gregory, J. Lahann, T. Wang, E. Cantu, W. M. Armstead, S. Mitragotri, and V. Muzykantov, "Red blood cell-hitchhiking boosts delivery of nanocarriers to chosen organs by orders of magnitude," *Nat. Commun.*, vol. 9, p. 2684, 2018.

[31] L. Wayteck, H. Dewitte, L. D. Backer, K. Breckpot, J. Demeester, S. C. D. Smedt, and K. Raemdonck, "Hitchhiking nanoparticles : Reversible coupling of lipid-based nanoparticles to cytotoxic T lymphocytes," *Biomaterials*, vol. 77, pp. 243–254, 2016.

[32] Y. Matsumura and H. Maeda, "A New Concept for Macromolecular Therapeutics in Cancer Chemotherapy: Mechanism of Tumoritropic Accumulation of Proteins and the Antitumor Agent Smancs," *Cancer Res.*, vol. 46, no. 8, pp. 6387–6392, 1986.

[33] K. Yokoi, T. Tanei, B. Godin, A. L. van de Ven, M. Hanibuchi, A. Matsunoki, J. Alexander, and M. Ferrari, "Serum biomarkers for personalization of nanotherapeutics- based therapy in different tumor and organ microenvironments," *Bone*, vol. 23, no. 1, pp. 1–7, 2014.

[34] C. H. Heldin, K. Rubin, K. Pietras, and A. Östman, "High interstitial fluid pressure - An obstacle in cancer therapy," *Nat. Rev. Cancer*, vol. 4, no. 10, pp. 806–813, 2004.

[35] B. Diop-Frimpong, V. P. Chauhan, S. Krane, Y. Boucher, and R. K. Jain, "Losartan inhibits collagen I synthesis and improves the distribution and efficacy of nanotherapeutics in tumors," *Proc. Natl. Acad. Sci. U. S. A.*, vol. 108, no. 7, pp. 2909–2914, 2011.

[36] C. R. Miller, B. Bondurant, S. D. McLean, K. A. McGovern, and D. F. O'Brien, "Liposome-cell interactions in vitro: Effect of liposome surface charge on the binding and endocytosis of conventional and sterically stabilized liposomes," *Biochemistry*, vol. 37, no. 37, pp. 12875–12883, 1998.

[37] K. Kettler, K. Veltman, D. van de Meent, A. van Wezel, and A. J. Hendriks, "Cellular uptake of nanoparticles as determined by particle properties, experimental conditions, and cell type," *Environ. Toxicol. Chem.*, vol. 33, no. 3, pp. 481–492, 2014.

[38] J. Lippincott-schwartz and G. W. Gould, "New roles for endosomes: from vesicular carriers to multi- purpose platforms," vol. 10, no. 4, pp. 287–292, 2013.

[39] J. P. Behr, "The proton sponge. A trick to enter cells the viruses did not exploit," *Chimia (Aarau).*, vol. 51, no. 1/2, pp. 34–36, 1997.

[40] W. J. Gradishar, "Albumin-bound paclitaxel: A next-generation taxane," *Expert Opin. Pharmacother.*, vol. 7, no. 8, pp. 1041–1053, 2006.

[41] L. Pelkmans, J. Kartenbeck, and A. Helenius, "Caveolar endocytosis of simian virus 40 reveals a new two-step vesicular-transport pathway to the ER," *Nat. Cell Biol.*, vol. 3, no. 5, pp. 473–483, 2001.

[42] A. L. Kiss and E. Botos, "Endocytosis via caveolae: Alternative pathway with distinct cellular compartments to avoid lysosomal degradation?," *J. Cell. Mol. Med.*, vol. 13, no. 7, pp. 1228–1237, 2009.

[43] K. Noguchi, K. Katayama, and Y. Sugimoto, "Human ABC transporter ABCG2/BCRP expression in chemoresistance: Basic and clinical perspectives for molecular cancer therapeutics," *Pharmgenomics. Pers. Med.*, vol. 7, no. 1, pp. 53–64, 2014.

[44] D. S. Miller, "Regulation of P-glycoprotein and other ABC drug transporters at the blood-brain barrier," *Bone*, vol. 23, no. 1, pp. 1–7, 2014.

[45] M. M. Gottesman, T. Fojo, and S. E. Bates, "Multidrug resistance in cancer: Role of ATP-dependent transporters," *Nat. Rev. Cancer*, vol. 2, no. 1, pp. 48–58, 2002.

[46] M. Dean, T. Fojo, and S. Bates, "Tumour stem cells and drug resistance," *Nat. Rev. Cancer*, vol. 5, no. 4, pp. 275–284, 2005.

[47] X. B. Xiong and A. Lavasanifar, "Traceable multifunctional micellar nanocarriers for cancer-targeted co-delivery of MDR-1 siRNA and doxorubicin," *ACS Nano*, vol. 5, no. 6, pp. 5202–5213, 2011.

[48] A. Sosnik, "Reversal of multidrug resistance by the inhibition of ATP-binding cassette pumps employing "Generally Recognized As Safe" (GRAS) nanopharmaceuticals: A review," *Adv. Drug Deliv. Rev.*, vol. 65, no. 13-14, pp. 1828–1851, 2013.

[49] D. F. Evans, G. Pye, R. Bramley, A. G. Clark, T. J. Dyson, and J. D. Hardcastle, "Measurement of gastrointestinal pH profiles in normal ambulant human subjects," *Gut*, vol. 29, no. 8, pp. 1035–1041, 1988.

[50] B. Homayun, X. Lin, and H. J. Choi, "Challenges and recent progress in oral drug delivery systems for biopharmaceuticals," *Pharmaceutics*, vol. 11, no. 3, 2019.

[51] J. C. Cuggino, E. R. O. Blanco, L. M. Gugliotta, C. I. Alvarez Igarzabal, and M. Calderón, "Crossing biological barriers with nanogels to improve drug delivery performance," *J. Control. Release*, vol. 307, no. April, pp. 221–246, 2019.

[52] R. Daneman and A. Prat, "The bloodbrain barrier," *South. African J. Anaesth. Analg.*, vol. 26, no. 6, pp. S32–S34, 2020.

[53] J. Zhang, J. Jin, and H. Zhao, "Surface-initiated free radical polymerization at the liquid-liquid interface: A one-step approach for the synthesis of amphiphilic janus silica particles," *Langmuir*, vol. 25, no. 11, pp. 6431–6437, 2009.

[54] Y. K. Takahara, S. Ikeda, S. Ishino, K. Tachi, K. Ikeue, T. Sakata, T. Hasegawa, H. Mori, M. Matsumura, and B. Ohtani, "Asymmetrically modified silica particles: A simple particulate surfactant for stabilization of oil droplets in water," *J. Am. Chem. Soc.*, vol. 127, no. 17, pp. 6271–6275, 2005.

[55] L. Petit, J. P. Manaud, C. Mingotaud, S. Ravaine, and E. Duguet, "Sub-micrometer silica spheres dissymmetrically decorated with gold nanoclusters," *Mater. Lett.*, vol. 51, no. 6, pp. 478–484, 2001.

[56] S. G. Jang, D. G. Choi, C. J. Heo, S. Y. Lee, and S. M. Yang, "Nanoscopic ordered voids and metal caps by controlled trapping of colloidal particles at polymeric film surfaces," *Adv. Mater.*, vol. 20, no. 24, pp. 4862–4867, 2008.

[57] Y. P. Zhao, D. X. Ye, G. C. Wang, and T. M. Lu, "Novel Nano-Column and Nano-Flower Arrays by Glancing Angle Deposition," *Nano Lett.*, vol. 2, no. 4, pp. 351–354, 2002.

[58] G. Nikravan, V. Haddadi-asl, and M. Salami-kalajahi, "Synthesis of dual temperature and pH-responsive yolk-shell nanoparticles by conventional etching and new deswelling approaches: DOX release behavior," *Colloids Surfaces B Biointerfaces*, vol. 165, pp. 1–8, 2018.

[59] K. B. Shepard, D. A. Christie, C. L. Sosa, C. B. Arnold, R. D. Priestley, K. B. Shepard, D. A. Christie, C. L. Sosa, and C. B. Arnold, "Patchy Janus particles with tunable roughness and composition via vapor-assisted deposition of macromolecules Patchy Janus particles with tunable roughness and composition via vapor-assisted deposition of macromolecules," *Adv. Funct. Mater.*, 2015.

[60] B. Y. Liang, J. H. Jordahl, H. Ding, X. Deng, and J. Lahann, "Uniform Coating of Microparticles using CVD Polymerization ÃÃ," pp. 288–293, 2015.

[61] A. M. Yake, A. S. Zahr, H. A. Jerri, M. V. Pishko, and D. Velegol, "Localized functionalization of individual colloidal carriers for cell targeting and imaging," *Biomacromolecules*, vol. 8, no. 6, pp. 1958–1965, 2007.

[62] V. Lopez, M. Rocio Villegas, V. Rodriguez, G. Villaverde, D. Lozano, A. Baeza, and M. Vallet-Regi, "Janus Mesoporous Silica Nanoparticles for Dual Targeting of Tumor Cells and Mitochondria," *Appl. Mater. Interfaces*, vol. 9, pp. 26697–26706, 2017.

[63] B. C. Geiger, S. Wang, R. F. P. Jr, A. J. Grodzinsky, and P. T. Hammond, "Cartilage-penetrating nanocarriers improve delivery and efficacy of growth factor treatment of osteoarthritis," vol. 1, no. November, 2018.

[64] D. Varadharajan, H. Turgut, J. Lahann, H. Yabu, and G. Delaittre, "Surface-Reactive Patchy Nanoparticles and Nanodiscs Prepared by Tandem Nanoprecipitation and Internal Phase Separation," *Adv. Funct. Mater.*, pp. 1–11, 2018.

[65] A. Shimoda, S.-i. Sawada, A. Kano, A. Maruyama, M. Winnik, and K. Akiyoshi, "Dual crosslinked hydrogel nanoparticles by nanogel bottom-up method for sustained-release delivery," *Colloids Surfaces B Biointerfaces*, vol. 99, pp. 38–44, 2012.

[66] J. Song, B. Wu, Z. Zhou, G. Zhu, Y. Liu, Z. Yang, L. Lin, G. Yu, F. Zhang, G. Zhang, H. Duan, G. D. Stucky, and X. Chen, "Double-Layered PlasmonicMagnetic Vesicles by Self-Assembly of Janus Amphiphilic GoldIron(II,III) Oxide Nanoparticles," *Angew. Chemie - Int. Ed.*, vol. 56, no. 28, pp. 8110–8114, 2017.

[67] N. Castro, D. Constantin, P. Davidson, and B. Abécassis, "Solution self-assembly of plasmonic Janus nanoparticles," *Soft Matter*, vol. 12, no. 48, pp. 9666–9673, 2016.

[68] S. W. Morton, M. J. Lee, Z. J. Deng, E. C. Dreaden, E. Siouve, K. E. Shopsowitz, N. J. Shah, M. B. Yaffe, P. T. Hammond, M. L. Mcmaster, S. Y. Kristinsson, I. Turesson, M. Bjorkholm, O. Landgren, S. W. Morton, M. J. Lee, Z. J. Deng, E. C. Dreaden, E. Siouve, K. E. Shopsowitz, N. J. Shah, M. B. Yaffe, and P. T. Hammond, "A nanoparticle-based combination chemotherapy delivery system for enhanced tumor killing by dynamic rewiring of signaling pathways," *Sci. Signal.*, vol. 7, may 2014.

[69] T. L. Reddy, K. Rao, S. G. Reddy, B. V. S. Reddy, J. S. Yadav, U. Bhadra, and M. P. Bhadra, "Simultaneous delivery of Paclitaxel and Bcl-2 siRNA via pH-Sensitive liposomal nanocarrier for the synergistic treatment of melanoma," no. June, pp. 1–12, 2016.

[70] C. Subramanian, P. T. White, B. N. Timmermann, J. J. Moon, M. S. Cohen, and A. Schwendeman, "Synthetic high-density lipoprotein nanodisks for targeted withalongolide delivery to adrenocortical carcinoma," pp. 6581–6594, 2017.

[71] Y. Guo, W. Yuan, B. Yu, R. Kuai, W. Hu, E. E. Morin, M. T. Garcia-Barrio, J. Zhang, J. J. Moon, A. Schendeman, and Y. E. Chen, "Synthetic High-Density Lipoprotein-Mediated Targeted Delivery of Liver X Receptors Agonist Promotes Atherosclerosis Regression.pdf," *EBio Med.*, 2018.

[72] K. P. Yuet, D. K. Hwang, R. Haghogooie, and P. S. Doyle, "Multifunctional Superparamagnetic Janus Particles," *Langmuir*, vol. 26, no. 6, pp. 4281–87, 2010.

[73] Z. Nie, W. Li, M. Seo, S. Xu, and E. Kumacheva, "Janus and ternary particles generated by microfluidic synthesis: Design, synthesis, and self-assembly," *J. Am. Chem. Soc.*, vol. 128, no. 29, pp. 9408–9412, 2006.

[74] K.-h. Roh, D. C. Martin, and J. Lahann, "Biphasic Janus particles with nanoscale anisotropy.," *Nat. Mater.*, vol. 4, no. 10, pp. 759–763, 2005.

[75] S. Hwang, K.-H. Roh, D. W. Lim, G. Wang, C. Uher, and J. Lahann, "Anisotropic hybrid particles based on electrohydrodynamic co-jetting of nanoparticle suspensions," *Phys. Chem. Chem. Phys.*, vol. 12, no. 38, p. 11894, 2010.

[76] Y. Wang, Y. Zhang, and B. Wang, "Fabrication of core shell micro / nanoparticles for programmable dual drug release by emulsion electrospraying," 2013.

[77] Y. Cao, B. Wang, Y. Wang, and D. Lou, "Dual Drug Release from Core Shell Nanoparticles with Distinct Release Profiles," *J. Pharm. Sci.*, vol. 103, no. 10, pp. 3205–3216, 2014.

[78] R. Nahire, M. K. Haldar, S. Paul, A. Mergoum, A. H. Ambre, K. S. Katti, K. N. Gange, D. Srivastava, K. Sarkar, and S. Mallik, "Polymer Coated Echogenic Lipid Nanoparticles with Dual Release Triggers," *Biomacromolecules*, vol. 14, no. 3, pp. 841–853, 2013.

[79] Z. J. Deng, S. W. Morton, E. Ben-Akiva, E. C. Dreaden, K. E. Shopsowitz, and P. T. Hammond, "Layer-by-layer nanoparticles for systemic codelivery of an anticancer drug and siRNA for potential triple-negative breast cancer treatment," *ACS Nano*, vol. 7, no. 11, pp. 9571–9584, 2013.

[80] L. Palanikumar, M. T. Jeena, K. Kim, J. Y. Oh, C. Kim, M.-h. Park, and J.-h. Ryu, "Spatiotemporally and Sequentially- Controlled Drug Release from Polymer Gatekeeper Hollow Silica Nanoparticles," *Sci. Rep.*, vol. 7, no. March, pp. 1–11, 2017.

[81] Y. Liu, B. Huang, J. Zhu, K. Feng, Y. Yuan, and C. Liu, "Dual-generation dendritic mesoporous silica nanoparticles for co-delivery and kinetically sequential drug release," *R. Soc. Chem.*, vol. 8, pp. 40598–40610, 2018.

[82] S. Hwang and J. Lahann, "Differentially degradable janus particles for controlled release applications.," *Macromol. Rapid Commun.*, vol. 33, no. 14, pp. 1178–83, 2012.

[83] S. Rahmani, A. M. Ross, T.-H. H. Park, H. Durmaz, A. F. Dishman, D. M. Prieskorn, N. Jones, R. A. Altschuler, and J. Lahann, "Dual Release Carriers for Cochlear Delivery," *Adv. Healthc. Mater.*, vol. 5, no. 1, pp. 94–100, 2016.

[84] M. S. Strozyk, D. J. D. Aberasturi, J. V. Gregory, M. Brust, J. Lahann, and L. M. Liz-marzán, "Spatial Analysis of Metal PLGA Hybrid Microstructures Using 3D SERS Imaging," vol. 27, p. 1701626, 2017.

[85] A. C. Misra, S. Bhaskar, N. Clay, and J. Lahann, "Multicompartmental particles for combined imaging and siRNA delivery," *Adv. Mater.*, vol. 24, no. 28, pp. 3850–3856, 2012.

[86] S. Rahmani, C. H. Villa, A. F. Dishman, M. E. Grabowski, D. C. Pan, H. Durmaz, A. C. Misra, L. Colón-Meléndez, M. J. Solomon, V. R. Muzykantov, and J. Lahann, "Long-circulating Janus nanoparticles made by electrohydrodynamic co-jetting for systemic drug delivery applications," *J. Drug Target.*, vol. 23, no. 7-8, pp. 750–758, 2015.

[87] R. P. Garay, R. El-Gewely, J. K. Armstrong, G. Garratty, and P. Richette, "Antibodies against polyethylene glycol in healthy subjects and in patients treated with PEG-conjugated agents," *Expert Opin. Drug Deliv.*, vol. 9, no. 11, pp. 1319–1323, 2012.

[88] P. Zhang, F. Sun, S. Liu, and S. Jiang, "Anti-PEG antibodies in the clinic: current issues and beyond PEGylation," *J. Control. Release*, vol. 284, pp. 183–193, 2016.

[89] K.-H. Roh, M. Yoshida, and L, "Water-Stable Biphasic Nanocolloids with Potential Use as Anisotropic Imaging Probes," *Nano Lett.*, vol. 7, no. 4, pp. 1081–1085, 2007.

[90] T.-H. H. Park, T. W. Eyster, J. M. Lumley, S. Hwang, K. J. Lee, A. Misra, S. Rahmani, and J. Lahann, "Photoswitchable Particles for On-Demand Degradation and Triggered Release," *Small*, vol. 9, no. 18, pp. 3051–3057, 2013.

[91] A. C. Misra, K. E. Luker, H. Durmaz, G. D. Luker, and J. Lahann, "CXCR4-Targeted Nanocarriers for Triple Negative Breast Cancers," *Biomacromolecules*, vol. 16, pp. 2412–2417, 2015.

[92] J. H. Jordahl, S. Ramcharan, J. V. Gregory, and J. Lahann, "Needleless Electrohydrodynamic Cojetting of Bicompartmental Particles and Fibers from an Extended Fluid Interface," *Macromol. Rapid Commun.*, vol. 38, no. 1, pp. 1–7, 2017.

[93] K. H. Roh, D. C. Martin, and J. Lahann, "Triphasic nanocolloids," *J. Am. Chem. Soc.*, vol. 128, no. 21, pp. 6796–6797, 2006.

[94] D. W. Lim, S. Hwang, O. Uzun, F. Stellacci, and J. Lahann, "Compartmentalization of gold nanocrystals in polymer microparticles using electrohydrodynamic co-jetting," *Macromol. Rapid Commun.*, vol. 31, no. 2, pp. 176–182, 2010.

[95] J. Yoon, K. J. Lee, and J. Lahann, "Multifunctional polymer particles with distinct compartments," *J. Mater. Chem.*, vol. 21, no. 24, pp. 8502–8510, 2011.

[96] S. Rahmani, T. H. Park, A. F. Dishman, and J. Lahann, "Multimodal delivery of irinotecan from microparticles with two distinct compartments," *J. Control. Release*, vol. 172, no. 1, pp. 239–245, 2013.

[97] E. Sokolovskaya, S. Rahmani, A. C. Misra, S. Brase, and J. Lahann, "Dual-stimuli-responsive microparticles," *ACS Appl. Mater. Interfaces*, vol. 7, no. 18, pp. 9744–9751, 2015.

[98] M. Á. Fernández-Rodríguez, S. Rahmani, C. K. Yu, M. Á. Rodríguez-Valverde, M. Á. Cabrerizo-Vílchez, C. A. Michel, J. Lahann, and R. Hidalgo-Álvarez, "Synthesis and interfacial activity of PMMA/PtBMA Janus and homogeneous nanoparticles at water/oil interfaces," *Colloids Surfaces A Physicochem. Eng. Asp.*, 2016.

[99] J. V. Gregory, D. R. Vogus, A. Barajas, M. A. Cadena, S. Mitragotri, and J. Lahann, "Programmable Delivery of Synergistic Cancer Drug Combinations Using Bicompartmental Nanoparticles," *Adv. Healthc. Mater.*, vol. 9, no. 21, pp. 1–11, 2020.

[100] G. I. Taylor, "Disintegration of water drops in an electric field," *Proc. R. Soc. A*, vol. 280, no. February, pp. 383–97, 1964.

[101] K. J. Lee, S. Hwang, J. Yoon, S. Bhaskar, T.-H. Park, and J. Lahann, "Compartmentalized photoreactions within compositionally anisotropic Janus microstructures.," *Macromol. Rapid Commun.*, vol. 32, no. 5, pp. 431–7, 2011.

[102] S. Bhaskar, K. M. Pollock, M. Yoshida, and J. Lahann, "Towards designer microparticles: simultaneous control of anisotropv, shape and size," *Small*, vol. 6, no. 3, pp. 404–411, 2010.

[103] K. J. Lee, J. Yoon, S. Rahmani, S. Hwang, S. Bhaskar, S. Mitragotri, and J. Lahann, "Spontaneous shape reconfigurations in multicompartmental microcylinders," *Proc. Natl. Acad. Sci.*, vol. 109, no. 40, pp. 16057–16062, 2012.

[104] J. V. Gregory, P. Kadiyala, R. Doherty, M. Cadena, S. Habeel, E. Ruoslahti, P. R. Lowenstein, M. G. Castro, and J. Lahann, "Systemic brain tumor delivery of synthetic protein nanoparticles for glioblastoma therapy," *Nat. Commun.*, vol. 11, no. 1, pp. 1–15, 2020.

[105] N. Habibi, S. Christau, L. J. Ochyl, Z. Fan, A. Hassani Najafabadi, M. Kuehnhammer, M. Zhang, M. Helgeson, R. Klitzing, J. J. Moon, and J. Lahann, "Engineered Ovalbumin Nanoparticles for Cancer Immunotherapy," *Adv. Ther.*, vol. 3, no. 10, p. 2000100, 2020.

[106] D. F. Quevedo, N. Habibi, J. V. Gregory, Y. Hernandez, T. D. Brown, R. Miki, B. N. Plummer, S. Rahmani, J. E. Raymond, S. Mitragotri, and J. Lahann, "Multifunctional Synthetic Protein Nanoparticles via Reactive Electrojetting," *Macromol. Rapid Commun.*, vol. 2000425, pp. 1–7, 2020.

[107] R. B. Mokhtari, T. S. Homayouni, N. Baluch, E. Morgatskaya, S. Kumar, B. Das, and H. Yeger, "Combination therapy in combating cancer," *Oncotarget*, vol. 8, no. 23, pp. 38022–38043, 2017.

[108] X. Xu, W. Ho, X. Zhang, N. Bertrand, and O. Farokhzad, "Cancer nanomedicine: From targeted delivery to combination therapy," *Trends Mol. Med.*, vol. 21, no. 4, pp. 223–232, 2015.

[109] J. B. Fitzgerald, B. Schoeberl, U. B. Nielsen, and P. K. Sorger, "Systems biology and combination therapy in the quest for clinical efficacy," *Nat. Chem. Biol.*, vol. 2, no. 9, pp. 458–466, 2006.

[110] J. Jia, F. Zhu, X. Ma, Z. W. Cao, Y. X. Li, and Y. Z. Chen, "Mechanisms of drug combinations: Interaction and network perspectives," *Nat. Rev. Drug Discov.*, vol. 8, no. 2, pp. 111–128, 2009.

[111] Z. Sheng, Y. Sun, Z. Yin, K. Tang, and Z. Cao, "Advances in computational approaches in identifying synergistic drug combinations," *Brief. Bioinform.*, vol. 19, no. 6, pp. 1172–1182, 2017.

[112] L. D. Mayer and A. S. Janoff, "Optimizing combination chemotherapy by controlling drug ratios," *Mol. Interv.*, vol. 7, no. 4, pp. 216–223, 2007.

[113] P. Nowak-Sliwinska, A. Weiss, X. Ding, P. J. Dyson, H. Van Den Bergh, A. W. Griffioen, and C. M. Ho, "Optimization of drug combinations using Feedback System Control," *Nat. Protoc.*, vol. 11, no. 2, pp. 302–315, 2016.

[114] S. Y. Qin, Y. J. Cheng, Q. Lei, A. Q. Zhang, and X. Z. Zhang, "Combinational strategy for high-performance cancer chemotherapy," *Biomaterials*, vol. 171, pp. 178–197, 2018.

[115] K. A. Ryall and A. C. Tan, "Systems biology approaches for advancing the discovery of effective drug combinations Rajarshi Guha," *J. Cheminform.*, vol. 7, no. 1, pp. 1–15, 2015.

[116] C. M. J. Hu and L. Zhang, "Nanoparticle-based combination therapy toward overcoming drug resistance in cancer," *Biochem. Pharmacol.*, vol. 83, no. 8, pp. 1104–1111, 2012.

[117] T. Patel, J. Zhou, J. M. Piepmeier, and W. M. Saltzman, "Polymeric nanoparticles for drug delivery to the central nervous system," *Adv. Drug Deliv. Rev.*, vol. 64, no. 7, pp. 701–705, 2012.

[118] S. Stolnik, L. Illum, and S. S. Davis, "Long circulating microparticulate drug carriers," *Adv. Drug Deliv. Rev.*, vol. 64, no. SUPPL., pp. 290–301, 2012.

[119] E. M. Pridgen, R. Langer, and O. C. Farokhzad, "Biodegradable, polymeric nanoparticle delivery systems for cancer therapy," *Nanomedicine*, vol. 2, no. 5, pp. 669–680, 2007.

[120] K. J. Lee, J. Yoon, and J. Lahann, "Recent advances with anisotropic particles," *Curr. Opin. Colloid Interface Sci.*, vol. 16, no. 3, pp. 195–202, 2011.

[121] Y. Qie, H. Yuan, C. A. Von Roemeling, Y. Chen, X. Liu, K. D. Shih, J. A. Knight, H. W. Tun, R. E. Wharen, W. Jiang, and B. Y. Kim, "Surface modification of nanoparticles enables selective evasion of phagocytic clearance by distinct macrophage phenotypes," *Sci. Rep.*, vol. 6, no. January, pp. 1–11, 2016.

[122] T. C. Chou and P. Talalay, "Quantitative analysis of dose-effect relationships: the combined effects of multiple drugs or enzyme inhibitors," *Adv. Enzyme Regul.*, vol. 22, pp. 27–55, jan 1984.

[123] E. M. Bachelder, T. T. Beaudette, K. E. Broaders, J. Dashe, and J. M. J. Fréchet, "Acetal-derivatized dextran: An acid-responsive biodegradable material for therapeutic applications," *J. Am. Chem. Soc.*, vol. 130, no. 32, pp. 10494–10495, 2008.

[124] H. M. Borteh, M. D. Gallovic, S. Sharma, K. J. Peine, S. Miao, D. J. Brackman, K. Gregg, Y. Xu, X. Guo, J. Guan, E. M. Bachelder, and K. M. Ainslie, "Electrospun acetalated dextran scaffolds for temporal release of therapeutics," *Langmuir*, vol. 29, no. 25, pp. 7957–7965, 2013.

[125] K. E. Broaders, J. A. Cohen, T. T. Beaudette, E. M. Bachelder, and J. M. Fréchet, "Acetalated dextran is a chemically and biologically tunable material for particulate immunotherapy," *Proc. Natl. Acad. Sci. U. S. A.*, vol. 106, no. 14, pp. 5497–5502, 2009.

[126] D. A. Yardley, L. Hart, L. Bosserman, M. N. Salleh, D. M. Waterhouse, M. K. Hagan, P. Richards, M. L. Desilvio, J. M. Mahoney, and Y. Nagarwala, "Phase II study evaluating lapatinib in combination with nab-paclitaxel in HER2-overexpressing metastatic breast cancer patients who have received no more than one prior chemotherapeutic regimen," *Breast Cancer Res. Treat.*, vol. 137, no. 2, pp. 457–464, 2013.

[127] A. Di Leo, H. L. Gomez, Z. Aziz, Z. Zvirbule, J. Bines, M. C. Arbushites, S. F. Guerrera, M. Koehler, C. Oliva, S. H. Stein, L. S. Williams, J. Dering, R. S. Finn, and M. F. Press, "Phase III, double-blind, randomized study comparing lapatinib plus paclitaxel with placebo plus paclitaxel as first-line treatment for metastatic breast cancer," *J. Clin. Oncol.*, vol. 26, no. 34, pp. 5544–5552, 2008.

[128] N. M. Iyengar, M. N. Fornier, S. M. Sugarman, M. Theodoulou, T. A. Troso-Sandoval, G. M. D'Andrea, P. R. Drullinsky, D. Gajria, S. B. Goldfarb, E. A. Comen, D. E. Lake, S. Modi, T. A. Traina, M. E. Lacouture, M. F. Chen, S. Patil, J. Baselga, L. Norton, C. A. Hudis, and C. T. Dang, "A Pilot Study of Dose-Dense Paclitaxel with Trastuzumab and Lapatinib for Node-negative HER2-Overexpressed Breast Cancer," *Clin. Breast Cancer*, vol. 16, no. 2, pp. 87–94, 2016.

[129] R. S. Finn, M. F. Press, J. Dering, M. Arbushites, M. Koehler, C. Oliva, L. S. Williams, and A. Di Leo, "Estrogen receptor, progesterone receptor, human epidermal growth factor receptor 2 (HER2), and epidermal growth factor receptor expression and benefit from lapatinib in a randomized trial of paclitaxel with lapatinib or placebo as first-line treatment in ," *J. Clin. Oncol.*, vol. 27, no. 24, pp. 3908–3915, 2009.

[130] J. Baselga, I. Bradbury, H. Eidtmann, S. Di Cosimo, E. De Azambuja, C. Aura, H. Gómez, P. Dinh, K. Fauria, V. Van Dooren, G. Aktan, A. Goldhirsch, T. W. Chang, Z. Horváth, M. Coccia-Portugal, J. Domont, L. M. Tseng, G. Kunz, J. H. Sohn, V. Semiglazov, G. Lerzo, M. Palacova, V. Probachai, L. Pusztai, M. Untch, R. D.

Gelber, and M. Piccart-Gebhart, "Lapatinib with trastuzumab for HER2-positive early breast cancer (NeoALTTO): A randomised, open-label, multicentre, phase 3 trial," *Lancet*, vol. 379, no. 9816, pp. 633–640, 2012.

[131] R. Butti, S. Das, V. P. Gunasekaran, A. S. Yadav, D. Kumar, and G. C. Kundu, "Receptor tyrosine kinases (RTKs) in breast cancer: Signaling, therapeutic implications and challenges," *Mol. Cancer*, vol. 17, no. 1, pp. 1–18, 2018.

[132] M. Vouri and S. Hafizi, "TAM receptor tyrosine kinases in cancer drug resistance," *Cancer Res.*, vol. 77, no. 11, pp. 2775–2778, 2017.

[133] Y. Wei, S. Xu, F. Wang, A. Zou, S. Zhang, Y. Xiong, S. Cao, Q. Zhang, Y. Wang, and X. Jiang, "A novel combined micellar system of lapatinib and paclitaxel with enhanced antineoplastic effect against human epidermal growth factor receptor-2 positive breast tumor in vitro," *J. Pharm. Sci.*, vol. 104, no. 1, pp. 165–177, 2015.

[134] A. Di Leo, H. L. Gomez, Z. Aziz, Z. Zvirbule, J. Bines, M. C. Arbushites, S. F. Guerrera, M. Koehler, C. Oliva, S. H. Stein, L. S. Williams, J. Dering, R. S. Finn, and M. F. Press, "Phase III, double-blind, randomized study comparing lapatinib plus paclitaxel with placebo plus paclitaxel as first-line treatment for metastatic breast cancer," *J. Clin. Oncol.*, vol. 26, pp. 5544–5552, dec 2008.

[135] A. J. Chien, J. A. Illi, A. H. Ko, W. M. Korn, L. Fong, L.-m. M. Chen, M. Kashani-Sabet, C. J. Ryan, J. E. Rosenberg, S. Dubey, E. J. Small, T. M. Jahan, N. M. Hylton, B. M. Yeh, Y. Huang, K. M. Koch, and M. M. Moasser, "A phase I study of a 2-day lapatinib chemosensitization pulse preceding nanoparticle albumin-bound paclitaxel for advanced solid malignancies," *Clin. Cancer Res.*, vol. 15, pp. 5569–5575, sep 2009.

[136] J. Perry, E. Ghazaly, C. Kitromilidou, E. H. McGrowder, S. Joel, and T. Powles, "A Synergistic Interaction between Lapatinib and Chemotherapy Agents in a Panel of Cell Lines Is Due to the Inhibition of the Efflux Pump BCRP," *Mol. Cancer Ther.*, vol. 9, no. 12, pp. 3322–3329, 2010.

[137] F. Li, M. Danquah, S. Singh, H. Wu, and R. Mahato, "Paclitaxel- and lapatinib-loaded lipopolymer micelles overcome multidrug resistance in prostate cancer," *Drug Deliv. Transl. Res.*, vol. 1, no. 6, pp. 420–428, 2011.

[138] P. D. Kelishady, E. Saadat, F. Ravar, H. Akbari, F. Dorkoosh, P. Dehghan Kelishady, E. Saadat, F. Ravar, H. Akbari, and F. Dorkoosh, "Pluronic F127 polymeric micelles for co-delivery of paclitaxel and lapatinib against metastatic breast cancer: Preparation, optimization and in vitro evaluation," *Pharm. Dev. Technol.*, vol. 20, no. 8, pp. 1009–1017, 2015.

[139] P. Dehghankelishadi, E. Saadat, F. Ravar, M. Safavi, M. Pordeli, M. Gholami, and F. A. Dorkoosh, "In vitro and in vivo evaluation of paclitaxellapatinib-loaded F127 pluronic micelles," *Drug Dev. Ind. Pharm.*, vol. 43, no. 3, pp. 390–398, 2017.

[140] F. Ravar, E. Saadat, P. D. Kelishadi, and F. A. Dorkoosh, "Liposomal formulation for co-delivery of paclitaxel and lapatinib, preparation, characterization and optimization," *J. Liposome Res.*, vol. 26, no. 3, pp. 175–187, 2016.

[141] H. Hu, Z. Lin, B. He, W. Dai, X. Wang, J. Wang, X. Zhang, H. Zhang, and Q. Zhang, "A novel localized co-delivery system with lapatinib microparticles and paclitaxel nanoparticles in a peritumorally injectable in situ hydrogel," *J. Control. Release*, vol. 220, pp. 189–200, 2015.

[142] D. Vergara, C. Bellomo, X. Zhang, V. Vergaro, A. Tinelli, V. Lorusso, R. Rinaldi, Y. M. Lvov, S. Leporatti, and M. Maffia, "Lapatinib/Paclitaxel polyelectrolyte nanocapsules for overcoming multidrug resistance in ovarian cancer.," *Nanomedicine*, vol. 8, pp. 891–9, aug 2012.

[143] S. Lee, W. Yang, K.-H. Lan, S. Sellappan, K. Klos, G. Hortobagyi, M.-C. Hung, and D. Yu, "Enhanced Sensitization to Taxol-induced Apoptosis by Herceptin Pretreatment in ErbB2-overexpressing Breast Cancer Cells," *Cancer Res.*, vol. 62, pp. 5703–5710, oct 2002.

[144] Y. S. Kwon, S. Y. Chun, K. S. Nam, and S. Kim, "Lapatinib sensitizes quiescent MDA-MB-231 breast cancer cells to doxorubicin by inhibiting the expression of multidrug resistance-associated protein-1," *Oncol. Rep.*, vol. 34, no. 2, pp. 884–890, 2015.

[145] S. Sengupta, D. Eavarone, I. Capila, G. Zhao, N. Watson, T. Kiziltepe, and R. Sasisekharan, "Temporal targeting of tumour cells and neovasculature with a nanoscale delivery system.," *Nature*, vol. 436, pp. 568–72, jul 2005.

[146] Z. Wang and P. C. Ho, "A nanocapsular combinatorial sequential drug delivery system for antiangiogenesis and anticancer activities.," *Biomaterials*, vol. 31, pp. 7115–23, sep 2010.

[147] Y. He, Z. Su, L. Xue, H. Xu, and C. Zhang, "Co-delivery of erlotinib and doxorubicin by pH-sensitive charge conversion nanocarrier for synergistic therapy," *J. Control. Release*, vol. 229, pp. 80–=92, 2016.

[148] M. J. Hawkins, P. Soon-Shiong, and N. Desai, "Protein nanoparticles as drug carriers in clinical medicine," *Adv. Drug Deliv. Rev.*, vol. 60, no. 8, pp. 876–885, 2008.

[149] T. O. Yeates, Y. Liu, and J. Laniado, "The design of symmetric protein nanomaterials comes of age in theory and practice," *Curr. Opin. Struct. Biol.*, vol. 39, pp. 134–143, 2016.

[150] K. Langer, S. Balthasar, V. Vogel, N. Dinauer, H. Von Briesen, and D. Schubert, "Optimization of the preparation process for human serum albumin (HSA) nanoparticles," *Int. J. Pharm.*, vol. 257, no. 1-2, pp. 169–180, 2003.

[151] U. G. Spizzirri, F. Iemma, F. Puoci, G. Cirillo, M. Curcio, O. I. Parisi, and N. Picci, "Synthesis of antioxidant polymers by grafting of gallic acid and catechin on gelatin," *Biomacromolecules*, vol. 10, no. 7, pp. 1923–1930, 2009.

[152] G. Cirillo, K. Kraemer, S. Fuessel, F. Puoci, M. Curcio, U. G. Spizzirri, I. Altimari, and F. Iemma, "Biological activity of a gallic acid-gelatin conjugate," *Biomacromolecules*, vol. 11, no. 12, pp. 3309–3315, 2010.

[153] N. Desai, "(Patent Application Publication Pub. No.: US 2017/0139001 A1," 2017.

[154] F. Kratz, "Albumin as a drug carrier: Design of prodrugs, drug conjugates and nanoparticles," *J. Control. Release*, vol. 132, no. 3, pp. 171–183, 2008.

[155] T. Peters, *All about albumin: biochemistry, genetics, and medical applications*. London: Academic Press Inc. (London) Ltd., 1995.

[156] S. Rhaese, H. Von Briesen, H. Rübsamen-Waigmann, J. Kreuter, and K. Langer, "Human serum albumin-polyethylenimine nanoparticles for gene delivery," *J. Control. Release*, vol. 92, no. 1-2, pp. 199–208, 2003.

[157] G. L. Francis, "Albumin and mammalian cell culture: Implications for biotechnology applications," *Cytotechnology*, vol. 62, no. 1, pp. 1–16, 2010.

[158] E. Engvall and P. Perlmann, "Enzyme-Linked Immunosorbent Assay, ELISA," *J. Immunol.*, vol. 109, no. 1, pp. 129–135, 1972.

[159] K. Bolaños, M. J. Kogan, and E. Araya, "Capping gold nanoparticles with albumin to improve their biomedical properties," *Int. J. Nanomedicine*, vol. 14, pp. 6387–6406, 2019.

[160] F. Cañaveras, R. Madueño, J. M. Sevilla, M. Blázquez, and T. Pineda, "Role of the functionalization of the gold nanoparticle surface on the formation of bioconjugates with human serum albumin," *J. Phys. Chem. C*, vol. 116, no. 18, pp. 10430–10437, 2012.

[161] F. E. Galdino, A. S. Picco, M. L. Sforca, M. B. Cardoso, and W. Loh, "Effect of particle functionalization and solution properties on the adsorption of bovine serum albumin and lysozyme onto silica nanoparticles," *Colloids Surfaces B Biointerfaces*, vol. 186, no. June 2019, p. 110677, 2020.

[162] W. D. Luedtke, U. Landman, Y. H. Chiu, D. J. Levandier, R. A. Dressler, S. Sok, and M. S. Gordon, "Nanojets, electrospray, and ion field evaporation: Molecular dynamics simulations and laboratory experiments," *J. Phys. Chem. A*, vol. 112, no. 40, pp. 9628–9649, 2008.

[163] C. Chauvierre, M. C. Marden, C. Vauthier, D. Labarre, P. Couvreur, and L. Leclerc, "Heparin coated poly(alkylcyanoacrylate) nanoparticles coupled to hemoglobin: A new oxygen carrier," *Biomaterials*, vol. 25, no. 15, pp. 3081–3086, 2004.

[164] H. Su, X. Liu, J. Du, X. Deng, and Y. Fan, "The role of hemoglobin in nitric oxide transport in vascular system," *Med. Nov. Technol. Devices*, vol. 5, no. April, p. 100034, 2020.

[165] E. H. Morgan, "Transferrin, biochemistry, physiology and clinical significance," *Mol. Aspects Med.*, vol. 4, no. 1, pp. 1–123, 1981.

[166] H. Li, H. Sun, and Z. M. Qian, "The role of the transferrin-transferrin-receptor system in drug delivery and targeting," *Trends Pharmacol. Sci.*, vol. 23, no. 5, pp. 206–209, 2002.

[167] K. Gkouvatsos, G. Papanikolaou, and K. Pantopoulos, "Regulation of iron transport and the role of transferrin," *Biochim. Biophys. Acta - Gen. Subj.*, vol. 1820, no. 3, pp. 188–202, 2012.

[168] G. Wilcox, "Insulin and insulin resistance," *Clin Biochem Rev*, vol. 26, no. 2, pp. 19–39, 2005.

[169] H. T. Akinbi, R. Epaud, H. Bhatt, and T. E. Weaver, "Bacterial Killing Is Enhanced by Expression of Lysozyme in the Lungs of Transgenic Mice," *J. Immunol.*, vol. 165, no. 10, pp. 5760–5766, 2000.

[170] J. A. Nash, T. N. S. Ballard, T. E. Weaver, and H. T. Akinbi, "The Peptidoglycan-Degrading Property of Lysozyme Is Not Required for Bactericidal Activity In Vivo," *J. Immunol.*, vol. 177, no. 1, pp. 519–526, 2006.

[171] J. LENS, "The solubility curve and the purity of insulin.," *J. Biol. Chem.*, vol. 164, no. 1, pp. 223–231, 1946.

[172] J. J. Verhoef, J. F. Carpenter, T. J. Anchordoquy, and H. Schellekens, "Potential induction of anti-PEG antibodies and complement activation toward PEGylated therapeutics," *Drug Discov. Today*, vol. 19, no. 12, pp. 1945–1952, 2014.

[173] C. Weber, C. Coester, J. Kreuter, and K. Langer, "Desolvation process and surface characterisation of protein nanoparticles," *Int. J. Pharm.*, vol. 194, no. 1, pp. 91–102, 2000.

[174] L. H. Estrada, S. Chu, and J. A. Champion, "Protein nanoparticles for intracellular delivery of therapeutic enzymes," *J. Pharm. Sci.*, vol. 103, no. 6, pp. 1863–1871, 2014.

[175] G. Rajpal and P. Arvan, *Disulfide Bond Formation*. Elsevier Inc., second edi ed., 2013.

[176] S. Fleischer, A. Shapira, O. Regev, N. Nseir, E. Zussman, and T. Dvir, "Albumin fiber scaffolds for engineering functional cardiac tissues," *Biotechnol. Bioeng.*, vol. 111, no. 6, pp. 1246–1257, 2014.

[177] C. D. Spicer and B. G. Davis, "Selective chemical protein modification," *Nat. Commun.*, vol. 5, 2014.

[178] C. Manach, A. Scalbert, C. Morand, C. Rémésy, and L. Jiménez, "Polyphenols: Food sources and bioavailability," *Am. J. Clin. Nutr.*, vol. 79, no. 5, pp. 727–747, 2004.

[179] S. Choubey, L. R. Varughese, V. Kumar, and V. Beniwal, "Medicinal importance of gallic acid and its ester derivatives: a patent review," *Pharm. Pat. Anal.*, vol. 4, no. 4, pp. 305–315, 2015.

[180] N. Kahkeshani, F. Farzaei, M. Fotouhi, S. S. Alavi, R. Bahramsoltani, R. Naseri, S. Momtaz, Z. Abbasabadi, R. Rahimi, M. H. Farzaei, and A. Bishayee, "Pharmacological effects of gallic acid in health and disease: A mechanistic review," *Iran. J. Basic Med. Sci.*, vol. 22, no. 3, pp. 225–237, 2019.

[181] J. L. Lombardi, "Lapping Composition and Methods UsingSame," 2005.

[182] A. Mohraz and M. J. Solomon, "Direct visualization of colloidal rod assembly by confocal microscopy," *Langmuir*, vol. 21, no. 12, pp. 5298–5306, 2005.

[183] J. a. Champion, Y. K. Katare, and S. Mitragotri, "Making polymeric micro- and nanoparticles of complex shapes.," *Proc. Natl. Acad. Sci. U. S. A.*, vol. 104, no. 29, pp. 11901–4, 2007.

[184] A. K. Singla, A. Garg, and D. Aggarwal, "Paclitaxel and its formulations," *Int. J. Pharm.*, vol. 235, no. 1-2, pp. 179–192, 2002.

[185] H. Gelderblom, J. Verweij, K. Nooter, and A. Sparreboom, "Cremophor EL: the drawbacks and advantages of vehicle selection for drug formulation," *Eur J Cancer*, vol. 37, no. 13, pp. 1590–1598, 2001.

[186] H. B. Ruttala and Y. T. Ko, "Liposome encapsulated albumin-paclitaxel nanoparticle for enhanced antitumor efficacy," *Pharm. Res.*, vol. 32, pp. 1002–1016, mar 2015.

[187] J.-M. Lee, T.-J. Yoon, and Y.-S. Cho, "Recent Developments in Nanoparticle-Based siRNA Delivery for Cancer Therapy," *Biomed Res. Int.*, vol. 2013, pp. 1–10, 2013.

[188] M. C. Cortizo and M. F. L. De Mele, "Cytotoxicity of copper ions released from metal: Variation with the exposure period and concentration gradients," *Biol. Trace Elem. Res.*, vol. 102, no. 1-3, pp. 129–141, 2004.

[189] E. BRESLOW, "Comparison of Cupric Ion-Binding Sites in Myoglobin Derivatives and," *J. Biol. Chem.*, vol. 239, no. 10, pp. 3252–3259, 1964.

[190] P. Arosio, B. Jaquet, H. Wu, and M. Morbidelli, "On the role of salt type and concentration on the stability behavior of a monoclonal antibody solution," *Biophys. Chem.*, vol. 168-169, pp. 19–27, 2012.

[191] W. Li, P. Prabakaran, W. Chen, Z. Zhu, Y. Feng, and D. Dimitrov, "Antibody Aggregation: Insights from Sequence and Structure," *Antibodies*, vol. 5, no. 3, p. 19, 2016.

[192] S. Muro, T. Dziubla, W. Qiu, J. Leferovich, X. Cui, E. Berk, and V. R. Muzykantov, "Endothelial targeting of high-affinity multivalent polymer nanocarriers directed to intercellular adhesion molecule 1," *J. Pharmacol. Exp. Ther.*, vol. 317, no. 3, pp. 1161–1169, 2006.

[193] S. Muro, C. Garnacho, J. A. Champion, J. Leferovich, C. Gajewski, E. H. Schuchman, S. Mitragotri, and V. R. Muzykantov, "Control of endothelial targeting and intracellular delivery of therapeutic enzymes by modulating the size and shape of ICAM-1-targeted carriers," *Mol. Ther.*, vol. 16, no. 8, pp. 1450–1458, 2008.

[194] A. K. Hubbard and R. Rothlein, "Intercellular adhesion molecule-1 (ICAM-1) expression and cell signaling cascades," *Free Radic. Biol. Med.*, vol. 28, no. 9, pp. 1379–1386, 2000.

[195] T. M. Bui, H. L. Wiesolek, and R. Sumagin, "ICAM-1: A master regulator of cellular responses in inflammation, injury resolution, and tumorigenesis," *Physiol. Behav.*, vol. 63, no. 8, pp. 1–18, 2014.

[196] X. Xie, X. Wu, J. Cui, H. Li, and X. Yan, "Increase ICAM-1 and LFA-1 expression by cerebrospinal fluid of subarachnoid hemorrhage patients: Involvement of TNF-α," *Brain Res.*, vol. 1512, pp. 89–96, 2013.

[197] M. J. Davies, J. L. Gordon, A. J. Gearing, R. Pigott, N. Woolf, D. Katz, and A. Kyriakopoulos, "The expression of the adhesion molecules ICAM1, VCAM1, PECAM, and Eselectin in human atherosclerosis," *J. Pathol.*, vol. 171, no. 3, pp. 223–229, 1993.

[198] C. Alifieris and D. T. Trafalis, "Glioblastoma multiforme: Pathogenesis and treatment," *Pharmacol. Ther.*, vol. 152, pp. 63–82, 2015.

[199] M. E. Davis, "Glioblastoma: Overview of Disease and Treatment," *Clin J Oncol Nurs*, vol. 20, no. 5, pp. 1–14, 2016.

[200] R. Stupp, W. P. Mason, M. J. van den Bent, M. Weller, B. Fisher, M. J. B. Taphoorn, K. Belanger, A. A. Brandes, C. Marosi, U. Bogdahn, J. Curschmann, R. C. Janzer, S. K. Ludwin, T. Gorlia, A. Allgeier, D. Lacombe, J. G. Cairncross, E. Eisenhauer, R. O. Mirimanoff, European Organisation for Research and Treatment of Cancer Brain Tumor and Radiotherapy Groups, and National Cancer Institute of Canada Clinical Trials Group, "Radiotherapy plus concomitant and adjuvant temozolomide for glioblastoma.," *N. Engl. J. Med.*, vol. 352, no. 10, pp. 987–96, 2005.

[201] O. Van Tellingen, B. Yetkin-Arik, M. C. De Gooijer, P. Wesseling, T. Wurdinger, and H. E. De Vries, "Overcoming the blood-brain tumor barrier for effective glioblastoma treatment," *Drug Resist. Updat.*, vol. 19, pp. 1–12, 2015.

[202] CBTRUS, "CBTRUS Statistical Report: Primary Brain and Central Nervous System Tumors Diagnosed in the United States in 2004-2008," 2012.

[203] J. E. Kim, M. Patel, J. Ruzevick, C. M. Jackson, and M. Lim, "STAT3 activation in glioblastoma: Biochemical and therapeutic implications," *Cancers (Basel).*, vol. 6, pp. 376–395, 2014.

[204] M. Abou-Ghazal, D. S. Yang, W. Qiao, C. Reina-Ortiz, J. Wei, L. Y. Kong, G. N. Fuller, N. Hiraoka, W. Priebe, R. Sawaya, and A. B. Heimberger, "The incidence, correlation with tumor-infiltrating inflammation, and prognosis of phosphorylated STAT3 expression in human gliomas," *Clin Cancer Res*, vol. 14, no. 24, pp. 8228–8235, 2008.

[205] D. Ganguly, M. Fan, C. H. Yang, B. Zbytek, D. Finkelstein, M. F. Roussel, and L. M. Pfeffer, "The critical role that STAT3 plays in glioma-initiating cells: STAT3 addiction in glioma," *Oncotarget*, vol. 9, no. 31, pp. 22095–22112, 2018.

[206] N. de la Iglesia, S. V. Puram, and A. Bonni, "STAT3 regulation of glioblastoma pathogenesis.," *Curr. Mol. Med.*, vol. 9, no. 5, pp. 580–90, 2009.

[207] V. Gajbhiye and N. K. Jain, "The treatment of Glioblastoma Xenografts by surfactant conjugated dendritic nanoconjugates," *Biomaterials*, vol. 32, no. 26, pp. 6213–6225, 2011.

[208] H. Gao, J. Qian, Z. Yang, Z. Pang, Z. Xi, S. Cao, Y. Wang, S. Pan, S. Zhang, W. Wang, X. Jiang, and Q. Zhang, "Whole-cell SELEX aptamer-functionalised poly(ethyleneglycol)-poly(ϵ-caprolactone) nanoparticles for enhanced targeted glioblastoma therapy," *Biomaterials*, vol. 33, no. 26, pp. 6264–6272, 2012.

[209] K. Shi, J. Zhou, Q. Zhang, H. Gao, Y. Liu, T. Zong, and Q. He, "Arginine-glycine-aspartic acid-modified lipid-polymer hybrid nanoparticles for docetaxel delivery in glioblastoma multiforme," *J. Biomed. Nanotechnol.*, vol. 11, no. 3, pp. 382–391, 2015.

[210] L. P. Ganipineni, B. Ucakar, N. Joudiou, R. Riva, C. Jérôme, B. Gallez, F. Danhier, and V. Préat, "Paclitaxel-loaded multifunctional nanoparticles for the targeted treatment of glioblastoma," *J. Drug Target.*, vol. 27, no. 5-6, pp. 614–623, 2019.

[211] T. Kang, M. Jiang, D. Jiang, X. Feng, J. Yao, Q. Song, H. Chen, X. Gao, and J. Chen, "Enhancing Glioblastoma-Specific Penetration by Functionalization of Nanoparticles with an Iron-Mimic Peptide Targeting Transferrin/Transferrin Receptor Complex," *Mol. Pharm.*, vol. 12, no. 8, pp. 2947–2961, 2015.

[212] T. Kang, Q. Zhu, D. Jiang, X. Feng, J. Feng, T. Jiang, J. Yao, Y. Jing, Q. Song, X. Jiang, X. Gao, and J. Chen, "Synergistic targeting tenascin C and neuropilin-1 for specific penetration of nanoparticles for anti-glioblastoma treatment," *Biomaterials*, vol. 101, pp. 60–75, 2016.

[213] F. Y. Yang, T. T. Wong, M. C. Teng, R. S. Liu, M. Lu, H. F. Liang, and M. C. Wei, "Focused ultrasound and interleukin-4 receptor-targeted liposomal doxorubicin for enhanced targeted drug delivery and antitumor effect in glioblastoma multiforme," *J. Control. Release*, vol. 160, no. 3, pp. 652–658, 2012.

[214] J. Zhou, T. R. Patel, R. W. Sirianni, G. Strohbehn, M.-Q. Zheng, N. Duong, T. Schafbauer, A. J. Huttner, Y. Huang, R. E. Carson, Y. Zhang, D. J. Sullivan, J. M. Piepmeier, and W. M. Saltzman, "Highly penetrative, drug-loaded nanocarriers improve treatment of glioblastoma.," *Proc. Natl. Acad. Sci. U. S. A.*, vol. 110, no. 29, pp. 11751–6, 2013.

[215] K. T. Householder, D. M. Diperna, E. P. Chung, G. M. Wohlleb, H. D. Dhruv, M. E. Berens, and R. W. Sirianni, "Intravenous delivery of camptothecin-loaded PLGA nanoparticles for the treatment of intracranial glioma," *Int. J. Pharm.*, vol. 479, no. 2, pp. 374–380, 2015.

[216] A. Gaudin, E. Song, A. R. King, J. K. Saucier-Sawyer, R. Bindra, D. Desmaële, P. Couvreur, and W. M. Saltzman, "PEGylated squalenoyl-gemcitabine nanoparticles for the treatment ofglioblastoma," *Biomaterials*, vol. 105, pp. 136–144, 2016.

[217] A. R. King, C. D. Corso, E. M. Chen, E. Song, P. Bongiorni, Z. Chen, R. K. Sundaram, R. S. Bindra, and W. M. Saltzman, "Local DNA Repair Inhibition for Sustained Radiosensitization of High-Grade Gliomas," *Mol. Cancer Ther.*, vol. 16, no. 8, pp. 1456–1469, 2017.

[218] C.-X. Zhang, W.-Y. Zhao, L. Liu, R.-J. Ju, L.-M. Mu, Y. Zhao, F. Zeng, H.-J. Xie, Y. Yan, and W.-L. Lu, "A nanostructure of functional targeting epirubicin liposomes dually modified with aminophenyl glucose and cyclic pentapeptide used for brain glioblastoma treatment," *Oncotarget*, vol. 6, no. 32, 2015.

[219] M. Kaluzova, A. Bouras, R. Machaidze, and C. G. Hadjipanayis, "Targeted therapy of glioblastoma stem-like cells and tumor non-stem cells using cetuximab-conjugated iron-oxide nanoparticles," *Oncotarget*, vol. 6, no. 11, 2015.

[220] A. Bouras, M. Kaluzova, and C. G. Hadjipanayis, "Radiosensitivity enhancement of radioresistant glioblastoma by epidermal growth factor receptor antibody-conjugated iron-oxide nanoparticles," *J. Neurooncol.*, vol. 124, no. 1, pp. 13–22, 2015.

[221] Z. R. Cohen, S. Ramishetti, N. Peshes-Yaloz, M. Goldsmith, A. Wohl, Z. Zibly, and D. Peer, "Localized RNAi therapeutics of chemoresistant grade IV glioma using hyaluronan-grafted lipid-based nanoparticles," *ACS Nano*, vol. 9, no. 2, pp. 1581–1591, 2015.

[222] F. Danhier, K. Messaoudi, L. Lemaire, J. P. Benoit, and F. Lagarce, "Combined anti-Galectin-1 and anti-EGFR siRNA-loaded chitosan-lipid nanocapsules decrease temozolomide resistance in glioblastoma: In vivo evaluation," *Int. J. Pharm.*, vol. 481, no. 1-2, pp. 154–161, 2015.

[223] G. Erel-Akbaba, L. A. Carvalho, T. Tian, M. Zinter, H. Akbaba, P. J. Obeid, E. A. Chiocca, R. Weissleder, A. G. Kantarci, and B. A. Tannous, "Radiation-induced targeted nanoparticle-based gene delivery for brain tumor therapy," *ACS Nano*, vol. 13, no. 4, pp. 4028–4040, 2019.

[224] Y. E. Seo, H. W. Suh, R. Bahal, A. Josowitz, J. Zhang, E. Song, J. Cui, S. Noorbakhsh, C. Jackson, T. Bu, A. Piotrowski-Daspit, R. Bindra, and W. M. Saltzman, "Nanoparticle-mediated intratumoral inhibition of miR-21 for improved survival in glioblastoma," *Biomaterials*, vol. 201, no. December 2018, pp. 87–98, 2019.

[225] L. Agemya, D. Friedmann-Morvinskib, V. R. Kotamrajua, L. Rotha, K. N. Sugaharac, O. M. Girardd, R. F. Mattreyd, I. M. Vermab, and Erkki Ruoslahti, "Targeted nanoparticle enhanced proapoptotic peptide as potential therapy for glioblastoma," *Proc. Natl. Acad. Sci.*, vol. 108, no. 42, pp. 17450–17455, 2011.

[226] K. R. Spindler and T. H. Hsu, "Viral disruption of the blood-brain barrier," *Trends Microbiol.*, vol. 20, no. 6, pp. 282–290, 2012.

[227] G. Gu, X. Gao, Q. Hu, T. Kang, Z. Liu, M. Jiang, D. Miao, Q. Song, L. Yao, Y. Tu, Z. Pang, H. Chen, X. Jiang, and J. Chen, "The influence of the penetrating peptide iRGD on the effect of paclitaxel-loaded MT1-AF7p-conjugated nanoparticles on glioma cells," *Biomaterials*, vol. 34, no. 21, pp. 5138–5148, 2013.

[228] G. Tabatabai, M. Weller, B. Nabors, M. Picard, D. Reardon, T. Mikkelsen, C. Ruegg, and R. Stupp, "Targeting integrins in malignant glioma," *Target. Oncol.*, vol. 5, no. 3, pp. 175–181, 2010.

[229] L. Bello, M. Francolini, P. Marthyn, J. Zhang, R. S. Carroll, D. C. Nikas, J. F. Strasser, R. Villani, D. A. Cheresh, and P. M. Black, "Alpha(v)beta3 and alpha(v)beta5 integrin expression in glioma periphery.," *Neurosurgery*, vol. 49, no. 2, pp. 380–389, 2001.

[230] N. Desai, V. Trieu, B. Damascelli, and P. Soon-Shiong, "SPARC Expression Correlates with Tumor Response to Albumin-Bound Paclitaxel in Head and Neck Cancer Patients," *Transl. Oncol.*, vol. 2, no. 2, pp. 59–64, 2009.

[231] C. Iancu, L. Mocan, C. Bele, A. I. Orza, F. A. Tabaran, C. Catoi, R. Stiufiuc, A. Stir, C. Matea, D. Iancu, L. Agoston-Coldea, F. Zaharie, and T. Mocan, "Enhanced laser thermal ablation for the in vitro treatment of liver cancer by specific delivery of multiwalled carbon nanotubes functionalized with human serum albumin," *Int. J. Nanomedicine*, vol. 6, no. 1, pp. 129–141, 2011.

[232] S. Kunigal, C. Gondi, M. Gujrati, S. S. Lakka, D. H. Dinh, W. C. Olivero, and J. S. Rao, "SPARC-Induced Migration of Glioblastoma Cell Lines via uPA- uPAR Signaling and Activation of Small GTPase RhoA," *PLoS One*, vol. 32, no. 7, pp. 736–740, 2017.

[233] W. A. Golembieski and S. A. Rempel, "cDNA array analysis of SPARC-modulated changes in glioma gene expression," *J. Neurooncol.*, vol. 60, no. 3, pp. 213–226, 2002.

[234] J. E. Schnitzer, "Gp60 Is an Albumin-Binding Glycoprotein Expressed By Continuous Endothelium Involved in Albumin Transcytosis By Continuous Endothelium Glycoprotein Expressed Involved in Albumin Transcytosis," *Am J Physiol.*, vol. 262, pp. 246–54, 1992.

[235] K. N. Sugahara, T. Teesalu, P. P. Karmali, V. R. Kotamraju, L. Agemy, O. M. Girard, D. Hanahan, R. F. Mattrey, and E. Ruoslahti, "Tissue-Penetrating Delivery of Compounds and Nanoparticles into Tumors," *Cancer Cell*, vol. 16, no. 6, pp. 510–520, 2009.

[236] K. N. Sugahara, T. Teesalu, P. P. Karmali, V. R. Kotamraju, L. Agemy, D. R. Greenwald, and E. Ruoslahti, "Co-administration of a Tumor-Penetrating Peptide Enhances the Efficacy of Cancer Drugs," *Science (80-.).*, vol. 328, no. 5981, pp. 1031–1035, 2010.

[237] X. Liu, J. Jiang, Y. Ji, J. Lu, R. Chan, and H. Meng, "Targeted drug delivery using iRGD peptide for solid cancer treatment," *Mol. Syst. Des. Eng.*, vol. 2, no. 4, pp. 370–379, 2017.

[238] W. Zhang, X. Qu, B. Chen, M. Snyder, B. Li, Y. Tang, H. Chen, W. Zhu, N. Yin, D. Li, X. Li, Y. Liu, J. Jillian, X.-y. Fu, M. Rubart, L.-s. Song, W. Shou, F. Hospital, P. U. Medical, and I. City, "A Pilot Study of Dose-Dense Paclitaxel With Trastuzumab and Lapatinib for Node-negative HER2-Overexpressed Breast Cancer," *Clin. Breast Cancer*, vol. 133, no. 1, pp. 48–61, 2017.

[239] L. Ma, Q. Chen, P. Ma, M. K. Han, Z. Xu, Y. Kang, B. Xiao, and D. Merlin, "IRGD-functionalized PEGylated nanoparticles for enhanced colon tumor accumulation and targeted drug delivery," *Nanomedicine*, vol. 12, no. 16, pp. 1991–2006, 2017.

[240] A. J. Pratt and I. J. MacRae, "The RNA-induced silencing complex: A versatile gene-silencing machine," *J. Biol. Chem.*, vol. 284, no. 27, pp. 17897–17901, 2009.

[241] M. Dominska and D. M. Dykxhoorn, "Breaking down the barriers: siRNA delivery and endosome escape," *J. Cell Sci.*, vol. 123, no. 8, pp. 1183–1189, 2010.

[242] W. T. Godbey, K. K. Wu, and A. G. Mikos, "Poly(ethylenimine)-mediated gene delivery affects endothelial cell function and viability," *Biomaterials*, vol. 22, no. 5, pp. 471–480, 2001.

[243] S. Barua and S. Mitragotri, "Challenges associated with penetration of nanoparticles across cell and tissue barriers: A review of current status and future prospects," *Nano Today*, vol. 9, no. 2, pp. 223–243, 2014.

[244] M. Candolfi, J. F. Curtin, W. S. Nichols, A. K. Muhammad, G. D. King, G. E. Pluhar, E. A. McNiel, J. R. Ohlfest, A. B. Freese, P. F. Moore, J. Lerner, P. R. Lowenstein, and M. G. Castro, "Intracranial glioblastoma models in preclinical neuro-oncology: Neuropathological characterization and tumor progression," *J. Neurooncol.*, vol. 85, no. 2, pp. 133–148, 2007.

[245] M. Longmier, P. L. Choyke, and H. Kobayashi, "Clearance Properties of Nano-sized Particles and Molecules as Imaging Agents: Consideration and Caveats," *Nanomedicine*, vol. 3, no. 5, pp. 703–717, 2008.

[246] A. Jahangiri, M. Dadmanesh, and K. Ghorban, "Suppression of STAT3 by S31-201 to reduce the production of immunoinhibitory cytokines in a HIF1-α-dependent manner: a study on the MCF-7 cell line," *Vitr. Cell. Dev. Biol. - Anim.*, vol. 54, no. 10, pp. 743–748, 2018.

[247] X. Sun, J. Wang, M. Huang, T. Chen, J. Chen, F. Zhang, H. Zeng, Z. Xu, and Y. Ke, "STAT3 promotes tumour progression in glioma by inducing FOXP1 transcription," *J. Cell. Mol. Med.*, vol. 22, no. 11, pp. 5629–5638, 2018.

[248] D. E. Johnson, R. A. O'Keefe, and J. R. Grandis, "Targeting the IL-6/JAK/STAT3 signalling axis in cancer," *Nat. Rev. Clin. Oncol.*, vol. 15, no. 4, pp. 234–248, 2018.

[249] M. Zheng, W. Tao, Y. Zou, O. C. Farokhzad, and B. Shi, "Nanotechnology-Based Strategies for siRNA Brain Delivery for Disease Therapy," *Trends Biotechnol.*, vol. 36, no. 5, pp. 562–575, 2018.

[250] S. You, R. Li, D. Park, M. Xie, G. L. Sica, Y. Cao, Z.-Q. Xiao, and X. Deng, "Disruption of STAT3 by Niclosamide Reverses Radioresistance of Human Lung Cancer," *Mol. Cancer Ther.*, vol. 13, no. 3, pp. 606–616, 2014.

[251] X. Li, H. Wang, X. Lu, and B. Di, "Silencing STAT3 with short hairpin RNA enhances radiosensitivity of human laryngeal squamous cell carcinoma xenografts in vivo," *Exp. Ther. Med.*, vol. 1, no. 6, pp. 947–953, 2010.

[252] K. Leder, K. Pitter, Q. Laplant, D. Hambardzumyan, B. D. Ross, T. A. Chan, E. C. Holland, and F. Michor, "Mathematical modeling of pdgf-driven glioblastoma reveals optimized radiation dosing schedules," *Cell*, vol. 156, no. 3, pp. 603–616, 2014.

[253] F. J. Núñez, F. M. Mendez, P. Kadiyala, M. S. Alghamri, M. G. Savelieff, M. B. Garcia-Fabiani, S. Haase, C. Koschmann, A. A. Calinescu, N. Kamran, M. Saxena, R. Patel, S. Carney, M. Z. Guo, M. Edwards, M. Ljungman, T. Qin, M. A. Sartor, R. Tagett, S. Venneti, J. Brosnan-Cashman, A. Meeker, V. Gorbunova, L. Zhao, D. M. Kremer, L. Zhang, C. A. Lyssiotis, L. Jones, C. J. Herting, J. L. Ross, D. Hambardzumyan, S. Hervey-Jumper, M. E. Figueroa, P. R. Lowenstein, and M. G. Castro, "IDH1-R132H acts as a tumor suppressor in glioma via epigenetic up-regulation of the DNA damage response," *Sci. Transl. Med.*, vol. 11, no. 479, pp. 1–14, 2019.

[254] S. D. Li and L. Huang, "Pharmacokinetics and biodistribution of nanoparticles," *Mol. Pharm.*, vol. 5, no. 4, pp. 496–504, 2008.

[255] P. Kadiyala, D. Li, G. Yang, C. Sau, W. Lai, J. Cichon, and W. Li, "High Density Lipoprotein-Mimicking Nanodiscs for Chemo- Immunotherapy against Glioblastoma Multiforme," vol. 13, no. 2, pp. 1365–1384, 2019.